UNIVERSIDAD COMPLUTENSE DE MADRID
FACULTAD DE CIENCIAS FÍSICAS

TESIS DOCTORAL

Nanostructuring and properties of polymer surfaces with applications in energy

Nanoestructuración y propiedades de superficies de polímeros con aplicaciones en energía

MEMORIA PARA OPTAR AL GRADO DE DOCTOR

PRESENTADA POR

Jing Cui

DIRECTORES

Aurora Nogales Ruiz
Esther Rebollar González

Madrid, 2017

UNIVERSIDAD COMPLUTENSE DE MADRID

FACULTAD DE CIENCIAS FÍSICAS

Tesis doctoral

Nanoestructuración y propiedades de superficies de polímeros con aplicaciones en energía

Nanostructuring and properties of polymer surfaces with applications in energy

Memoria para optar al título de Doctor

Presentada por Jing Cui

Directores: Aurora Nogales (IEM-CSIC)
Esther Rebollar (IQFR-CSIC)

Madrid, 2016

CSIC
CONSEJO SUPERIOR DE INVESTIGACIONES CIENTÍFICAS

Nanoestructuración y propiedades de superficies de polímeros con aplicaciones en energía

Nanostructuring and properties of polymer surfaces with applications in energy

Memoria presentada para optar al título de Doctor en Ciencias Físicas por la Universidad Complutense de Madrid

Presentada por Jing Cui

Directores: Aurora Nogales (IEM-CSIC)
Esther Rebollar (IQFR-CSIC)

2016, Madrid

Dedicated to my family

致家人

Acknowledgement

During more than four years, I had the luck to work and learn in the SOFTMATPOL (IEM-CSIC) group. This opportunity was possible thanks to the China Scholarship Council (CSC) that funded the doctoral research at IEM-CSIC.

A long list of people comes to my head. I have to thank them for many things.

First and foremost, I would like to thank my Thesis supervisors, Dr. Aurora Nogales (IEM-CSIC) and Dr. Esther Rebollar (IQFR-CSIC), not only for having always time to dedicate to me, but also for their trust and their altruistic assistance, that is what has really led this Thesis to succeed.

Also, thanks to everyone who contributed to this work, especially Prof. Tiberio Ezquerra, Dr. Alejandro Sanz, Dr. Daniel Martinez-Tong, Dr. Margarita Hernández and Dr. Mari Cruz García-Gutiérrez, for their helpful discussions within the group. I have learned many things and also I enjoyed my time with them. Thanks too to Dr. Carolina García (IQFR-CSIC), Prof. Jose Vicente García Ramos (IEM-CSIC) and Dr. Juan Rodríguez-Hernández (ICTP-CSIC), for their engagement in scientific and technical collaboration.

As part of my research training, I consider myself lucky to study in Máster/Doctorado de Alta Especialización en Plásticos y Caucho at the Instituto de Ciencia y Tecnología de Polímeros (ICTP-CSIC), in collaboration with Universidad Internacional Menéndez Pelayo. There I met nice professors like Prof. Fernando Catalina, Prof. Miguel Angel López-Manchado, Dr Raquel Verdejo, …

I am also thankful for the kindness and support of many people in Madrid, especially the staff at Instituto de Estructura de la Materia (IEM-CSIC), for their great job in charge of all the bureaoucracy during my doctoral period, keeping my work/life balanced. Also, thanks to Consuelo and Eva from Almacén at Instituto Rocasolano (IQFR-CSIC).

I do not want to forget to mention my gratitude to all my colleagues from this fantastic group, SOFTMATPOL. I would like to remember here both present and past members, for taking me under their wings when I first arrived in Madrid, and for providing such a friendly and relaxed atmosphere at work: Dr. Amelia Linares, Dr. Esperanza Cagiao, Dr. Daniel Rueda, Dr. José Carlos Canalda, and especially my office mates, Dr. Michela Soccio, Dr. Jaime J. Hernández, Dr. Ignacio Martín Fabiani, M. Sc Alvaro Rodríguez and M. Sc Edgar Gutiérrez. Some of the people in the paragraphs above should also be in this list, but I will not mention them twice.

At the Master time, I met really nice classmates: José Antonio, Guiomar, Alicia, Sheyla, to name a few. Thanks for taking interest in a graduate student who was too shy to ask questions in class.

In summary, thank you friends in Madrid and in China. May I wish our friendship last forever!

I left my family for the end, to whom I am greatly indebted. Thanks to my parents for their love, patience and support that helped me to finish this Thesis. Thanks to my sister and brother, for their unconditional care of our parents while I am away.

Table of Contents

Abstract

The integration of functional polymers in organic electronics has attracted great interest for their potential application in photovoltaics or diodes due to their characteristics such as high chemical tenability, low temperature processing, light weight and durability, among others. The incorporation of polymers into nowadays devices, that tend towards miniaturization, rises several challenges. In general, the macroscopic properties of polymers are closely related to their structure, that is hierarchical, from the nanometer to the millimeter scale. Hence, from a fundamental viewpoint, understanding the effect of the above mentioned miniaturization in the structure and physical phenomena would provide control over the properties of the nanoscaled polymer materials, helping in the design of new potential applications. In this Thesis we have attempted to fulfill the objective of preparing binary systems formed by pairs of functional polymers or pairs of organics materials, and understanding the modification of certain polymer properties when nanostructuring them, mainly in their surfaces.

For the preparation of these binary systems we employed different methodologies: direct solution blending (Chapter 3, blends of donor/acceptor organic compounds, Chapter 4, blends of semiconducting and ferroelectric polymers), bilayer structures from semiconducting/ ferroelectric polymers, prepared by sequential spin coating (Chapter 4) and nanostructuring of a ferroelectric polymer in the form of nanospheres to be incorporated in a semiconducting polymer film (Chapter 4). In Chapter 3, the conduction mechanism and the molecular dynamics on a bulk heterojunction formed by a binary blend of donor/acceptor organic compounds have been studied by dielectric spectroscopy. In Chapter 4, the modification of the ferroelectric properties in poly(vinylidene fluoride- trifluoroethylene) copolymers due to nanostructuring and to the combination with a semiconducting polymer have been addressed by Piezoresponse force microscopy. Nanostructured functional polymer surfaces were prepared by laser techniques, mainly Laser Induced Periodic Surface Structures (LIPSS). In Chapter 5, we first report on the creation of LIPSS on a model polymer: polystyrene. This allowed us to address all the possible characteristics of the material and the substrate that may affect the formation and quality of LIPSS (Chapter 5). The obtained know-how from that study is the basis of the surface nanostructuring of functional systems, like a semiconducting polymer, poly(3-hexylthiophene), P3HT (Chapter 5), and a more complex binary system formed by bilayer of semiconducting/ferroelectric polymer (Chapter 6). In this latter case, the challenge of using laser techniques to structure a non-absorbing polymer (the ferroelectric one) is tackled. In Chapters 5 and 6, the inner crystalline structure of the polymer thin films has been addressed by using X ray scattering techniques in grazing incidence geometry. The main results of this work are the understanding on the modification of the conduction mechanism in a binary system with respect to the one component mechanism, the control over the parameters that rule the formation of LIPSS on a polymer thin film, its application to more complicated functional polymer structures and the modification of the ferroelectricity in ferroelectric polymer nanostructures due to the presence of a semiconducting polymer adjacent phase. The main conclusion of this Thesis is that, it is very important to comprehend the role of fundamental parameters on the underlying physical processes in the construction of a functional polymer surface by nanostructuring.

Resumen

La integración de polímeros funcionales en la electrónica orgánica es de gran interés por su potencial aplicación en dispositivos fotovoltaicos y diodos, debido principalmente a características tales como la alta resistencia química, la posibilidad de procesado a baja temperatura, su ligereza y durabilidad, entre otras. La incorporación de polímeros en los dispositivos actuales que tienden a la miniaturización afronta varios retos. En general, las propiedades macroscópicas de polímeros están estrechamente relacionadas con su estructura, que es jerárquica desde la escala de los nanómetros a la milimétrica. Por lo tanto, desde el punto de vista fundamental, comprender el efecto de la mencionada miniaturización en la estructura y los fenómenos físicos de estos polímeros proporcionaría control sobre las propiedades de los materiales poliméricos incorporados en dispositivos ayudando al diseño de nuevas aplicaciones potenciales. En esta Tesis hemos tratado de cumplir con el objetivo de preparar sistemas binarios formados por pares de polímeros funcionales o pares de materiales orgánicos, y comprender las variaciones de ciertas propiedades del polímero cuando se nanoestructura, sobre todo cuando se crean superficies nanoestructuradas.

Para la preparación de estos sistemas binarios se emplearon diferentes metodologías: la mezcla directa en solución (Capítulo 3, mezclas de los compuestos orgánicos donadores / aceptores, Capítulo 4, mezclas de polímeros semiconductores y ferroeléctricos), las estructuras de dos capas de polímeros semiconductores / ferroeléctricos, preparadas por ‘spin coating’ secuencial (Capítulo 4) y nanoestructuración de polímero ferroeléctrico en forma de nanoesferas que se incorpora a una película de polímero semiconductor (Capítulo 4). En lo que se refiere al estudio de procesos físicos fundamentales en estos sistemas, en el Capítulo 3, el mecanismo de conducción y la dinámica molecular en una heterounión en volumen formada por la mezcla de compuestos orgánicos donador / aceptor se ha estudiado mediante espectroscopia dieléctrica. En el Capítulo 4, la modificación de las propiedades ferroeléctricas en copolímeros al azar de poli(fluoruro de vinilideno) y poli(trifluoroetileno) debida a nanoestructuración y a la combinación con polímeros semiconductores han sido abordadas por Microscopía de Piezorespuesta. Por otro lado, se han creado superficies nanoestructuradas de polímeros funcionales mediante técnicas láser, principalmente se crearon *Laser Induced Periodic Surface Structures* (LIPSS) en un polímero semiconductor, y también en un polímero modelo. Mediante el estudio sistemático de la creación de LIPSS en el polímero modelo, poliestireno, evaluamos el efecto de las características del material y del sustrato en la calidad de las estructuras obtenidas (Capítulo 5). El conocimiento adquirido en ese estudio permitió afrontar la nanoestructuración de

superficies de sistemas funcionales, tales como superficies de polímero semiconductor, poli(3-hexiltiofeno), P3HT (Capítulo 5), y la superficie de un sistema binario más complejo formado por dos capas de polímero semiconductor / polímero ferroeléctrico (Capítulo 6). En este último caso, se añadía el reto de la utilización de técnicas láser para estructurar un polímero no absorbente (el ferroeléctrico). En los Capítulos 5 y 6, la estructura cristalina interna de las películas delgadas de polímero se ha estudiado mediante el uso de técnicas de dispersión de rayos X en geometría de incidencia rasante.

Los principales resultados de este trabajo son la comprensión de la modificación del mecanismo de conducción en un sistema binario con respecto al mecanismo de un único componente, el control sobre los parámetros que gobiernan la formación de LIPSS en una película fina de polímero, y su aplicación a estructuras más complicadas de polímeros funcionales, y finalmente la modificación de la ferroelectricidad en nanoestructuras de polímeros ferroeléctricos, debido a la presencia de una fase adyacente polímero semiconductor.

Para terminar, la conclusión principal de esta tesis es que, es crucial comprender el papel de los parámetros fundamentales en los procesos físicos subyacentes en la construcción de una superficie nanoestructurada de polímeros funcionales.

List of symbols and abbreviations

2D	Two-dimension
$\mathrm{\alpha}$	Inverse localization length
α	Linear absorption coefficient
α_i	Incident angle of X-ray scattering
$\boldsymbol{\alpha}$	Exit angle of X-ray scattering
$\Delta\varepsilon$	Relaxation strength
ε	Extinction coefficient
ε^*	Complex dielectric permittivity
ε'	Real part of the dielectric permittivity
ε''	Imaginary part of the dielectric permittivity
γ^d	Dispersive component of the surface free energy
γ_l^d	Dispersive component of the surface free energy of the liquid
γ_l^p	Polar component of the surface free energy of the liquid
γ_l	Surface free energy of the liquid
γ_l^+	Electron-acceptor component of the surface free energy of liquid
γ_l^-	Electron-donor component of the surface free energy of liquid
γ_s	Surface free energy of the solid
γ_s^d	Dispersive component of the surface free energy of the solid
γ_s^p	Polar component of the surface free energy of the solid
γ_s^+	Electron-acceptor component of the surface free energy of solid
γ_s^-	Electron-donor component of the surface free energy of solid
γ_{sl}	Interfacial tension between the liquid and solid
γ^p	Polar component of the surface free energy
κ	Thermal conductivity
λ	Wavelength
μ	Electrical mobility of charge carriers
$\mathrm{\theta}$	Laser incidence angle
$\boldsymbol{\theta}$	X-ray scattering angle
θ	Contact angle
ρ	Density
σ	Energetic disorder parameter
σ_{dc}	dc conductivity

σ^*	Complex dielectric conductivity
σ'	Real part of dielectric conductivity
σ''	Imaginary part of dielectric conductivity
τ	Pulse duration
ω	Angular frequency
$\mathrm{\omega}$	Out-of-plane scattering angle
ζ	Thermal diffusion length
A	Absorbance
A	Acceptor
c	Concentration of polymer solution
c	Specific heat at constant pressure
d	Spacing from Bragg's law
D	Donor
D	Thermal diffusivity
$\Delta \mathrm{T}$	Temperature increase
$\mathrm{E_a}$	Activation energy
$\mathrm{E_a^{dipolar}}$	Activation energy for the dipolar process
$\mathrm{E_a^{dc}}$	Activation energy for the conduction process
$\mathrm{E_c}$	Coercive Field
E_c	Largest barrier in the hopping conduction
$\mathrm{E_g}$	Gap energy
f	Frequency
F	Laser fluence
F_0	Incident laser fluence
$\mathrm{F_c}$	Critical frequency
G	Glass
H	Ripples depth
I	Intensity of the transmitted light
$\mathrm{I_0}$	Intensity of the incident light
k	Boltzman constant
$\overrightarrow{K_\iota}, \overrightarrow{K_f}$	Incidence wave vector, scattered wave vector
l	Optical path/ film thickness
L	Period of ripples
M^*	Complex dielectric module
M'	Real part of the dielectric module
M''	Imaginary part of the dielectric module
$\mathrm{M_n}$	Number average molecular weight

$\mathrm{M_w}$	Weight average molecular weight
n	Refractive index
n	Number density of charge carriers
n_i	Numerical fraction of molecules of molar mass M_i
N	Number of pulses
$\mathrm{N_i}$	Number of molecules of molar mass M_i,
N	Degree of polymerization
q, q_x,q_y, q_z	Scattering vector and x,y and z components of the reciprocal scattering vector
Q	Quartz
R	Gas constant
$\mathrm{R_a}$	Average roughness
Si	Silicon
t	Time after the laser pulse
t_d	Thermal diffusion time
T	Temperature
T	Transmittance
$\mathrm{T_c}$	Curie temperature
$\mathrm{T_g}$	Glass transition temperature
$\mathrm{T_m}$	Melting temperature
$\mathrm{V_c}$	Coercive voltage
W	Probability of hopping
x	Depth from the film surface
AAO	Anodic Aluminium Oxide
ac	Alternating Current
AFM	Atomic Force Microscopy
BDS	Broadband Dielectric Spectroscopy
BHJ	Bulk Heterojunctions
BNN	Barton-Nakajima Namikawa
C-AFM	Conductive AFM
CA	Contact angle
$CHCl_3$	Chloroform
dc	Direct Current
DMA	N,N-Dimethylacetamide
ESRF	European Synchrotron Radiation Facility
FeRAM	Ferroelectric Random Access Memory
FeFET	Ferroelectric Field-Effect Transistors

GISAXS	Grazing Incidence Small Angle X-ray Scattering
GIWAXS	Grazing Incidence Wide Angle X-ray Scattering
HH	Head-to-Head coupling
HT	Head-to-Tail coupling
HOMO	Highest Occupied Molecular Orbital
I-V	Current–Voltage curve in C-AFM
IR	Infrared
KPFM	Kelvin Probe Force Microscopy
LIL	Laser Interference Lithography
LIPSS	Laser Induced Period Surface Structure
LUMO	Lowest Unoccupied Molecular Orbital
MEK	Methyl Ethyl Ketone
MFM	Magnetic Force Microscopy
NIR	Near InfraRed
NPs	NanoParticles
OFETs	Organic Field-Effect Transistors
OLEDs	Organic Light-Emitting Diodes
OPVs	Organic PhotoVoltaics
OWRK-model	Owens, Wendt, Rabel and Kaelble model
PA	Polyacetylene
PEMA	Polyethylmethacrylate
PLLA-b-PEO	Poly(Levo-lactide acide)-b-Poly(ethylene oxide) copolymers
P3AT	Poly(3-alkyl) thiophene
P3HT	Poly(3-hexylthiophene-2,5-diyl)
PC6$_{1}$BM	Phenyl-C61-butyric acid methyl ester
PC$_{71}$BM	Phenyl-C71-butyric acid methyl ester
PDI	Polydispersity index
PE	Polyethylene
PFM	Piezoresponse Force Microscopy
PS	Poly(styrene)
PTrFE	Poly(trifluoroethylene)
PVDF	Polyvinylidenefluoride
P(VDF-TrFE)	Poly(vinylidene fluoride - trifluoro ethylene)
QNM	Quantitative Nanomechanical Mapping
RR-P3HT	Regioregular P3HT
SAXS	Small Angle X-Ray Scattering
SC	Spin coated films

SPM	Scanning Probe Microscopy
THF	Tetrahydrofurane
ToF	Time of flight
TT	Tail-to-Tail coupling
UV	Ultraviolet
UV-Vis	Ultraviolet-Visible
VRH	Variable-Range Hopping
WAXS	Wide Angle X-Ray Scattering

1

Introduction

Polymers, also known as macromolecules, are the type of materials probably most used in everyday life [1]. Their unique combination of properties, like low weight, flexibility and low cost provides versatility for a handful of applications [1]. Polymers are long chain molecules consisting of a large number of repeated units linked by covalent bonds [2]. The origin of polymers as a user material can be traced in history back to the beginning of last century [1]. However, it was after the Second World War that polymer production blasted with the development of acrylic polymers, polystyrene (PS), nylon, polyurethanes and specially, polyethylene (PE) [3]. These mentioned polymers were named as commodity polymers, since they became indispensable in food and goods packaging, cabling or tubing [4]. However, in the last decades, with the development of modern synthesis techniques for polymer synthesis [4] material scientists are seeking to develop functional polymers with very specialized properties for applications like tissue engineering [5], drug delivery [6], polymeric sensors [7] and flexible electronic devices [8], among others. Specifically, in this last mentioned field, a strong research effort is focused on the development of plastic solar cells and in the use of polymers for information storage. In organic solar cells, the idea is to use semiconducting polymers to harvest energy directly from sunlight and convert it into electricity [9]. An organic solar cell is an electricity generating device comprised of thin layers of conductors, and photoelectrically active organic compounds. Organic photovoltaics offer light-weight, low-cost, flexible and easily scalable energy conversion. They convert energy based on a donor and an acceptor material [10], which can be two different organic dyes, a polymer and a small molecule, a polymer and an ensemble of semiconductor or oxide nanoparticles, or variations on these combinations. Research on the use of polymers for low cost-low weight information storage has progressed through the preparation of nanostructured polymers with a particular property that can be used as a 0-1 information unit. One of the properties employed for that purpose is ferroelectricity. Some polymers, like odd numbered nylons [11] and poly(vinylidene fluoride) (PVDF) based polymers [12] exhibit ferroelectricity and are suitable materials for the development of information storage applications [8].

In many of the applications mentioned above, polymers are processed within nano to microscale dimensions. This may have some impact on their properties when compared to those of the same bulk polymer [13]. In this Thesis, the preparation of nanostructured polymers with interest in photovoltaics and in ferroelectric information storing applications has been tackled. This Introduction is structured in the following way: Firstly, a short description of the main general polymer properties is presented. Secondly, we have prepared a review of the state of the art in the field of semiconducting polymers for photovoltaics. Later on, nowadays research on ferroelectric polymer miniaturization for information storing is revisited. Finally, we have described different methods for nanostruscturing polymers in general, and functional polymers, like ferroelectric and semiconducting polymers, in particular. We conclude the Introduction with a presentation of the structure of this Thesis.

1.1 Polymers and their main properties

A polymer molecule is obtained from a low molar mass compounds through a polymerization process. The number of the chemical repeat units which build the polymer chain is called the degree of polymerization (N) [2]. Since most of the polymerization reactions result in a mixture of macromolecules with a broad range of molar masses, the mass must be expressed statistically in order to describe the distribution of chain lengths. The most commonly used are the number average molar mass (M_n) and the weight average molar mass (M_w) [2]. M_n is defined as:

$$\overline{M_n} = \frac{\sum_i N_i M_i}{\sum_i N_i} = \sum_i n_i M_i \tag{1- 1}$$

Where N_i is the number of molecules of molar mass M_i, and n_i is the numerical fraction of those molecules. The M_w is given by:

$$\overline{M_w} = \frac{\sum_i N_i M_i^2}{\sum_i N_i M_i} \tag{1- 2}$$

Typical molecular weight distribution of a polymer is shown in Figure 1.1. In most cases the relationship between the average molar masses follows $\overline{M_w} > \overline{M_n}$. M_w and M_n are equal only for a perfectly monodisperse polymer.

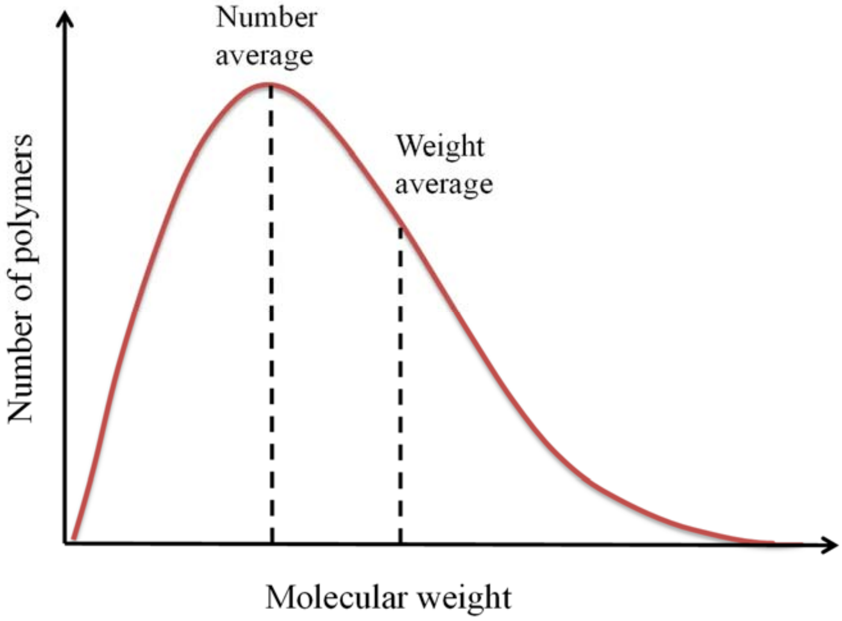

Figure 1.1 Typical molecular weight distribution of a polymer.

Thus polydispersity index (PDI) is defined as the ratio between the weight-average and number-average molar mass, i.e. $PDI = \frac{M_w}{M_n}$ and is a characteristic feature of a polymer since it is a way of describing the width of the molecular mass distribution [2].

When a polymer consists of only one type of repeating unit (A) is known as homopolymer (…-A-A-A-A-…). However, variations of the chemical structure by combining different monomers (A, B, etc.) give rise to copolymers. According to the relative position of the different components, copolymers can be classified into block copolymers, random copolymers and gradient copolymers [14]. Schematics of homopolymer and copolymer molecular structures are shown in Figure 1.2. In random copolymers the repeating units can be found at any site, without following any pattern. However, if the two monomers are linked with a short-range order with preferred sequences over the long range they form block copolymers (Figure 1.2b).

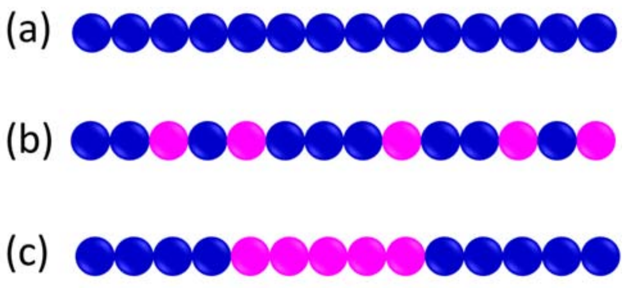

Figure 1.2 (a) Homopolymer and different classes of copolymers (unit A , unit B): (b) radom copolymer and (c) block copolymer.

Since polymers are long chain molecular structures, with a statistically defined molecular weight, in almost all cases it is thermodynamically not possible to obtain a polymer material which is hundred per cent crystalline. When a polymer is cooled down from its melt, depending on the cooling conditions and on the polymer properties, the system can be either into the glassy state or into the semicrystalline state. In the glassy state, the chains are frozen in a disordered state, and at certain temperatures above what is defined as the glass transition temperature (T_g), they start to exhibit segmental dynamics [2], i.e. cooperative motions of long segments of the chain. In the case of semicrystalline polymers, crystals are organized in a hierarchical way, exhibiting different degrees of ordering depending on the length scale explored.

Figure 1.3 displays schematically structures found in a semicrystalline polymer that exhibits spherulitic morphology. From microns to Angstroms, different levels of organization are found. On the micrometer scale, superstructures like spherulites [2] or axialites [15] are found. These superstructures are formed by stacks of almost parallel crystal lamellae with amorphous material sandwiched between adjacent crystals (shown in Figure 1.3b) [14]. The polymer crystal lamellae consists of one-dimensional chain-fold sequences (Figure 1.3c). Different from the classical polymers which crystallize in spherulites, conjugated polymers like poly(3-alkylthiophene)s (P3ATs) rather crystallize in nanorod or nanofiber, and particular details will be illustrated specifically.

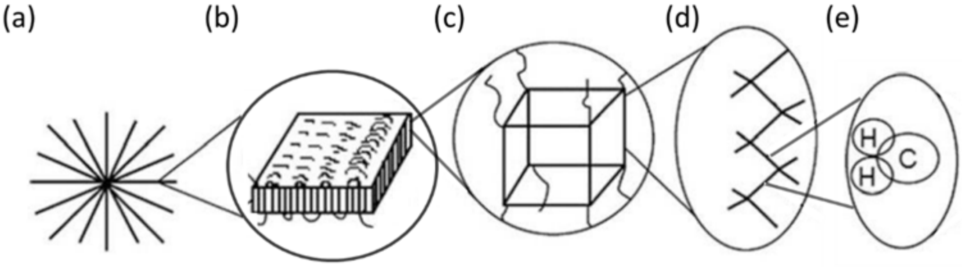

Figure 1.3 Morphological hierarchy exhibited by crystallizing PE from the melt. (a) spherulites, (b) lamellar crystals, (c) crystal units, (d) chain arrangement and (e) chain unit [16].

1.2 Semi-conducting organic materials for photovoltaics

As mentioned before, energy conversion in organic photovoltaics (OPVs) is based on the formation of a heterojunction between a donor (D) and an acceptor (A) material. A particular case of this heterojunction is formed by a polymer that acts as a donor and a low molecular weight organic compound acting as an acceptor.

In general, when a conducting material absorbs a photon from the solar spectrum, an excited state is formed. In semiconductors like silicon, the exciton binding energy is very small and therefore the electron and the hole can separate producing a current. This is called the photovoltaic effect [17]. In the case of organic materials, the process is similar, but the difference relies on the binding energy of the exciton, which is very high in organics systems. Current cannot be generated without dissociation of the exciton. That means that the electron and the hole in the exciton need to be separated so that they can move away from each other and generate current. To overcome this problem, the structure of the organic cells includes two materials, an electron donor and an electron acceptor. This formulation is called heterojunction. In it, there is an interface between those two materials that the excitons must reach in order to disassociate. To design efficient organic solar cells one should consider the distance that the exciton needs to diffuse during its lifetime in order to reach this interface. If the interface is further than the distance that the exciton can diffuse within its lifetime, no current will be produced. To properly formulate a heterojunction for OPVs these issues need to be considered. On one side, thinner films will allow shorter distances to the interface for the exciton to diffuse, but they have the drawback of poor photon absorption. One of the most promising heterojunction is called bulk heterojunction (BHJ), created by two interpenetrating network of the donor and acceptor materials [18]. The photoexcitation recombination lengths in organic systems are typically around 10 nm. Therefore, the length scale for self-assembly between must be of the order of 10–20 nm. The formation of the D/A interpenetrating networks requires that the component materials phase separate with domains in the range of 10 – 20 nm, that the interfacial energy favors high surface area and that both components fully percolate establishing connected pathways to the electrodes [19,20]. The interfacial area between the donor material and the acceptor is a critical factor for the performance of the OPVs [9,21]. To maximize these interfacial area, several methodologies have been introduced, like enhancing phase separation by solvent or thermal annealing [22,23] or by building tailor made geometries like interdigitated blends [24]. In the list of organic compounds that can act as donor and acceptor, the paradigmatic pair formed by a conjugated polymer and a fullerene derivative is the most studied [25]. In general, polymers are known for their excellent electrical insulation properties. However, there exists a class of polymer materials, whose special chemical structure enables electrical current transport. They are known as semi-conducting polymers or intrinsically conducting polymers, or also conjugated polymers. Their main chain consists of alternating single and double bonds. The study of conjugated polymer materials started in 1977, when Heeger, MacDiarmid and Shirakawa discovered the conductivity of polyacetylene (PA), for which they were awarded the Nobel Prize in Chemistry in 2000 [26]. Examples of semiconducting polymers are shown in Figure 1.4.

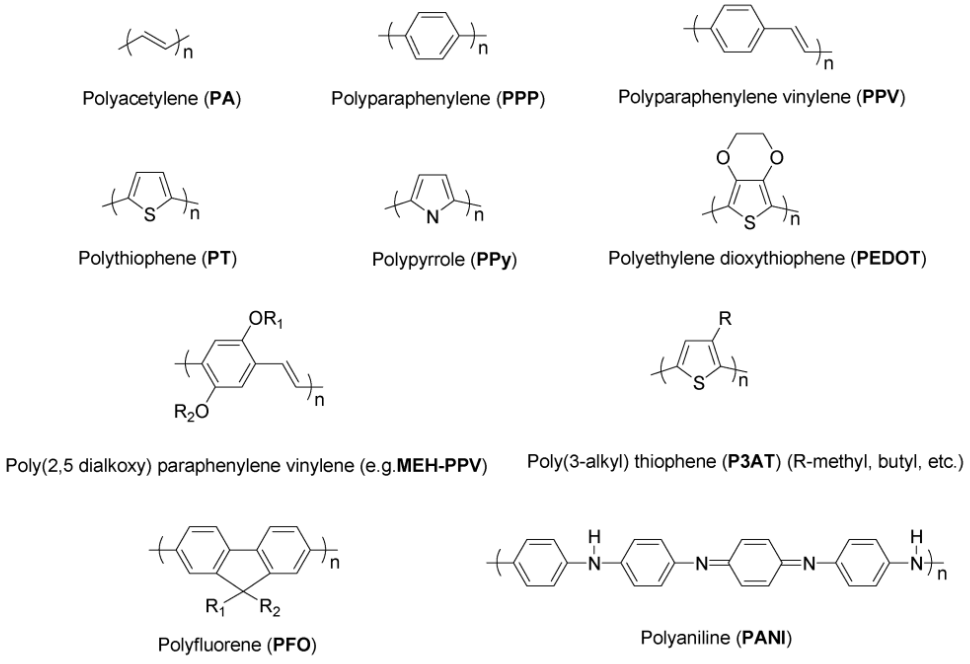

Figure 1.4 Molecular structure of some semiconducting polymers [27].

The conductivity of conjugated polymers is generally described by using energy bands originated from energy levels associated with their peculiar orbital structure. Conjugated polymers have backbones of continuous sp^2 hybridized carbon centers. The valence electron of each of these centers resides in a p_z orbital, orthogonal to the other three σ-bonds [27]. All the p_z orbitals combine with each other to form a delocalized set of orbitals that extend to what is called the conjugation length. These combined conjugated π orbitals form a one dimensional energy band. In conjugated polymers, the force along the chain is strong due to σ- and π-bonds while between chains, weaker van der Waals forces or hydrogen bonds interaction act. This results in anisotropic carrier mobilites. Thus conjugated polymers are also called ¨quasi-one-dimensional¨ semiconducting materials [27].

The energy gap (E_g) of conjugated polymers decreases with increasing the conjugation length [28]. In general, the gap (around 2 eV) is too large to be overcome by thermal activation. In terms of light absorption, only wavelengths corresponding to photon energies higher than E_g are absorbed, and since the band gap of organic semiconducting polymers is around 2 eV (620 nm), they exhibit a strong light absorption in visible [29].

Among the most promising semiconducting polymer materials to be used in OPVs as donors are P3ATs conjugated polymers, with rigid main chains and flexible side chains. The rigid π–conjugated main chain provides the semiconducting character and the flexible side chain prevents strong main chain interaction and favors the solubility and processability of the material [30-32].

1.2.1 The donor: poly(3-hexylthiophene-2,5-diyl) (P3HT)

Belonging to this family, Poly(3-hexylthiophene-2,5-diyl) (P3HT) has been used in this Thesis as a semiconducting polymer. The chemical structure of P3HT is shown in Figure 1.5a, and it consists of a π-conjugated backbone of thiophene units and pendant alkyl groups.

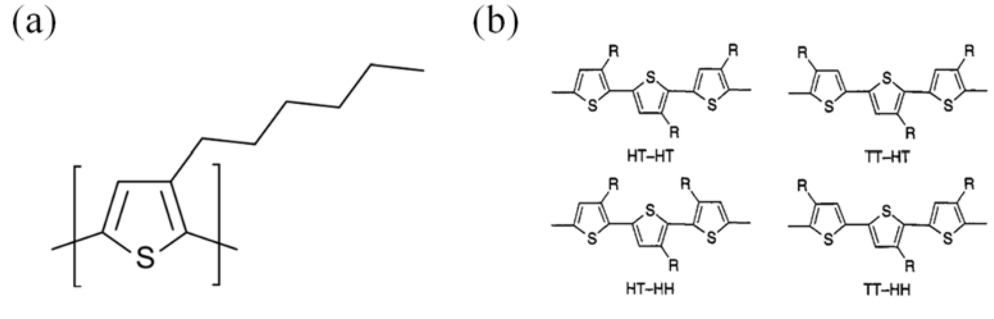

Figure 1.5 Chemical structure of (a) P3HT and (b) the regiochemical isomers [33].

Depending on the position of the lateral alkylic chain with respect of the main chain axes, P3HT can be found in the form of three different regioisomers: head-to-head coupling (HH), head-to-tail coupling (HT), and tail-to-tail coupling (TT). The polymer can present different degrees of regioregularity depending on the combination of the four types of couplings, as illustrated in

(Figure 1.5b): HT-HT, HT-HH, TT-HT, and TT-HH [34]. Regioregular P3HT (RR-P3HT) is referred to the case in which the main chain is formed only by HT-HT coupling, whereas regiorandom or irregular P3HT contains a mixture of the different couplings [33]. Due to the geometry of the HT couplings, regiorandom P3HT exhibits a short and random conjugation length due to twists away from planarity, whereas RR-P3HT can form planar conformation with extended π-conjugation, and self-assembles into a well-organized structure that favors the increase in the charge mobility (10^{-2}-10^{-3} $cm^2V^{-1}s^{-1}$), making it a promising material for its applications in electronic devices, for example, OPVs cells, organic field-effect transistors (OFETs), and organic light-emitting diodes (OLEDs) among others [27,35-37].

In terms of molecular packing, the chemical incompatibility between the conjugated polythiophene backbone and the alkyl side chains gives rise to a semicrystalline arrangement as the one shown in Figure 1.6.

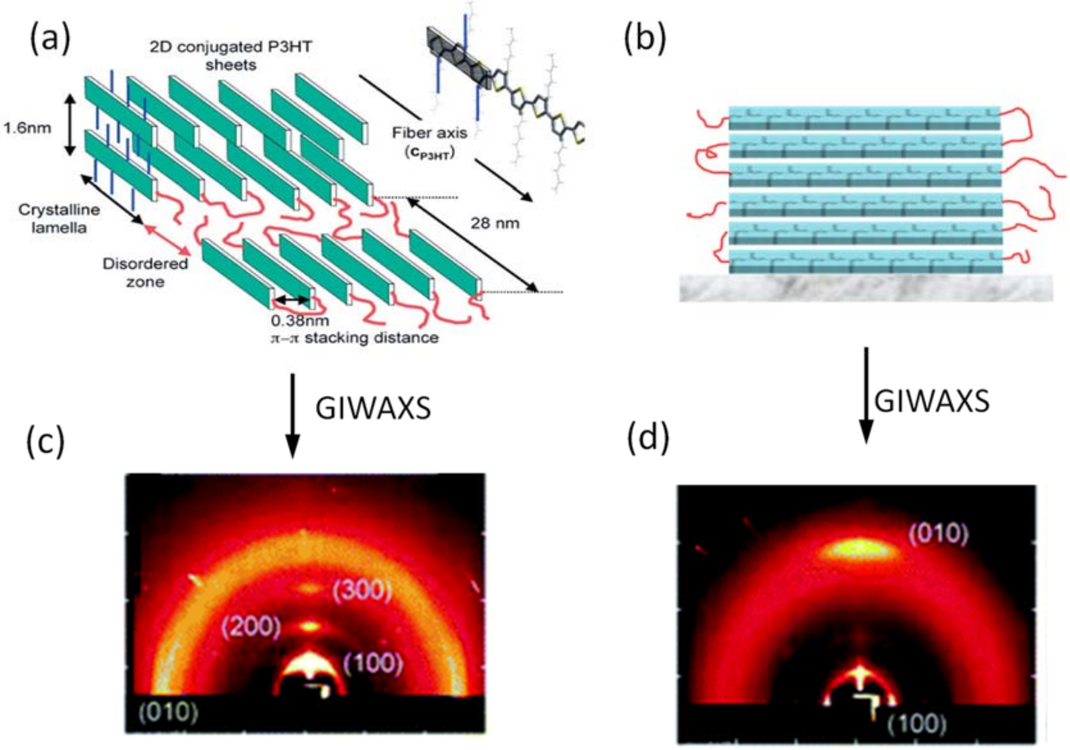

Figure 1.6 (Top) Schematic of the semicrystalline structure of P3HT at three main length scales: (a) edge-on and (b) face-on crystallite orientation and (Bottom) corresponding X-ray diffraction patterns taken by Grazing Indicence Wide Angle X-Ray Scattering (GIWAXS). Image (a) comes from [38], c and d are edited from [39].

The backbone tends to self-assemble into π-stacked polythiophene, forming two-dimensional (2D) sheets [40]. The periodic microstructure of P3HT exhibits a hierarchical order in three different length scales: a π-π stacking distance of 0.38 nm between RR-P3HT sheets, a distance of 1.6 nm between RR-P3HT backbones separated by alkyl side chains, and semi-crystalline lamella with a periodicity of 28 nm. The amorphous zones of P3HT consist of end chains and tied segments (red lines in Figure 1.6a) [38]. In thin films, the P3HT molecules exhibit preferential orientations with the chain axis aligned along the substrate and the π-conjugated sheets either edge-on (Figure 1.6a) or flat-on (Figure 1.6b) with respect to the substrate [41]. The two different orientations can be identified by Grazing Incidence Wide-Angle X-Ray Scattering (GIWAXS). Details of GIWAXS measurements will be described in Chapter 2. As an example, Figure 1.6c and 1.6d present 2D GIWAXS patterns for edge-on and face-on orientations, showing different intensity distributions of the (100) reflections due to layer structure and the (010) reflections due to π-π stacking [39]. For the edge-on crystals, the preferential orientation is with the (100)-axis normal to the film and the (010)-axis in the plane of the film (Figure 1.6c). In contrast, for the face-on orientation, the crystallites are preferentially oriented with the (100)-axis in the plane and the (010)-axis normal to the film (Figure 1.6d) [39].

1.2.2 The acceptor: [6,6]-phenyl C_{71}-butyric acid methyl ester ($PC_{71}BM$)

Fullerene derivatives are generally the organic molecules used as acceptors in OPVs [42-47]. The most widely used in combination with P3HT is [6,6]-phenyl C61-butyric acid methyl ester ($PC_{61}BM$), a C60 fullerene molecule functionalized with diazoalkanes, which is a solution processable material [42-46,48-50]. More recently, a similar material, but with a C70 fullerene instead of the C60 has been also used (Figure 1.7) [51]. Comparing with its counterpart $PC_{61}BM$, $PC_{71}BM$ possesses stronger absorption in the visible range and therefore an increased sunlight harvesting [10,52].

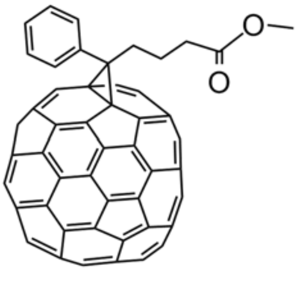

Figure 1.7 Chemical structure of $PC_{71}BM$ [51].

1.2.3 P3HT/PCBM blends

It is now generally accepted that the morphology of P3HT/PCBM blends consists of at least three phases: a polymer-rich ordered domain, a disordered domain where amorphous polymer chains are mixed with the fullerene derivative; and, at high fullerene contents a fullerene-rich domain

[48,53]. The development of the morphology and the thermodynamics of it has been widely studied [21,41,42] and several studies have addressed the impact of the developed morphology on the performance of the devices [54-57].

However, the role of the developed morphology on both charge generation and transport mechanism through the different phases is also a key factor to rationalize the design of new systems that improve device performances [58,59]. The precise mechanism of charge transport on these blend systems is not fully understood. As mentioned before, the conduction mechanism in P3HT is related to the motion of charge carriers delocalized along the macromolecular chains. However, both chemical inhomogeneity and structural disorder (crosslinks, dead ends, crystallinity, etc.) inherent to polymers, limit the conjugation length. The direct current (dc) electrical conductivity in materials with disorder can be described by a phonon-assisted hopping of electrons among randomly distributed localized states [60-62]. Charge transport can occur, not only on the macromolecular backbone (intra-chain hopping) but also between different macromolecules (inter-chain hopping) [60-62]. Thus, the degree of disorder can determine charge transport in OPVs [63]. In this respect, the need to understand and characterize the charge carrier energy levels of the different phases on a BHJ has been addressed. Sweetman et al. [64] have characterized the position of the valence bands in the different phases of a collection of polymer-D/A material blends by a combination of different techniques. They have demonstrated the existence of energetic offsets between the different phases. These energetic offsets are key factors in order to improve charge separation and reduce recombination in polymer solar cells. In this Thesis, we have attempted to address this issue by experimentally studying the molecular dynamics of P3HT/$PC_{71}BM$ blends by dielectric spectroscopy.

1.3 Polymers for data storing applications

Information technology is a very important part of our lives nowadays (mobile phones, personal computers, videogames, etc.). They all use data storing devices, that are becoming smaller and smaller. In general, they are built from semiconductors technology. However, there is an increasing demand for higher capacity and lower consumption. Recently ferroelectric polymers have been explored to provide such functionalities framed in the field of all-organics electronic prototypes. Layer by layer approaches have been used to fabricate devices, such as diodes [65] [66], and transistors [8], where thin films of ferroelectric polymers with other materials, such as semiconducting polymers [67] and inorganic alloys [68]. One of the potential applications of ferroelectric polymers is as memory storing media [69-71], taking profit of the ferroelectric character of these systems and of the easiness to be structured at the nanoscale.

Ferroelectricity, named in analogy with ferromagnetism, is the property of certain dielectrics that exhibit spontaneous electric polarization. This polarization can be reversed in direction by the application of an appropriate electric field. In ferroelectric materials, their crystals are formed by structural units that can be considered as small electric dipoles. These electric dipoles may spontaneously line up forming domains. The orientation of these domains can be tuned by applying an external electric field. Reversing the external field reverses the predominant orientation of the ferroelectric domains, although there will be a lag of the orientation behind the change of the field. This lag of electric polarization behind the applied electric field is the ferroelectric hysteresis. The ferroelectricity was first discovered by Valasek in 1921 in the Rochelle salt ($KNaC_4O_6\cdot 4H_2O$) [72], and ferroelectric devices are now widely used in transducers (since ferroelectric materials are piezoelectric), thermistors, sensors and memory capacitors [73,74]. Compared with inorganic compounds, the study of the ferroelectricity in polymers started some decades later in particular in 1969 by Kawai [75]. Although several other polymers like nylon also exhibits ferroelectricity [11,76], PVDF based polymers are the most attractive ones because of their large remnant polarization, short switching time and good thermal stability [77,78]. Ferroelectric electronic memories are devices which retain retrievable digital data over a time interval using materials that exhibit ferroelectricity. Random copolymers of PVDF and polytrifluoroethylene, (PTrFE) Poly(vinylidene fluoride -trifluoro ethylene), with abbreviated name P(VDF-TrFE), have been considered as potential candidates to be included in novel electronic devices [79-82]. The electric bistability of ferroelectric materials can be used for ferroelectric random access memory (FeRAM) and ferroelectric field-effect transistors (FeFET) [79-83].

In the seek of better performances, ferroelectric polymers have been combined with semiconducting polymers [84-86]. These blends merge the polarization switching ability of ferroelectrics, with the conductivity and rectification properties of semiconducting polymers and they can be used as storage media [65]. In all ferroelectric capacitors the read-out of the polarization charge is destructive [87]. However, in combination with a semiconducting polymer, the distribution of charges in the semiconducting polymer phase prevents this destruction, allowing multiple reading cycles [65]. In this line, Jonas and coworkers [66] fabricated regular arrays of P(VDF-TrFE) nanodots embedded in organic layers of P3HT to be used as organic high density non-volatile memories.

1.3.1 Ferroelectric polymers: PVDF and copolymers of PVDF with PTrFE, P(VDF-TrFE)

The chemical structure of PVDF and that of the copolymers with TrFE is presented in Figure 1.8, PVDF is a semicrystalline material that has several crystalline forms [88]. The α form, which is the one obtained under normal processing conditions, is not ferroelectric, since, due to the conformation of the chain in the crystal structure, the dipole moments inside the molecule cancel each other [88].

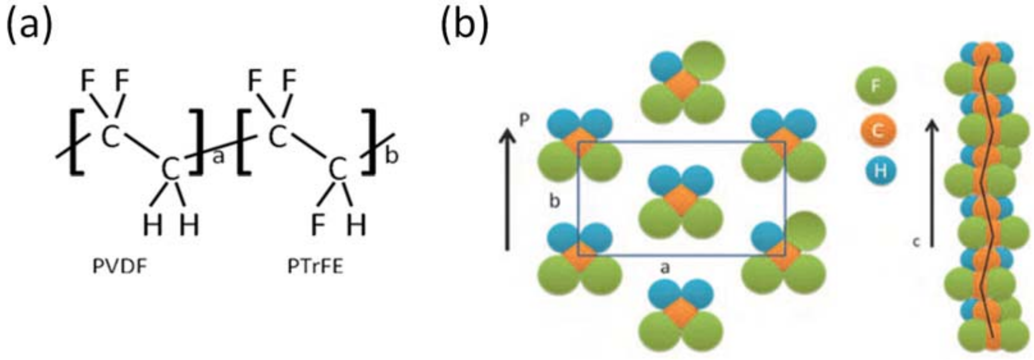

Figure 1.8 (a) The chemical formula of P(VDF-TrFE) random copolymer, and (b) scheme of the β phase crystal structure: (left) in ab plane, and (right) along the c axis [89].

To obtain other polar crystalline phases from PVDF, and therefore, to induce ferroelectricity, it is necessary crystallize under pressure or strain, in order to force the chains into a polar conformation [78,88]. However, the copolymer P(VDF-TrFE) crystallizes into a polar phase, named β phase [90], under normal processing conditions. In Figure 1.8b, a scheme of the crystalline β phase of the P(VDF-TrFE) copolymers is presented. In this phase, the molecules are in a distorted, all-trans (TTTT) zigzag planar configuration. The dipoles formed by the hydrogen and fluorine atoms lead to a large spontaneous electric polarization along the b axis parallel to the C-F dipole moment, and perpendicular to the polymer chain (Figure 1.8b) [89]. The β phase of the copolymers transits to a non-polar paraelectric phase at a given temperature, the Curie temperature, T_c [91,92].

In the β phase of P(VDF-TrFE), the crystals are formed by structural units that can be considered as small electric dipoles. These electric dipoles may spontaneously line up forming domains. The orientation of these domains can be switched by applying an external electric field, as is schematically shown in Figure 1.9. A change in the sign of the electric field produces a 180º rotation of dipole moments formed -CF_2- around the chain axis, provided the electric field is larger enough to overcome the energy barrier for dipole rotation [88]. Reversing the external field reverses the predominant orientation of the ferroelectric domains, although there will be some ferroelectric hysteresis [93]. Typical hysteresis loops are shown in Figure 1.9b, where the dependence of the electric displacement versus the applied electric field is presented. The polarization would show a similar dependence. This permanent polarization present even under the release of the electric field can be used for memory devices associating the polarization states

$+P_r$ and $-P_r$ with a Boolean 1 and 0 information bits [87]. The field needed to trigger this flipping is called the coercive field (E_c).

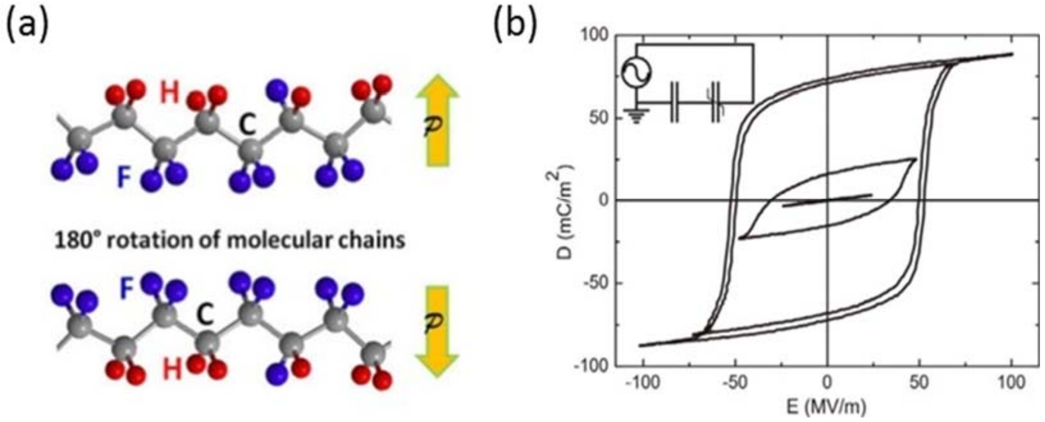

Figure 1.9 (a) schematic molecular structure and Ferroelectric switching [94], and (b) typical hysteresis loop (electric Displacement (D) versus electric field (E)) for P(VDF-TrFE) polymer [81].

1.3.2 Fundamental aspects in ferroelectric polymers to be taken into account for applications

Building electronic devices based on ferroelectric polymers is a task where many fundamental aspects of polymers physics need to be taken into account. In general, these devices are based on polymer thin films post-processed in certain ways. The applicability of ferroelectric polymers is based on the remnant polarization which originates from the alignment of intrinsic dipole moments inside the crystalline phase, and thus the control of the crystalline domains is a crucial aspect.

When a thin film of P(VDF-TrFE) is obtained from deposition of a solution on a given substrate, the interaction between polymer chains and substrate significantly affects the molecular chain orientation [95]. For example thin films prepared by spin coating and subsequently melted and recrystallized show different orientation of the polarization due to the preferential orientation of the crystals with the *b* axis, which is the responsible for the ferroelectricity [96-98]. Two typical orientations of the crystalline P(VDF-TrFE) lamella can be obtained. They are named edge-on and face-on orientation, and are schematically shown in Figure 1.10a and Figure 1.10b respectively. On the edge-on orientation, lamellae are perpendicular to the substrate, with the chain direction parallel to it [99], while in the face-on morphology, the chain direction is perpendicular to the substrate as the lamellae are parallel to it. These crystalline orientations are commonly investigated by using GIWAXS, like the crystalline structure of thin P3HT films mentioned in Section 1.2.1. Typical 2D GIWAXS patterns of P(VDF-TrFE) film with the two different lamellae orientations are displayed in Figure 1.10b and Figure 1.10c. The high intensity of the (110)/(200) reflections on the meridian indicates the preferential existence of edge-on lamellae whereas the strong intensity of these reflections on the equator is due to the presence of face-on lamellae [100]. It has been observed that in ultrathin films of P(VDF–TrFE) the thermal history and thickness rule the crystal orientation and its correlation with local polarization reversal [101,102]. Also it has been shown that the T_c depends on the film thickness [103,104].

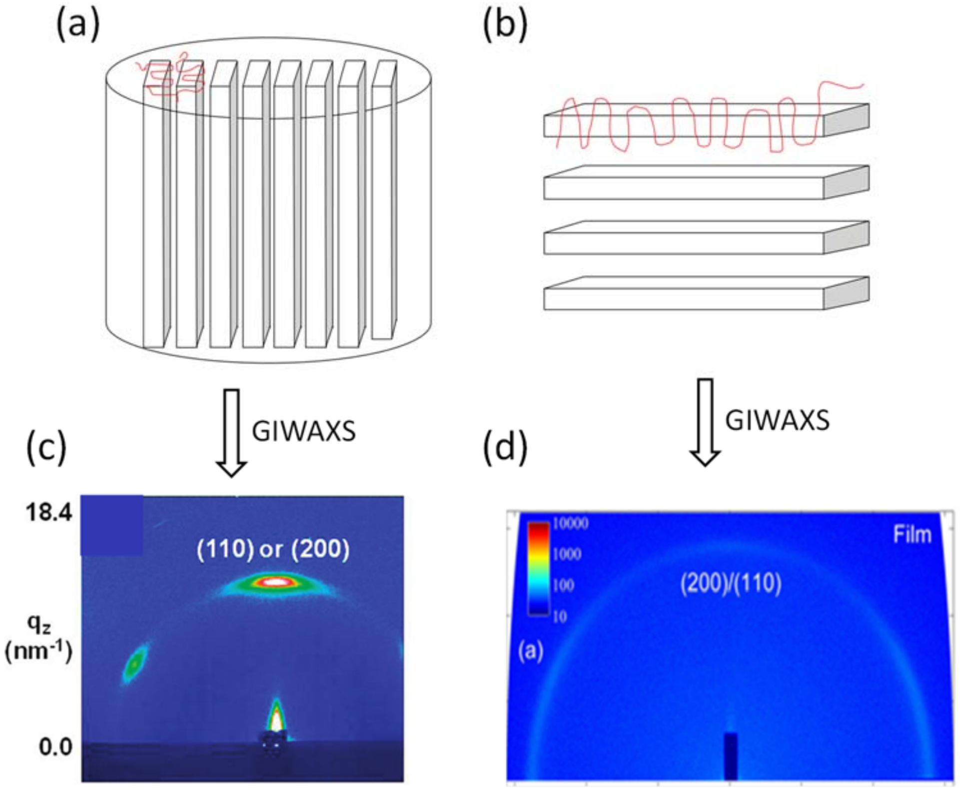

Figure 1.10 Two typical P(VDF-TrFE) chain orientation: (a) edge-on and (b) face-on [105], and corresponding 2D GIWAXS patterns: (c) edge-on and (d) face-on. Images c and d are edited from [99] and [100].

To be included in applications like high-density data storage devices, the ferroelectric polymers should be processed in the micro and even nanoscale. The idea is to be able to isolate ferroelectric domains in such a way that they can act as independent bits for writing/reading stored information. The use of nanopatterned surfaces in organic ferroelectric devices has shown to improve the ferroelectric response of the polymers [106,107], enhancing the storage information density by controlling molecular architecture [100,108]. In this sense, arrays of P(VDF-TrFE) nanostructures, in the form of nanogratings [100,109], nanorods [79,110], nanopillars [111,112] or other objects with nanometer sizes [113] have been fabricated and its ferroelectricity has been studied. In these works research has been focused on the modification of aspects like crystallinity, preferential orientation of the crystalline domains, crystal sizes due to confinement, since at least one of the feature dimensions has nanoscale lengths [101,114,115]. In studies on thin films of P(VDF-TrFE) under different crystallization conditions it has been found that flat-on crystals do not display polarization switching, whereas the edge-on crystals do, upon application of a vertical electric field, and the edge-on lamella exhibit the same coercive field, independently of the film thickness. [101].

In the case of ferroelectric/semiconducting polymers, one of the advantages is that the above mentioned structures can be fabricated from solution or melt processing. Due to their high enthalpy of mixing, phase separation occurs between the two polymers, forming a composite material with both ferroelectric and semiconducting areas. By changing the blend ratios, the conductive and ferroelectric properties and their individual area can be tuned [8].

1.4 Controlled morphology of polymer nanostructure

Controlling the morphology of phase separated blends or modifying the surface of functional polymers will enhance the suitability for these systems for potential applications. In this Thesis we have explored the possibilities for controlling phase separation, by several techniques, including polymer blending in a bilayer morphology, preparation of ferroelectric nanospheres and subsequent embedding of them into a semiconducting polymer, nanostructuring of polymer layers and bilayers by laser techniques, among others, in order to explore the appropriate route for applicability. The state of the art of the nanostructuring techniques used in this Thesis is reviewed below.

1.4.1 Polymer nanoparticles

Nanoparticles (NPs) exhibit unique physical properties different to those of the same bulk material due to the large surface area-volume ratio and new confinement effects [116]. Polymer NPs can be prepared by single polymer materials or combining different ones, such as pair of donor polymer/acceptor systems [117-119] or core-shell structures [120] among others. Besides applications, polymer NPs have been used as an appropriate morphology to study physical properties under 3D confinement [121-123]. In this sense it has been observed that the T_g in amorphous polymer NPs increases compared to the bulk, due to the decrease of entropy of polymer chains in these confined conditions as less polymer conformations become available [121,122,124,125]. In the case of semicrystalline polymer NPs, they exhibit reduced crystal size and the increase of the grain boundaries, which, for P3HT and P(VDF-TrFE), has probed to enhance their applicability in OPVs and miniaturized electronic devices [123,126].

The formation of polymer NPs can be categorized into two groups: 1) polymerization from its monomers [119] and 2) nanoprecipitation from the previously synthetized polymer [119]. In latter case, different methods, such as solvent evaporation and nanoprecipitation [119,121,127] have been developed. In this way, polymer NPs from polymers as diverse as polystyrene (PS) [122,127], polyethylmethacrylate (PEMA) [121], poly(L-lactid acid)-b-poly(ethylene oxide) copolymers (PLLA-b-PEO) [128], P3HT [117,123] or P(VDF-TrFE) [126] have been prepared. Once polymer NPs are obtained, they can be used alone or embedded in other polymer matrix to enhance the sought properties.

1.4.2 Surface modification methods

Modification of functional polymer surfaces is required for a variety of applications, which can go from the preparation of substrates for cell adhesion [129], microelectronic devices or superhydrophobicity [130]. Fabrication and modification of polymer surfaces at the nano and microscale, can be achieved by means of two main lines of work: The first one consist of adapting techniques that are already suitable for that purpose at the macroscale such as nanoimprinting [131,132], or direct laser writing [133,134]. The second line would be to take profit of instabilities occurring at polymer surfaces and be able to control them for the pursued purpose. These instabilities include wrinkling due to mismatching between the mechanical properties of two layers [135], polymer thin film dewetting [136,137], phase separation of polymer blends, among others. In this Thesis, two main techniques have been used to modify surfaces: dewetting of polymer surfaces by the influence of the substrate and formation of periodic structures induced by laser.

1.4.2.1 Dewetting of polymer films

Dewetting is referred as the process in which a non-wetting thin liquid film on a substrate breaks up into droplets. It plays an important role in industrial process as lubrication, liquid coating, printing and spray quenching [138]. Dewetting is considered a surface instability. Once the instability occurs, its relaxation towards equilibrium produces the modification of the surface topography to minimize the surface energy [139]. The resulting morphology arises from the balance between destabilizing (Van der Waals forces, polar interactions or electrostatic interactions) and stabilizing forces (surface tension) [140]. Controlling the resultant morphology in a dewetting surface can provide an interesting tool to obtain complex patterns via self-organization that otherwise would be very difficult to obtain. Recently, the use of patterned substrates [140,141] has allowed to obtain undulating polymer surfaces, where the surface undulations are in phase with the underlying substrate patterns, or a variety of ordered arrays of aligned droplets, isolated strips of polymers, etc.

The wettability of the substrate by the polymer solution also affects the final morphology [142]. In order to characterize the wettability of the substrate and its surface energy, contact angle (CA) measurements are performed. In this Thesis we have observed that dewetting of a polymer on top of another polymer layer can be triggered by the thickness of the bottom polymer layer. This opens the possibility of forming binary self-organized polymer surfaces with complementary properties by careful choice of the polymer substrate and its thickness.

1.4.2.2 Laser induced periodic surface structures (LIPSS)

Laser techniques are employed in material processing and, more specifically, surfaces modification [143], since the interaction of laser light with a material can induce changes to the local chemistry, the local crystal structure or the local morphology [143].

Compared with other lithography processes, including soft lithography [144-146], nanoimprint lithography [131,132] and templating by anodic aluminium oxide (AAO) membranes [113] among others, laser nanostructuring techniques avoid the need for sophisticated facilities like clean rooms or the fabrication of delicate stamps, and they can be applied to different polymer materials in large areas [133,134,147]. Laser Interference Lithography (LIL) has been used to create linear grooves in polymer surfaces with the only requirement that the polymer absorbs efficiently the employed laser light [147]. These techniques involve the interference of two or more laser beams in the polymer surface. With only one laser beam, periodic structures on polymer surfaces can also be obtained. In particular, Laser Induced Periodic Surface Structures (LIPSS) on polymers, which can be obtained by using intense laser pulses, is considered a potential alternative strategy to lithography processes for obtaining functional nanopatterned polymer surface structures [148-150], and is one of the techniques employed in this Thesis to modify polymer surfaces. LIPSS have been observed and studied since first reported by Birnbaum in a series of semiconductor materials [151]. After that LIPSS have been produced on different materials using lasers with pulse duration ranging from nano- to femtoseconds and wavelengths from the IR to the UV spectral regions [133,148,152-154].

To obtain LIPSS, the polymer surface is exposed to a given number of pulses of a linearly polarized laser beam within a narrow fluence range well below the ablation threshold [155-157]. It is important to note that ripples formation is originated from a self-organization process and not caused by ablation, being the amount of material removed during laser irradiation negligible [158]. Figure 1.11 displays the schematic of LIPSS formed on a film. For LIPSS formed with nanosecond laser pulses, two main stages can be considered: (i) interference at the surface, and (ii) surface response to it. The interference between the incident and reflected/refracted laser light with the scattered light near the surface, results in LIPSS with a characteristic size in the order of magnitude of the wavelength of the laser beam.

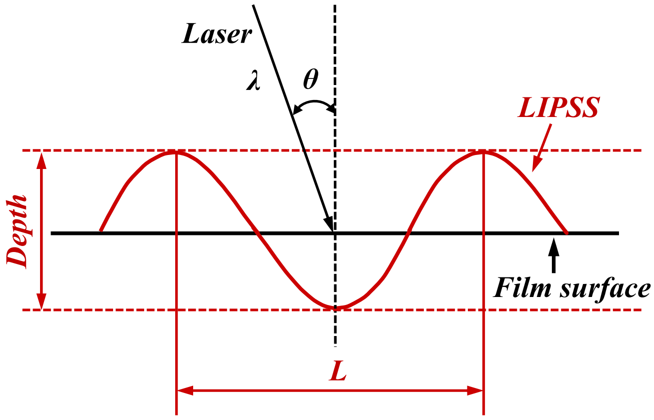

Figure 1.11 Schematic of surface corrugation of LIPSS formed on a film.

The period of the obtained ripples (L) is related to the laser wavelength (λ) and to the angle of incidence of the radiation. The spacing of the structures can be described by the following expression [143]:

$$L = \frac{\lambda}{n - \sin\theta} \tag{1- 3}$$

Where n is the effective refractive index of the material, and θ the incidence angle of the laser beam with respect to the normal to the sample plane.

The features of LIPSS might be affected by the polymer properties, which are dependent not only on the chemical composition, but also on the polymer state. However, the mechanism of ripple formation on polymer surfaces is complex and still not completely well understood. Various processes have been proposed to be involved in the formation mechanism, for example, processes like thermal and nonthermal scissoring of polymer chains, amorphization, local surface melting, ablation, photooxidation, material transport and rearrangement, have been suggested to have a role in ripples formation [150,155,157,159-161]. More recently it has been reported that when a polymer film is irradiated with a laser beam at a wavelength efficiently absorbed, the surface temperature increases and in order to obtain LIPSS, the temperature should be enough to grant polymer chain mobility. In particular, temperature should be either above T_g for the case of amorphous polymer, allowing polymer chains to rearrange [148,149], or above its melting temperature (T_m) in the case of a semicrystalline polymer so that melting of the surface crystallites occurs providing enough polymer dynamics [162] and the redistribution of the material [161]. Despite the number of works published on the temperature evolution during LIPSS formation [149,155,163], several key issues remain unclear: how does the temperature evolve during pulses accumulation in polymer surface? Does the underlying substrate have any influence on LIPSS formation? Csete et al observed [161] that linear LIPSS are formed in films with thickness above a minimum thickness value. Thus, they are obtained for free-standing films with thicknesses in the range of microns, whereas for supported films thinner than 60 nanometers the line-shaped structures are transformed into droplets, due to laser induced polymer melting and subsequent dewetting on the substrate.

Another important prerequisite for LIPSS formation is that the material has a moderate or good light absorption at the specific irradiation wavelength. However, in the case of ferroelectric polymers like the PVDF based copolymers, no structuring takes place due to the poor optical absorption of PVDF in the UV-visible region. Additionally, its semicrystalline spherulitic morphology also further hinders the material reorganization during irradiation [149,164]. This absorption limitation has been recently overcome by preparing a bilayer polymer film in which the bottom layer absorbs light at the specified wavelength, while the top layer is formed by the non-absorbing polymer [164]. Based on this approach, LIPSS can be obtained for other non-absorbing polymers, which greatly broaden the range of applications of the technique.

The fact that LIPSS can be prepared either in spin-coated or in free standing polymer films, makes it a potential method to obtain large processed surface area and good quality samples. The characteristic surface structure formed by this method, can be used to tailor a great variety of surface properties such as adhesion and friction, or color generated by superficial gratings [133,162,165].

1.5 Outline of the Thesis

In summary, in this Thesis, the possibility of controlling the surface structure of functional polymers with applications in electronic devices and OPVs has been explored. The Thesis has been organized in the following way: The materials and the variety of techniques employed are explained in chapter 2. After that, in chapter 3 the results on the relation between the conductivity mechanism and molecular dynamics in blends from a donor polymer and an acceptor molecule are presented. In chapter 4, several approaches to control phase separation in polymer blends from two functional polymers, a ferroelectric and a semiconducting one are explored. In chapter 5, the surface modification of a model polymer by laser pulses is related to the thermal and optical properties of the substrates employed. The obtained knowledge is again used to induce periodic surface structures in a functional polymer, a semiconducting polymer. In chapter 6, an approach to obtain these periodic surface structures by repeated pulsed laser illumination in non-absorbing functional polymers (ferroelectric polymer) is shown. Finally, in chapter 7, the conclusions of this work are enumerated.

1.6 References

[1] Chanda, M. and Roy, S. K. *Industrial Polymers, Specialty Polymers, and Their Applications*. Vol. 74 (CRC press, US, 2008).

[2] Strobl, G. R. *The Physics of Polymers: Concepts for Understanding Their Structures and Behavior*. (Springer, Berlin Heidelberg, 1997).

[3] McKelvey, J. M. *Polymer Processing*. (John Wiley & Sons, New York, 1962).

[4] Braun, D., Cherdron, H., Rehahn, M., Ritter, H. and Voit, B. *Polymer Synthesis: Theory and Practice: Fundamentals, Methods, Experiments*. (Springer, Verlag Berlin Heidelberg, 2012).

[5] Freed, L. E., Vunjak-Novakovic, G., Biron, R. J., Eagles, D. B., Lesnoy, D. C., Barlow, S. K. and Langer, R. Biodegradable Polymer Scaffolds for Tissue Engineering. *Nature Biotechnology* **12**, 689-693 (1994).

[6] Pandey, R. and Khuller, G. K. Polymer Based Drug Delivery Systems for Mycobacterial Infections. *Current Drug Delivery* **1**, 195-201 (2004).

[7] Osada, Y. and Rossi, D. E. D. *Polymer Sensors and Actuators*. (Springer, Verlag Berlin Heidelberg, 2000).

[8] Naber, R. C. G., Asadi, K., Blom, P. W. M., de Leeuw, D. M. and de Boer, B. Organic Nonvolatile Memory Devices Based on Ferroelectricity. *Advanced Materials* **22**, 933-945 (2010).

[9] Mayer, A. C., Scully, S. R., Hardin, B. E., Rowell, M. W. and McGehee, M. D. Polymer-based Solar Cells. *Materials Today* **10**, 28-33 (2007).

[10] Hou, J. and Guo, X. in *Organic Solar Cells: Materials and Device Physics* (ed Choy) 17-42 (Springer, 2013).

[11] Mathur, S. C., Scheinbeim, J. I. and Newman, B. A. Piezoelectric Properties and Ferroelectric Hysteresis Effects in Uniaxially Stretched Nylon-11 Films. *Journal of Applied Physics* **56**, 2419-2425 (1984).

[12] Mao, D., Quevedo-Lopez, M. A., Stiegler, H., Gnade, B. E. and Alshareef, H. N. Optimization of Poly(vinylidene fluoride-trifluoroethylene) Films as Non-volatile Memory for Flexible Electronics. *Organic Electronics* **11**, 925-932 (2010).

[13] Zhang, C., Guo, Y. and Priestley, R. D. Glass Transition Temperature of Polymer Nanoparticles under Soft and Hard Confinement. *Macromolecules* **44**, 4001-4006 (2011).

[14] Sperling, L. H. *Introduction to Physical Polymer Science*. (John Wiley & Sons, New York, 2005).

[15] Bassett, D. C., Keller, A. and Mitsuhashi, S. New Features in Polymer Crystal Growth from Concentrated Solutions. *Journal of Polymer Science Part A: General Papers* **1**, 763-788 (1963).

[16] Hu, W. *Polymer Physics: A Molecular Approach*. (Springer Verlag, Wien, 2013).

[17] Hersch, P. and Zweibel, K. *Basic Photovoltaic Principles and Methods*. (Solar Energy Research Inst., Golden, CO (USA), 1982).

[18] Heeger, A. J. 25th Anniversary Article: Bulk Heterojunction Solar Cells: Understanding the Mechanism of Operation. *Advanced Materials* **26**, 10-28 (2014).

[19] Westacott, P., Tumbleston, J. R., Shoaee, S., Fearn, S., Bannock, J. H., Gilchrist, J. B., Heutz, S., deMello, J., Heeney, M., Ade, H., Durrant, J., McPhail, D. S. and Stingelin, N. On the Role of Intermixed Phases in Organic Photovoltaic Blends. *Energy & Environmental Science* **6**, 2756-2764 (2013).

[20] Huang, Y., Kramer, E. J., Heeger, A. J. and Bazan, G. C. Bulk Heterojunction Solar Cells: Morphology and Performance Relationships. *Chemical Reviews* **114**, 7006-7043 (2014).

[21] Ruderer, M. A., Guo, S., Meier, R., Chiang, H.-Y., Koerstgens, V., Wiedersich, J., Perlich, J., Roth, S. V. and Mueller-Buschbaum, P. Solvent-induced Morphology in Polymer-Based Systems for Organic Photovoltaics. *Advanced Functional Materials* **21**, 3382-3391 (2011).

[22] Chen, D., Nakahara, A., Wei, D., Nordlund, D. and Russell, T. P. P3HT/PCBM Bulk Heterojunction Organic Photovoltaics: Correlating Efficiency and Morphology. *Nano Letters* **11**, 561-567 (2011).

[23] Erb, T., Zhokhavets, U., Hoppe, H., Gobsch, G., Al-Ibrahim, M. and Ambacher, O. Absorption and Crystallinity of Poly(3-hexylthiophene)/fullerene Blends in Dependence on Annealing Temperature. *Thin Solid Films* **511–512**, 483-485 (2006).

[24] Balderrama, V. S., Albero, J., Granero, P., Ferre-Borrull, J., Pallares, J., Palomares, E. and Marsal, L. F. Design, Fabrication and Charge Recombination Analysis of an Interdigitated Heterojunction Nanomorphology in P3HT/PC70BM Solar Cells. *Nanoscale* **7**, 13848-13859 (2015).

[25] García-Valverde, R., Cherni, J. A. and Urbina, A. Life Cycle Analysis of Organic Photovoltaic Technologies. *Progress in Photovoltaics: Research and Applications* **18**, 535-558 (2010).

[26] Shirakawa, H., Louis, E. J., MacDiarmid, A. G., Chiang, C. K. and Heeger, A. J. Synthesis of Electrically Conducting Organic Polymers: Halogen Derivatives of Polyacetylene, (CH)x. *Journal of the Chemical Society, Chemical Communications*, 578-580 (1977).

[27] Heeger, A. J. Semiconducting Polymers: the Third Generation. *Chemical Society Reviews* **39**, 2354-2371 (2010).

[28] Blom, P. W. M. and Vissenberg, M. C. J. M. Charge Transport in Poly(p-phenylene vinylene) Light-emitting Diodes. *Materials Science and Engineering: R: Reports* **27**, 53-94 (2000).

[29] Heeger, A. J. Semiconducting and Metallic Polymers: The Fourth Generation of Polymeric Materials. *The Journal of Physical Chemistry B* **105**, 8475-8491 (2001).

[30] Garnier, F. Scope and Limits of Organic–based Thin–film Transistors. *Philosophical Transactions of the Royal Society of London. Series A: Mathematical, Physical and Engineering Sciences* **355**, 815-827 (1997).

[31] Kelley, T. W., Baude, P. F., Gerlach, C., Ender, D. E., Muyres, D., Haase, M. A., Vogel, D. E. and Theiss, S. D. Recent Progress in Organic Electronics: Materials, Devices, and Processes. *Chemistry of Materials* **16**, 4413-4422 (2004).

[32] Tsutsui, T. and Fujita, K. The Shift from “Hard” to “Soft” Electronics. *Advanced Materials* **14**, 949-952 (2002).

[33] Pappenfus, T. M., Hermanson, D. L., Kohl, S. G., Melby, J. H., Thoma, L. M., Carpenter, N. E., da Silva Filho, D. A. and Bredas, J.-L. Regiochemistry of Poly(3-hexylthiophene): Synthesis and Investigation of a Conducting Polymer. *Journal of Chemical Education* **87**, 522-525 (2010).

[34] Chen, T.-A., Wu, X. and Rieke, R. D. Regiocontrolled Synthesis of Poly(3-alkylthiophenes) Mediated by Rieke Zinc: Their Characterization and Solid-State Properties. *Journal of the American Chemical Society* **117**, 233-244 (1995).

[35] Facchetti, A. π-Conjugated Polymers for Organic Electronics and Photovoltaic Cell Applications. *Chemistry of Materials* **23**, 733-758 (2011).

[36] Wang, C., Dong, H., Hu, W., Liu, Y. and Zhu, D. Semiconducting π-conjugated Systems in Field-effect Transistors: A Material Odyssey of Organic Electronics. *Chemical Reviews* **112**, 2208-2267 (2012).

[37] AlSalhi, M. S., Alam, J., Dass, L. A. and Raja, M. Recent Advances in Conjugated Polymers for Light Emitting Devices. *International Journal of Molecular Sciences* **12**, 2036-2054 (2011).

[38] Brinkmann, M. and Wittmann, J. C. Orientation of Regioregular Poly(3-hexylthiophene) by Directional Solidification: A Simple Method to Reveal the Semicrystalline Structure of a Conjugated Polymer. *Advanced Materials* **18**, 860-863 (2006).

[39] Sirringhaus, H., Brown, P. J., Friend, R. H., Nielsen, M. M., Bechgaard, K., Langeveld-Voss, B. M. W., Spiering, A. J. H., Janssen, R. A. J., Meijer, E. W., Herwig, P. and de Leeuw, D. M. Two-dimensional Charge Transport in Self-organized, High-mobility Conjugated Polymers. *Nature* **401**, 685-688 (1999).

[40] Prosa, T. J., Winokur, M. J., Moulton, J., Smith, P. and Heeger, A. J. X-ray Structural Studies of Poly(3-alkylthiophenes): An Example of an Inverse Comb. *Macromolecules* **25**, 4364-4372 (1992).

[41] Brady, M. A., Su, G. M. and Chabinyc, M. L. Recent Progress in the Morphology of Bulk Heterojunction Photovoltaics. *Soft Matter* **7**, 11065-11077 (2011).

[42] Moulé, A. J. and Meerholz, K. Controlling Morphology in Polymer–fullerene Mixtures. *Advanced Materials* **20**, 240-245 (2008).

[43] Zhao, J., Swinnen, A., Van Assche, G., Manca, J., Vanderzande, D. and Mele, B. V. Phase Diagram of P3HT/PCBM Blends and Its Implication for the Stability of Morphology. *The Journal of Physical Chemistry B* **113**, 1587-1591 (2009).

[44] Hopkinson, P. E., Staniec, P. A., Pearson, A. J., Dunbar, A. D. F., Wang, T., Ryan, A. J., Jones, R. A. L., Lidzey, D. G. and Donald, A. M. A Phase Diagram of the P3HT:PCBM Organic Photovoltaic System: Implications for Device Processing and Performance. *Macromolecules* **44**, 2908-2917 (2011).

[45] Lilliu, S., Agostinelli, T., Pires, E., Hampton, M., Nelson, J. and Macdonald, J. E. Dynamics of Crystallization and Disorder during Annealing of P3HT/PCBM Bulk Heterojunctions. *Macromolecules* **44**, 2725-2734 (2011).

[46] Parnell, A. J., Cadby, A. J., Mykhaylyk, O. O., Dunbar, A. D. F., Hopkinson, P. E., Donald, A. M. and Jones, R. A. L. Nanoscale Phase Separation of P3HT PCBM Thick Films As Measured by Small-Angle X-ray Scattering. *Macromolecules* **44**, 6503-6508 (2011).

[47] Newman, C. R., Frisbie, C. D., da Silva Filho, D. A., Brédas, J.-L., Ewbank, P. C. and Mann, K. R. Introduction to Organic Thin Film Transistors and Design of n-channel Organic Semiconductors. *Chemistry of Materials* **16**, 4436-4451 (2004).

[48] Yin, W. and Dadmun, M. A New Model for the Morphology of P3HT/PCBM Organic Photovoltaics from Small-angle Neutron Scattering: Rivers and Streams. *ACS Nano* **5**, 4756-4768 (2011).

[49] To, T. T. and Adams, S. Modelling of P3HT:PCBM Interface Using Coarse-Grained Forcefield Derived from Accurate Atomistic Forcefield. *Physical Chemistry Chemical Physics* **16**, 4653-4663 (2014).

[50] Vajjala Kesava, S., Dhanker, R., Kozub, D. R., Vakhshouri, K., Choi, U. H., Colby, R. H., Wang, C., Hexemer, A., Giebink, N. C. and Gomez, E. D. Mesoscopic Structural Length Scales in P3HT/PCBM Mixtures Remain Invariant for Various Processing Conditions. *Chemistry of Materials* **25**, 2812-2818 (2013).

[51] Romero-Borja, D., Maldonado, J.-L., Barbosa-García, O., Rodríguez, M., Pérez-Gutiérrez, E., Fuentes-Ramírez, R. and de la Rosa, G. Polymer Solar Cells Based on P3HT:PC71BM Doped at Different Concentrations of Isocyanate-treated Graphene. *Synthetic Metals* **200**, 91-98 (2015).

[52] Li, L., Zhang, F., Wang, J., An, Q., Sun, Q., Wang, W., Zhang, J. and Teng, F. Achieving EQE of 16,700% in P3HT:PC71BM Based Photodetectors by Trap-assisted Photomultiplication. *Scientific Reports* **5**, 9181-9187 (2015).

[53] Kohn, P., Rong, Z., Scherer, K. H., Sepe, A., Sommer, M., Müller-Buschbaum, P., Friend, R. H., Steiner, U. and Hüttner, S. Crystallization-Induced 10-nm Structure Formation in P3HT/PCBM Blends. *Macromolecules* **46**, 4002-4013 (2013).

[54] Nicolet, C., Deribew, D., Renaud, C., Fleury, G., Brochon, C., Cloutet, E., Vignau, L., Wantz, G., Cramail, H., Geoghegan, M. and Hadziioannou, G. Optimization of the Bulk Heterojunction Composition for Enhanced Photovoltaic Properties: Correlation between the Molecular Weight of the Semiconducting Polymer and Device Performance. *The Journal of Physical Chemistry B* **115**, 12717-12727 (2011).

[55] Wang, T., Pearson, A. J., Lidzey, D. G. and Jones, R. A. L. Evolution of Structure, Optoelectronic Properties, and Device Performance of Polythiophene: Fullerene Solar Cells During Thermal Annealing. *Advanced Functional Materials* **21**, 1383-1390 (2011).

[56] Machui, F., Langner, S., Zhu, X., Abbott, S. and Brabec, C. J. Determination of the P3HT:PCBM Solubility Parameters Via a Binary Solvent Gradient Method: Impact of Solubility on the Photovoltaic Performance. *Solar Energy Materials and Solar Cells* **100**, 138-146 (2012).

[57] Deribew, D., Pavlopoulou, E., Fleury, G., Nicolet, C., Renaud, C., Mougnier, S.-J., Vignau, L., Cloutet, E., Brochon, C., Cousin, F., Portale, G., Geoghegan, M. and Hadziioannou, G.

Crystallization-Driven Enhancement in Photovoltaic Performance through Block Copolymer Incorporation into P3HT:PCBM Blends. *Macromolecules* **46**, 3015-3024 (2013).

[58] Moliton, A. and Hiorns, R. C. Review of Electronic and Optical Properties of Semiconducting π-conjugated Polymers: Applications in Optoelectronics. *Polymer International* **53**, 1397-1412 (2004).

[59] Cheung, D. L., McMahon, D. P. and Troisi, A. Computational Study of the Structure and Charge-transfer Parameters in Low-molecular-mass P3HT. *The Journal of Physical Chemistry B* **113**, 9393-9401 (2009).

[60] Ezquerra, T. A., Rühe, J. and Wegner, G. Hopping Conduction in 3,4-cycloalkylpolypyrrole Perchlorates: A Model Study of Conductivity in Polymers. *Chemical Physics Letters* **144**, 194-198 (1988).

[61] Wegner, G. and Ruhe, J. The Structural Background of Charge-carrier Motion in Conducting Polymers. *Faraday Discussions of the Chemical Society* **88**, 333-349 (1989).

[62] Capaccioli, S., Lucchesi, M., Rolla, P. A. and Ruggeri, G. Dielectric Response Analysis of a Conducting Polymer Dominated by the Hopping Charge Transport. *Journal of Physics: Condensed Matter* **10**, 5595 (1998).

[63] McMahon, D. P. and Troisi, A. Organic Semiconductors: Impact of Disorder at Different Timescales. *ChemPhysChem* **11**, 2067-2074 (2010).

[64] Sweetnam, S., Graham, K. R., Ngongang Ndjawa, G. O., Heumüller, T., Bartelt, J. A., Burke, T. M., Li, W., You, W., Amassian, A. and McGehee, M. D. Characterization of the Polymer Energy Landscape in Polymer:Fullerene Bulk Heterojunctions with Pure and Mixed Phases. *Journal of the American Chemical Society* **136**, 14078-14088 (2014).

[65] Asadi, K., de Leeuw, D. M., de Boer, B. and Blom, P. W. M. Organic Non-volatile Memories from Ferroelectric Phase-separated Blends. *Nature Materials* **7**, 547-550 (2008).

[66] Nougaret, L., Kassa, H. G., Cai, R., Patois, T., Nysten, B., van Breemen, A. J. J. M., Gelinck, G. H., de Leeuw, D. M., Marrani, A., Hu, Z. and Jonas, A. M. Nanoscale Design of Multifunctional Organic Layers for Low-power High-density Memory Devices. *ACS Nano* **8**, 3498-3505 (2014).

[67] Cai, R., Kassa, H. G., Marrani, A., van Breemen, A. J. J. M., Gelinck, G. H., Nysten, B., Hu, Z. and Jonas, A. M. An Organic Ferroelectric Field Effect Transistor with Poly(vinylidene fluoride-co-trifluoroethylene) Nanostripes as Gate Dielectric. *Applied Physics Letters* **105**, 113111-113115 (2014).

[68] Bae, I., Kim, R. H., Hwang, S. K., Kang, S. J. and Park, C. Laser-induced Nondestructive Patterning of a Thin Ferroelectric Polymer Film with Controlled Crystals using Ge8Sb2Te11 Alloy Layer for Nonvolatile Memory. *ACS Applied Materials & Interfaces* **6**, 15171-15178 (2014).

[69] Kusuma, D. Y. and Lee, P. S. Ferroelectric Tunnel Junction Memory Devices Made from Monolayers of Vinylidene Fluoride Oligomers. *Advanced Materials* **24**, 4163-4169 (2012).

[70] Khan, M. A., Bhansali, U. S. and Alshareef, H. N. High-performance Non-volatile Organic Ferroelectric Memory on Banknotes. *Advanced Materials* **24**, 2165-2170 (2012).

[71] Hwang, S. K., Bae, I., Kim, R. H. and Park, C. Flexible Non-volatile Ferroelectric Polymer Memory with Gate-controlled Multilevel Operation. *Advanced Materials* **24**, 5910-5914 (2012).

[72] Valasek, J. Piezo-Electric and Allied Phenomena in Rochelle Salt. *Physical Review* **17**, 475-481 (1921).

[73] Haertling, G. H. Ferroelectric Ceramics: History and Technology. *Journal of the American Ceramic Society* **82**, 797-818 (1999).

[74] Ghayour, H. and Abdellahi, M. A Brief Review of the Effect of Grain Size Variation on the Electrical Properties of BaTiO3-based Ceramics. *Powder Technology* **292**, 84-93 (2016).

[75] Heiji, K. The Piezoelectricity of Poly (vinylidene fluoride). *Japanese Journal of Applied Physics* **8**, 975-976 (1969).

[76] Nalwa, H. S. *Ferroelectric Polymers: Chemistry: Physics, and Applications*. (CRC Press, US, 1995).

[77] Noda, K., Ishida, K., Kubono, A., Horiuchi, T., Yamada, H. and Matsushige, K. Remanent Polarization of Evaporated Films of Vinylidene Fluoride Oligomers. *Journal of Applied Physics* **93**, 2866-2870 (2003).

[78] Furukawa, T., Date, M. and Fukada, E. Hysteresis Phenomena in Polyvinylidene Fluoride Under High Electric Field. *Journal of Applied Physics* **51**, 1135-1141 (1980).

[79] Ducharme, S. and Gruverman, A. Ferroelectrics: Start the Presses. *Nature Materials* **8**, 9-10 (2009).

[80] Mandal, D., Yoon, S. and Kim, K. J. Origin of Piezoelectricity in an Electrospun Poly(vinylidene fluoride-trifluoroethylene) Nanofiber Web-Based Nanogenerator and Nano-Pressure Sensor. *Macromolecular Rapid Communications* **32**, 831-837 (2011).

[81] Naber, R. C. G., Tanase, C., Blom, P. W. M., Gelinck, G. H., Marsman, A. W., Touwslager, F. J., Setayesh, S. and de Leeuw, D. M. High-performance Solution-processed Polymer Ferroelectric Field-effect Transistors. *Nature Materials* **4**, 243-248 (2005).

[82] Chang, C., Tran, V. H., Wang, J., Fuh, Y.-K. and Lin, L. Direct-write Piezoelectric Polymeric Nanogenerator with High Energy Conversion Efficiency. *Nano Letters* **10**, 726-731 (2010).

[83] Dawber, M., Rabe, K. M. and Scott, J. F. Physics of Thin-film Ferroelectric Oxides. *Reviews of Modern Physics* **77**, 1083-1130 (2005).

[84] van Breemen, A., Zaba, T., Khikhlovskyi, V., Michels, J., Janssen, R., Kemerink, M. and Gelinck, G. Surface Directed Phase Separation of Semiconductor Ferroelectric Polymer Blends and their Use in Non-volatile Memories. *Advanced Functional Materials* **25**, 278-286 (2015).

[85] Khikhlovskyi, V., van Breemen, A. J. J. M., Michels, J. J., Janssen, R. A. J., Gelinck, G. H. and Kemerink, M. 3D-morphology Reconstruction of Nanoscale Phase-separation in Polymer Memory Blends. *Journal of Polymer Science Part B: Polymer Physics* **53**, 1231-1237 (2015).

[86] Braz, T., Ferreira, Q., Mendonça, A. L., Ferraria, A. M., do Rego, A. M. B. and Morgado, J. Morphology of Ferroelectric/conjugated Polymer Phase-separated Blends Used in Nonvolatile Resistive Memories. Direct Evidence for a Diffuse Interface. *The Journal of Physical Chemistry C* **119**, 1391-1399 (2015).

[87] Scott, J. F. *Ferroelectric Memories*. (Springer, Verlag Berlin Heidelberg, 2000).

[88] Lovinger, A. J. Ferroelectric Polymers. *Science* **220**, 1115-1121 (1983).

[89] Mao, D., Gnade, B. E. and Quevedo-Lopez, M. A. in *Ferroelectrics - Physical Effects* (ed Lallart) (InTech, 2011).

[90] Furukawa, T. Ferroelectric Properties of Vinylidene Fluoride Copolymers. *Phase Transitions* **18**, 143-211 (1989).

[91] Kim, K. J., Kim, G. B., Vanlencia, C. L. and Rabolt, J. F. Curie Transition, Ferroelectric Crystal Structure, and Ferroelectricity of a VDF/TrFE(75/25) Copolymer 1. The Effect of the Consecutive Annealing in the Ferroelectric State on Curie Transition and Ferroelectric Crystal Structure. *Journal of Polymer Science Part B: Polymer Physics* **32**, 2435-2444 (1994).

[92] Choi, J., Borca, C. N., Dowben, P. A., Bune, A., Poulsen, M., Pebley, S., Adenwalla, S., Ducharme, S., Robertson, L., Fridkin, V. M., Palto, S. P., Petukhova, N. N. and Yudin, S. G. Phase Transition in the Surface Structure in Copolymer Films of Vinylidene Fluoride (70%) with Trifluoroethylene (30%). *Physical Review B* **61**, 5760-5770 (2000).

[93] Fang, D. and Liu, J. *Fracture Mechanics of Piezoelectric and Ferroelectric Solids*. (Springer, Berlin, 2013).

[94] Hu, W. J., Juo, D.-M., You, L., Wang, J., Chen, Y.-C., Chu, Y.-H. and Wu, T. Universal Ferroelectric Switching Dynamics of Vinylidene Fluoride-trifluoroethylene Copolymer Films. *Scientific Reports* **4**, 4772-4779 (2014).

[95] Tsutsumi, N., Yoda, S. and Sakai, W. Infrared Spectra and Ferro-electricity of Ultra-thin Films of Vinylidene Fluoride and Trifluoroethylene Copolymer. *Polymer International* **56**, 1254-1260 (2007).

[96] Park, Y. J., Kang, S. J., Park, C., Kim, K. J., Lee, H. S., Lee, M. S., Chung, U.-I. and Park, I. J. Irreversible Extinction of Ferroelectric Polarization in P(VDF-TrFE) Thin Films upon Melting and Recrystallization. *Applied Physics Letters* **88**, 242908 242901-242903 (2006).

[97] Lee, J. S., Prabu, A. A. and Kim, K. J. Annealing Effect upon Chain Orientation, Crystalline Morphology, and Polarizability of Ultra-thin P(VDF-TrFE) Film for Nonvolatile Polymer Memory Device. *Polymer* **51**, 6319-6333 (2010).

[98] Bune, A. V., Fridkin, V. M., Ducharme, S., Blinov, L. M., Palto, S. P., Sorokin, A. V., Yudin, S. G. and Zlatkin, A. Two-dimensional Ferroelectric Films. *Nature* **391**, 874-877 (1998).

[99] Kang, S. J., Bae, I., Shin, Y. J., Park, Y. J., Huh, J., Park, S.-M., Kim, H.-C. and Park, C. Nonvolatile Polymer Memory with Nanoconfinement of Ferroelectric Crystals. *Nano Letters* **11**, 138-144 (2011).

[100] Martinez-Tong, D. E., Soccio, M., Garcia-Gutierrez, M. C., Nogales, A., Rueda, D. R., Alayo, N., Perez-Murano, F. and Ezquerra, T. A. Improving Information Density in Ferroelectric Polymer Films by Using Nanoimprinted Gratings. *Applied Physics Letters* **102**, 191601-191605 (2013).

[101] Wu, Y., Li, X., Weng, Y., Hu, Z. and Jonas, A. M. Orientation of Lamellar Crystals and Its Correlation with Switching Behavior in Ferroelectric P(VDF-TrFE) Ultra-thin Films. *Polymer* **55**, 970-977 (2014).

[102] Zhu, H., Yamamoto, S., Matsui, J., Miyashita, T. and Mitsuishi, M. Ferroelectricity of Poly(vinylidene fluoride) Homopolymer Langmuir-blodgett Nanofilms. *Journal of Materials Chemistry C* **2**, 6727-6731 (2014).

[103] Prabu, A. A., Kim, K. J. and Park, C. Effect of Thickness on the Crystallinity and Curie Transition Behavior in P(VDF/TrFE) (72/28) Copolymer Thin Films using FTIR-transmission Spectroscopy. *Vibrational Spectroscopy* **49**, 101-109 (2009).

[104] Tsutsumi, N., Ueyasu, A., Sakai, W. and Chiang, C. K. Crystalline Structures and Ferroelectric Properties of Ultrathin Films of Vinylidene Fluoride and Trifluoroethylene Copolymer. *Thin Solid Films* **483**, 340-345 (2005).

[105] Lau, K., Liu, Y., Chen, H. and Withers, R. L. Effect of Annealing Temperature on the Morphology and Piezoresponse Characterisation of Poly(vinylidene fluoride-trifluoroethylene) Films via Scanning Probe Microscopy. *Advances in Condensed Matter Physics* **2013**, 5 (2013).

[106] Cauda, V., Stassi, S., Bejtka, K. and Canavese, G. Nanoconfinement: an Effective Way to Enhance PVDF Piezoelectric Properties. *ACS Applied Materials & Interfaces* **5**, 6430-6437 (2013).

[107] Cauda, V., Torre, B., Falqui, A., Canavese, G., Stassi, S., Bein, T. and Pizzi, M. Confinement in Oriented Mesopores Induces Piezoelectric Behavior of Polymeric Nanowires. *Chemistry of Materials* **24**, 4215-4221 (2012).

[108] Chen, X.-Z., Li, Q., Chen, X., Guo, X., Ge, H.-X., Liu, Y. and Shen, Q.-D. Nano-Imprinted Ferroelectric Polymer Nanodot Arrays for High Density Data Storage. *Advanced Functional Materials* **23**, 3124-3129 (2013).

[109] Li, Z.-D., Shen, Z.-K., Hui, W.-Y., Qiu, Z.-J., Qu, X.-P., Chen, Y.-F. and Liu, R. Pattern Transfer of Nano-scale Ferroelectric PZT Gratings by a Reversal Nanoimprint Lithography. *Microelectronic Engineering* **88**, 2037-2040 (2011).

[110] Garcia-Gutierrez, M.-C., Linares, A., Martin-Fabiani, I., Hernandez, J. J., Soccio, M., Rueda, D. R., Ezquerra, T. A. and Reynolds, M. Understanding Crystallization Features of P(VDF-TrFE) Copolymers under Confinement to Optimize Ferroelectricity in Nanostructures. *Nanoscale* **5**, 6006-6012 (2013).

[111] Kassa, H. G., Nougaret, L., Cai, R., Marrani, A., Nysten, B., Hu, Z. and Jonas, A. M. The Ferro- to Paraelectric Curie Transition of a Strongly Confined Ferroelectric Polymer. *Macromolecules* **47**, 4711-4717 (2014).

[112] Chen, D., Zhao, W. and Russell, T. P. P3HT Nanopillars for Organic Photovoltaic Devices Nanoimprinted by AAO Templates. *ACS Nano* **6**, 1479-1485 (2012).

[113] Hong, C.-C., Huang, S.-Y., Shieh, J. and Chen, S.-H. Enhanced Piezoelectricity of Nanoimprinted Sub-20 nm Poly(vinylidene fluoride–trifluoroethylene) Copolymer Nanograss. *Macromolecules* **45**, 1580-1586 (2012).

[114] Yang, L., Li, X., Allahyarov, E., Taylor, P. L., Zhang, Q. M. and Zhu, L. Novel Polymer Ferroelectric Behavior via Crystal Isomorphism and the Nanoconfinement Effect. *Polymer* **54**, 1709-1728 (2013).

[115] Hahm, S.-W., Kim, D. and Khang, D.-Y. One-dimensional Confinement in Crystallization of P(VDF-TrFE) Thin Films with Transfer-printed Metal Electrode. *Polymer* **55**, 175-181 (2014).

[116] Liz-Marzán, L. M. and Kamat, P. V. *Nanoscale Materials*. (Springer, US, 2003).

[117] Landfester, K., Montenegro, R., Scherf, U., Güntner, R., Asawapirom, U., Patil, S., Neher, D. and Kietzke, T. Semiconducting Polymer Nanospheres in Aqueous Dispersion Prepared by a Miniemulsion Process. *Advanced Materials* **14**, 651-655 (2002).

[118] Kietzke, T., Neher, D., Landfester, K., Montenegro, R., Guntner, R. and Scherf, U. Novel Approaches to Polymer Blends Based on Polymer Nanoparticles. *Nature Materials* **2**, 408-412 (2003).

[119] Rao, J. P. and Geckeler, K. E. Polymer Nanoparticles: Preparation Techniques and Size-control Parameters. *Progress in Polymer Science* **36**, 887-913 (2011).

[120] Lu, X.-Y., Wu, D.-C., Li, Z.-J. and Chen, G.-Q. Polymer Nanoparticles. *Progress in Molecular Biology and Translational Science* **104**, 299-323 (2011).

[121] Martínez-Tong, D. E., Soccio, M., Sanz, A., García, C., Ezquerra, T. A. and Nogales, A. Chain Arrangement and Glass Transition Temperature Variations in Polymer Nanoparticles under 3D-Confinement. *Macromolecules* **46**, 4698-4705 (2013).

[122] Martínez-Tong, D. E., Cui, J., Soccio, M., García, C., Ezquerra, T. A. and Nogales, A. Does the Glass Transition of Polymers Change Upon 3D Confinement? *Macromolecular Chemistry and Physics* **215**, 1620-1624 (2014).

[123] Labastide, J. A., Baghgar, M., Dujovne, I., Venkatraman, B. H., Ramsdell, D. C., Venkataraman, D. and Barnes, M. D. Time- and Polarization-resolved Photoluminescence of Individual Semicrystalline Polythiophene (P3HT) Nanoparticles. *The Journal of Physical Chemistry Letters* **2**, 2089-2093 (2011).

[124] Mi, Y., Xue, G. and Wang, X. Glass Transition of Nano-sized Single Chain Globules. *Polymer* **43**, 6701-6705 (2002).

[125] Guo, Y., Morozov, A., Schneider, D., Chung, J. W., Zhang, C., Waldmann, M., Yao, N., Fytas, G., Arnold, C. B. and Priestley, R. D. Ultrastable Nanostructured Polymer Glasses. *Nature Materials* **11**, 337-343 (2012).

[126] Martínez-Tong, D. E., Soccio, M., Sanz, A., García, C., Ezquerra, T. A. and Nogales, A. Ferroelectricity and Molecular Dynamics of Poly(vinylidenefluoride-trifluoroethylene) Nanoparticles. *Polymer* **56**, 428-434 (2015).

[127] Zhang, C., Pansare, V. J., Prud'homme, R. K. and Priestley, R. D. Flash Nanoprecipitation of Polystyrene Nanoparticles. *Soft Matter* **8**, 86-93 (2012).

[128] Lee, J., Cho, E. C. and Cho, K. Incorporation and Release Behavior of Hydrophobic Drug in Functionalized Poly(d,l-lactide)-block–poly(ethylene oxide) Micelles. *Journal of Controlled Release* **94**, 323-335 (2004).

[129] Ranella, A., Barberoglou, M., Bakogianni, S., Fotakis, C. and Stratakis, E. Tuning Cell Adhesion by Controlling the Roughness and Wettability of 3D Micro/nano Silicon Structures. *Acta Biomaterialia* **6**, 2711-2720 (2010).

[130] Li, X.-M., Reinhoudt, D. and Crego-Calama, M. What do We Need for a Superhydrophobic Surface? A Review on the Recent Progress in the Preparation of Superhydrophobic Surfaces. *Chemical Society Reviews* **36**, 1350-1368 (2007).

[131] Aryal, M., Trivedi, K. and Hu, W. C. Nano-Confinement Induced Chain Alignment in Ordered P3HT Nanostructures Defined by Nanoimprint Lithography. *ACS Nano* **3**, 3085-3090 (2009).

[132] Pfadler, T., Coric, M., Palumbiny, C. M., Jakowetz, A. C., Strunk, K.-P., Dorman, J. A., Ehrenreich, P., Wang, C., Hexemer, A., Png, R.-Q., Ho, P. K. H., Mueller-Buschbaum, P., Weickert, J. and Schmidt-Mende, L. Influence of Interfacial Area on Exciton Separation and Polaron Recombination in Nanostructured Bilayer All-polymer Solar Cells. *ACS Nano* **8**, 12397-12409 (2014).

[133] Rebollar, E., Castillejo, M. and Ezquerra, T. A. Laser Induced Periodic Surface Structures on Polymer Films: From Fundamentals to Applications. *European Polymer Journal* **73**, 162-174 (2015).

[134] Martín-Fabiani, I., Siegel, J., Riedel, S., Boneberg, J., Ezquerra, T. A. and Nogales, A. Nanostructuring Thin Polymer Films with Optical Near Fields. *ACS Applied Materials & Interfaces* **5**, 11402-11408 (2013).

[135] Rodríguez-Hernández, J. Wrinkled Interfaces: Taking Advantage of Surface Instabilities to Pattern Polymer Surfaces. *Progress in Polymer Science* **42**, 1-41 (2015).

[136] Chen, X.-C., Li, H.-M., Fang, F., Wu, Y.-W., Wang, M., Ma, G.-B., Ma, Y.-Q., Shu, D.-J. and Peng, R.-W. Confinement-induced Ordering in Dewetting and Phase Separation of Polymer Blend Films. *Advanced Materials* **24**, 2637-2641 (2012).

[137] Luo, C., Xing, R. and Han, Y. Ordered Pattern Formation from Dewetting of Polymer Thin Film with Surface Disturbance by Capillary Force Lithography. *Surface Science* **552**, 139-148 (2004).

[138] Craster, R. V. and Matar, O. K. Dynamics and Stability of Thin Liquid Films. *Reviews of Modern Physics* **81**, 1131-1198 (2009).

[139] Reiter, G., Sferrazza, M. and Damman, P. Dewetting of Thin Polymer Films at Temperatures Close to the Glass Transition. *The European Physical Journal E* **12**, 133-138 (2003).

[140] Mukherjee, R., Sharma, A. and Steiner, U. in *Generating Micro- and Nanopatterns on Polymeric Materials* 217-265 (Wiley-VCH Verlag GmbH & Co. KGaA, 2011).

[141] Roy, S., Ansari, K. J., Jampa, S. S. K., Vutukuri, P. and Mukherjee, R. Influence of Substrate Wettability on the Morphology of Thin Polymer Films Spin-coated on Topographically Patterned Substrates. *ACS Applied Materials & Interfaces* **4**, 1887-1896 (2012).

[142] Jurak, M. and Chibowski, E. Wettability and Topography of Phospholipid DPPC Multilayers Deposited by Spin-coating on Glass, Silicon, and Mica Slides. *Langmuir* **23**, 10156-10163 (2007).

[143] Bäuerle, D. W. *Laser Processing and Chemistry*. (Springer, Verlag Berlin Heidelberg, 2011).

[144] Schift, H. Nanoimprint Lithography: An Old Story in Modern Times? A Review. *Journal of Vacuum Science & Technology B* **26**, 458-480 (2008).

[145] Guo, L. J. Nanoimprint Lithography: Methods and Material Requirements. *Advanced Materials* **19**, 495-513 (2007).

[146] Na, S.-I., Kim, S.-S., Jo, J., Oh, S.-H., Kim, J. and Kim, D.-Y. Efficient Polymer Solar Cells with Surface Relief Gratings Fabricated by Simple Soft Lithography. *Advanced Functional Materials* **18**, 3956-3963 (2008).

[147] Martin-Fabiani, I., Riedel, S., Rueda, D. R., Siegel, J., Boneberg, J., Ezquerra, T. A. and Nogales, A. Micro- and Submicrostructuring Thin Polymer Films with Two and Three-beam Single Pulse Laser Interference Lithography. *Langmuir* **30**, 8973-8979 (2014).

[148] Martín-Fabiani, I., Rebollar, E., Pérez, S., Rueda, D. R., García-Gutiérrez, M. C., Szymczyk, A., Roslaniec, Z., Castillejo, M. and Ezquerra, T. A. Laser-induced Periodic Surface Structures Nanofabricated on Poly(trimethylene terephthalate) Spin-coated Films. *Langmuir* **28**, 7938-7945 (2012).

[149] Rebollar, E., Perez, S., Hernandez, J. J., Martin-Fabiani, I., Rueda, D. R., Ezquerra, T. A. and Castillejo, M. Assessment and Formation Mechanism of Laser-induced Periodic Surface Structures on Polymer Spin-coated Films in Real and Reciprocal Space. *Langmuir* **27**, 5596-5606 (2011).

[150] Bolle, M., Lazare, S., Le Blanc, M. and Wilmes, A. Submicron Periodic Structures Produced on Polymer Surfaces with Polarized Excimer Laser Ultraviolet Radiation. *Applied Physics Letters* **60**, 674-676 (1992).

[151] Birnbaum, M. Semiconductor Surface Damage Produced by Ruby Lasers. *Journal of Applied Physics* **36**, 3688-3689 (1965).

[152] Rebollar, E., Perez, S., Hernandez, M., Domingo, C., Martin, M., Ezquerra, T. A., Garcia-Ruiz, J. P. and Castillejo, M. Physicochemical Modifications Accompanying UV Laser Induced Surface Structures on Poly(ethylene terephthalate) and Their Effect on Adhesion of Mesenchymal Cells. *Physical Chemistry Chemical Physics* **16**, 17551-17559 (2014).

[153] Ivanov, M. and Rochon, P. Infrared-laser-induced Periodic Surface Structure in Azo-dye Polymer. *Applied Physics Letters* **84**, 4511-4513 (2004).

[154] Rebollar, E., Vazquez de Aldana, J. R., Martin-Fabiani, I., Hernandez, M., Rueda, D. R., Ezquerra, T. A., Domingo, C., Moreno, P. and Castillejo, M. Assessment of Femtosecond Laser Induced Periodic Surface Structures on Polymer Films. *Physical Chemistry Chemical Physics* **15**, 11287-11298 (2013).

[155] Csete, M. and Bor, Z. Laser-induced Periodic Surface Structure Formation on Polyethylene-terephthalate. *Applied Surface Science* **133**, 5-16 (1998).

[156] Csete, M., Hild, S., Plettl, A., Ziemann, P., Bor, Z. and Marti, O. The Role of Original Surface Roughness in Laser-induced Periodic Surface Structure Formation Process on Poly-carbonate Films. *Thin Solid Films* **453–454**, 114-120 (2004).

[157] Csete, M., Eberle, R., Pietralla, M., Marti, O. and Bor, Z. Attenuated Total Reflection Measurements on Poly-carbonate Surfaces Structured by Laser Illumination. *Applied Surface Science* **208–209**, 474-480 (2003).

[158] Pérez, S., Rebollar, E., Oujja, M., Martín, M. and Castillejo, M. Laser-induced Periodic Surface Structuring of Biopolymers. *Applied Physics A* **110**, 683-690 (2013).

[159] Bolle, M. and Lazare, S. Characterization of Submicrometer Periodic Structures Produced on Polymer Surfaces with Low-fluence Ultraviolet Laser Radiation. *Journal of Applied Physics* **73**, 3516-3524 (1993).

[160] Bolle, M. and Lazare, S. Large Scale Excimer Laser Production of Submicron Periodic Structures on Polymer Surfaces. *Applied Surface Science* **69**, 31-37 (1993).

[161] Csete, M., Marti, O. and Bor, Z. Laser-induced Periodic Surface Structures on Different Poly-carbonate Films. *Applied Physics A* **73**, 521-526 (2001).

[162] Rodríguez-Rodríguez, Á., Rebollar, E., Soccio, M., Ezquerra, T. A., Rueda, D. R., Garcia-Ramos, J. V., Castillejo, M. and Garcia-Gutierrez, M.-C. Laser-Induced Periodic Surface Structures on Conjugated Polymers: Poly(3-hexylthiophene). *Macromolecules* **48**, 4024-4031 (2015).

[163] Tsutsumi, N. and Fujihara, A. Pulsed Laser Induced Spontaneous Gratings on a Surface of Azobenzene Polymer. *Applied Physics Letters* **85**, 4582-4584 (2004).

[164] Martínez-Tong, D. E., Rodríguez-Rodríguez, Á., Nogales, A., García-Gutiérrez, M.-C., Pérez-Murano, F., Llobet, J., Ezquerra, T. A. and Rebollar, E. Laser Fabrication of Polymer Ferroelectric Nanostructures for Nonvolatile Organic Memory Devices. *ACS Applied Materials & Interfaces* **7**, 19611-19618 (2015).

[165] Cui, J., Rodríguez-Rodríguez, Á., Hernández, M., García-Gutiérrez, M.-C., Nogales, A., Castillejo, M., González, D. M., Müller-Buschbaum, P., Ezquerra, T. A. and Rebollar, E. On the Laser Induced Periodic Surface Structures of P3HT and of its Blend with PC71BM. *Submitted to ACS Applied Materials & Interfaces* (2016).

2

Samples & techniques

This chapter is composed of three parts. Part 1 gives a description of all the materials involved in the Thesis. Part 2 provides a detailed description of the experimental techniques related to the preparation of polymer nanoparticles and thin films. In Part 3 the characterization techniques used for the evaluation of physical and structural properties of the studied polymers are explained.

2.1 Materials

In this part, the polymers used to prepare NPs or thin films are introduced. Besides, some non-polymer materials like the fullerene derived material $PC_{71}BM$ and solvents are presented here.

2.1.1 Poly(3-hexylthiophene-2,5-diyl), P3HT

The chemical structure of poly(3-hexylthiophene-2,5-diyl), (P3HT) [1] has been presented in Chapter 1 (Section 1.2.1). Two batches of P3HT with similar molecular weight were used (batches M101 and M102). Both of them are obtained from Ossila Ltd., and the detailed characteristics are displayed in Table 2.1.

Table 2.1 Details of P3HT.

Polymer	M_w (g/mol)	PDI	Regioregularty
P3HT M101	65,500	2.04	96.6%
P3HT M102	65,200	2.2	95.7%

P3HT from batch M101 was used for casting films in the dielectric spectroscopy study, while batch M102 was used for thin films preparation and LIPSS formation.

2.1.2 Poly(vinylidene fluoride -trifluoro ethylene), P(VDF-TrFE)

The chemical structure of P(VDF-TrFE) copolymers has been shown previously [2] (Chapter 1, Section 1.3.1). In this work, P(VDF-TrFE) was purchased from Piezotech S.A.S. (France) and used as received. Details and information for the P(VDF-TrFE) copolymer used in this Thesis are listed in Table 2.2.

Table 2.2 Details of P(VDF-TrFE) copolymer.

Polymer	Ratio of VDF:TrFE	M_w (g/mol)	PDI
P(VDF-TrFE)	76:24	367,000	1.72

P(VDF-TrFE) pellets were used for preparing NPs and thin films.

2.1.3 Poly(styrene), PS

Poly(styrene) (PS) is an aromatic polymer derived from petroleum, and synthesized from phenyl-ethylene monomer [3]. The chemical structure is shown in Figure 2.1, and it consists of a long hydrocarbon chain where alternating carbon centers are attached to the aromatic benzene ring [3,4]. The free-radical polymerized atactic PS is an amorphous polymer, which is in a glassy state at room temperature, and it present a T_g, around 106 ºC. Moreover, PS exhibits excellent mechanical properties, safe and easy-processing, making it widely used in food packaging, appliances, consumer electronics and medical applications [5].

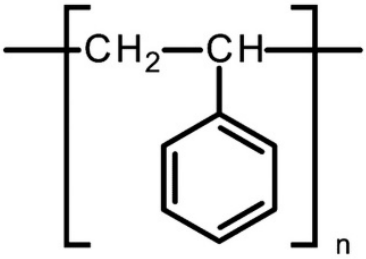

Figure 2.1 The chemical structure of PS.

In this work, PS was obtained from Polymer Source Inc (Batch P8647-S), and details are listed in Table 2.3.

Table 2.3 Details of PS.

Polymer	M_w (g/mol)	PDI
PS	555,00	1.07

PS thin films were prepared by spin coating on silicon, glass and quartz substrates.

2.1.4 [6,6]-phenyl C_{71}-butyric acid methyl ester, $PC_{71}BM$

The structure of [6,6]-phenyl C_{71}-butyric acid methyl ester ($PC_{71}BM$) has been described in Chapter 1 (section 1.2.2). In this work, $PC_{71}BM$ with a molecular mass of 1031 g/mol was purchased from Ossila Ltd. (Product Code M113). The used $PC_{71}BM$ batch is a mixture of 95% $PC_{71}CBM$ and 5% $PC_{61}BM$ as specified by the manufacturer. Throughout this work, $PC_{71}BM$ was used in solution for preparing blend films with P3HT.

2.1.5 Solvents

Several solvents were used in this work for the different polymer materials and preparation methods. Information of solvents used is listed in the Table 2.4.

Table 2.4 Information of solvents.

Solvent		**Boiling Point °C**	**Water miscibility**	**Density (25 °C) g/mL**	**Polymers dissolved**
Trichloromethane (Chloroform)	$CHCl_3$	61.2	No	1.489	P3HT $PC_{71}BM$ PS
Tetrahydrofuran	THF	66	Yes	0.8892	P3HT P(VDF-TrFE)
N,N-dimethylacetamide	DMA	165	Yes	0.937	P(VDF-TrFE)
Methyl ethyl ketone	MEK	78	No	0.805	P(VDF-TrFE)

Others solvents were also used, for example, acetone was used to clean all glass containers and substrates, and 2-propanol was used for cleaning silicon substrates. Piranha solution (H_2O_2:H_2SO_4 =1:3) was prepared to treat silicon wafers in order to enhance hydrophobicity of its surface for spin coating in particular cases. Additionally, glycerol and paraffin oil were used for CA measurements.

2.2 Preparation of samples

In this section, the different preparation methods of the samples involved in this Thesis will be described.

2.2.1 Casted films of P3HT and P3HT/$PC_{71}BM$ blends

Polymer blends of the semiconducting polymer P3HT and $PC_{71}BM$ were prepared for dielectric spectroscopy characterization. For this purpose, the corresponding amounts of P3HT and $PC_{71}BM$ for each blend (50/50 and 90/10) were dissolved in $CHCl_3$ at a total concentration of 120 g/L, sealed and stirred at 400 rpm for 20 hours at room temperature. The mixture P3HT/$PC_{71}BM$ solution was carefully casted on an electrode, which was previously cleaned in ultrasonic bath and dried under nitrogen flow. Then, films were dried at room temperature for 2 days, and moved into a vacuum oven to continue drying at room temperature for one week in order to eliminate residual solvent. Following the same procedure, P3HT films were prepared. The resulting films thicknesses are around 0.2 mm as measured by a micrometer.

2.2.2 P(VDF-TrFE) nanoparticles

The dialysis nanoprecipitation, first mentioned by C. Zhang et al in 2012 for nanoprecipitation of PS nanospheres [6], is used in this Thesis to prepare P(VDF-TrFE) NPs.

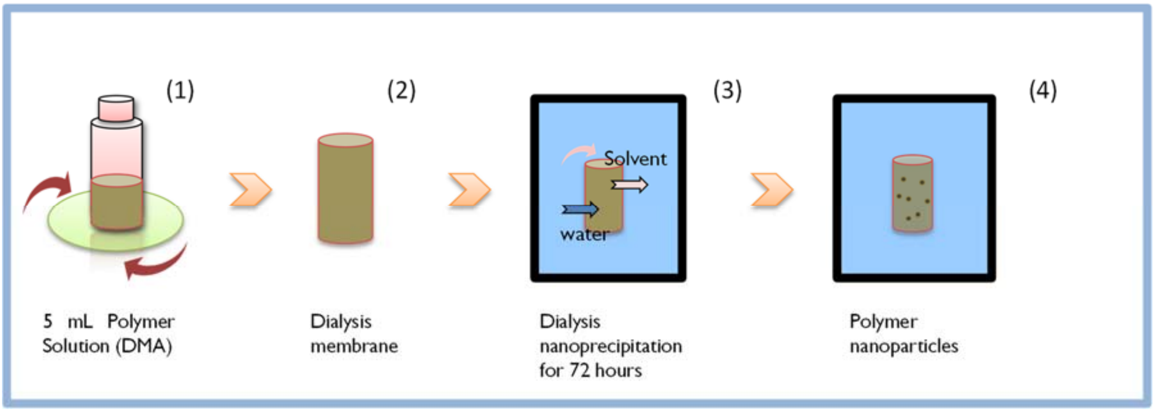

Figure 2.2 Scheme of the precipitation method.

This protocol is illustrated in Figure 2.2. First P(VDF-TrFE) polymer solution was prepared at a fixed concentration of 5 mg/mL, using DMA as solvent and stirring 20 hours at room temperature. Then the polymer solution was transferred into a dialysis membrane, which was previously cleaned with distilled water and DMA. The membrane, after being sealed at both ends, was immersed in a large volume of distilled water. The different concentration of DMA inside and outside the membrane results in DMA and water molecular exchange to establish chemical equilibrium. Low concentration of polymer solution is required to ensure that the polymer chains are in a dispersed state and able to separate into nanodomains. During the dialysis procedure, water refreshment was needed for several times to overcome the chemical equilibrium, till DMA in the membrane was completely replaced. The resulting NPs suspension was filtered through a syringe filter in order to remove large aggregates [7].

2.2.3 Polymer thin films by spin coating

Spin coating method, due to its easy and fast operation, low cost and the fact that produces relatively flat surfaces, has become one of the most popular methods for thin films preparation [8,9].

The schematic of the spin coating process is displayed in Figure 2.3. The whole process can be divided into several stages: (i) a polymer solution is deposited on a substrate, which can be silicon, glass, etc., depending on the demands, (ii) the substrate is rapidly accelerated to the desired rotation rate, and liquid flows radially, owing to the action of centrifugal force, (iii) the film becomes thinner slowly and (iv) solvent evaporation dominates drying. The steps (iii) and (iv) are controlled by the solution viscosity and the solvent evaporation, which can impact on the final coating thickness and on the roughness [9].

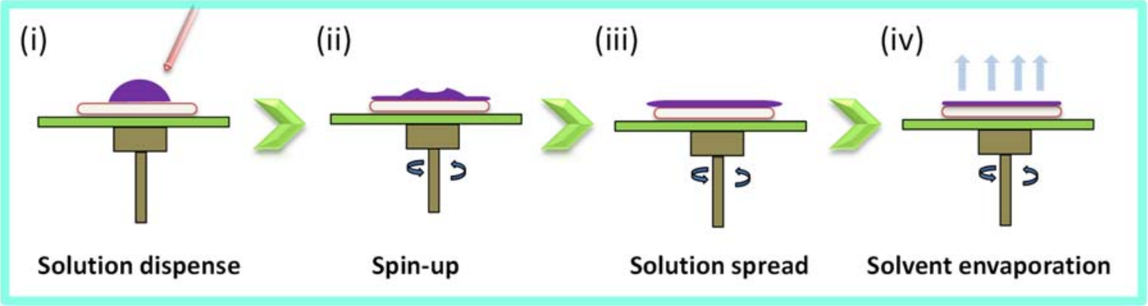

Figure 2.3 Schematic of spin coating for producing a thin film.

Polymer thin films studied in this Thesis will be introduced below. Two spin coaters, one home-made equipment and a commercial one (Laurell, WS-650 Series), were used with similar rotation speed, under ambient condition.

2.2.3.1 Single layer thin films

PS SINGLE LAYERS

PS thin films were prepared by spin coating using the home-made spin coater. All substrates, silicon wafers (100) (Wafer World Inc.) polished on both surfaces, glass (microscope slides, Thermo Scientific) and quartz substrates (UQG Optics) were cut into pieces of 1 cm × 1 cm and cleaned with $CHCl_3$. PS was solved in $CHCl_3$ by stirring for 10 min at 300 rpm at room temperature and afterwards it was filtered by using a syringe with a filter. A fixed amount of 0.2 mL of polymer solution was instantly dropped on a substrate placed in the center of a rotating metallic horizontal plate, with a rotation speed of 2380 rpm kept during 2 min. The thickness of PS thin films was adjusted by modifying the concentration of the polymer solution. An initial PS solution with concentration of 30 g/L was diluted into 25, 20, 15, 10 and 8 g/L, and then spin-coated onto the substrates under the same rotation conditions. The relationship of thickness of prepared films and their concentration is displayed in Figure 2.4.

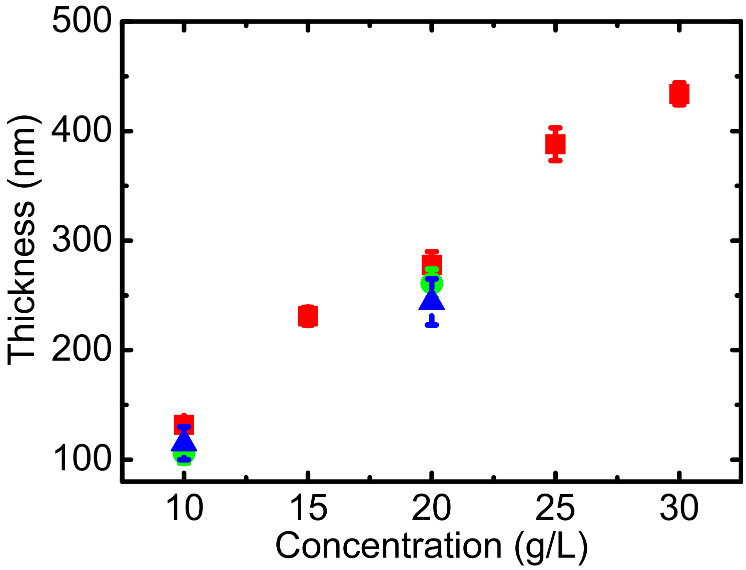

Figure 2.4 Dependence of thickness of PS films on the solution concentration for the different substrates: silicon (🟥), glass (▲) and quartz (●).

PS free-standing films were also prepared by casting PS solution (with concentration of 60 g/L) onto glass substrates. Samples were dried in vacuum oven at room temperature for one week, and then manually removed from substrate. The thickness of free-standing PS film, measured by a micrometer was 150 μm.

P3HT SINGLE LAYERS

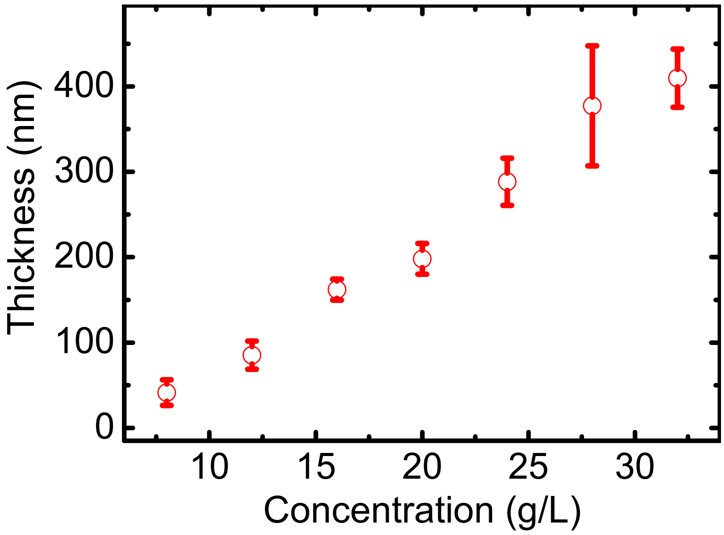

Figure 2.5 Thickness of the prepared P3HT films as a function of concentration.

P3HT thin films were prepared using the spin coater Laurell. P3HT (M101) powder was dissolved in $CHCl_3$ with a concentration of 32 mg/mL, stirring for 30 minutes at room temperature. The prepared solution was diluted into various concentrations: 28, 24, 20, 16, 12 and 8 mg/mL. Conductive Silicon wafers were cut into pieces of 2 cm × 2 cm, cleaned by acetone and 2-propanol and then dried under Nitrogen flow. A fixed volume of 0.2 mL solution was spin-coated on silicon wafer at 2400 rpm for 2 min. The film thickness was varied by varying the solution concentration. The concentration dependence for the thickness of the prepared P3HT films is displayed in Figure 2.5.

P(VDF-TRFE) SINGLE LAYERS

P(VDF-TrFE) thin films were prepared following a similar protocol than that used for preparing P3HT films. First P(VDF-TrFE) was dissolved in MEK with a concentration of 20 mg/mL, stirring for 3 hours at 72 ºC. Then, it was diluted into different concentrations: 17, 15, 12, 10, 7, 5, 4, 3 and 2 mg/mL. Non-conductive Silicon wafers were cleaned as explained previously for the preparation of P3HT thin films. A fixed volume of 0.2 mL of the P(VDF-TrFE) solution was spin-coated on the silicon wafer fixed at the Laurell spin coater, with 2400 rpm for 2 min. The relationship between the thickness and the solution concentration is shown in Figure 2.6**.**

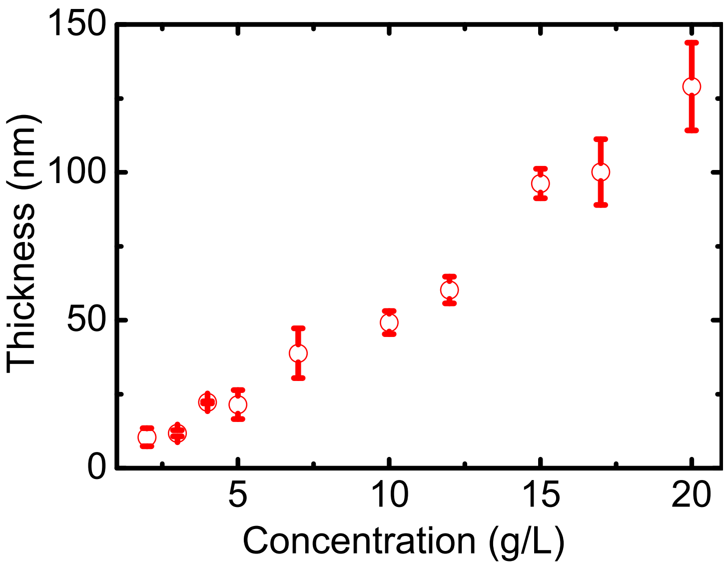

Figure 2.6 Dependence of thickness of P(VDF-TrFE) films on the concentration.

2.2.3.2 Bilayers

The bilayers were prepared using the procedure introduced in a previous work [7]. First P3HT (M102) was spin-coated on conductive silicon using the same conditions as the ones used for

P3HT single layers. Afterwards, solutions of P(VDF-TrFE) in MEK with different concentration were spin-coated on the top of the prepared P3HT films. Since MEK does not dissolve P3HT, bilayers of the two different polymers are formed. In this set of experiments, different concentrations of both polymers are prepared, and thus bilayers with different thicknesses are obtained.

2.2.3.3 P3HT/P(VDF-TrFE) blends thin films

P3HT/P(VDF-TrFE) 50/50 wt% blends were prepared by spin coating using the Laurell spin coater. The same amount of P3HT and P(VDF-TrFE) (12 mg) were dissolved in their co-solvent THF with a total concentration of 24 mg/mL. The blend was stirred for 4 hours at 41 ºC and then diluted into 16 mg/mL and 8 mg/mL, respectively. The conductive silicon wafers were first treated with piranha solution and then put onto the hot plate pre-heated to 41 ºC. After that, the blend was dropped onto the pre-heated silicon wafers immediately and spin-coated at 2400 rpm for 2 min.

2.2.3.4 P3HT layer with embedded P(VDF-TrFE) nanoparticles

In order to dry the P(VDF-TrFE) NPs prepared as described in section 2.2.2, water was removed by lyophilization process at -100 ºC. For that, the sample is frozen while being centrifuged and the pressure is reduce to sublimate the frozen liquid and extracte it. As a result, the nanoparticles are recovered in the form of a liquid free-powder. Once dried, P(VDF-TrFE) NPs were redispersed in a non-solvent, $CHCl_3$ in this case, by ultrasonication for 15 min at room temperature. Afterwards, the same amount of P3HT, which is soluble in $CHCl_3$, was added to the suspension, and further ultrasonicated for 15 min. In this way, NPs were dispersed in a P3HT solution in $CHCl_3$. The solution was then spin-coated at 2400 rpm for 2 min using the homemade spin coater onto the conductive silicon wafers previously treated by piranha solution. The schematic is shown in Figure 2.7.

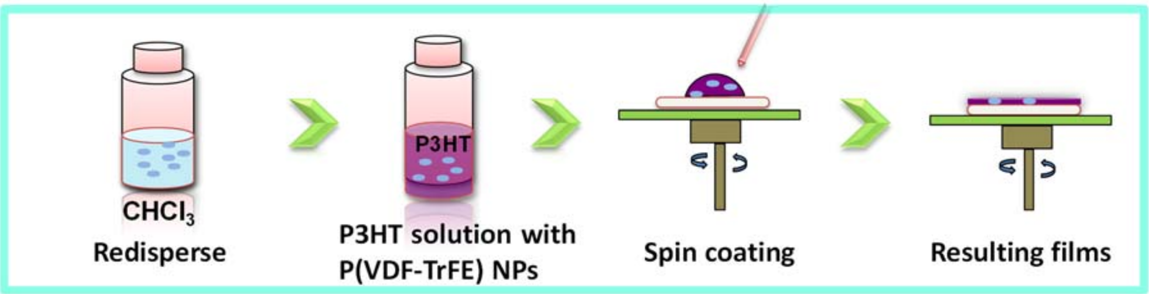

Figure 2.7 Schematic of the preparation of P3HT film with embedded P(VDF-TrFE) NPs.

By tuning the concentration of the solution, different thicknesses of the nanocomposites were obtained.

2.2.4 Laser induced periodic surface structures (LIPSS)

2.2.4.1 LIPSS on PS film

Laser irradiation of PS films was carried out in ambient air under normal incidence, with the linearly polarized laser beam of a Q-switched Nd:YAG laser (Lotis TII LS-2131M, pulse duration τ = 8 ns full width half-maximum) at a repetition rate of 10 Hz. The fourth harmonic, at a wavelength λ = 266 nm was used for the experiments, since at this wavelength PS absorbs efficiently with an absorption coefficient of 1.6×10^5 m^{-1}, measured by UV-Vis spectroscopy. The fluence of irradiation was determined by measuring the laser energy in front of the sample with a joulemeter (Gentec-E, QE25SP-H-MB-D0) and by calculating the area of the irradiated spots after delimitating the beam with an iris of 0.29 cm diameter. The spin-coated PS films were irradiated as a function of the number of pulses (up to several thousands) at a constant fluence of 10 mJ/cm^2, and moreover, with a constant number of pulses in the range of fluences of 7−13 mJ/cm^2.

2.2.4.2 LIPSS on P3HT single layer and P3HT/P(VDF-TrFE) bilayer

P3HT single layers and P3HT/P(VDF-TrFE) bilayers were irradiated by using the second harmonic, with a wavelength of λ= 532 nm, of the Q-switched Nd:YAG laser Lotis TII LS-2131M, since P3HT absorbs efficiently at this wavelength (α_{532}= 8.62×10^6 m^{-1}). The repetition rate was kept at 10 Hz. The irradiation of P3HT single layers was performed with 3600 pulses at a fluence in the range from 23.4 to 31.2 mJ/cm^2, as determined by measuring the laser energy in front of the sample and considering an irradiated spot with a diameter of 5 mm. Bilayers were irradiated at a constant fluence of 26 mJ/cm^2 with 3600 pulses.

2.3 Physical and structural characterization

2.3.1 Scanning probe microscopy (SPM)

2.3.1.1 Atomic force microscopy (AFM)

Since the invention of the atomic force microscope (AFM) by Gerd Binnig, Calvin F. Quate and Christoph Gerber in 1986 [10], a whole family of scanning probe microscopy (SPM) techniques based upon different physical interactions has been developed. AFM has become an important technique to provide images of samples in various environments (vacuum, atmosphere, and liquid) with three-dimensional information at the nanometer scale in real space [11,12].

The basic principle of AFM techniques is the measurement of the vertical motion of a cantilever beam with ultra-small mass as it scans a surface. At the end of the cantilever a tip is attached which detects the topography of the sample surface. The nanoscale probe is usually made of Si_3N_4 or silicon. The imaging modes of AFM are divided into three major categories according to whether the tip contacts the sample: the contact mode, tapping mode, and non-contact mode [13-15]. The schematic illustration of the setup and working principle of AFM is shown in Figure 2.8. As the probe approaches the surface, the force caused by the interaction between the sample and the tip induces either a deflection of the cantilever probe (contact mode) or an amplitude change (tapping mode) [16]. The force is measured by detecting the deflection of the cantilevers. To do that, a laser beam is reflected from the reverse side of the cantilever surface onto a position-sensitive array of photodiodes (a quadrant photodiode detector divided into four parts). The reflected light position on the photodetector, which indicates the deflection of the cantilever, is detected and converted to an electrical signal read by a computer, and thus the surface information is recorded [16,17].

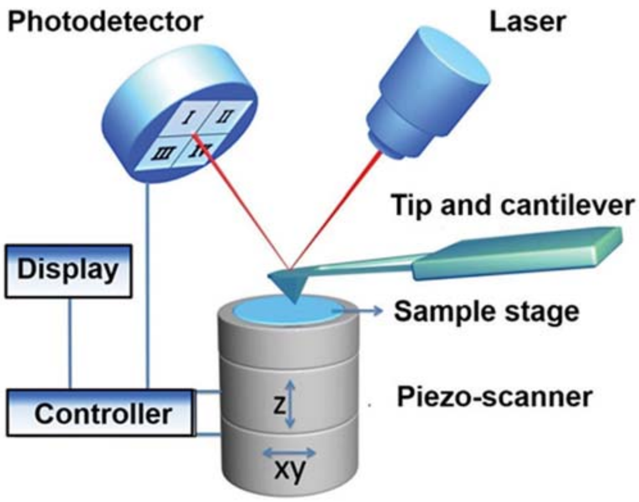

Figure 2.8 Schematic diagram of atomic force microscopy [17].

The measurement of the different interactions between the tip and the sample surface led to the creation of a variety of other scanning probe microscopies, such as the magnetic force microscopy (MFM) which measures the magnetic structure of the surface [18], Kelvin probe force microscopy (KPFM) which measures the local surface potential [19], quantitative nanomechanical mapping (QNM) which measures the mechanical properties at the nanoscale [19,20], piezoresponse force microscopy (PFM) which measures the ferroelectric response of the films [21,22], and conductive AFM (C-AFM) which measures the electrical conductivity [23]. All these SPM techniques provide us the unique opportunity to characterize different properties at the nanoscale.

2.3.1.2 Piezoresponse force microscopy (PFM)

PFM is performed using AFM in Contact Mode. The main principle is based on the reverse piezoelectric effect, which means that the applied electric field affects the ferroelectric sample resulting in a change of its dimensions [24]. The tip used in PFM is usually made of, or coated with, a conductive material, and acts as a top electrode. The schematic of the principle of PFM and the material surface response are presented in Figure 2.9**.**

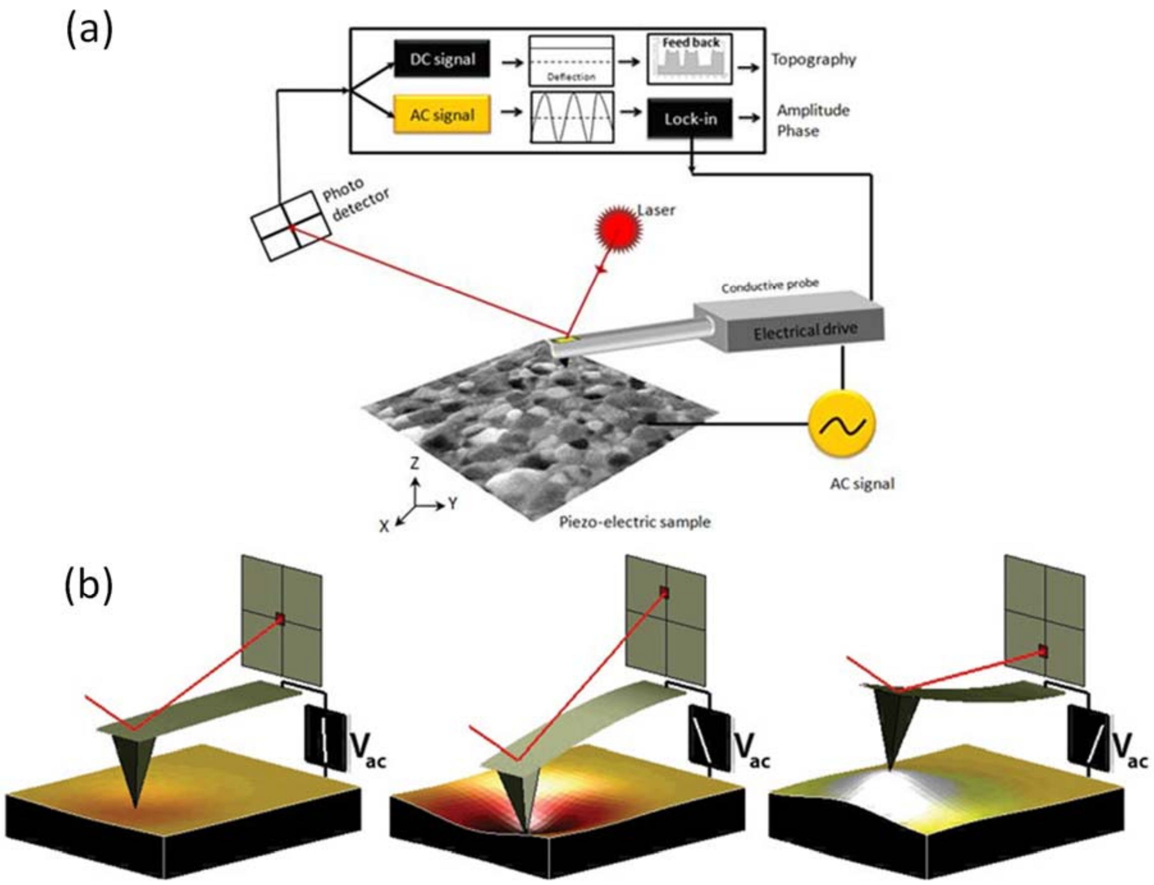

Figure 2.9 (a) Schematic diagram of PFM and (b) Response of material surface [25].

The AFM probe tip scans the surface while an Alternating Current (ac) voltage is applied between the tip and the sample. Because of the reverse piezoelectric effect the sample will locally expand or contract according to the electric field, and this change is measured by the deflection of the cantilever having its tip in contact with the sample. If the initial polarization of the electrical domain of the sample is parallel to the applied electric field, the domain would experience a vertical expansion. Such expansion can bend the AFM cantilever upwards, resulting in an increased deflection compared to the signal before applying the electric field. Conversely, if the initial domain polarization is anti-parallel to the applied electric field, the domain would contract resulting in a decreased cantilever deflection. In such situation, the amount of cantilever deflection change is directly related to the amount of expansion or contraction of the sample electric domains, hence proportional to the applied electric field. If the polarization vector is perpendicular to the electric field, there is no piezoelectric deformation along the field direction, but a shear strain appears in the ferroelectric material, leading to displacements of the sample surface parallel to itself, along the polarization direction. By analyzing the PFM amplitudes and the PFM phases of the normal and torsion cantilever vibrations, the topographical features and the ferroelectric response of a ferroelectric sample can be measured simultaneously. If the bias turns into a field of magnitude above its coercive field, the ferroelectric domains will align along the direction of the field. Due to the hysteresis, when the field is turned off, the dipole moment of the molecules will remain pointing towards the direction imposed [25,26].

2.3.1.3 Conductive Atomic Force Microscopy (C-AFM)

The operation of the conductive AFM is similar to PFM, by using an AFM probe coated by a conductive layer as a nanometer-scale electrical probe. A bias voltage is applied between the tip and the sample and while the conductive probe scans the sample surface in contact, the electric current between the sample and the tip is measured through an electric current amplifier. In this way, the topography and the conductivity over the sample surface can be obtained simultaneously.

There are two standard measuring geometries [27]. As shown in Figure 2.10, the vertical geometry measures the out-of-plane current through the material between the AFM probe and a conductive substrate, whereas the horizontal geometry measures in-plane current through material between the AFM probe and a patterned electrode on an insulating substrate. In operation, current may be recorded at a constant voltage as a function of position, for current mapping, or recorded as a function of voltage at a sample position, for current-voltage (I-V) characterization [28-30].

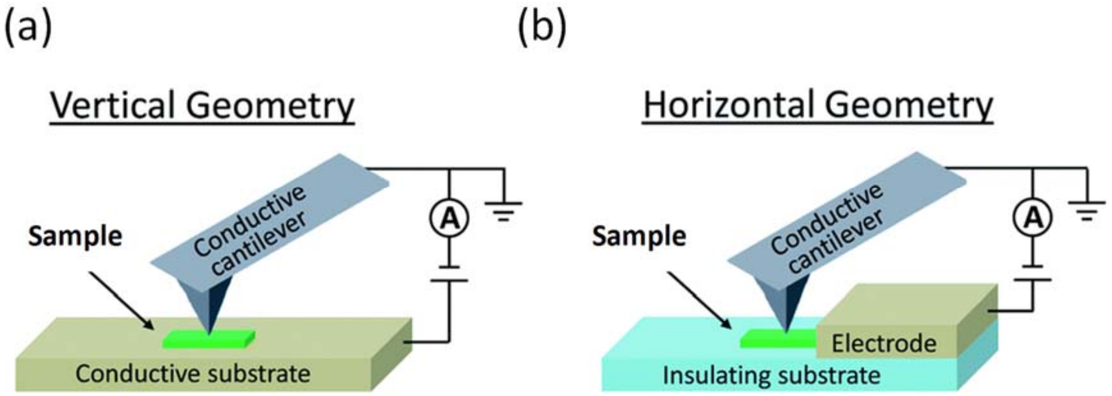

Figure 2.10 Schematic illustration of (a) the vertical geometry and (b) the horizontal geometry for C-AFM measurements [27].

2.3.1.4 Applications of SPM in this Thesis

TOPOGRAPHIC FEATURES

The morphology of prepared samples was inspected under ambient conditions using a Multimode 8 AFM (Bruker) with a Nanocope V controller (Bruker). The topography AFM images were collected in tapping mode using silicon probes NSG-30 (NT-MDT) which are standard rectangular shape silicon cantilevers and have a typical tip curvature radius of ~ 6 nm. Topographical images were collected from multiple locations to examine the film uniformity. Analysis and output of images were carried out using the NanoScope Analysis software 1.50 (Bruker).

Additionally, thickness of the spin-coated films, including single layer and bilayer films, was measured by AFM in tapping mode. A scratch was made on the surface of the films and the step between the substrate and the polymer layer was quantified in different locations of several samples. The average roughness R_a, which indicates the arithmetic average of the deviations in height from the center plane of the sample.was obtained by the software Nanoscope Analysis 1.50.

PFM

PFM measurements were carried out using the same equipment, in the piezoresponse mode. The microscope was used in contact mode, using mild measuring conditions in order to avoid damaging the samples. To ensure electrical contact, the sample was glued to the conducting substrate by conductive epoxy (CW2400, Chemtronics). The probes used are SCM-PIC (Bruker) which are coated with a conductive PtIr layer and have a low spring constant (0.2~0.4 N/m) and a tip with radius of ca. 20 nm. The PFM out-of-plane signal was taken by applying an ac voltage of 2 V at a frequency of 60 kHz between sample and tip.

Hysteresis cycles were recorded applying a tip bias ramp from -12 to 12 V at a frequency of 0.1 Hz and collection of 1024 points. Local poling was carried out using the tip as the top electrode and applying, in every case, a dc bias (± 12 V) for 100 s. The control of points and lines drawn in the ferroelectric phase was made by the Point & Shoot protocol, available in the Nanoscope 8.15 software.

C-AFM

AFM measurements were done using the same microscope equipped with a C-AFM module, and employing the same conductive tip as the one used in PFM mode. The sample was fixed as in PFM measurements. As the conducting probe scans the sample, a bias of -5 V was applied, and the current was measured by a preamplifier.

2.3.2 X-Ray scattering

2.3.2.1 Working principles

X-rays are electromagnetic waves with wavelength in the range of 10^{-11}–10^{-8} m produced when an electron beam is accelerated by a sufficiently high-voltage electric field [31], or when highly accelerated electron beams bombard metallic targets under vacuum. X-ray scattering and diffraction was are well established techniques for investigating the structure of matter [32]. The conventional application of X-ray scattering is performed in transmission geometry, in which X-rays are normal to the surface of the sample. The schematic X-ray scattering in transmission geometry is shown in Figure 2.11.

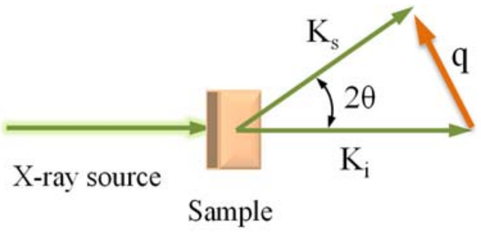

Figure 2.11 Schematic of X-ray scattering process.

When an X-ray with a wavelength λ is scattered, a scattering vector, q, can be defined as the difference between the incident wave vector $\overrightarrow{K_{\imath}}$ and the scattered vector $\overrightarrow{K_f}$, that is

$$\vec{\boldsymbol{q}} = \overrightarrow{\boldsymbol{K_{\imath}}} - \overrightarrow{\boldsymbol{K_f}} \qquad (2\text{- }1)$$

As shown in Figure 2.11a, the angle between $\overrightarrow{K_{\imath}}$ and $\overrightarrow{K_f}$ is $2\boldsymbol{\theta}$. The moduli of the momenta are the same because the scattering is elastic, that is, there is no change in the photon energy, and thus:

$$\left|\overrightarrow{\boldsymbol{K_{\imath}}}\right| = \left|\overrightarrow{\boldsymbol{K_f}}\right| = \frac{\boldsymbol{2\pi}}{\boldsymbol{\lambda}} \qquad (2\text{- }2)$$

The modulus of the scattering vector is $q = \frac{4\pi}{\lambda}\sin\boldsymbol{\theta}$.

According to the Bragg´s law [33], the relation between the length-scale of order d, radiation wavelength λ and scattering angle $2\boldsymbol{\theta}$ can be expressed as:

$$\boldsymbol{d} = \frac{\boldsymbol{n\lambda}}{\boldsymbol{2\sin\theta}} \qquad (2\text{- }3)$$

The relationship between q and the d is established as:

$$\boldsymbol{q} = \frac{\boldsymbol{2\pi}}{\boldsymbol{d}} \qquad (2\text{- }4)$$

Structural information on the desired length-scale, from atomic level (unit cell of the crystals) up to several micrometers (spherulites), can be investigated by studying different ranges of the magnitude of the scattering vector q, through different ranges of the scattering angle **θ** [34]. The larger scattering angle, the smaller length scale probed. For polumer materials, two different modes, Small Angle X-Ray Scattering (SAXS) and Wide Angle X-Ray Scattering (WAXS), are normally performed. WAXS, with scattering angle $2\boldsymbol{\theta} > 3^{o}$, identifies the structure of crystal unit cell at atomic length scale, while SAXS studies the microstructure at larger length scales, with a small scattering angle $2\boldsymbol{\theta} < 1^{o}$.

Besides the classical X-ray diffraction and scattering performed in laboratory based sources, analysis of polymer thin films and in-situ experiments, which need high brilliance or low exposure time, are typically performed by using synchrotron radiation facilities. Synchrotron radiation is produced when electrons orbit in a magnetic field and lose energy continuously in the form of electromagnetic radiation emitted tangentially from the orbit [35]. The sketch of a synchrotron radiation facility is illustrated in Figure 2.12.

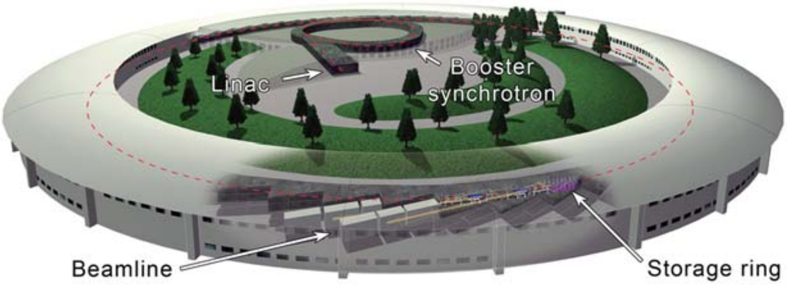

Figure 2.12 Scheme of a synchrotron radiation ring [36].

Electrons, once produced by an electron gun, are accelerated in a linear accelerator (Linac), and then are transferred to the circular accelerator, synchrotron, guided by a bending magnet where they are strongly accelerated till reaching energies of several millions of electron volts (MeV). Once the electrons reach the expected energy, they enter the storage ring and can be considered in a quasistationary situation. The storage rings consist of a circular ring-like structure in which the electrons follow circular paths at speed close that of light. The circular trajectory is defined by an array of magnets, called bending magnets, located at defined places of the ring. X-ray radiation is produced tangentially to the ring by “bremsstrahlung” effect when the electrons are force to curve their trajectories by the action of the bending magnets. Additional auxiliary components such as insertion devices (either undulators or wigglers) may be used to in orther to increment the photon energy obtained from the bending magnets radiation characteristics (broad band, narrow band, etc.). These X-rays are guided into the beamlines (work stations) to perform experiments [32,37].

2.3.2.2 X-ray scattering application in this Thesis

Grazing Incidence Small Angle X-ray Scattering (GISAXS) and Grazing Incidence Wide Angle X-ray Scattering (GIWAXS) experiments were performed by using synchrotron radiation at DUBBLE beamline (BM26B) of the European Synchrotron Radiation Facility (ESRF) in Grenoble, France. A conceptual scheme of the set-up is shown in Figure 2.13.

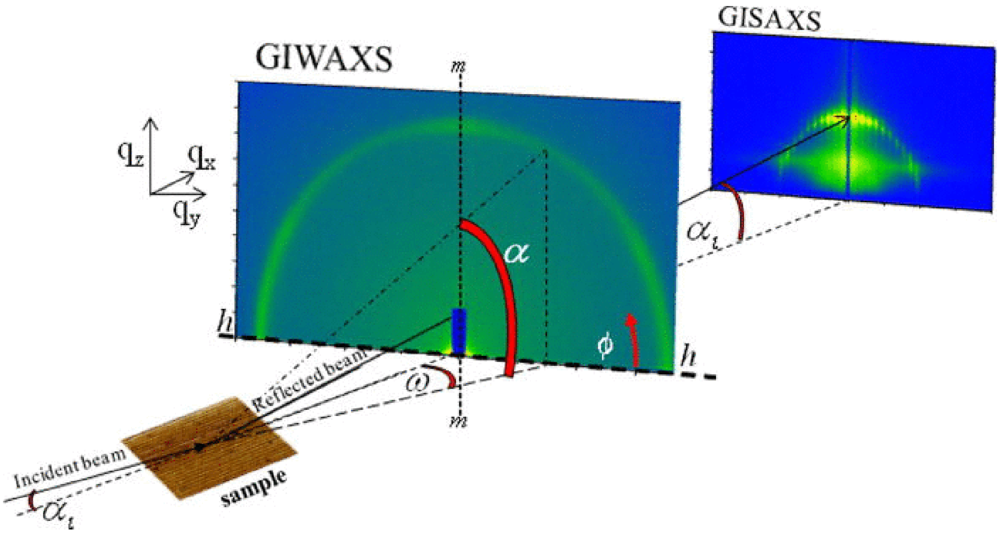

Figure 2.13 Conceptual scheme of a GISAXS and GIWAXS experiment. α_i and $\boldsymbol{\alpha}$ are the incidence angle and exit angle, respectively. ω is the scattering angle out of the meridian.

As presented in Figure 2.13, a X-ray beam is directed on a sample surface with an incident angle α_i, respect to the surface. The X ray beam is scattered by the sample, and then recorded by a detector. A vertical plane, known as the scattering plane is defined by both the incident and reflected beams which intersects the detector along the meridian, m-m line ($\omega = 0^o$). GISAXS patterns show the scattering intensity collected by the detector above the horizon line (h-h, exit angle $\boldsymbol{\alpha} = 0°$) which corresponds to the intersection of the sample plane with the detector plane. By introducing the orthogonal scattering vector q_z and q_y, structural information perpendicular and parallel to the film plane can be obtained. Each point (y,z) of the pattern is defined by the angular coordinates (ω, α) or by means of the corresponding components (q_y, q_z) of the reciprocal scattering vector q. The angles and the components of the reciprocal vector are related by the expressions [32]:

$$q_y = \frac{2\pi}{\lambda} \sin \omega \cos \boldsymbol{\alpha} \qquad (2\text{- }5)$$

$$\boldsymbol{q_z = \frac{2\pi}{\lambda}(\sin \alpha_i + \sin \alpha)} \qquad (2\text{- }6)$$

In this work, an X-ray wavelength of λ=0.103 nm, with a beam size (horizontal× vertical) of 0.7 mm × 0.3 mm in the sample was employed for the measurements. In grazing incidence experiments, the sample was placed with its surface horizontal and parallel to the X-ray beam and at a height which intercepted half of the beam intensity. Then, the sample was tilted in order to reach an incidence angle between the sample surface and the beam, with an exposition time of 5 s for each incident angle. Different incidence angles of 0.14, 0.2, 0.3 and 0.4º were used in order to obtain information at different depth of the film. GISAXS patterns were taken using a Pilatus 1M detector of 981 × 1043 pixels, pixel size 172 μm × 172 μm, located at 7.2 m from the sample.

For GIWAXS measurements the sample-to-detector distance is reduced in relation to that used in GISAXS. In this case the scattered intensity was recorded by a Frelon detector of 2048 × 2048 pixels with a size of 46.8 μm × 46.8 μm per pixel. A sample-detector distance of 79.3 mm was used. As in the case of GISAXS measurements, the incidence angle (α_i) was set to 0.14-0.4º. Patterns acquired with an exposition time of 10 s were corrected from background scattering. Both GISAXS and GIWAXS patterns were analyzed by the Fit2D software [38].

2.3.3 Broadband dielectric spectroscopy (BDS)

2.3.3.1 Working principle

Broadband Dielectric Spectroscopy (BDS) is an experimental technique to study the molecular dynamics of a variety of materials within a large frequency range at different temperatures. BDS enables the study of relaxation phenomena with applications in liquid state physics, material science, biology, and engineering [39]. BDS measures the complex dielectric permittivity $\varepsilon^* = \varepsilon'(\omega) - i\varepsilon''(\omega)$ as a function of frequency in a wide temperature range, where the dielectric permittivity ε' is the real component, the dielectric loss ε'' is the imaginary component, and ω is the angular frequency of the external electric field $\omega = 2\pi f$.

Results of dielectric experiments can be presented using three different representations as a function of frequency in order to emphasize particular aspects of the dynamics: the complex permittivity ε*, the complex conductivity σ* = σ' + iσ'' and the complex electric modulus M* = M' + iM''. In the case of conducting polymers, it is difficult to describe their dynamics using the dielectric permittivity, as the conductivity contributes to a sharp increase in the ε'' function at low frequencies and can mask the segmental relaxation of the polymer chain [39]. This difficulty can be avoided by analyzing the dielectric properties of semiconducting polymers by using either the electric modulus formalism M*(ω) or the electric conductivity σ* (ω) representations to represent the dielectric data.

These complex quantities ε*, σ*, and M* are related one to each other according to the following equations [39,40]:

$$M^*(\omega) = \frac{1}{\varepsilon^*(\omega)} = \frac{1}{(\varepsilon' - i\varepsilon'')} = \frac{i\varepsilon_0\omega}{\sigma^*(\omega)} \tag{2- 7}$$

The real part M’ and imaginary part M’’ of M* can be determined from permittivity

$$M^*(f) = \frac{1}{\varepsilon^*} = M' + iM'' = \frac{\varepsilon'}{\varepsilon'^2 + \varepsilon''^2} + i\frac{\varepsilon''}{\varepsilon'^2 + \varepsilon''^2} \tag{2- 8}$$

While

$$\sigma^*(f) = j\omega\varepsilon_0\varepsilon^*(f) = \sigma' + i\sigma'' = \omega\varepsilon_0\varepsilon'' + i\omega\varepsilon_0\varepsilon' \tag{2- 9}$$

All these representations are completely equivalent but they emphasize different aspects of the underlying mechanisms of charge transport.

To obtain all the above mentioned dielectric magnitudes, a parallel plate capacitor is formed with the sample as a dielectric. Then the impedance is measured as a function of frequency. From the measured impedance values and the geometric factors of the capacitors, ε*, M* or σ* can be obtained [39].

2.3.3.2 Application of BDS in this Thesis

In the studies performed in this Thesis, samples were casted onto circular gold coated metal electrodes. Then, an upper gold coated metal disc (1 cm in diameter) was placed on top of the samples. BDS measurements were performed over a broad frequency window, $10^{-1} < f\text{(Hz)} < 10^7$ and a temperature range of $- 150 < T$ (ºC) < 150. Data were taken upon heating. To cover the above mentioned frequency range, a Novocontrol ALPHA dielectric interface integrated in a broadband dielectric spectrometer was employed. The temperature was controlled by a nitrogen jet (QUATRO from Novocontrol) with a temperature error during every single frequency sweep of ± 0.1 °C.

2.3.4 UV-Vis-NIR spectroscopy

2.3.4.1 Working principle

UV-Vis-NIR absorption spectroscopy is a measurement of light attenuation when it passes through a sample. When a sample is exposed to the light energy that matches the energy difference between a possible electronic transition within the molecule, a fraction of the light energy is absorbed by the molecule and the electrons are promoted to the higher energy state orbital [41].

A spectrometer records the degree of absorption by a sample at different wavelengths and the resulting plot of absorbance *(A)* versus wavelength (λ) gives the absorption spectrum.

When monochromatic radiation passes through a homogeneous solution in a cell, the intensity of the emitted radiation depends on the optical path (*l*) and concentration (c) of the solution. According to the Beer-Lambert Law, the concentration of a substance in solution is directly proportional to the absorbance, A, of the solution. I_0 is the intensity of the incident radiation and I is the intensity of the transmitted radiation. The ratio I/I_0 is called transmittance (T), and absorbance and transmittance are related by the expression [41,42]

$$A = Log\frac{I_0}{I} = \mathrm{Log}\frac{1}{T} = \varepsilon cl \quad (2\text{- }10)$$

where ε is the extinction coefficient, i.e. a constant which only depends on the nature of the molecule and the radiation wavelength.

In the case of films we can simplify this expression as

$$A = \alpha l \quad (2\text{- }11)$$

where α is the absorption coefficient at a given wavelength and l is the film thickness.

2.3.4.2 Application of UV-Vis-NIR spectroscopy in this Thesis

Based on the Beer-Lambert Law equation, the absorption coefficient of the different polymer films, including PS, P(VDF-TrFE), P3HT and its based blends are measured in this work. Absorption spectra of polymer films were obtained from a UV-Vis-NIR spectrophotometer (UV-3600, Shimadzu), in the wavelength range from 190 nm to 1100 nm. The spectrophotometer is interfaced to a personal computer loaded with the UVProbe software. The baseline was obtained by scanning two clean quartz windows, and the absorption spectrum of each sample was measured with the film deposited on a quartz window.

The measured films, P3HT and its based blends were spin-coated from their solutions slowly onto 2 mm thick quartz wafers while PS and P(VDF-TrFE) films were prepared by drop casting. The thickness of the samples was estimated to be between 300 and 500 nm by confocal microscopy.

2.3.5 Contact angle measurements

The wettability can be characterized by contact angle (CA) measurements in a simple, rapid and sensitive way. From the CA measurements it is possible to calculate the surface free energy by using different methodologies.

One often applied model is the one by Owens, Wendt, Rabel and Kaelble (OWRK-model) which considers the geometric mean of the dispersive and polar parts of the liquid surface tension and of the solid surface energy [43,44]. According to the Young's equation there is a relationship between the CA (θ), the surface tension of the liquid (γ_l), the interfacial tension between the liquid and solid (γ_{sl}) and the surface free energy of the solid (γ_s):

$$\gamma_s = \gamma_{sl} + \gamma_l cos\theta \tag{2- 12}$$

The interfacial tension γ_{sl} is calculated based on the two surface tensions γ_s and γ_l and the interactions between the phases. These interactions are interpreted as the geometric mean of a dispersive part γ^d and a polar part γ^p of the surface tension or surface free energy:

$$\boldsymbol{\gamma_{sl} = \gamma_s + \gamma_l - 2(\sqrt{\gamma_s^d \gamma_l^d} + \sqrt{\gamma_s^p \gamma_l^p})} \tag{2- 13}$$

At least two liquids with known dispersive and polar parts of the surface tension are required to determine the surface free energy of the solid, wherein at least one of the liquids must have a polar part > 0. Substituting this expression in the Young equation a linear equation of the type *y = slope x + c* can be obtained:

$$\frac{\gamma_l(1+\cos\theta)}{2\sqrt{\gamma_l^d}} = \sqrt{\gamma_s^p}\sqrt{\frac{\gamma_l^p}{\gamma_l^d}} + \sqrt{\gamma_s^d} \tag{2- 14}$$

In this expression *y* and *x* contain the known quantities (the CA and the dispersive and polar parts of the surface tension of the liquids chosen as tests). The dispersive and polar parts of the solid surface energy are contained in the axis intercept and in the slope. These parameters can be evaluated creating a regression line when contact angles of at least two test liquids are measured. In this case the liquids listed in Table 2.5 are employed.

A different model is the one based on Young-Dupre theory that was later improved by van Oss, Chaudhury and Good [45,46]. This model gives information on the Liftshitz-van der Waals and electron-donor and electron-acceptor components, allowing the assessment of both apolar and polar interactions respectively. To that purpose the following equation is used:

$$\gamma_l \ (1 + cos\theta) = 2(\gamma_s^d \gamma_l^d)^{1/2} + 2(\gamma_s^+ \gamma_l^-)^{1/2} + 2(\gamma_l^+ \gamma_s^-)^{1/2} \tag{2- 15}$$

where θ is the CA of the liquid drop on the solid surface and γ_l is the surface free energy of the liquid probe. γ_s^d and γ_l^d are the apolar components of the solid and the liquid, respectively; γ_s^+ and γ_l^+ are the electron-acceptor (polar ones), while γ_s^- and γ_l^- are the electron-donor components of the surface free energy of solid and liquid, respectively. The term γ_s^d of a solid surface is calculated using the CA value of an apolar liquid probe. The total liquid free energy is the sum of the apolar component and the polar one, and since for apolar liquids $\gamma_l^+ = \gamma_l^- = 0$, then, $\gamma_l = \gamma_l^d$. In this case Equation (2- 15) can be rewritten as:

$$\gamma_s^d = \gamma_l \ (1 + cos\theta)^2/4 \tag{2- 16}$$

In this Thesis, the use of paraffin oil as apolar liquid allowed us to calculate γ_s^d, employing the values of the surface free energy components listed in Table 2.5. Once γ_s^d is known, the unknown values of γ_s^+ and γ_s^- were calculated by solving the equation (2- 15) for the pair water-glycerol (using again the corresponding parameters listed in Table 2.5).

Finally, to determine the total surface energy of the polymer films (γ_s) equations (2- 15) and (2-16) are used, which relate the total surface energy with dispersion (γ_s^d) and acid-base (γ_s^p) components:

$$\gamma_s = \gamma_s^d + \gamma_s^p \tag{2- 17}$$

$$\gamma_s^p = 2(\gamma_s^+ \gamma_s^-)^{1/2} \tag{2- 18}$$

Table 2.5 Surface free energy components of the liquids probes (mJ m^{-2}).

Liquid	γ_l	γ_l^d	γ_l^p	γ_l^+	γ_l^-
Water	72.8	21.8	51	25.5	25.5
Glycerol	64	34	30	3.92	57.4
Paraffin oil	28.9	28.9	0	0	0

In this work, the CA measurements were carried out at room temperature and ambient humidity using a pocket goniometer PG2 (FIBRO system) [47]. The CA values were determined by the sessile drop technique. Two polar liquids, water and glycerol, and one apolar liquid, paraffin oil, were chosen (glycerol and paraffin oil were supplied by sigma-Aldrich). During measurements, a droplet of each liquid probe with a volume of around 5 μL was deposited on a dry and clean polymer surface. Static CA values were measured inmediately after the formation of sessile drops of liquid on the surface. For each sample, at least three measurements were carried out and the results readily averaged. Figure 2.14 presents an example of CAs measurement for water dropped at P3HT thin film.

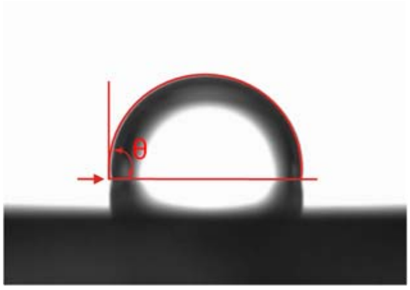

Figure 2.14 Example of CA measurements with a drop of water on the P3HT thin film.

2.4 References

[1] Pappenfus, T. M., Hermanson, D. L., Kohl, S. G., Melby, J. H., Thoma, L. M., Carpenter, N. E., da Silva Filho, D. A. and Bredas, J.-L. Regiochemistry of Poly(3-hexylthiophene): Synthesis and Investigation of a Conducting Polymer. *Journal of Chemical Education* **87**, 522-525 (2010).

[2] Mao, D., Gnade, B. E. and Quevedo-Lopez, M. A. in *Ferroelectrics - Physical Effects* (ed Lallart) (InTech, 2011).

[3] Barón, M., Hellwich, K.-H., Hess, M., Horie, K., Jenkins Aubrey, D., Jones Richard, G., Kahovec, J., Kratochvíl, P., Metanomski, W. V., Mormann, W., Stepto Robert, F. T., Vohlídal, J. and Wilks Edward, S. in *Pure and Applied Chemistry* Vol. 81 1131 (2009).

[4] Maul, J., Frushour, B. G., Kontoff, J. R., Eichenauer, H., Ott, K.-H. and Schade, C. in *Ullmann's Encyclopedia of Industrial Chemistry* (Wiley-VCH Verlag GmbH & Co. KGaA, 2000).

[5] McKelvey, J. M. *Polymer Processing*. (John Wiley & Sons, New York, 1962).

[6] Zhang, C., Pansare, V. J., Prud'homme, R. K. and Priestley, R. D. Flash Nanoprecipitation of Polystyrene Nanoparticles. *Soft Matter* **8**, 86-93 (2012).

[7] Martínez-Tong, D. E. *Confinamiento en Nanoestructuras Poliméricas: Preparación Propiedades, Aplicaciones e Implicaciones Físicas*, 2015).

[8] Chen, B. T. Investigation of the Solvent-evaporation Effect on Spin Coating of Thin Films. *Polymer Engineering & Science* **23**, 399-403 (1983).

[9] Hall, D. B., Underhill, P. and Torkelson, J. M. Spin Coating of Thin and Ultrathin Polymer Films. *Polymer Engineering & Science* **38**, 2039-2045 (1998).

[10] Binnig, G., Quate, C. F. and Gerber, C. Atomic Force Microscope. *Physical Review Letters* **56**, 930-933 (1986).

[11] Fotiadis, D. Atomic Force Microscopy for the Study of Membrane Proteins. *Current Opinion in Biotechnology* **23**, 510-515 (2012).

[12] Song, Y. J., Otte, A. F., Shvarts, V., Zhao, Z., Kuk, Y., Blankenship, S. R., Band, A., Hess, F. M. and Stroscio, J. A. Invited Review Article: A 10 mK Scanning Probe Microscopy Facility. *Review of Scientific Instruments* **81**, 121101-121133 (2010).

[13] Zhong, Q., Inniss, D., Kjoller, K. and Elings, V. B. Fractured Polymer/silica Fiber Surface Studied by Tapping Mode Atomic Force Microscopy. *Surface Science Letters* **290**, L688-L692 (1993).

[14] Geisse, N. A. AFM and Combined Optical Techniques. *Materials Today* **12**, 40-45 (2009).

[15] Magonov, S. N., Elings, V. and Whangbo, M. H. Phase Imaging and Stiffness in Tapping-mode Atomic Force Microscopy. *Surface Science* **375**, L385-L391 (1997).

[16] Magonov, S. N. and Reneker, D. H. Characterization of Polymer Surfaces with Atomic Force Microscopy. *Annual Review of Materials Science* **27**, 175-222 (1997).

[17] Shan, Y. and Wang, H. The Structure and Function of Cell Membranes Examined by Atomic Force Microscopy and Single-Molecule Force Spectroscopy. *Chemical Society Reviews* **44**, 3617-3638 (2015).

[18] Rugar, D., Mamin, H. J., Guethner, P., Lambert, S. E., Stern, J. E., McFadyen, I. and Yogi, T. Magnetic Force Microscopy: General Principles and Application to Longitudinal Recording Media. *Journal of Applied Physics* **68**, 1169-1183 (1990).

[19] Finot, E., Leonenko, Y., Moores, B., Eng, L., Amrein, M. and Leonenko, Z. Effect of Cholesterol on Electrostatics in Lipid−protein Films of a Pulmonary Surfactant. *Langmuir* **26**, 1929-1935 (2010).

[20] Dokukin, M. E. and Sokolov, I. Quantitative Mapping of the Elastic Modulus of Soft Materials with HarmoniX and PeakForce QNM AFM Modes. *Langmuir* **28**, 16060-16071 (2012).

[21] Zhao, C., Guo, M., Lu, Y. and Wang, Q. Ferroelectric Poly(vinylidene fluoride-trifluoroethylene-chlorotrifluoroethylene)s: Effect of Molecular Weight on Dielectric Property. *Macromolecular Symposia* **279**, 52-58 (2009).

[22] Trolier-McKinstry, S., Griggio, F., Yaeger, C., Jousse, P., Zhao, D., Bharadwaja, S. S. N., Jackson, T. N., Jesse, S., Kalinin, S. V. and Wasa, K. Designing Piezoelectric Films for Micro Electromechanical Systems. *IEEE Transactions on Ultrasonics, Ferroelectrics, and Frequency Control* **58**, 1782-1792 (2011).

[23] Karagiannidis, P. G., Kassavetis, S., Pitsalidis, C. and Logothetidis, S. Thermal Annealing Effect on the Nanomechanical Properties and Structure of P3HT:PCBM Thin Films. *Thin Solid Films* **519**, 4105-4109 (2011).

[24] Alexe, M. and Gruverman, A. *Nanoscale Characterisation of Ferroelectric Materials: Scanning Probe Microscopy Approach*. (Springer, Berlin Heidelberg, 2004).

[25] Proksch, R. and Kalinin, S. *Piezoresponse Force Microscopy with Asylum Research AFMs*, <https://www.asylumresearch.com/Applications/PFMAppNote/PFMAppNote.shtml> (2008).

[26] Kholkin, A. L., Kalinin, S. V., Roelofs, A. and Gruverman, A. in *Scanning Probe Microscopy: Electrical and Electromechanical Phenomena at the Nanoscale* (eds Kalinin & Gruverman) 173-214 (Springer New York, 2007).

[27] Mativetsky, J. M., Loo, Y.-L. and Samori, P. Elucidating the Nanoscale Origins of Organic Electronic Function by Conductive Atomic Force Microscopy. *Journal of Materials Chemistry C* **2**, 3118-3128 (2014).

[28] Nxumalo, J. N., Shimizu, D. T. and Thomson, D. J. Cross-sectional Imaging of Semiconductor Device Structures by Scanning Resistance Microscopy. *Journal of Vacuum Science & Technology B* **14**, 386-389 (1996).

[29] Dai, H., Wong, E. W. and Lieber, C. M. Probing Electrical Transport in Nanomaterials: Conductivity of Individual Carbon Nanotubes. *Science* **272**, 523-526 (1996).

[30] Klein, D. L. and McEuen, P. L. Conducting Atomic Force Microscopy of Alkane Layers on Graphite. *Applied Physics Letters* **66**, 2478-2480 (1995).

[31] Roe, R. J. *Methods of X-ray and Neutron Scattering in Polymer Science*. (Oxford University Press, London, 2000).

[32] Ezquerra, T. A., Garcia-Gutierrez, M. C., Nogales, A. and Gomez, M. *Applications of Synchrotron Light to Scattering and Diffraction in Materials and Life Sciences*. Vol. 776 (Springer, Verlag Berlin Heidelberg, 2009).

[33] Bragg, W. H. and Bragg, W. L. The Reflection of X-rays by Crystals. *Proceedings of the Royal Society of London. Series A* **88**, 428-438 (1913).

[34] Akpalu, Y. A. Scattering from Polymers. *Polymer Reviews* **50**, 1-13 (2010).

[35] Stribeck, N. *X-ray Scattering of Soft Matter*. (Springer, Verlag Berlin Heidelberg, 2007).

[36] ESRF. *what is a Synchrotron?*, <http://www.esrf.eu/about/synchrotron-science/synchrotron> (2016).

[37] Mobilio, S., Boscherini, F. and Meneghini, C. *Synchrotron Radiation:Basics, Methods and Applications*. (Springer, Verlag Berlin Heidelberg, 2015).

[38] *The FIT2D Home Page*, <http://www.esrf.eu/computing/scientific/FIT2D/> (2016).

[39] Kremer, F. and Schönhals, A. *Broadband Dielectric Spectroscopy*. (Springer, Verlag Berlin Heidelberg, 2003).

[40] Hodge, I. M., Ngai, K. L. and Moynihan, C. T. Comments on the Electric Modulus Function. *Journal of Non-Crystalline Solids* **351**, 104-115 (2005).

[41] Jentoft, F. C. in *Advances in Catalysis* Vol. Volume 52 129-211 (Academic Press, 2009).

[42] Tissue, B. M. in *Characterization of Materials* (John Wiley & Sons, Inc., 2002).

[43] Kaelble, D. H. Dispersion-polar Surface Tension Properties of Organic Solids. *The Journal of Adhesion* **2**, 66-81 (1970).

[44] Owens, D. K. and Wendt, R. C. Estimation of the Surface Free Energy of Polymers. *Journal of Applied Polymer Science* **13**, 1741-1747 (1969).

[45] Van Oss, C. J. and Good, R. J. Prediction of the Solubility of Polar Polymers by Means of Interfacial Tension Combining Rules. *Langmuir* **8**, 2877-2879 (1992).

[46] Van Oss, C. J., Chaudhury, M. K. and Good, R. J. Interfacial Lifshitz-Van Der Waals and Polar Interactions in Macroscopic Systems. *Chemical Reviews* **88**, 927-941 (1988).

[47] Rebollar, E., Perez, S., Hernandez, M., Domingo, C., Martin, M., Ezquerra, T. A., Garcia-Ruiz, J. P. and Castillejo, M. Physicochemical Modifications Accompanying UV Laser Induced Surface Structures on Poly(ethylene terephthalate) and Their Effect on Adhesion of Mesenchymal Cells. *Physical Chemistry Chemical Physics* **16**, 17551-17559 (2014).

3

Conductivity and relaxation of P3HT/$PC_{71}BM$ bulk blends

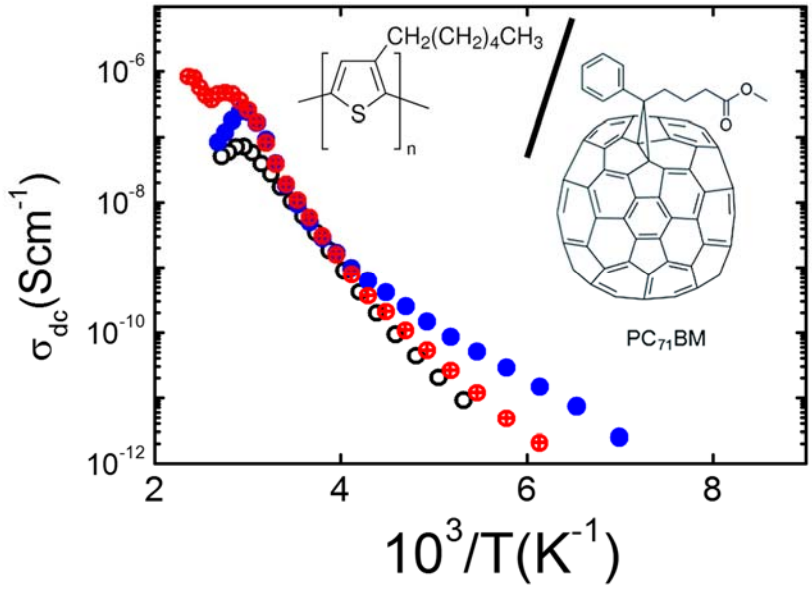

In this chapter we have characterized a series of P3HT/PC$_{71}$BM blends by broadband dielectric spectroscopy. By means of this technique both the molecular dynamics of the side chains and the electrical conductivity have been investigated over a wide temperature and frequency ranges. From the low temperature dependence of the electrical conductivity we have been able to determine the energetic offsets of the different systems. In addition, from the dependence of the electrical conductivity with temperature in the high temperature range, estimates of an energy disorder parameter were calculated and the results were compared with those obtained in the literature through measurements of the hole and electron mobilities. From both kinds of estimations we propose that conductivity spectroscopy can be a suitable technique for addressing these questions.

3.1 Samples

P3HT and P3HT/PC$_{71}$BM blend were prepared following the protocol described previously in Chapter 2. (Section 2.2.1). The details of prepared samples and labels are shown in Table 3.1.

Table 3.1 Labels of prepared samples according their corresponding concentration.

Label	**P3HT (mg)**	**PC$_{71}$BM (mg)**	**Chloroform (mL)**	**Concentration (mg/mL)**
P3HT	120	-	1	120
HTCBM10	90	10	1	100
HTCBM50	50	50	0.6	167

3.2 Absorption properties

UV-Vis spectra of P3HT and its blends with PC$_{71}$BM are collected in Figure 3.1. Pristine P3HT exhibits a broad and structured maximum in the region between 500 and 650 nm, with three well resolved bands at 520 nm, 556 and 606 nm indicated by arrows in Figure 3.1. These three bands are typically attributed to the ordered lamellar phase of P3HT and are related to the π–π* transition [1]. The band at 556 nm can be attributed to the absorption of extended conjugation lengths and the band at 606 nm is attributed to the interchain interaction. Also in Figure 3.1, the UV-Vis spectra for PC$_{71}$BM has been presented. PC$_{71}$BM exhibit a non-negligible absorption in the 500-620 nm range and a very intense absorption band around 240 nm. The UV-Vis absorption spectrum for the HTCBM10 blend is very similar to that of pristine P3HT. However, an enhancement of the low energy band (located at 606 nm) and also an increase of absorption in the 300-400 nm regions are observed. The presence of vibronic structure in the as-cast P3HT indicates that it is possible to reach an ordered state via the casting process. Upon the addition of $PC_{71}BM$, the loss of vibronic structure indicates a disruption of internal order within the P3HT phase. It is known that at low concentration, fullerene derivatives mix with the amorphous phase of P3HT. Also, it has been reported that at this low concentrations, fullerene derivatives are mixed into the amorphous part, and they can act as nucleating agents for the P3HT chains [2]. This would explain the relative increase of the 606 nm shoulder in the absorption spectrum of HTCBM10 sample compared to that of P3HT. This effect points towards an incipient blue shift in this sample.

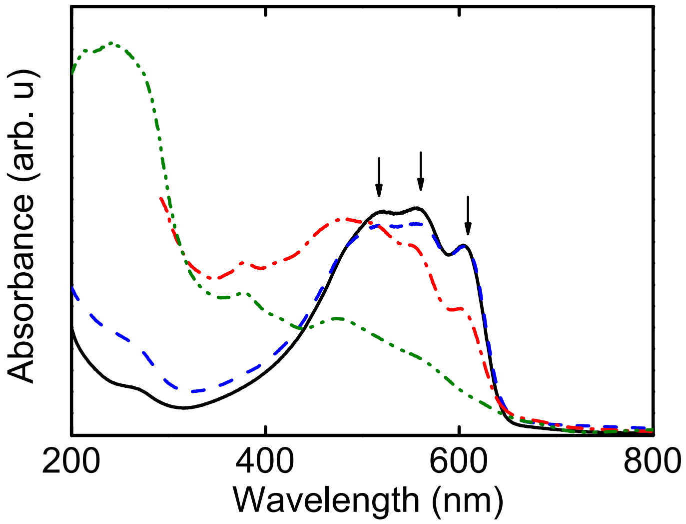

Figure 3.1 UV–Vis absorption spectra of P3HT film (black), HTCBM10 (dashed blue), HTCBM50 (dashed dotted red) and $PC_{71}BM$ (dashed dotted dotted green). Arrows indicate the position of the most characteristic bands of P3HT. Curves have been normalized to the sample thickness.

A more significant difference is observed in the spectrum of the HTCBM50 sample in comparison with that of P3HT. This blend exhibits an absorption maximum at 479 nm with shoulders at 515 and 550 nm accompanied by a reduced maximum at 606 nm. The reduction of this band suggests that the presence of $PC_{71}BM$ induces a weakening of the interchain interaction. This disordering effect of fullerene derivatives on the crystalline phase of P3HT has been previously discussed [3]. Also, a new band appears at 378 nm, that is consistent with the absorption of $PC_{71}BM$ and therefore can be attributed to $PC_{71}BM$ rich regions [4]. The blue shift in the HTCBM50 sample has been attributed in the literature not only to a decrease in the average conjugation length caused by increased chain disorder, resulting in a weakening of the interchain interaction but also to a non-photoinduced charge transfer between P3HT and fullerene derivative molecules [5].

3.3 Electric conductivity and dielectric relaxation of P3HT and P3HT/PC$_{71}$BM

3.3.1 Electric conductivity and dielectric relaxation of P3HT

Figure 3.2 shows the temperature and frequency dependence of the real part of conductivity (σ') values of the pure P3HT casted film. σ' increases with frequency, and with temperature. Two main temperature regions are observed. Below -75 ºC, σ'(ω) increases linearly with frequency in the whole frequency range. Above -75 ºC, a plateau appears at the low frequency side where σ'(f) is frequency independent up to a certain frequency (critical frequency F_c) above which the conductivity bends, increasing linearly with frequency. The plateau value of σ' increases with temperature. This plateau value of σ'(f) corresponds to the dc conductivity (σ_{dc}) [6].

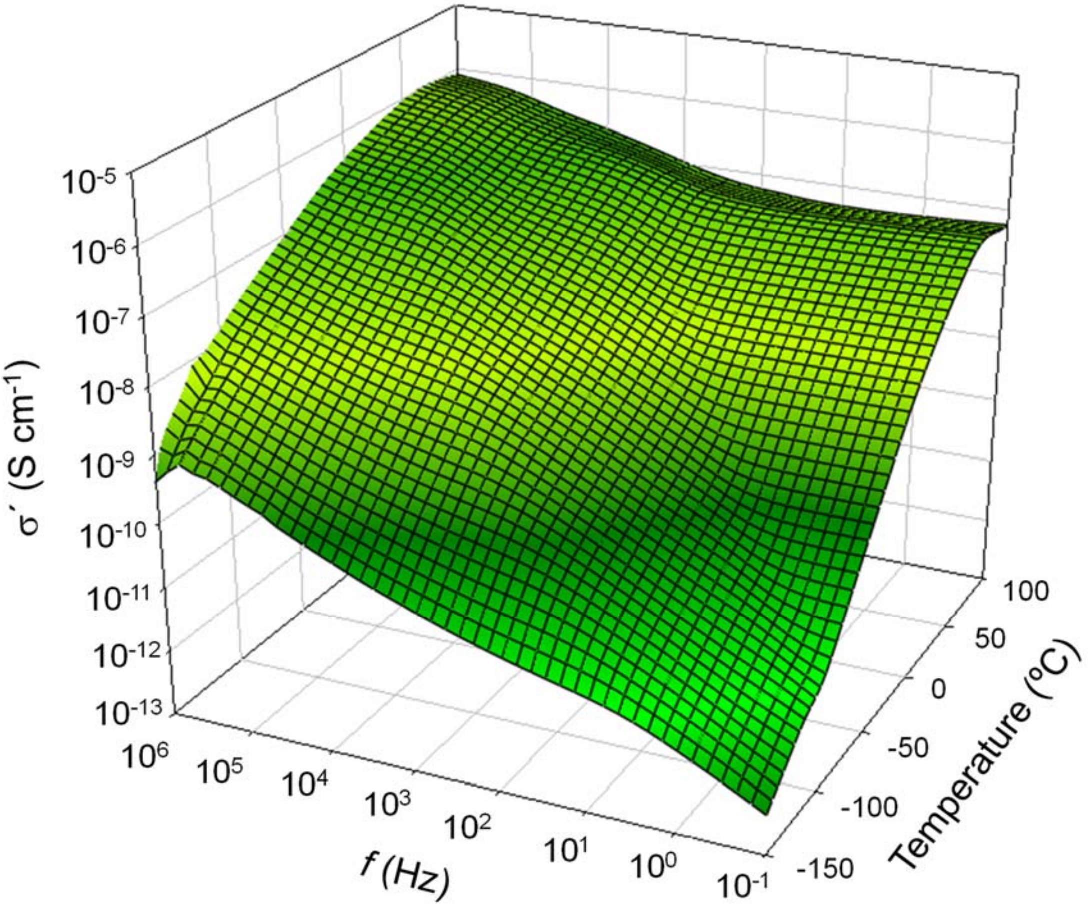

Figure 3.2 Dependence of the real part of the ac conductivity (σ') with frequency and temperature for pristine P3HT.

Values of Log$_{10}$(σ_{dc}) and Log$_{10}$(F_c) are represented in Figure 3.3a and Figure 3.3b respectively, as a function of the reciprocal temperature. As observed in Figure 3.3a, Log$_{10}$(σ_{dc}) increases with increasing temperature at the shadowed zone in a nearly linear fashion (Arrhenius behavior) up to a certain temperature (around 330 K). The continuous line represents the linear fitting at selected temperatures.

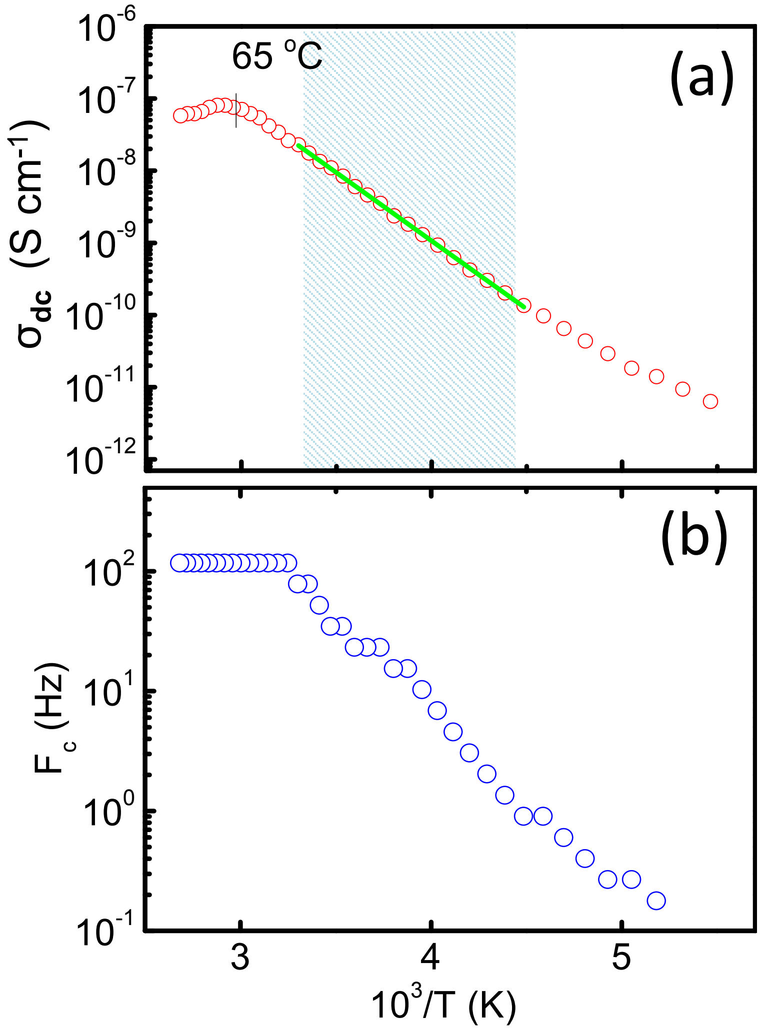

Figure 3.3 (a) dc conductivity (σ_{dc}) of P3HT as a function of the reciprocal temperature (green continuous line represents linear fitting at selected range of temperatures), and (b) critical frequency (F_c) as a function of reciprocal temperature.

Comparing Figure 3.3a and b, it is possible to observe that the plateau value σ_{dc} and the critical frequency F_c follow a very similar behavior. The relation between the σ_{dc} and F_c is shown in Figure 3.4.

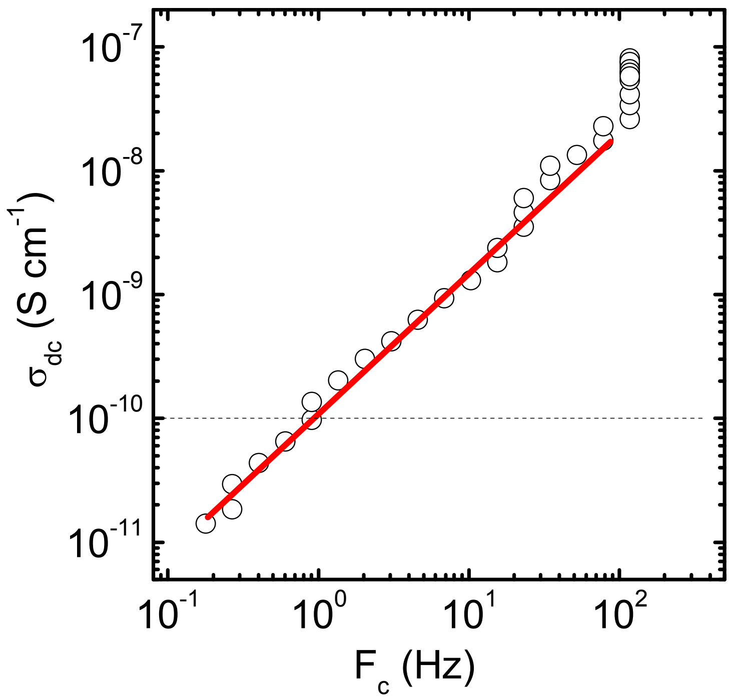

Figure 3.4 Results of dc electric conductivity (σ_{dc}) of P3HT on a Log - Log scale as a function of the critical frequency (F_c).

In fact, as observed in Figure 3.4, the logarithm of the critical frequency $Log_{10}(F_c)$ vs $Log_{10}(\sigma_{dc})$ exhibits a nearly linear tendency in almost the whole frequency range with a slope close to 1. This dependency is known as the Barton-Nakajima Namikawa (BNN)-relation and it indicates that the dc and ac conductivity are based on the same mechanism of charge transport [6].

Figure 3.5a and b show plots of the real and imaginary part of the complex permittivity ($\varepsilon^*=\varepsilon'-i\varepsilon''$) for P3HT as a function of frequency for selected temperatures. In systems with a strong conduction component and alternative representation of the dielectric values can be used in order to emphasize particular aspects of the dynamics. Precisely, the complex dielectric constant (ε^*), the complex conductivity ($\sigma^*=\sigma'+i\sigma''$) and the complex dielectric modulus ($M^*=M'+iM''$) representations can be used [6]. All these magnitudes can be considered as different representations of the same process, related by equation (2-7).

Depending on the aspect to be emphasized, it may be convenient to choose a particular one of those representations.

As observed in Figure 3.5a, the dielectric permittivity ε' exhibits a step like behavior, whereas the dielectric loss ε'' is dominated by conductivity effects characterized by a strong increase as frequency decreases. This is particularly significant at high temperatures. At low temperatures a maximum in ε'' is observed, indicated by arrows in the figure. This maximum shifts towards higher frequencies as temperature increases, which may indicate the presence of a dipolar relaxation. However, at high temperatures, this contribution is hidden by the presence of another feature in the form of a linear decay of Log$_{10}$(ε'') with Log$_{10}$(*f*), that can be associated with a conduction process. For P3HT, at low temperatures, Log$_{10}$(σ') follows a linear monotonic increase with Log$_{10}$(*f*).

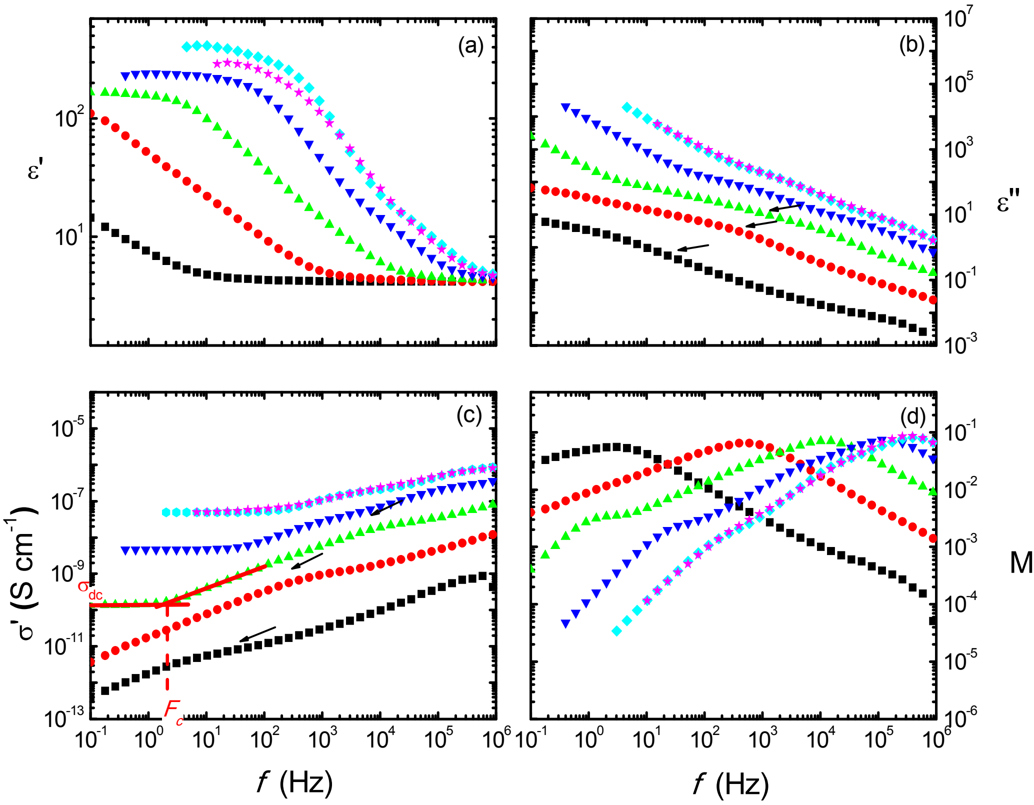

Figure 3.5 (a) Real and (b) imaginary parts of the complex dielectric permittivity, (c) real part of the complex conductivity and (d) imaginary part of the dielectric modulus as a function of frequency for selected temperatures for P3HT: (■) 123 K, (●)173 K, (▲) 223 K, (▼) 273 K, (◆) 323 K, (★) 373 K. The arrows in (b) and (c) indicate the presence of a dielectric relaxation process.

3.3.2 Electrical conductivity and dielectric relaxation of P3HT/PC$_{71}$BM blends

Figure 3.6 shows the dielectric relaxation data obtained for a HTCBM50 blend. Figure 3.6a and Figure 3.6b show the values of the real and imaginary part of ε* as a function of frequency for selected temperatures respectively. These results are qualitatively similar to those obtained for P3HT. The dielectric permittivity ε' exhibits a step like behavior, whereas the dielectric loss ε'' is dominated by conductivity effects with and incipient maximum in ε'' at high temperatures. As commented above, for this case, some features are better observed in the conductivity (σ', Figure 3.6c) and the dielectric modulus (M'', Figure 3.6d) representations. At low temperatures, Log$_{10}$(σ') follows a monotonic increase with Log$_{10}$(*f*). In this case the dielectric process observed in the ε'' plot can be detected superimposed at low frequencies. At higher temperatures Log$_{10}$(σ') exhibits a plateau at low frequencies together with a quasilinear increase above the critical frequency. In the dielectric modulus representation (Figure 3.6d), the imaginary part, M'', exhibits a clear maximum. At elevated temperatures this maximum is bimodal with a shoulder appearing at lower frequencies.

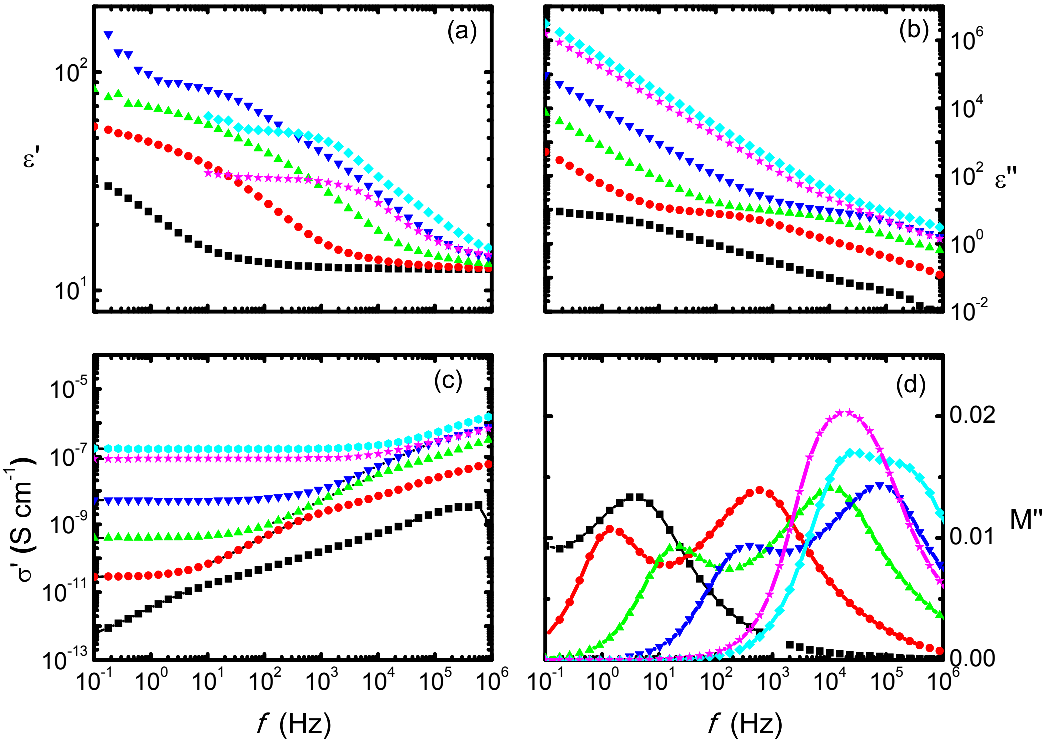

Figure 3.6 (a) Real and (b) imaginary part of the complex dielectric permittivity, (c) real part of the complex conductivity and (d) imaginary part of the dielectric modulus M'' as a function of frequency for selected temperatures for HTCBM50 (■) 123 K, (●) 173 K, (▲) 223 K, (▼) 273 K, (◆) 323 K, (★) 373 K. Continuous lines through the data points in M'' are guides to the eye.

In order to separate the conduction process from the dipolar contributions, the dielectric modulus representation has been used [7-10]. The evolution of the position of these maxima in M" is presented in Figure 3.7b in logarithmic scale where the frequency of faster process (F_1), i.e. the one appearing first at lower temperatures, and that of the slowest one (F_2), appearing at higher temperatures, have been plotted as a function of the reciprocal temperature. The faster process exhibits an Arrhenius behavior from very low temperature up to around 330 K. The activation energy for the fastest process can be estimated to be $E_{a,1}$= 200 meV (see Table 3.2). As observed in Figure 3.7b, the frequency of maximum M'' for the slower relaxation, F_2, exhibits similar values and temperature dependency than those of the critical frequency F_c from the conductivity representation. Therefore, in a first approach we can assume that both correspond to the same physical process, i.e., the conduction process.

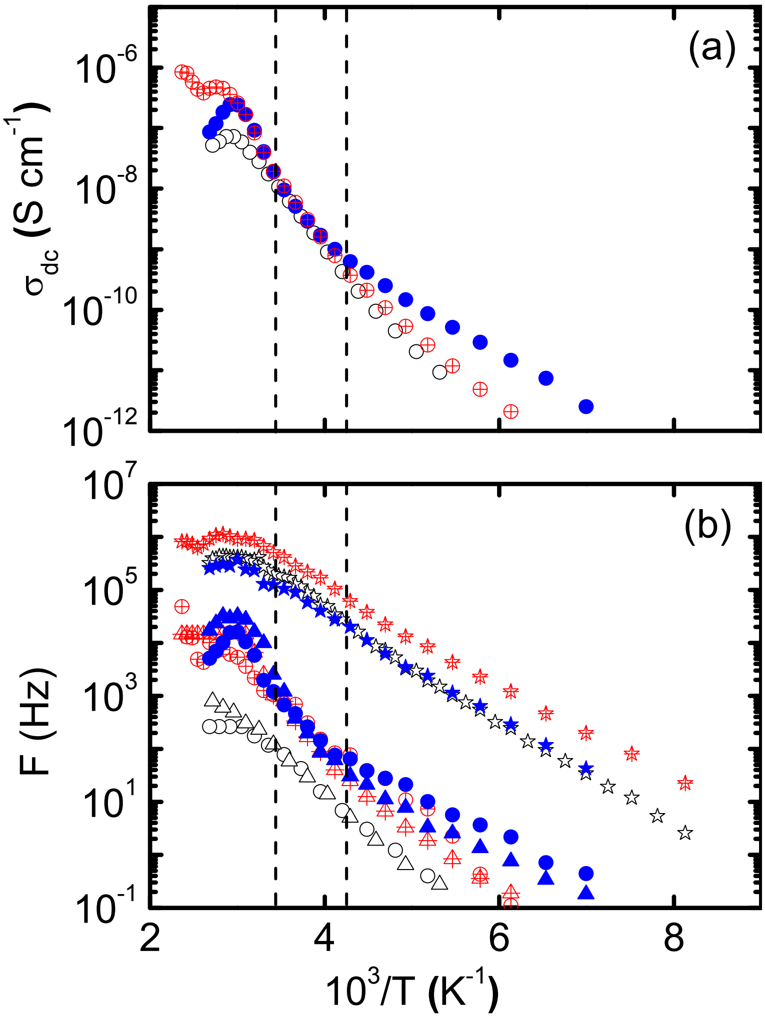

Figure 3.7 (a) dc conductivity (σ_{dc}) and (b) characteristic frequency (F_c) for HTCBM10 (Crossed Symbols) and HTCBM50 (Filled symbols). In (a) σ_{dc} as a function of the reciprocal temperature obtained from the dependence of σ' vs *f*. In (b) Frequencies at which M'' exhibits a maximum. (☆) Maximum in M" for the fast process (F_1) and (△) maximum in M" for the slow process (F_2). In (b) circles represent F_c obtained from the σ' representation. The conductivity of P3HT (open symbols) is also included for comparison.

The representation of σ_{dc} as a function of F_c was shown in Figure 3.8, like P3HT, σ_{dc} and F_c also fulfill the BNN relation in the case of the blends. However, despite the qualitative similarities in the behavior of pure P3HT and the P3HT/PC$_{71}$BM blends, several quantitative differences are found that will be discussed below.

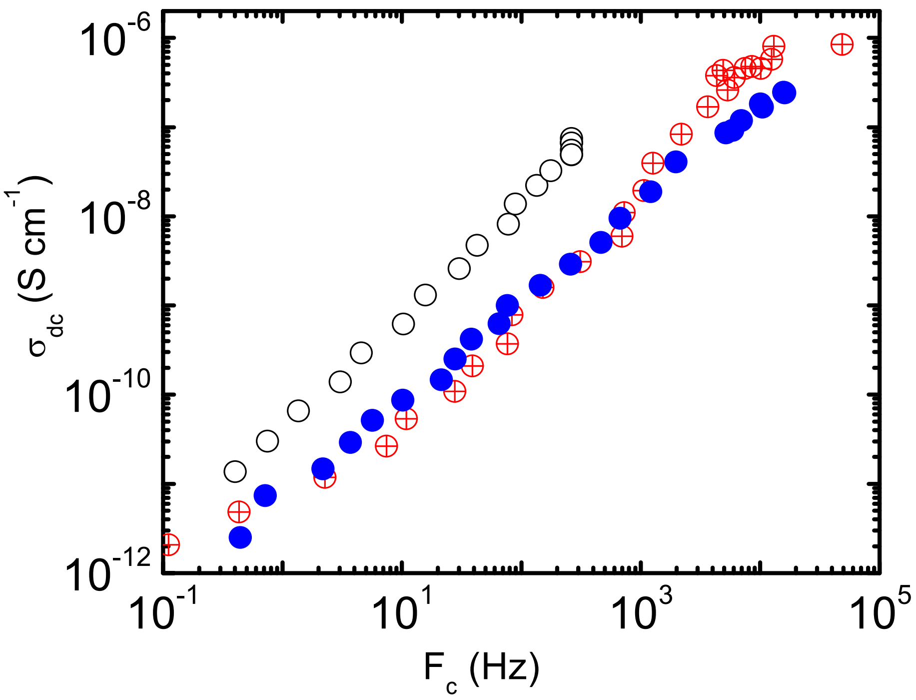

Figure 3.8 dc conductivity (σ_{dc}) as a function of the critical frequency (F_c) HTCBM10 (Crossed Symbols) and HTCBM50 (Filled symbols). P3HT was also included (open symbols) for comparison. F_c is obtained from the σ' representation.

3.4 Relaxation behavior of P3HT and fullerene based blend

3.4.1 Dipolar relaxation at low temperature process

As observed in the dielectric modulus representation, a fast relaxation appears at low temperatures. This fast relaxation observed both in the neat P3HT and in the blends follows an Arrhenius behavior in a wide temperature range, from low temperature up to around 330K. The fact that this relaxation appears in the neat polymer and in the blends suggests that it can be assigned to a process occurring in the polymer. Its Arrhenius behavior and the low temperatures where this relaxation can be observed are characteristics of local motions. The activation energy from this relaxation is very similar in P3HT and in the blends, with a value of around 200 meV (see Table 3.2). It is well known that P3HT develops a nanophase separated morphology where main chains form a layered crystalline structure with hexyl groups between layers [11]. This organization resembles that of other comb-like polymers with a lateral alkyl chain like poly(n-alkyl acrylates) [12], poly(n-alkyl methacrylates) [12,13] or poly(alkylene oxides) [14]. Recently, Arbe et al. have studied by Neutron Spin Echo, with selective labeling, the dynamical behavior of two poly(alkyl methacrylates) with different number of carbons in the side chain, precisely nCs = 4 and nCs =6 [15]. They found a peculiar dynamic behavior for the side chain group which they interpret as due to the strong dynamical asymmetry between the main chain and the side chain. In this work, the observed low temperature relaxation in P3HT, can be associated to the motion of three to four CH_2 as well as the local motion of loose chain ends within amorphous alkyl chains [16]. In principle, this process should be very similar to the so called γ_2 process described for polyethylene (PE) exhibiting activation energies between 200 and 250 meV [15]. The activation energy for this PE-like relaxation is not significantly affected by the presence of the $PC_{71}BM$ component in the blends suggesting that the local dipolar relaxation of the hexyl chains is not modified by the fullerene derivative. It is worth mentioning that at higher temperatures the Arrhenius behavior of the fast process tends to be arrested. This is likely due to changes in the main chain conformation as it will be discussed in the following section.

Table 3.2 Activation energy for the dipolar process ($E_a^{dipolar}$) obtained from the Arrhenius representation (Figure 3.7), and for the conduction process ($E_a^{\sigma dc}$), obtained from the Arrhenius representation of Log σ_{dc} versus $1/T$ at low temperatures (Figure 3.7). Energetic disorder parameter σ estimated from equation (3- 4) assuming the same dependency for σ_{dc} than for μ.

	$E_a^{dipolar}$ (meV)	$E_a^{\sigma_{dc}}$ (meV) (T<240 K)	σ (meV) (240<T<285 K)
P3HT	204	300	100
HTCBM10	183	238	110
HTCBM50	186	165	114

3.4.2 Electrical conductivity at high temperature

As reviewed in the introduction, in P3HT electrical conductivity arises from the delocalization of the π-bonds formed from overlapping p_z-orbitals. The energy gap of these systems decreases with increasing the conjugation length [17]. RR-P3HT is known to have relatively high hole mobilities due to the self-organization produced by the regular side-chains which induce a well-ordered two dimensional lamellar structure [18]. In general, electrical conductivity, σ_{dc} is expressed as:

$$\sigma_{dc} = n\mu e \ (Scm^{-1}) \quad (3\text{- }1)$$

where μ (cm^2 V^{-1} s^{-1}) is the electrical mobility and n the number density of charge carriers of charge e. Although there is not a general unified view about the electric conduction mechanism in semiconducting polymers it has been accepted that in several cases their electrical conductivity can be well described by the theory of hopping conduction between localized states in a three-dimensional system with a certain level of disorder [19]. According to the theory of hopping conduction between localized states in a three-dimensional disordered material, the probability of hopping, W, of a charge carrier between two sites separated by a distance R is given by:

$$W \propto \exp(-2\alpha R)\exp(\frac{-E_a}{kT}) \qquad (3\text{- }2)$$

where α is the inverse localization length and E_a is the energy barrier between the energy state of the two sites. At low temperatures, due to energetic considerations, hopping is possible not only between nearest neighbors but also among remote sites being the hopping frequency small. In this case electrical conductivity can be described by Mott's law of variable-range hopping (VRH model) as:

$$\sigma_{dc} = \sigma_o \exp(-\frac{T_0}{T^{1/4}}) \qquad (3\text{- }3)$$

If one considers that conductivity heterogeneity exists in the material, like for example in granular materials, then intergrain distance and grain energy play a role and conductivity becomes percolation controlled [20,21]. In this case a $T^{-1/4}$ temperature dependence of log conductivity is predicted at low temperatures while a stronger temperature dependence, T^{-a} ($1/2 < a < 1$), is expected at higher temperatures. In some cases, high heterogeneity in conductivity may produce conducting "islands" embedded in non-conducting regions. Then fluctuation induced tunneling among conducting regions is possible as reported for highly doped polyacetylene [22]. It is worth mentioning that at high temperatures thermal activation provokes that hopping between nearest-neighbors is more likely to occur. In this case the electrical conductivity is expected to follow a standard Arrhenius temperature dependence as described by equation (3- 3) and observed experimentally for several semiconducting polymers [23,24]. In order to discuss the conduction mechanism in our materials we have plotted in Figure 3.9, the dependence of the derivative of the logarithm of the conductivity with respect to the reciprocal temperature. In this representation an Arrhenius dependency should appear as a constant whose level is directly proportional to the activation energy (proportionality constant R, being R the gas constant). According to Figure 3.9 the conductivity process for P3HT and the blends exhibits an Arrhenius temperature dependence from low temperature up to around 240 K. The activation energy for the conduction process (slow process) can be estimated from this graph and it has been presented in Table 3.2. This behavior is compatible with equation (3- 3) considering the relatively high temperature range investigated (T > 143 K) in comparison with other studies [21,24].

As mentioned above, the conductivity in a semiconductor is proportional to both the mobility of the charge carriers and the density of them. Both magnitudes depend on temperature. Several authors have studied the dependence of hole mobility with temperature in P3HT [25-27]. Mozer et al [26] performed time-of-flight (ToF) experiments in order to determine the hole mobility in RR-P3HT and found that the zero field mobility presents an activation energy of 290 meV, very similar to the one found in this work for the conduction process in P3HT at low temperatures. This suggests that the density of carriers in this low temperature regime can be considered nearly constant. In P3HT and in the blends, the low temperature Arrhenius behavior is lost at temperatures around 240 K (indicated in Figure 3.9 by the first from low temperature dashed line). In the temperature range above 240 K stronger temperature dependence seems to appear, that can be interpreted in terms of the Gaussian Disorder Model [28].

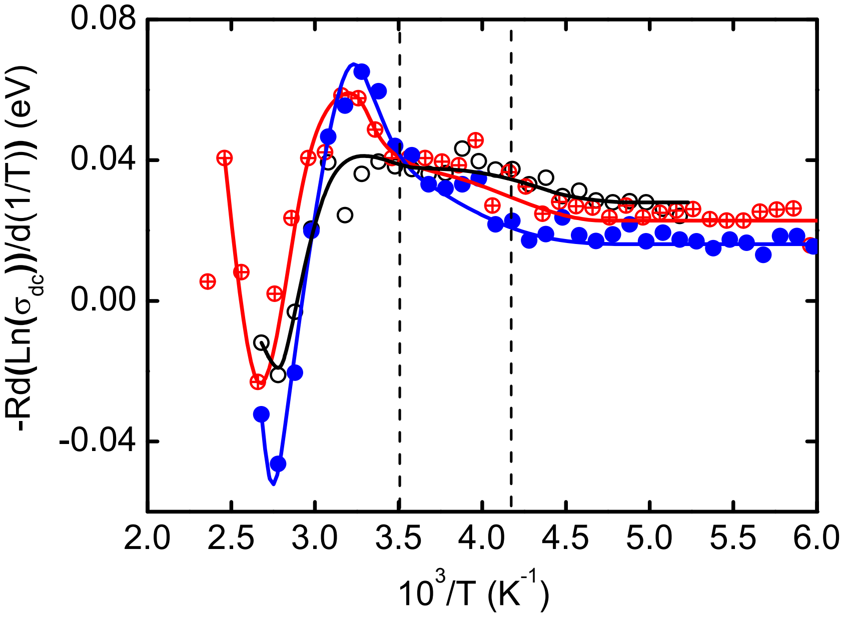

Figure 3.9 Derivative of the logarithm of the conductivity with respect to the reciprocal temperature, scaled by –R, as a function of the reciprocal temperature for P3HT (open symbols), HTCBM10 (crossed Symbols) and HTCBM50 (filled symbols). Dashed lines indicate the change in tendency, from an Arrhenius behavior (lower temperature) to a T^{-2} dependency (See $Log_{10}(\sigma_{dc})$ vs $Log_{10}(F_c)$ in Figure 3.10) (region between the lines).

This model takes into account that hopping across a material with disorder takes place among sites whose energies follow a certain distribution, Gaussian for example. In this case, Monte Carlo simulation techniques have shown that the zero field electrical mobility can follow a non-Arrhenius temperature dependence of the type:

$$\mu(T) = \mu_0 \exp(-(2\sigma/3kT)^2) \qquad (3\text{-} 4)$$

Where σ is the width of the Gaussian distribution, μ_0 is a prefactor and k is the Boltzman constant. Under this framework the conductivity results might be interpreted [28]. Taking into account that conjugated polymers, as any other polymer, are highly disordered molecular solids and due to the more or less random positions of the chemical and conformational defects, there can be a broad distribution of effective conjugation lengths of the chain segments. Assuming that the bulk conductivity might follow the same temperature dependence as that of the hole mobility, the conductivity has been plotted in a semilogarithmic scale as a function of the inverse of the square temperature (Figure 3.10), in order to calculate the energetic disorder.

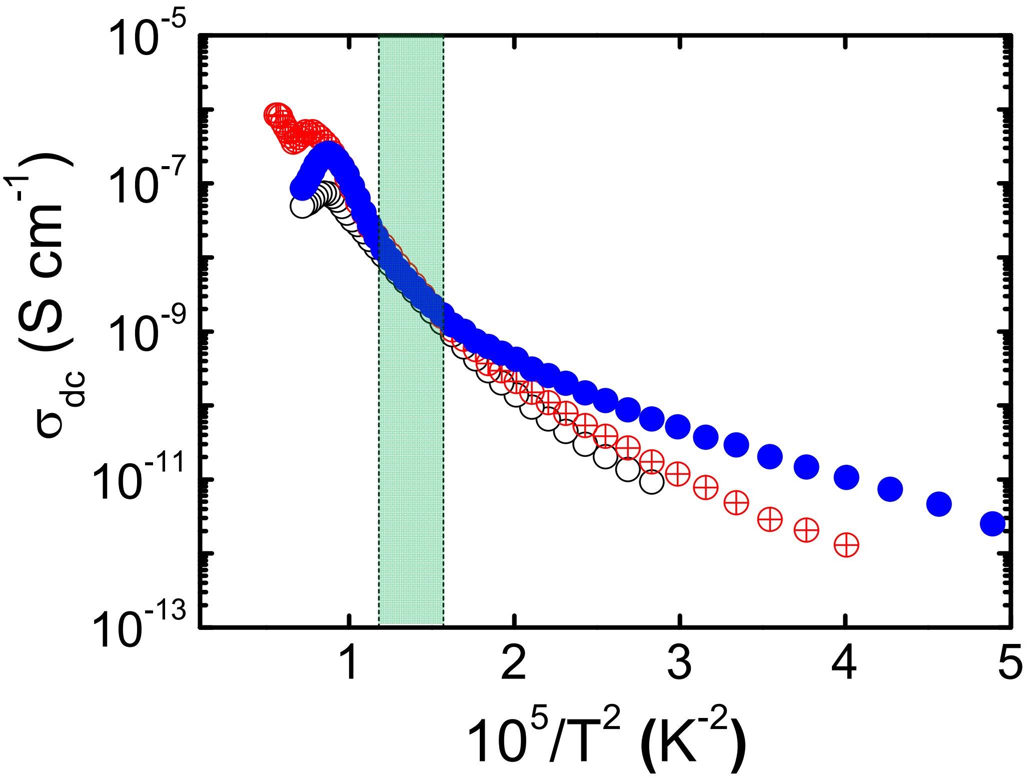

Figure 3.10 Conductivity (σ_{dc}) as a function of the square of the reciprocal temperature for P3HT (open symbols), HTCBM10 (crossed Symbols) and HTCBM50 (filled symbols). The area between the dashed lines corresponds to the region of linearity, from which the energetic disorder values have been calculated.

A clear linear tendency is observed for P3HT and for the blends, in the temperature range from 240 K to 285 K ($1.74\ 10^{-}\ K^{-2}$ to $1.2\ 10^{5}\ K^{2}$) (shadowed area in Figure 3.10). From this linear dependency, a value of $\sigma = 100$ meV for the energetic disorder is obtained. The value for the energetic disorder estimated here is similar to the ones obtained for neat P3HT obtained by ToF measurements (70 meV obtained by Mosser et al. [26] and 120 meV by Shen et al.[27]) supporting the validity of the present approach. At temperatures above 285 K, the linearity is lost.

This effect has also been observed in mobility measurements on neat P3HT, although occurring at higher temperatures [27]. Yawaza et al. investigated by Infrared Spectroscopy and Nuclear Magnetic Resonance the dependency with temperature of the molecular motions in P3HT [29,30]. They observed that the onset of the twisting motions of thiophene ring, that is the responsible for the decrease in the conjugation length, occurs at temperatures slightly below room temperature, that is where we observe the loss of linearity in the $\mathrm{Log}_{10}(\sigma_{dc})$ vs $1/T^2$ plot. This twisting motion in the main chain induces a transition from a crystal to a plastic crystal phase in P3HT, in which the translational order is preserved, but the main chain presents some twisting mobility. They attribute to this phenomenon the blue shift observed in the intrachain band observed by UV-Vis spectroscopy [29,30]. It is worth mentioning that the glass transition temperature of P3HT has been reported [31] to be around 283 K, which is the temperature where the loss of linearity in the $\mathrm{Log}_{10}(\sigma_{dc})$ vs $1/T^2$ plot is observed. Correlating this interpretation with our results, the deviation from linearity in Figure 3.10 and the subsequent decrease in the conductivity at temperatures around 330 K can be attributed to both the twisting relaxation of the thiophene rings and the onset of the glass transition of P3HT. Also these effects can be the responsible for the curvature of the Arrhenius plot corresponding to the high frequency fast process discussed in the previous section.

3.4.3 Estimation of the energetic offsets in the blends of P3HT/$PC_{71}BM$ by BDS

It has been suggested that charge separation and recombination in polymer solar cells can be affected by the energetic offsets between the charge transport energy levels in different morphological phases of polymer/fullerene BHJ [32,33]. BHJ are multiphase systems [34] that draw a complicated energy landscape. For P3HT/PCBM blends it is accepted that the BHJ consists of a P3HT crystalline phase, an amorphous P3HT rich region mixed with fullerene molecules and depending on the concentration of PCBM, a segregated PCBM crystalline phase [35,36]. For pure P3HT, variations in regioregularity of the system affect the crystallinity, and therefore induce changes in the band gap of the polymer [37,38]. Also, it is acknowledged that the interactions between the amorphous P3HT chains and the fullerene derivative molecules modify the energy landscape for charge transport. Therefore, the characteristic heterogeneity of BHJ induces energetic offsets between the different phases that may favor the charge transport [33]. In fact, our results show that the dc conducting behavior in the P3HT/$PC_{71}BM$ blends is manifested at lower temperatures than in P3HT. A plateau in σ' at low frequencies is observed in the blends for temperatures as low as 140 K, whereas in P3HT this plateau does not appear until $T = 190$ K. In the low temperature range ($T < 240$ K) the activation energy of the conduction process is smaller in the blends than in the neat P3HT (See Table 3.2). This effect is more pronounced in the HTCBM50 sample, which is the one with higher amount of $PC_{71}BM$. Also in agreement with these results, Mauer et al. [25] have reported much lower temperature dependence of the hole and electron mobilities in a 1/1 P3HT/PCBM blend than the one obtained for hole mobility in pristine P3HT. In line with that, the blends used here exhibit a similar tendency, showing a decrease in activation energy at low temperatures with increasing the $PC_{71}BM$ amount. This decrease in activation energy in the presence of the fullerene derivative might be understood in the context of the intimate interaction between P3HT and $PC_{71}BM$ molecules. As mentioned above, the observed blue shift in the UV absorption spectrum in the blends have been attributed in the literature to a decrease in the interchain interactions [3] and also to a non photoinduced charge transfer between the two molecules [5]. As observed, there is a difference of approximately 135 meV between the activation energy at low temperature for P3HT and that of the HTCBM50 system. This value is in accordance with the value for the energetic offset obtained by Sweetnam et al. [33] by cyclic voltammetry, UV−Vis spectroscopy, and ultraviolet photoelectron spectroscopy. In that work the authors emphasize the role of intermolecular interactions between the fullerene derivative and the polymer in the energetic offset in the local polymer band gap. The agreement between the energetic offset obtained by Sweetnam et al. [33] and the one estimated here from the differences in activation energy encourages us to propose conductivity spectroscopy as a simple method for estimating the energy offsets in polymer/fullerene BHJ.

3.5 Conclusion

We have investigated the dynamics and frequency dependent conductivity of P3HT and blends with $PC_{71}BM$ by means of BDS. A low temperature relaxation is observed in P3HT, that is attributed to the local motion of the hexyl lateral chains, and that is very similar to a polyethylene-like relaxation and to the one observed in other comb like polymers with hexyl lateral chains. This relaxation is also observed, and not affected by the presence of $PC_{71}BM$ in the blends. The other process observed in the present experiments is a conduction process. The dependence with temperature of the conductivity can be separated into two regions: The low temperature region, where the conductivity exhibits an Arrhenius behavior, and the high temperature region, where the temperature dependence of the conductivity can be described by the Gaussian Disorder model. In the low temperature region, the activation energy decreases when increasing the $PC_{71}BM$ content. The variation of the activation energy provides estimation for the energetic offsets in the valence band of the system, induced by the presence of the fullerene derivative molecules. In the high temperature region, we have estimated an energetic disorder parameter which appears to be independent of the amount of $PC_{71}BM$.

3.6 References

[1] Chen, T.-A., Wu, X. and Rieke, R. D. Regiocontrolled Synthesis of Poly(3-alkylthiophenes) Mediated by Rieke Zinc: Their Characterization and Solid-State Properties. *Journal of the American Chemical Society* **117**, 233-244 (1995).

[2] Chou, K. W., Yan, B., Li, R., Li, E. Q., Zhao, K., Anjum, D. H., Alvarez, S., Gassaway, R., Biocca, A., Thoroddsen, S. T., Hexemer, A. and Amassian, A. Spin-cast Bulk Heterojunction Solar Cells: A Dynamical Investigation. *Advanced Materials* **25**, 1923-1929 (2013).

[3] Chirvase, D., Parisi, J., Hummelen, J. C. and Dyakonov, V. Influence of Nanomorphology on the Photovoltaic Action of Polymer–fullerene Composites. *Nanotechnology* **15**, 1317-1323 (2004).

[4] Falke, S., Eravuchira, P., Materny, A. and Lienau, C. Raman Spectroscopic Identification of Fullerene Inclusions in Polymer/fullerene Blends. *Journal of Raman Spectroscopy* **42**, 1897-1900 (2011).

[5] Shrotriya, V., Ouyang, J., Tseng, R. J., Li, G. and Yang, Y. Absorption Spectra Modification in Poly(3-hexylthiophene): Methanofullerene Blend Thin Films. *Chemical Physics Letters* **411**, 138-143 (2005).

[6] Kremer, F. and Schönhals, A. *Broadband Dielectric Spectroscopy.* (Springer, Verlag Berlin Heidelberg, 2003).

[7] Wojnarowska, Z., Knapik, J., Díaz, M., Ortiz, A., Ortiz, I. and Paluch, M. Conductivity Mechanism in Polymerized Imidazolium-based Protic Ionic Liquid [HSO3–BVIm][OTf]: Dielectric Relaxation Studies. *Macromolecules* **47**, 4056-4065 (2014).

[8] Roling, B. What do Electrical Conductivity and Electrical Modulus Spectra Tell Us about the Mechanisms of Ion Transport Processes in Melts, Glasses, and Crystals? *Journal of Non-Crystalline Solids* **244**, 34-43 (1999).

[9] Adrjanowicz, K., Kaminski, K., Dulski, M., Jasiurkowska-Delaporte, M., Kolodziejczyk, K., Jarek, M., Bartkowiak, G., Hawelek, L., Jurga, S. and Paluch, M. Dynamic Glass Transition and Electrical Conductivity Behavior Dominated by Proton Hopping Mechanism Studied in the Family of Hyperbranched Bis-MPA Polyesters. *Macromolecules* **47**, 5798-5807 (2014).

[10] Kramarenko, V. Y., Ezquerra, T. A. and Privalko, V. P. Relationships Between Conductivity and Local Topology in Heterocyclic Polymer Networks. *Physical Review E* **67**, 031801 (2003).

[11] Prosa, T. J., Winokur, M. J., Moulton, J., Smith, P. and Heeger, A. J. X-ray Structural Studies of Poly(3-alkylthiophenes): An Example of an Inverse Comb. *Macromolecules* **25**, 4364-4372 (1992).

[12] Beiner, M. and Huth, H. Nanophase Separation and Hindered Glass Transition in Side-chain Polymers. *Nature Materials* **2**, 595-599 (2003).

[13] Arbe, A., Genix, A. C., Colmenero, J., Richter, D. and Fouquet, P. Anomalous Relaxation of Self-assembled Alkyl Nanodomains in High-order Poly(n-alkyl methacrylates). *Soft Matter* **4**, 1792-1795 (2008).

[14] Gerstl, C., Brodeck, M., Schneider, G. J., Su, Y., Allgaier, J., Arbe, A., Colmenero, J. and Richter, D. Short and Intermediate Range Order in Poly(alkylene oxide)s. A Neutron Diffraction and Molecular Dynamics Simulation Study. *Macromolecules* **45**, 7293-7303 (2012).

[15] Arbe, A., Genix, A. C., Arrese-Igor, S., Colmenero, J. and Richter, D. Dynamics in Poly(n-alkyl methacrylates): A Neutron Scattering, Calorimetric, and Dielectric Study. *Macromolecules* **43**, 3107-3119 (2010).

[16] Matsuo, M., Bin, Y., Xu, C., Ma, L., Nakaoki, T. and Suzuki, T. Relaxation Mechanism in Several Kinds of Polyethylene Estimated by Dynamic Mechanical Measurements, Positron Annihilation, X-Ray and 13C Solid-state NMR. *Polymer* **44**, 4325-4340 (2003).

[17] Tourillon, G. in *Handbook of Conducting Polymers* Vol. 1 (ed Skotheim) (Marcel Dekker, 1986).

[18] Tremel, K. and Ludwigs, S. in *P3HT Revisited – From Molecular Scale to Solar Cell Devices* Vol. 265 *Advances in Polymer Science* (ed Ludwigs) Ch. 288, 39-82 (Springer, 2014).

[19] Mott, N. F. and Davis, E. A. *Electronic Processes in Non-Crystalline Materials*. (Clarendon Press : Oxford, 1979).

[20] Sheng, P. and Klafter, J. Hopping Conductivity in Granular Disordered Systems. *Physical Review B* **27**, 2583-2586 (1983).

[21] Glatzhofer, D. T., Ulanski, J. and Wegner, G. Controlled Conductivity Behaviour in Poly(p-styrenesulphonate) Salts of Polypyrrole. *Polymer* **28**, 449-453 (1987).

[22] Schimmel, T., Rieβ, W., Gmeiner, J., Denninger, G., Schwoerer, M., Naarmann, H. and Theophilou, N. DC-conductivity on a New Type of Highly Conducting Polyacetylene, N-(CH)x. *Solid State Communications* **65**, 1311-1315 (1988).

[23] Ezquerra, T. A., Rühe, J. and Wegner, G. Hopping Conduction in 3,4-cycloalkylpolypyrrole Perchlorates: A Model Study of Conductivity in Polymers. *Chemical Physics Letters* **144**, 194-198 (1988).

[24] Wegner, G. and Ruhe, J. The Structural Background of Charge-carrier Motion in Conducting Polymers. *Faraday Discussions of the Chemical Society* **88**, 333-349 (1989).

[25] Mauer, R., Kastler, M. and Laquai, F. The Impact of Polymer Regioregularity on Charge Transport and Efficiency of P3HT:PCBM Photovoltaic Devices. *Advanced Functional Materials* **20**, 2085-2092 (2010).

[26] Mozer, A. J. and Sariciftci, N. S. Negative Electric Field Dependence of Charge Carrier Drift Mobility in Conjugated, Semiconducting Polymers. *Chemical Physics Letters* **389**, 438-442 (2004).

[27] Shen, X., Duzhko, V. V. and Russell, T. P. A Study on the Correlation Between Structure and Hole Transport in Semi-crystalline Regioregular P3HT. *Advanced Energy Materials* **3**, 263-270 (2013).

[28] Bässler, H. Charge Transport in Disordered Organic Photoconductors a Monte Carlo Simulation Study. *Physica Status Solidi (B)* **175**, 15-56 (1993).

[29] Yazawa, K., Inoue, Y., Yamamoto, T. and Asakawa, N. Dynamic Structure of Regioregulated Poly(alkylthiophene)s. *The Journal of Physical Chemistry B* **112**, 11580-11585 (2008).

[30] Yazawa, K., Inoue, Y., Shimizu, T., Tansho, M. and Asakawa, N. Molecular Dynamics of Regioregular Poly(3-hexylthiophene) Investigated by NMR Relaxation and an Interpretation of Temperature Dependent Optical Absorption. *The Journal of Physical Chemistry B* **114**, 1241-1248 (2010).

[31] Zhao, Y., Yuan, G., Roche, P. and Leclerc, M. A Calorimetric Study of the Phase Transitions in Poly(3-hexylthiophene). *Polymer* **36**, 2211-2214 (1995).

[32] Chen, D., Nakahara, A., Wei, D., Nordlund, D. and Russell, T. P. P3HT/PCBM Bulk Heterojunction Organic Photovoltaics: Correlating Efficiency and Morphology. *Nano Letters* **11**, 561-567 (2011).

[33] Sweetnam, S., Graham, K. R., Ngongang Ndjawa, G. O., Heumüller, T., Bartelt, J. A., Burke, T. M., Li, W., You, W., Amassian, A. and McGehee, M. D. Characterization of the Polymer Energy Landscape in Polymer:Fullerene Bulk Heterojunctions with Pure and Mixed Phases. *Journal of the American Chemical Society* **136**, 14078-14088 (2014).

[34] Yin, W. and Dadmun, M. A New Model for the Morphology of P3HT/PCBM Organic Photovoltaics from Small-angle Neutron Scattering: Rivers and Streams. *ACS Nano* **5**, 4756-4768 (2011).

[35] Hopkinson, P. E., Staniec, P. A., Pearson, A. J., Dunbar, A. D. F., Wang, T., Ryan, A. J., Jones, R. A. L., Lidzey, D. G. and Donald, A. M. A Phase Diagram of the P3HT:PCBM Organic Photovoltaic System: Implications for Device Processing and Performance. *Macromolecules* **44**, 2908-2917 (2011).

[36] Parnell, A. J., Cadby, A. J., Mykhaylyk, O. O., Dunbar, A. D. F., Hopkinson, P. E., Donald, A. M. and Jones, R. A. L. Nanoscale Phase Separation of P3HT PCBM Thick Films As Measured by Small-angle X-ray Scattering. *Macromolecules* **44**, 6503-6508 (2011).

[37] Osterloh, F. E., Holmes, M. A., Chang, L., Moulé, A. J. and Zhao, J. Photochemical Charge Separation in Poly(3-hexylthiophene) (P3HT) Films Observed with Surface Photovoltage Spectroscopy. *The Journal of Physical Chemistry C* **117**, 26905-26913 (2013).

[38] Noriega, R., Rivnay, J., Vandewal, K., Koch, F. P. V., Stingelin, N., Smith, P., Toney, M. F. and Salleo, A. A General Relationship Between Disorder, Aggregation and Charge Transport in Conjugated Polymers. *Nature Materials* **12**, 1037-1043 (2013).

4

Controlling the morphology of phase separated blends

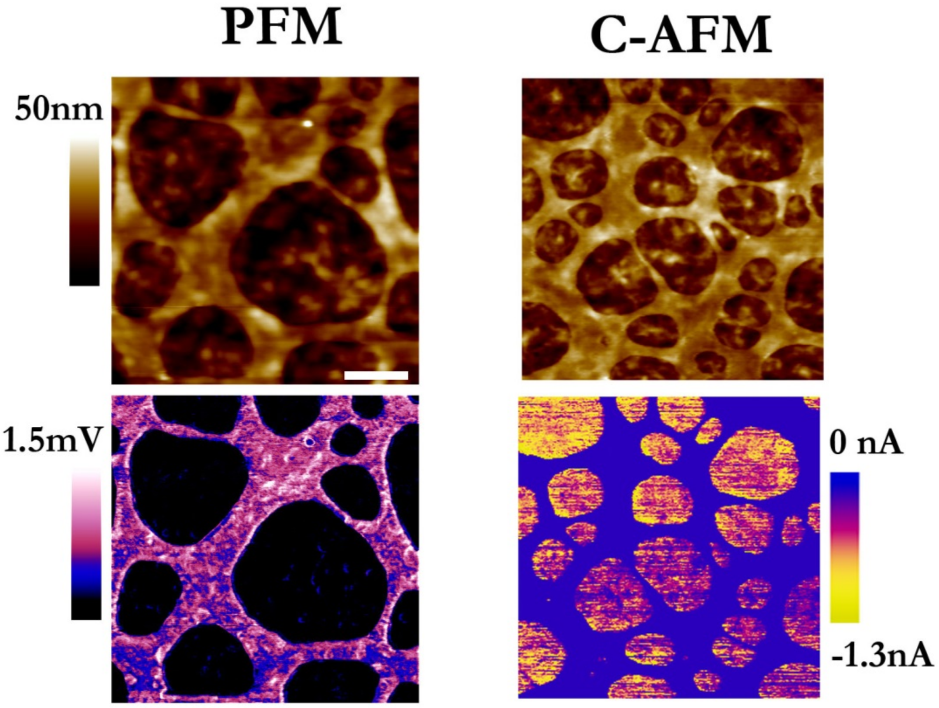

In this chapter, we report on the preparation and characterization of several architectures of P3HT/P(VDF-TrFE) blends. The first architecture is obtained by spin coating after direct solution blending. The second blend architecture investigated is a mixture of ferroelectric polymer NPs embedded in a continuous P3HT matrix. The ferroelectric behavior of these nanocomposites was evaluated. It was shown before that the P(VDF-TrFE) NPs are ferroelectric when they are measured independently. Here we investigate how this ferroelectricity is affected by the surrounding semiconducting polymer matrix. Finally, a bilayer blend architecture which consists of a bottom layer of P3HT and a top layer of P(VDF-TrFE) has been prepared. The effect of the different thicknesses of each of the layers on the obtained morphology is addressed.

4.1 Thin films of phase separated P3HT/P(VDF-TrFE) blends prepared by solution mixing

The description of the preparation of thin films from blends of P(VDF-TrFE) and P3HT 50/50 wt% was shown in Chapter 2 (Section 2.2.3.3).

4.1.1 Topography of P3HT/P(VDF-TrFE) blend prepared from direct solution mixing

In order to obtain blend films with different thickness, the total concentration of polymer in the solution was varied. The topography of the spin-coated blend films was characterized by AFM in tapping mode and the corresponding height images are shown in Figure 4.1a-c.

As observed in Figure 4.1a-c it looks as if there were two different type of domains, with a clear height difference, which may be an indication of phase separation. This result is further confirmed by the height profile below its corresponding topography map, from which it is observed that the differences between the height on higher and lower domains increases as the concentration of the solution increases. With such a large difference in the height of the domains, it is complicated to estimate the average thickness by the method described in Chapter 2 (Section 2.3.1.1). In this case, therefore, we have estimated two thickness values of the separated domains for each sample, the higher domain and the lower domain. These results are plotted as a function of concentration and presented in Figure 4.2. The thicknesses of both domains increase with the concentration at differently extent. More specifically, the lower domains exhibit smaller thickness increase than the higher ones. The thickness of the higher domains is less homogeneous than that of the lower ones.

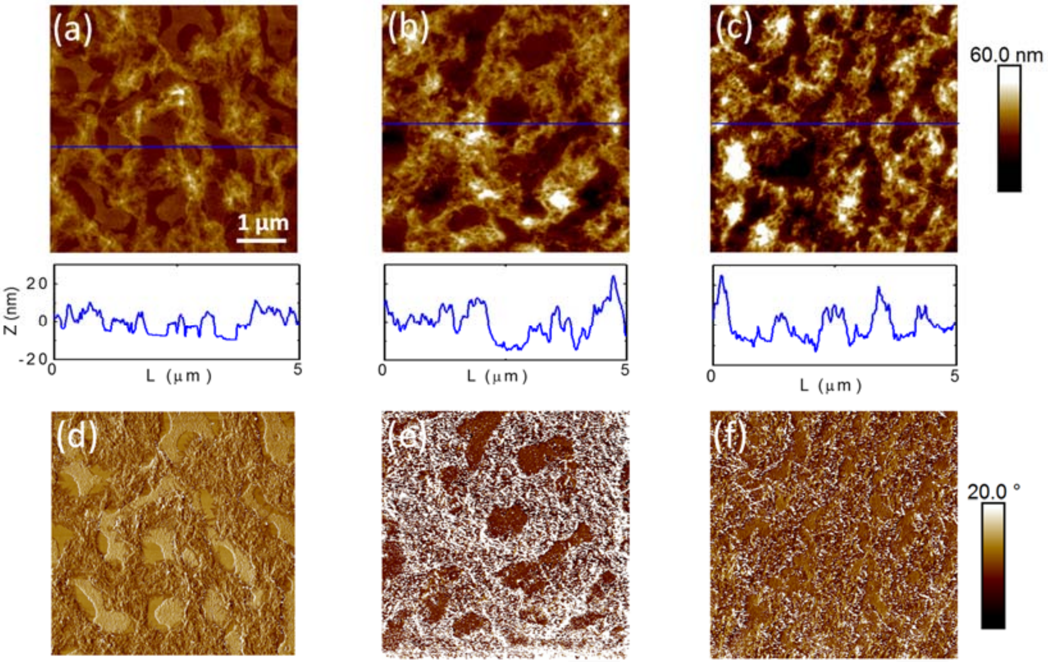

Figure 4.1 AFM height images (5 µm × 5 µm) of P3HT/P(VDF-TrFE) 50/50 wt% blend films spin-coated from solution with different total concentrations at 41°C (THF as solvent): (a) 8 g/L, (b) 16 g/L and (c) 24 g/L, respectively. The corresponding tapping phase maps are also presented in the bottom row (d-f). The plots in the middle are the height profiles along the blue lines displayed in height images.

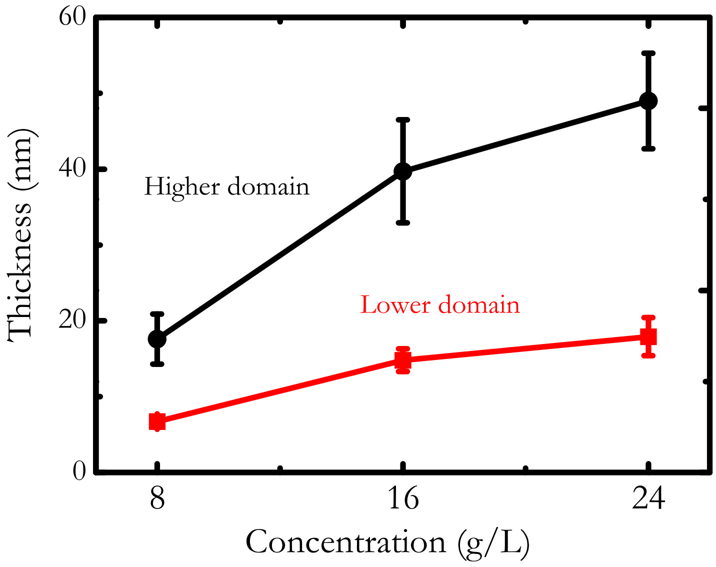

Figure 4.2 Estimation of the film thickness of two domains in the blend films deposited onto conductive silicon wafers as a function of the solutions concentration. The continuous lines are used to guide the eye.

Figure 4.1d-e shows the corresponding tapping phase images. Comparison of height and tapping phase images reveals that the areas with different height exhibit different mechanical properties. The domains with similar mechanical properties have a characteristic size of around 500 nm. This is an indication of phase separation, although the morphology depends slightly on the thickness of the film. In fact, the domain sizes are decreasing with increasing the thickness, implying higher mixing in the thicker films. Tapping images shown in Figure 4.1d-f allow concluding that there are two different types of domains in the sample. However, with the only information provided by tapping AFM, it is not possible to assign different domains to each component, or, to the bare silicon substrate.

In order to clearly identify whether the domains observed in Figure 4.1 correspond to areas rich in each of the two components of the blends, or, on the contrary, they correspond to bare silicon, selective AFM based techniques were employed. On one hand, C-AFM measures the hole current between the tip and the sample, and therefore is sensible to the semiconducting part of the blend, the P3HT rich phase. On the other hand, PFM measures the expansion of the domains under an applied field on the tip, and therefore, is sensible to the ferroelectric part of the blend, P(VDF-TrFE), in this case. Both techniques have been described in Chapter 2 (Section 2.3.1.2 and section 2.3.1.3).

4.1.2 Identification of the P3HT and P(VDF-TrFE) phases in the blend by electric AFM techniques: C-AFM and PFM

4.1.2.1 C-AFM on P3HT/P(VDF-TrFE) blends

The hole current between the tip and the sample was used to map the surface of the blends, by using C-AFM with an applied voltage of -5 V between the substrate and the tip. Films with two different thicknesses, 8 g/L and 24 g/L are characterized. The obtained map of the hole current across the semiconducting/ferroelectric polymer blends together with its topography, is shown in Figure 4.3a, b. As mentioned above, since P3HT is a semiconducting polymer and P(VDF-TrFE) is a ferroelectric polymer, the contrast in the electrical current map arises from this different conducting character of P3HT and P(VDF-TrFE) domains. Regions that present hole current (negative current values in Figure 4.3), would correspond to P3HT rich domains (yellow regions or white circles in the current map, Figure 4.3), whereas regions with zero current are those in purple color within the green circles and correspond to non conducting domains.

The hole current between the tip and the sample was used to map the surface of the blends, by using C-AFM with an applied voltage of -5 V between the substrate and the tip. Films with two different thicknesses, 8 g/L and 24 g/L are characterized. The obtained map of the hole current across the semiconducting/ferroelectric polymer blends together with its topography, is shown in

Figure 4.3a, b. As mentioned above, since P3HT is a semiconducting polymer and P(VDF-TrFE) is a ferroelectric polymer, the contrast in the current map arises from this different character of P3HT and P(VDF-TrFE) domains. Regions that present hole current (negative current values in Figure 4.3), would correspond to P3HT rich domains (yellow regions or white circles in the current map, Figure 4.3), whereas regions with 0 current values that do not exhibit any charge motion (purple colors or green circles), correspond to not conducting domains.

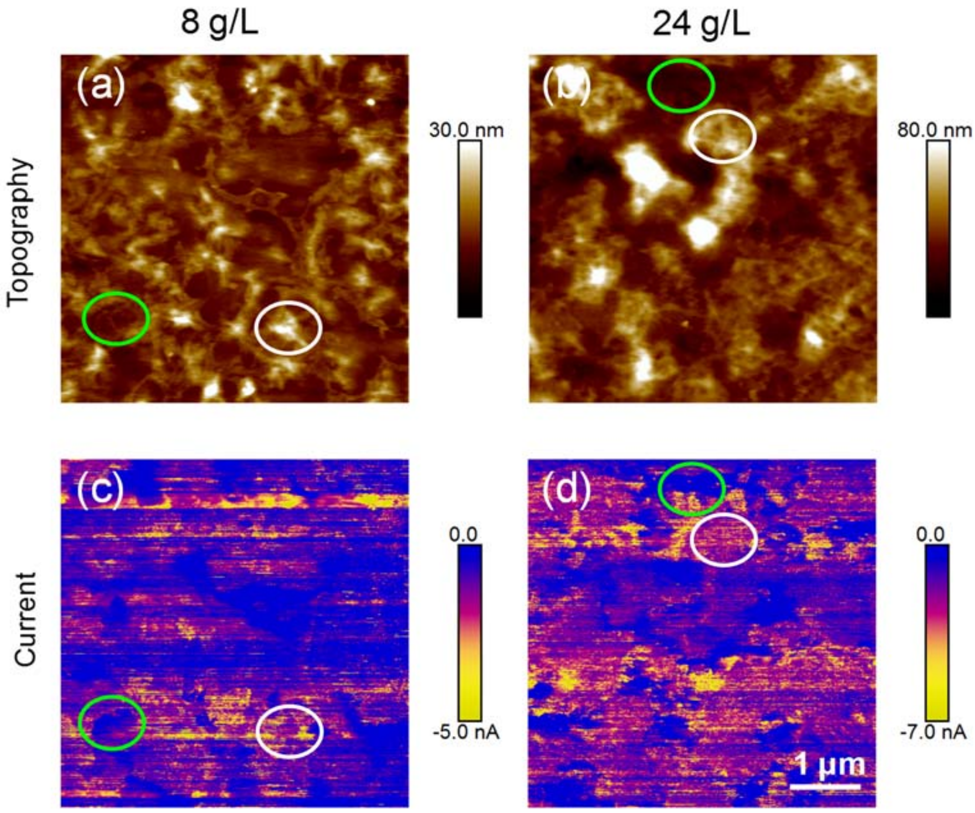

Figure 4.3 (a, b) AFM height topography (5 μm× 5 μm) and (c, d) C-AFM maps of P3HT/P(VDF-TrFE) (50/50) blend on conductive silicon of (left column) 8 g/L and (right column) 24 g/L. Selected domains are marked with the circles.

Comparing the current maps with the corresponding height images, it is possible to conclude that the areas that show non-zero hole current are those with higher height in the topography. Provided that hole current in this binary systems can only occur in the P3HT phase, it is possible to conclude that these higher regions are P3HT rich domains.

4.1.2.2 Ferroelectricity of P(VDF-TrFE) domains

The PFM maps on the thinner and thicker films of P3HT/P(VDF-TrFE) blend are presented in Figure 4.4.

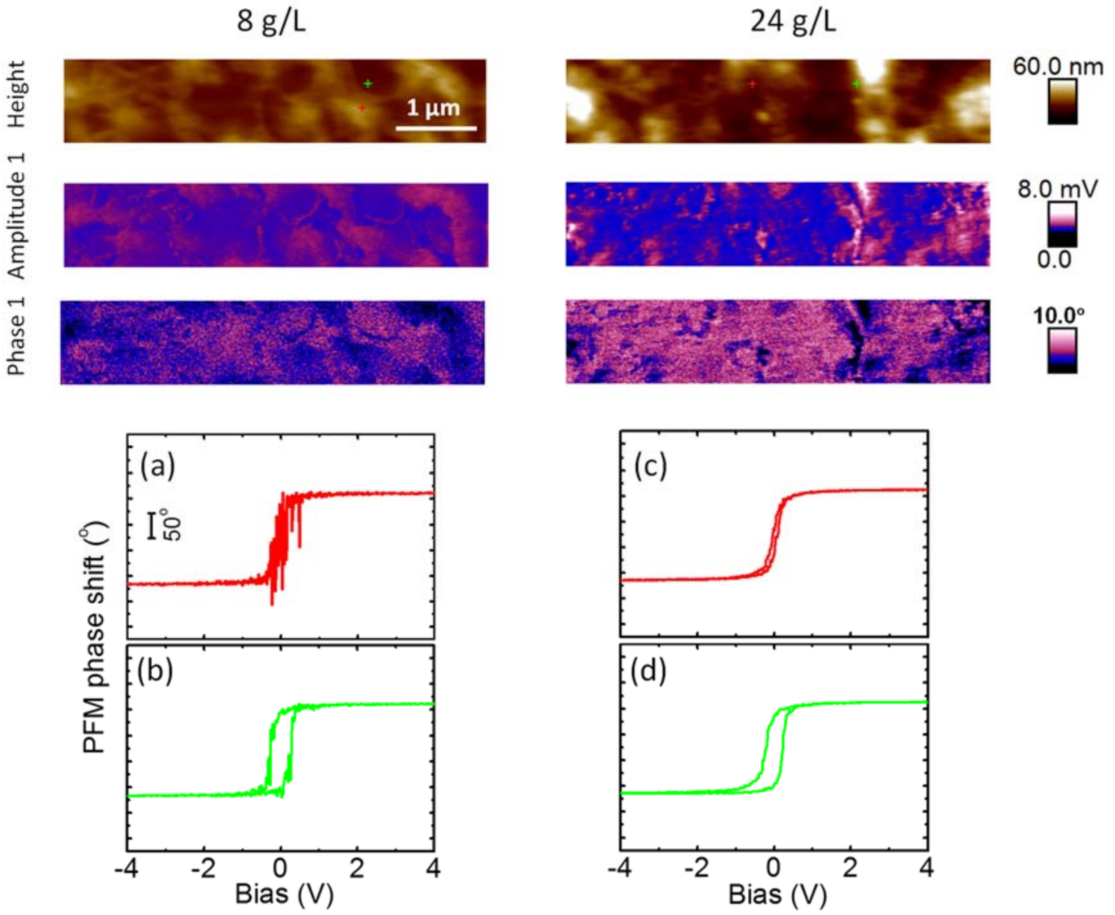

Figure 4.4 AFM height topography (5 µm× 1 µm) and PFM maps of the intensity and out-of-plane phase maps of (left column) 8 g/L and (right column) 24 g/L spin-coated P3HT/P(VDF-TrFE) (50/50) blend on conductive silicon. Regarding the maps, the top panel correspond to the topography maps, the mid panel correspond to the PFM amplitude maps and the bottom panels corresponds to the out-of-plane PFM phase. Corresponding phase shift as a function of the applied bias for marked domains are shown in the bottom: (a, b) 8 g/L and (c, d) 24 g/L. The color of the curves indicates from which marked regions in the PFM panels they have been obtained.

In Figure 4.4, the top images display the topography obtained in contact mode, leading to basically the same results as the ones obtained by tapping mode (Figure 4.1). The PFM results shown in the same figure (central and bottom panels) for the films with two different thicknesses, are the PFM out-of-plane amplitude and out-of-plane phase respectively. As described in Chapter 2 (Section 2.3.1.2) this out-of-plane response is related to the deformation of the ferroelectric material under the effect of the applied field, due to the reverse piezoelectric effect and it can provide information on the polarization state of the ferroelectric polymer. In this way, regions with non-zero values of the measured out-of-plane amplitude indicate that the measured domains present a component of the polarization in the direction of the applied field. The out-of-plane phase values measured are due to the lag between the applied alternating field and the shift in the polarization due to that field. Since, from the two components of the blends, only the ferroelectric polymer presents a net polarization that can be shifted by the applied field, PFM experiments allow identifying the ferroelectric domains in the blend. In this case, for the studied system and other similar ones [1] consisting of a semiconducting/ferroelectric mixture, C-AFM and PFM are complementary AFM based techniques to identify one and the other component. Comparing the height and PFM results, it is possible to assign for 8 g/L film, the lower height regions to those zones exhibiting ferroelectric response, as observed both in the values of PFM out-of-plane amplitude and the out-of-plane phase. As observed in the maps, the out-of-plane phase present a larger lag with respect to the applied field in the regions with lower height. By presenting the phase shift as a function of the applied voltage, it is possible to observe that in the domains with larger height, the phase transits from one value to another, and the transit occurs at 0 V. Reversing the sign of the voltage produces exactly the same shift in the phase, and the transit occurs at 0 V no matter the starting and finishing sign of the voltages. However, in the domains with lower height, the transit occurs at a non zero voltage value, called the coercive voltage V_c and the out-of-plane phase shows some hysteresis. This is related to the permanent polarization in the material that gives rise to the ferroelectric effect, since, these materials have a net polarization even in the absence of an applied voltage. These results together allow the final assignation of the different domains in the blends, where regions with higher heights correspond to P3HT rich domains and regions with lower height correspond to P(VDF-TrFE) rich domains.

The non-zero voltage at which the out-of-plane phase suddenly changes, the coercive voltage, is of about 0.25 V for the ferroelectric domains in the case of the thinner films and of 0.28V in the case of the thicker films. The coercive field is calculated from dividing the coercive voltage by the thickness of the system. For the 8 g/L sample, the thickness of the ferroelectric domains is in the range of 7 nm. This gives a coercive field value of around 36 MV/m. In the case of the 24 g/L sample, the thickness of the ferroelectric domains has been estimated to be 18 nm, and the coercive voltage is around 0.28 V. With those values a coercive field of around 15 MV/m is estimated. These values are similar to the ones reported for spin-coated P(VDF-TrFE) thin films [2].

In all this section we have observed that, even though P3HT and P(VDF-TrFE) domains are separated, their final morphology can only be slightly tuned by controlling the film thickness via the concentration of the spin-coated solution. But in general, the final morphology consists of a random distribution of P(VDF-TrFE) and P3HT domains without having control of their size, shape and distribution, and therefore they are hard to be considered in the design of a hypothetical device.

4.2 P(VDF-TrFE) nanoparticles embedded in P3HT continuous films

To achieve a higher control in the morphology of phase separated ferroelectric/semiconducting polymer blends, we have designed a procedure where the P(VDF-TrFE) domains have a preformed shape. For that we have prepared phase separated P3HT/P(VDF-TrFE) blends by dispersing P(VDF-TrFE) NPs in a continuous P3HT matrix.

4.2.1 Preparation of the semiconducting polymer/ferroelectric polymer nanoparticles blends

P(VDF-TrFE) NPs were prepared by using dialysis nanoprecipitation described in Chapter 2 (Section 2.2.2.2). The morphology and size distribution of the prepared P(VDF-TrFE) NPs has been studied previously [3]. The P(VDF-TrFE) NPs, were dried by lyophilization, and subsequently were redistributed in a P3HT solution in $CHCl_3$. This protocol was design on the hypothesis that the P(VDF-TrFE) NPs will not be modified in this redispersion since P(VDF-TrFE) is insoluble in $CHCl_3$. In this way, P3HT/ P(VDF-TrFE) NPs composites were prepared. The thickness of the prepared P3HT/P(VDF-TrFE) NPs composites and their labels are listed in Table 4.1.

Table 4.1 Details of the prepared P3HT/P(VDF-TrFE) NPs composites and the estimated thickness.

Label	P3HT (mg)	P(VDF-TrFE) nanoparticles	$CHCl_3$ (mL)	Total concentration (mg/mL)	Thickness (nm)
HT-1	2.5	-	1	2.5	29±2
HT/Fr1	2.5	2.5	1	5	34±2
HT-2	5	-	1	5	48±4
HT/Fr2	5	5	1	10	180±41

For the same concentration of P3HT, thicker films are obtained in the presence of P(VDF-TrFE) NPs. This effect is more evident in the case of the films prepared from higher concentration.

4.2.2 Topography of P3HT/P(VDF-TrFE) nanoparticles composites

The topography images of P3HT films with embedded P(VDF-TrFE) NPs are displayed in Figure 4.5. The corresponding neat P3HT thin films prepared from solutions with the same concentration than that of nanocomposites are also presented for the sake of comparison (Figure 4.5a and c). P3HT films, both with concentration of 2.5 g/L (labeled as HT-1) and 5 g/L (labeled as HT-2), form homogeneous continuous films with roughness values lower than 5 nm. However, nanocomposites formed by the P(VDF-TrFE) NPs embedded in the continuous P3HT films, HT/Fr-1 and HT/Fr-2 exhibit particle-like protuberances that can be attributed to the NPs distributed throughout the P3HT film (Figure 4.5b and d).

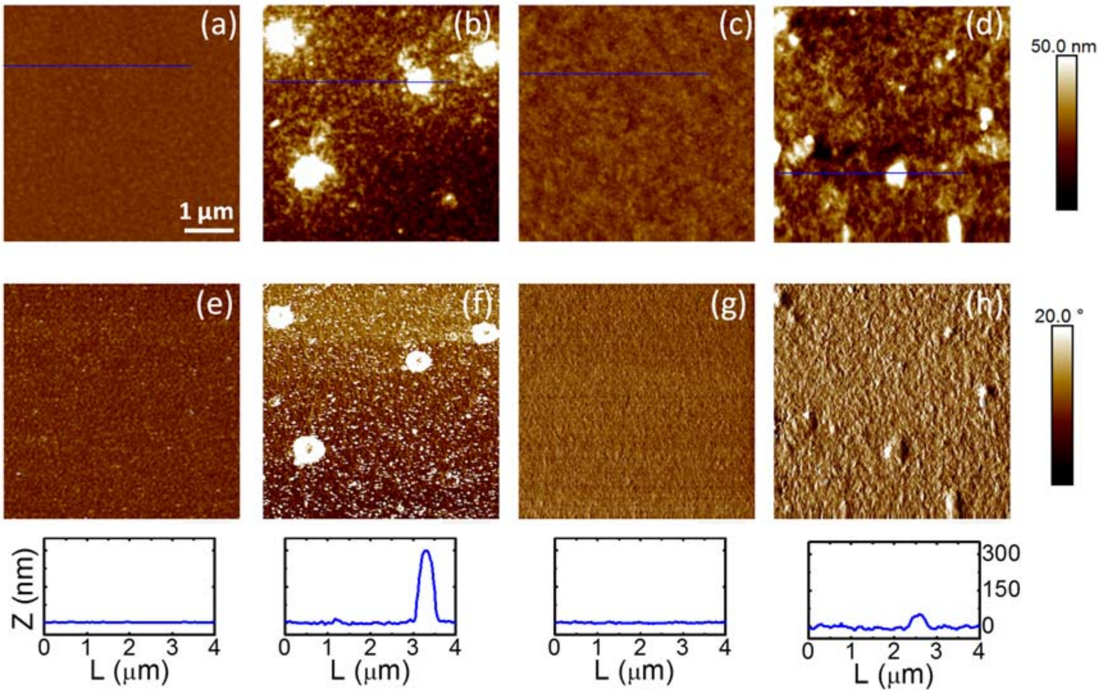

Figure 4.5 AFM topography (5 µm× 5 µm) of (top) height and (middle) tapping phase images for (a, e) HT-1 film, (b, f) HT/Fr-1 film, (c, g) HT-2 film and (d, h) HT/Fr-2. The bottom figures are height profiles corresponding to the line marked in the height images.

The tapping phase images of HT/Fr-1 and HT/Fr-2 reveal that these particles-like protuberances are from a different phase than the continuous matrix. From the topography we can say that the dispersion procedure does not affect the morphology of the ferroelectric NPs. The difference in thickness between HT/Fr-2 and that of pure P3HT film (HT-2, Table 4.1), together with the particle shape protuberances observed in Figure 4.5 indicates that P(VDF-TrFE) NPs can be buried inside P3HT and therefore produce an increase of the film thickness. This effect is weaker in the case of HT/Fr-1, due to fewer amount of P(VDF-TrFE) NPs used.

The different solution concentration produces different thickness for the continuous P3HT film. Because of that, the height of the P(VDF-TrFE) protuberances is larger in the case of HT/Fr-1, as can be observed in the height profiles, corresponding to the marked lines in the tapping height images (Figure 4.5). This observation indicates that only a part of the P(VDF-TrFE) NPs is covered by P3HT in the case of the HT/Fr-1 sample whereas in the HT/Fr-2 sample, a large portion of the P(VDF-TrFE) NPs is buried inside the P3HT film. In the next paragraph we will study the effect of this situation on the ferroelectric properties of both systems.

4.2.3 Evidence of ferroelectricity in the P3HT/P(VDF-TrFE) nanoparticles composites

The ferroelectric properties of the embebded ferroelectric NPs were tested by PFM. Figure 4.6 shows the height maps obtained in contact mode AFM for the nanocomposites studied. After locating in the height image regions where the particles were observed (marked with a blue square in the Figure 4.6), PFM as a function of the applied voltage was performed. For the sake of comparison, PFM measurements as a function of the applied voltage were also performed in regions without particles (marked with a red square in Figure 4.6). The change in the out-of-plane PFM phase as a function of the applied voltage in both type of regions is presented in Figure 4.6c and d for the HT/Fr-1 sample and Figure 4.6e and f for the HT/Fr-2 sample.

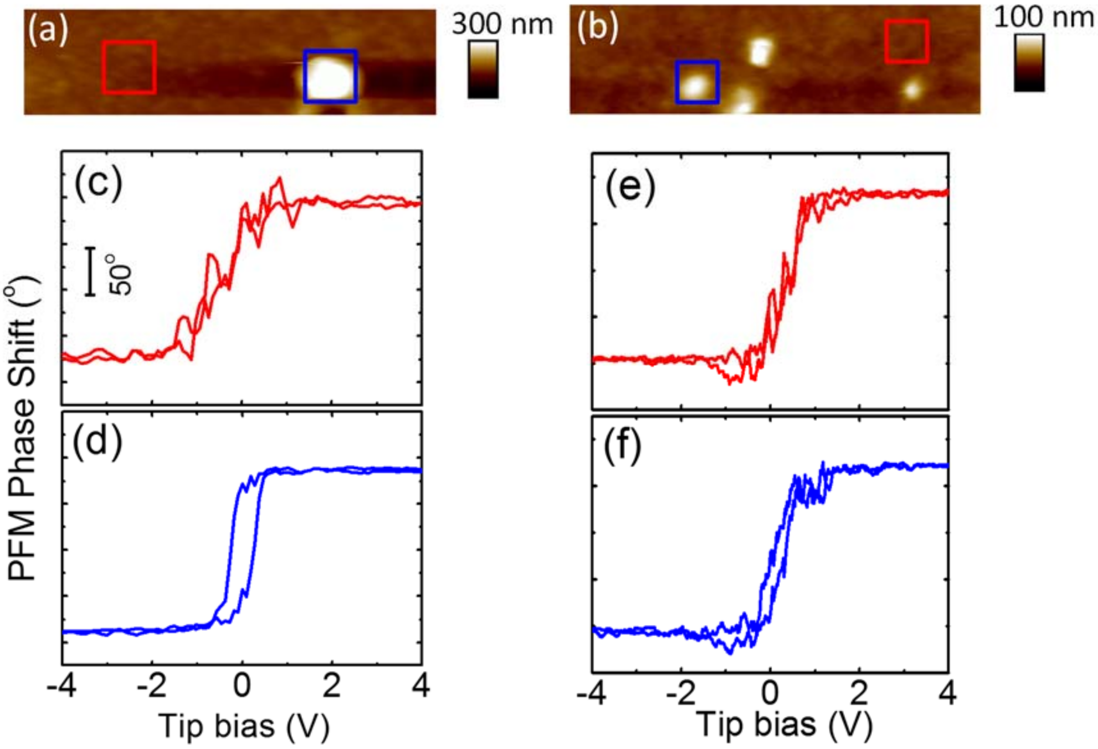

Figure 4.6 AFM tapping images (5 μm× 1 μm) of (a) HT/Fr-1 and (b) HT/Fr-2. Below each height image its corresponding PFM phase shift is displayed as a function of applied electric field in regions (c, e) without NPs and (d, f) with NPs. Colors of the curves correspond to the color of the marking squares in the AFM height images.

As expected, the out-of-plane PFM phase shows no hysteresis in the continuous P3HT phase. However, in both nanocomposites, the out-of-plane PFM phase shows a small hysteresis when the PFM experiment is carried out on the protuberance region. The existence of this hysteresis verifies that the P(VDF-TrFE) NPs into the nanocomposite have ferroelectric properties. The hysteresis area of the protuberances in the HT/Fr-2 sample is smaller (Figure 4.6 right). This result will be discussed later.

In order to address if the presence of the ferroelectric NPs modify the semiconducting polymer film, in the P3HT/P(VDF-TrFE) nanocomposites C-AFM was performed. In this way, a current map of the polymer nanocomposites surface was obtained by applying a tip bias of -5 V. Figure 4.7 shows topography and current map acquired on the P3HT/P(VDF-TrFE) nanocomposites of HT/Fr-1. Comparing the topography with the current image simultaneously recorded, it is possible to observe regions with different conductivity properties. The yellow regions in current map are those zones that show non-zero current, and therefore, they can be attributed to conductive P3HT. Blue regions, are those that present zero values of the current, and as observed, they correspond to the protuberances in the topography, and therefore, can be associated to P(VDF-TrFE) NPs. The regions of P3HT surrounding the ferroelectric NPs exhibit non-zero current but slightly lower than that of the regions located far away of the ferroelectric NPs. As it has been pointed out by Khikhlovskyi et al. [1], the polarization sign of the ferroelectric domains affect the charge transport of the surrounding semiconducting polymer. This might be the reason for the inhomogeneity of the charge transport in the P3HT regions.

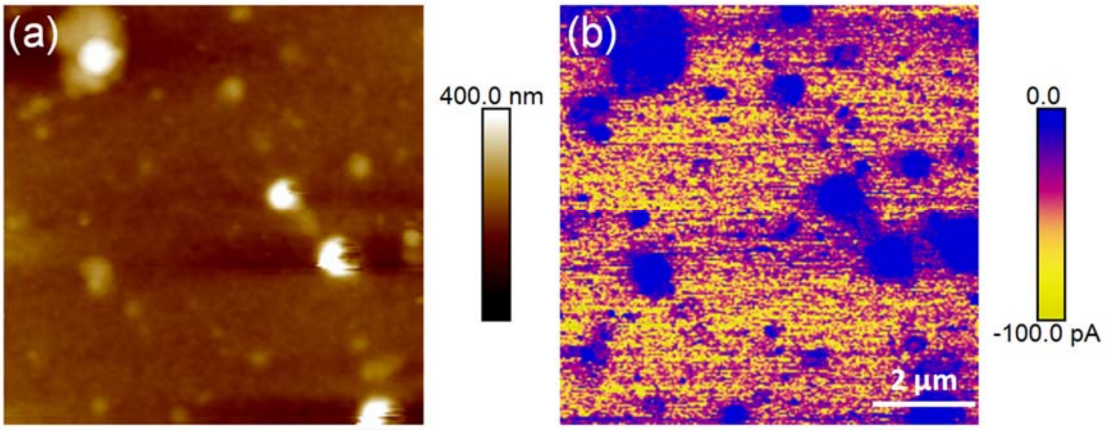

Figure 4.7 C-AFM measurement for HT/Fr-1 (a) height image and (b) current image (dc tip bias, -5 V).

Summarizing, these results allow us to deduce that the protuberances observed in the topography images are the ferroelectric polymer NPs, and that their ferroelectric properties are kept in the nanocomposites, allowing them to be considered as suitable systems for information storage by

PFM. However, the small hysteresis shown by the ferroelectric NPs will produce a low contrast with respect of the non-ferroelectric behavior of the continuous P3HT film. In order to improve that, we have explored the possibility of enhancing the ferroelectricity by annealing the system.

4.2.4 Annealing effect on the ferroelectric response for P(VDF-TrFE) nanoparticles

Since the ferroelectricity of the P(VDF-TrFE) is originated from the presence of permanent dipoles in the crystalline phase and from its response to an external electric field, the larger the crystal size, the more the ferroelectric effect will be enhanced. It has been previously proven in the literature that the preparation of P(VDF-TrFE) in the form of NPs, lowers the crystallinity with respect to that of the bulk [3]. On the other hand, in the literature it has also been demonstrated that, when compared with continuous P(VDF-TrFE) films, nanoconfinement offers the advantage of limiting the extension of the switch of the polarization, allowing the selective writing of small regions [2,4-6]. To enhance the crystallinity, a well-known method is to anneal P(VDF-TrFE) at temperatures close to its Curie temperature T_c [7-10]. With this idea in mind, the as-prepared nanocomposites were isothermally annealed at 130 ºC for 30 minutes. This temperature was chosen since it is below ferro-para transition of the P(VDF-TrFE) [3,11]. The topography of the samples after annealing is shown in Figure 4.8. Compared with the as-prepared P3HT/P(VDF-TrFE), one can observe that the annealing process does not modify the morphology of the system that still consists in nearly spherical protuberances out of a continuous film.

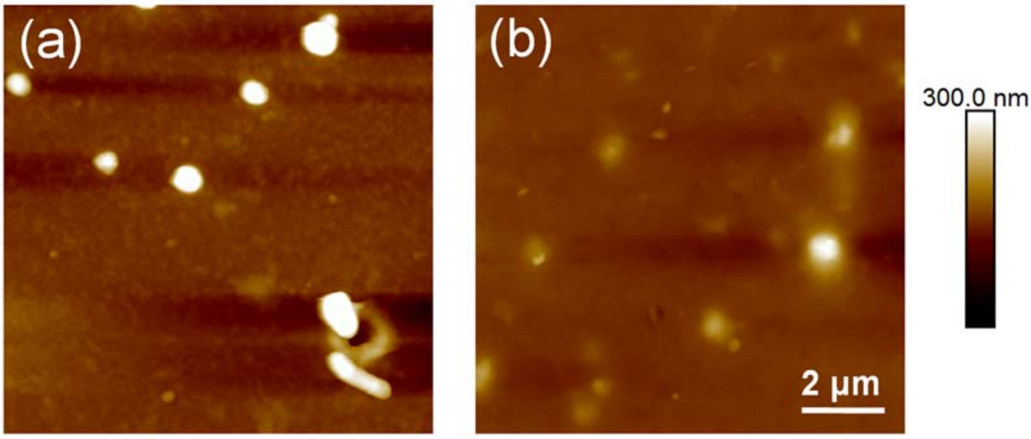

Figure 4.8 AFM height images (5 μm× 5 μm) after isothermal annealing at 130 ºC for 30 minutes for (a) HT/Fr-1 and (b) HT/Fr-2.

In order to assess the enhancement of the ferroelectric properties, similar PFM experiments to the ones described in the previous section (Section 2.3.1.2 and 2.3.1.4) were performed. Figure 4.9 presents the out-of-plane PFM phase as a function of the applied tip bias for the two annealed

P(VDF-TrFE)/P3HT nanocomposites, for sample HT/Fr-1. The curves corresponding to the as-prepared samples are plotted here again for the sake of comparison. A clear change is observed in the hysteresis shown by the nanocomposites after annealing. The hysteresis is larger after annealing, indicating an increase of the coercive field. To understand this effect, one should consider that in ferroelectric polymers, the ferroelectricity is related to the 180º-flipping of permanent dipoles in the crystals formed by the fold packed of long chains. Thus, their ferroelectric properties are intimately dependent upon the internal crystal structure, nanoconfinement effects and inter-domain interactions or coupling, etc. [12]. It has been reported that narrow hysteresis cycles are due to small ferroelectric domains that are able to accommodate only a few dipoles, thus decreasing cooperative coupling among domains [13]. Due to the preparation procedure of the P(VDF-TrFE) NPs (Chapter 2, Section 2.2.2.2) they have isotropically distributed crystals and have lower crystallinity and higher amount of the paraelectric phase compared to that of the bulk [3]. Besides, due to the geometric confinement, the crystal growth of P(VDF-TrFE) NPs is restricted [14], and may contain only a small ferroelectric domain. As a result, the ferroelectric domains would be confined to each NP, and therefore, they will not have almost coupling interaction among them [15] finally resulting in a reduction of the spontaneous polarization and thus small hysteresis [16]. The observed widening of the hysteresis upon annealing can be attributed to the increase in crystallinity. Annealing the nanocomposites at temperatures close to their Curie temperature increases the crystallinity in the NPs and removes possible gauche defects [10], increasing therefore the size of the ferroelectric domains. This has the effect of enhancing the ferroelectric properties, probably due to an increase and perfection of the crystalline domains and therefore, to an increase in the ferroelectric domains.

The coercive field is calculated from dividing the coercive voltage by the thickness of the system (diameter in case of the nanospheres). In the case of the as-prepared HT/Fr-1 sample, the average diameter of the P(VDF-TrFE) NPs is in the range of 280 nm [3]. This gives a coercive field value of around 1.8 MV/m, considering the coercive voltage is around 0.5 V (Figure 4.8a). This obtained value of E_c for the embedded P(VDF-TrFE) NPs is much lower compared with the one corresponding to spin-coated thin films (25 MV/m) [2] or bulk samples (50 MV/m) [17]. Also, higher values of E_c have been reported in other P(VDF-TrFE) nanostructures with similar characteristic size such as nanopillars [6], nanoarrays obtained from nanoimprinting (size 80 nm) [18], with E_c around 10 MV/m. One should consider that these nanostructures have been generated by processes that imply annealing at high temperatures and under the effect of pressure, which would enhance the crystallinity and the crystal size. Also, in those cases, the interaction between polymer chains and the supporting substrates may template the crystallinity and therefore, increase the ferroelectric domains [19]. The low value of E_c obtained for the as prepared P(VDF-TrFE) NPs embedded in P3HT could offer advantages in order to incorporate the NPs in devices such as FeRAM, since it will allow reading and writing information by polarization switching with low electric fields. However, it will show a very small ferroelectric contrast. In the case of the annealed nanocomposites, for the thinner sample (HT/Fr-1) the coercive field is similar to that reported for nanopillars [6] and nanoarrays obtained from nanoimprinting [18], in the present case 10 MV/m. For the thicker films (HT/Fr-2), the coercive field is smaller, and both systems exhibit a good ferroelectric contrast, combining the two appropriate requirements for FeRAM devices.

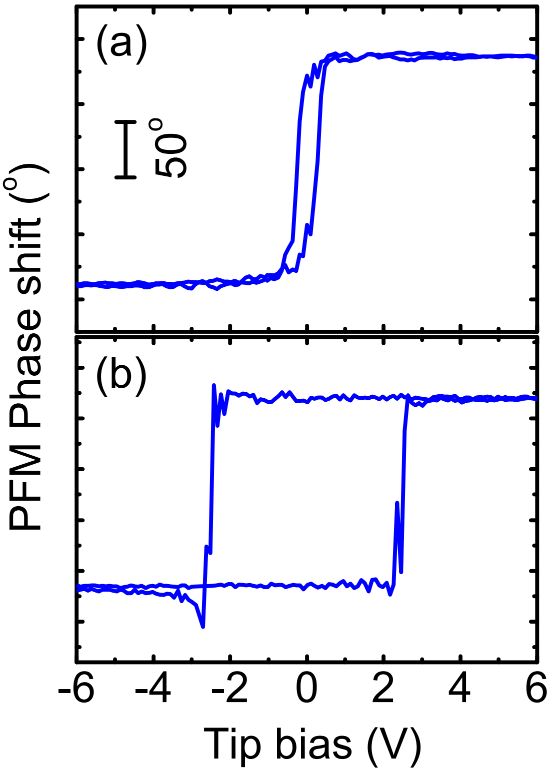

Figure 4.9 PFM phase shift as a function of applied electric field for HT/Fr-1: (a) as-prepared sampe, and (b) after annealing sample.

4.3 Study of P(VDF-TrFE)/P3HT morphology in bilayer system

As we showed before, phase separation of the investigated P3HT/P(VDF-TrFE) 50/50 wt% blend results in a distribution of irregular shaped domains of each polymer. Alternatively, we have proposed a method to control at least the shape of the ferroelectric domains. In the present section, bilayered blends of the two polymers are described.

Samples including P(VDF-TrFE) and P3HT single layers, as well as bilayers are prepared according to the procedure introduced in Chapter 2 (Section 2.2.3.1 and 2.2.3.2). The following labeling code has been assigned to the samples. Samples are labeled as NXXYY, where XX corresponds to the concentration in g/L of the solution used to prepare the P3HT layer and YY corresponds to the concentration in g/L used to prepare the P(VDF-TrFE) layer. As an example, a sample labeled as N0802 corresponds to a bilayer formed by a P3HT layer obtained by spin coating a 8g/L solution and a P(VDF-TrFE) layer obtained by spin coating on top of the previously formed P3HT layer from a 2 g/L solution.

4.3.1 Topography and thickness of P3HT and P(VDF-TrFE) single layers

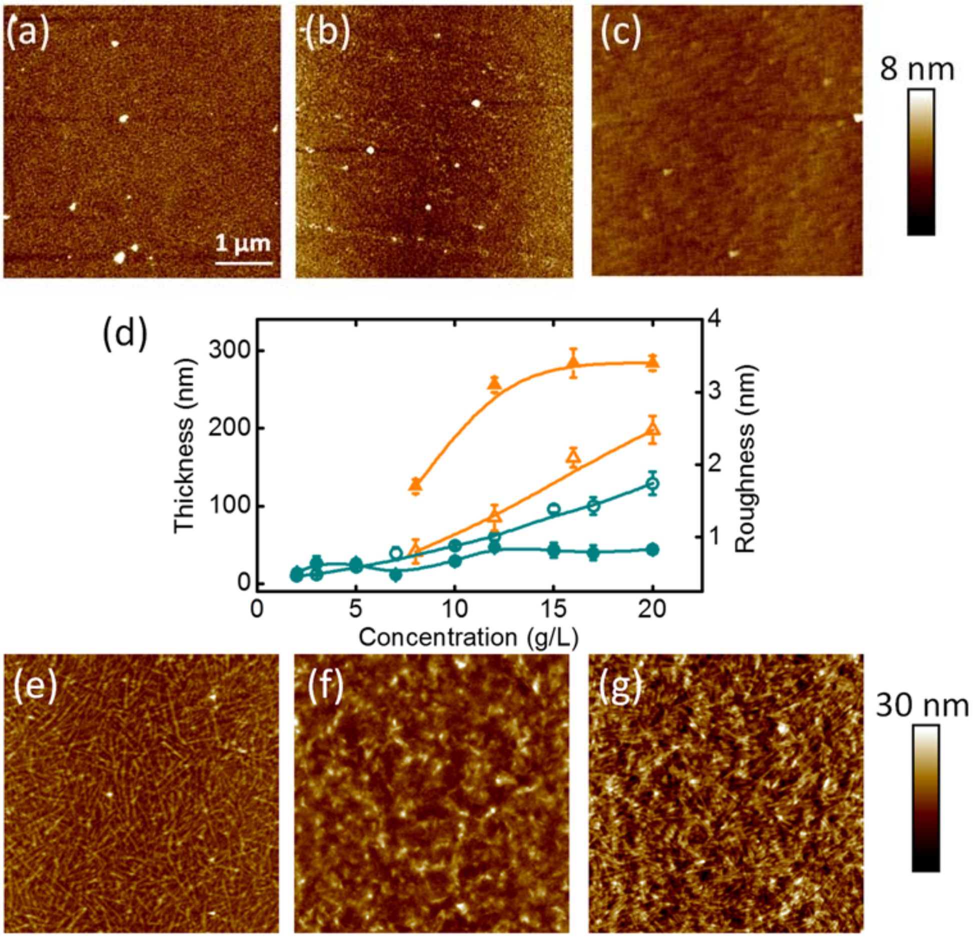

Figure 4.10 AFM topography (5 µm× 5 µm) of monolayers of P(VDF-TrFE) on silicon: (a) Samples N0003, (b) N0007 and (c) N0015. (d). Dependence of the thickness (open symbols) and the roughness (filled symbols) of the thin films prepared from different solution concentration. (O) P(VDF-TrFE) and (△) P3HT single layers. Bottom: AFM topography of the single layers of P3HT (e) N0800, (f) N1600 and (g) N2000.

Figure 4.10 (a-c) shows the topography of spin-coated thin films of P(VDF-TrFE) directly onto a silicon substrate, with different concentrations. For very low concentrations, the topography consists of a smooth surface with low roughness, with small protuberances. The topography of the P3HT single layer films is presented in Figure 4.10(e-g), from which we can find the surface of the P3HT films exhibits a fibrillar morphology, more or less packed depending on the concentration of the solution. More concentrated solutions give rise to a more packed morphology, whereas in the thinner films obtained from less concentrated solutions, the mesh of fibrils is looser.

Figure 4.10d shows the dependence of the thickness and roughness of P3HT and P(VDF-TrFE) single layers as a function of concentration. The thickness of both single layers increases almost linearly with the solution concentration. The P(VDF-TrFE) films have a roughness below 1 nm, regardless of the thickness. The roughness of the P3HT films increases with thickness and tends to a constant value for thicker films.

The dependence of the total thickness of the prepared bilayers, as a function of P(VDF-TrFE) concentration is shown in Figure 4.11. As it was shown in Figure 4.10, the thickness of single layers of P(VDF-TrFE) prepared directly onto a silicon substrate increases almost linearly with the solution concentration. However, this is not the case for the P(VDF-TrFE) layers prepared on top of a P3HT film. In the case of the bilayer, the thickness of the P(VDF-TrFE) layer obtained from low concentrations does not increase linearly or it does not increase at all with increasing the concentration. In the case of P(VDF-TrFE) films prepared on thicker P3HT substrates, the thickness dependence with the concentration is even more complex, exhibiting a local maximum around 3 g/L.

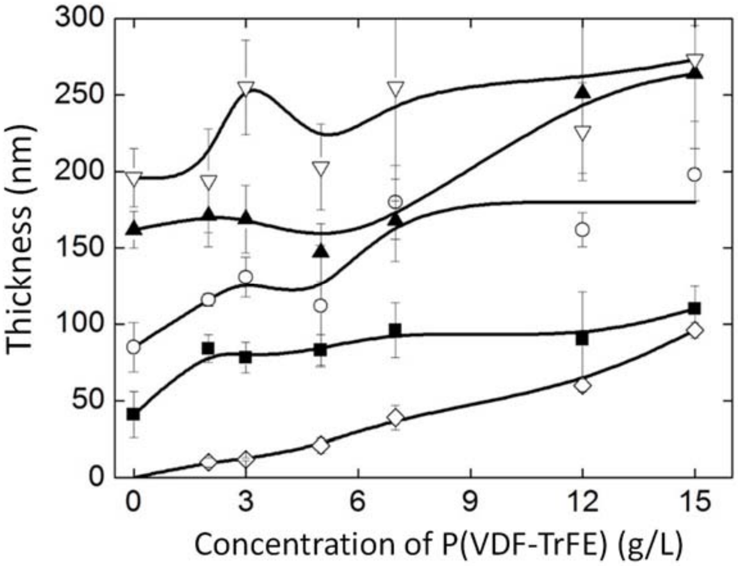

Figure 4.11 Thickness of the bilayers as a function of the concentration of the P(VDF-TrFE) solution in MEK. Different series correspond to different thickness of the P3HT substrate according to the code: (◇) N00XX, (■) N08XX, (○) N12XX, (▲) N16XX and (▽) N20XX. Continuous lines are eye guides.

4.3.1 Dewetting for the prepared bilayers

Figure 4.12 shows the topography of bilayers formed by spin coating P(VDF-TrFE) solutions on top of P3HT films with different thicknesses. As observed, in the formed polymer bilayers, the morphology of the bottom one, i.e, the P3HT layer, will affect the quality of the top one, i.e, P(VDF-TrFE) layer. The effect is more obvious in the P(VDF-TrFE) film formed from the lowest concentration solution NXX02. In this case, the P(VDF-TrFE) film exhibits dewetting regardless of the thickness of the underlying P3HT layer, as revealed by the existence of holes in the surface. However, the size of such holes depends on the thickness of the bottom layer. The holes are relatively small and dispersed for sample N0802, but as the thickness of the bottom layer increases the size of the holes increases and finally, as for example in sample N2002 they coalesce and the surface consists of an imperfect honey comb structure with walls and pores. Similar tendency is observed for NXX03 samples, although the coalescence between different holes is not observed in this case. Finally, for thicker top layers, almost no dewetting is observed, although the surface is rougher as the bottom layer thickness increases.

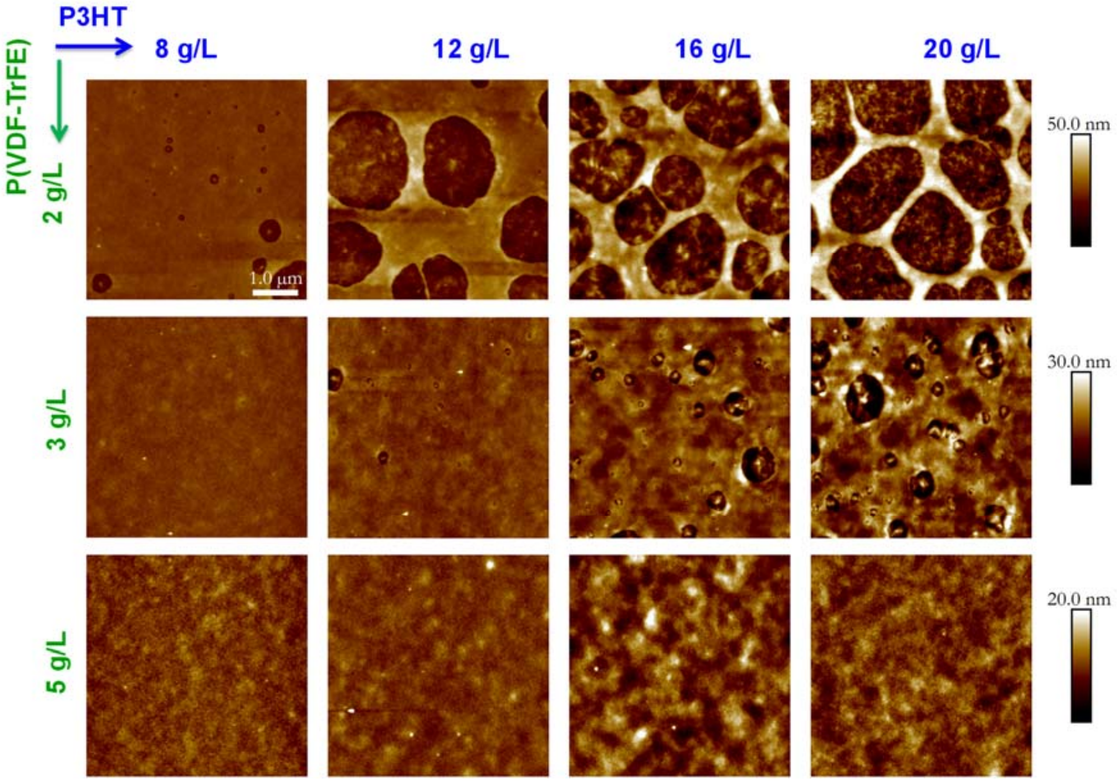

Figure 4.12 AFM topography of different P(VDF-TrFE) solutions on silicon supported P3HT films with different thicknesses. In the figure, the concentration of the P3HT solution from which the P3HT layers were prepared is shown.

4.3.2 Determination of the hole nature by PFM and C-AFM

To check whether the holes in samples NXX02, shown in Figure 4.12 are dry holes or if the bottom of them is formed by a thinner continuous ferroelectric polymer, AFM based techniques that provide contrast between both polymers, were used. As already stated in the case of the system of ferroelectric polymer NPs on a P3HT matrix, PFM maps can be obtained, taking advantage of the ferroelectricity of the P(VDF-TrFE) copolymer (top layer). On the other hand, considering that P3HT is a p-type semiconducting polymer, C-AFM experiment should show hole mobility in the P3HT domains.

Figure 4.13 shows the PFM and C-AFM maps of a N1602 bilayer. In the case of the PFM map (Figure 4.13b), it can be observed that the regions that offer a non-negligible PFM amplitude, and therefore, those that are ferroelectric, are those that are higher in the topography, whereas the bottom of the holes do not show piezo electric response, and therefore they are not ferroelectric. This result indicates that the morphology of the P(VDF-TrFE) layer in this case consists of dry holes. To further confirm this conclusion, C-AFM current images are shown in Figure 4.13d. The current image of the sample with hole morphology shows that top layer is not conductive but the bottom of the holes exhibits finite current, evidencing that this part of the hole is P3HT.

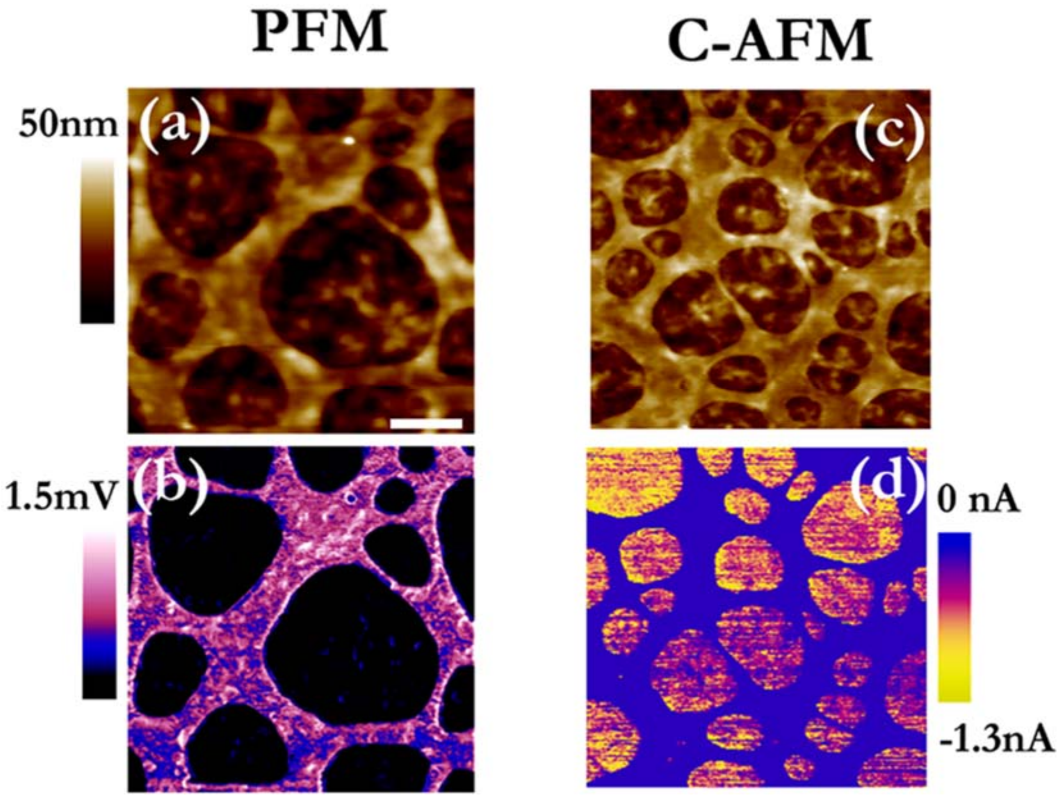

Figure 4.13 C-AFM measurements for the N1602 bilayer, (a) and (c) height images, (b) PFM out of phase amplitude, (d) C-AFM current image.

4.3.3 Characterization of the surface energy of the P3HT substrates

In order to understand why the thickness of the underlying P3HT substrate affects the obtained dewetting pattern obtained for P(VDF-TrFE) top layer, the CA of P(VDF-TrFE) polymer solutions on those substrates, was measured. The dependence of the CA for the different P(VDF-TrFE) concentrations is presented in Figure 4.14.

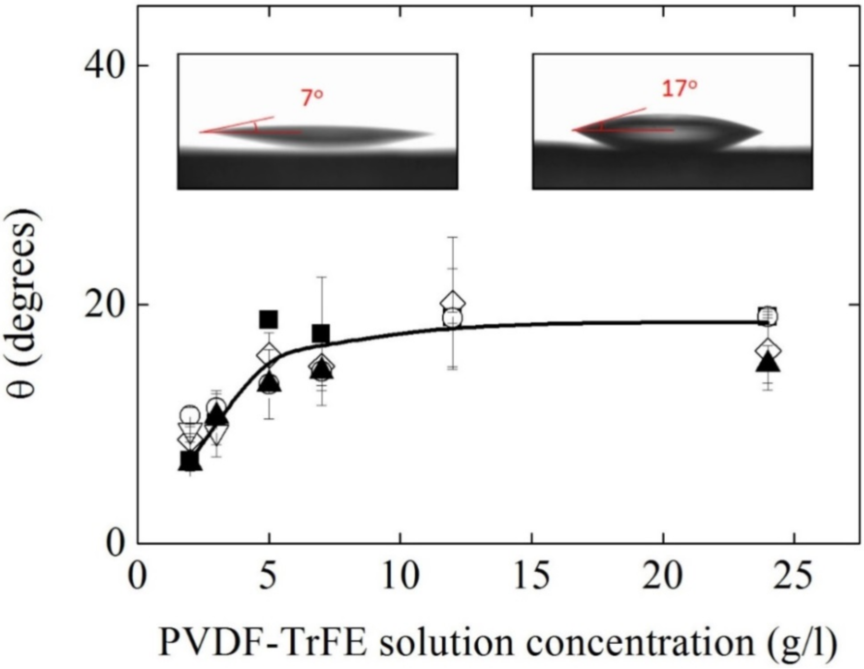

Figure 4.14 Contact angle CA, measured by the sessile drop method, of the different concentration of P(VDF-TrFE) solution on top of P3HT layers of different thickness: (◇) N00XX, (■) N08XX, (○) N12XX, (▲) N16XX and (▽) N20XX. Drop of 2 g/L (left inset) and 7 g/L (right inset) P(VDF/TrFE) solution in MEK on a silicon wafer coated with a P3HT film prepared from a 8 g/L solution in $CHCl_3$.

As observed in Figure 4.14, for the same P(VDF-TrFE) solution concentration, the wetting is almost independent of the thickness of the P3HT substrate. However, for a given thickness of the P3HT substrate, the solutions with lower concentration wet better the substrate than the ones with higher polymer concentration. This observation indicates that the samples that present a stronger dewetting effect when spin-coated with the creation of holes, however, are those whose starting solution wets the P3HT better. This effect might be related to the solvent evaporation rate during the spin-coating. As the solution wets better the substrate, the area exposed to evaporation is larger. In this way, the solvent would evaporate more efficiently, not allowing the polymer to be evenly distributed, and therefore producing a film with holes. In order to further understand the differences between the final morphology depending on the characteristics of the bottom P3HT layer, the surface energy of each of the substrates has been characterized.

The origin of the observed effect of hole formation dependence with the P3HT layer thickness for the same P(VDF-TrFE) concentration must be found then on the long range interaction in the bilayer system. To quantify these interactions, surface free energy of the different samples was calculated. To do that two different procedures were used as explained in Chapter 2 (Section 2.3.5). The measurement of the CA of different liquids having different polarities is needed. In this case, water, glycerol and paraffin oil were used. The obtained CA of the above mentioned liquids on the surfaces of a bare silicon wafer, on P3HT films with different thicknesses on silicon and on a P(VDF-TrFE) film are shown in Table 4.2.

Table 4.2 CA values for P3HT and P(VDF-TrFE) single layers with different thicknesses for different liquids.

	Sample	Water	Glycerol	Paraffin oil
Silicon	0000	63±5	69±2	18±4
P3HT	0800	96±1	88±1	30.9±0.5
	1600	95.5±0.3	90±2	36±3
	2400	89±9	90±2	35±1
P(VDF-TrFE)	0002	--	73±1	32.0±0.1
	0004	87±1	74.5±0.1	32.1±0.6

The surface free energy and its components were first determined by the OWRK-model detailed in Chapter 2 (Section 2.3.5), so that information about the polar part and the dispersive part is obtained. The calculated values are listed in Table 4.3.

Table 4.3 Surface free energy and its components (in mJ m^{-2}) for the different P3HT and P(VDF-TrFE) single layers with different thicknesses and for bare silicon as determined by the OWRK method. Errors are estimated in ca. 10%.

		γ_s^p	γ_s^d	γ_s
Silicon		14.7	23.5	38.2
P3HT	**N0800**	1.6	23.5	25.1
	N1600	2.0	21.8	23.8
	N2400	3.5	20.9	24.4
P(VDF-TrFE)	**N0002**	5.1	24.7	29.8
	N0004	4.5	24.6	29.1

From these results it is observed that in the case of P3HT the polar component increases when thickness increases while the dispersive component decreases. Considering that in P(VDF-TrFE) the apolar component is the most important one, this could explain that wetting of P(VDF-TrFE) on P3HT is less efficient when P3HT thickness increases. Additionally, although slightly, the total surface energy of P3HT decreases with its thickness, which implies a decrease in the wettability. The surface free energy was also calculated by the van Oss-Chaudhury-Good method, and the results obtained by this method are listed in Table 4.4.

Table 4.4 Surface free energy and its components (in mJ m^{-2}) for the different P3HT and P(VDF-TrFE) single layers with different thicknesses and for bare silicon as calculated by the van Oss, Chaudhury and Good method. Errors are estimated in ca. 10%.

		γ_s^d	γ_s^-	γ_s^+	γ_s^p	γ_s
Silicon		27.5	28.2	0.09	3.2	30.7
P3HT	**N0800**	24.9	3	0.005	0.24	25.1
	N1600	23.6	1.9	0.013	0.31	23.9
	N2400	23.8	5.9	0.13	1.75	25.6
P(VDF-TrFE)	**N0004**	24.7	4	1	4	28.7

The results obtained by this method are similar to the ones shown for the OWRK method. Thus, the polar component increases for P3HT as its thickness increases. In fact, both the electron-acceptor and the electron-donor components increase, corresponding to the acidic and basic character respectively, while in contrast the apolar component remains constant or slightly decreases.

These results are in accordance with AFM results of bilayers that showed that when spin-coating of P(VDF-TrFE) onto P3HT layer is performed, the stronger dewetting effect occurs for thicker P3HT substrates.

4.4 Conclusion

In this chapter we have presented different approaches to control the phase separation in binary systems composed of a semiconducting polymer P3HT and a ferroelectric random copolymer P(VDF-TrFE). In the first part, the morphology and characteristics of the system obtained by spin coating the two polymers blended on a common solvent is described. Results show that phase separation gives rise to films of P3HT/P(VDF-TrFE) with roughness comparable to film thickness.

Secondly, we propose a method to obtain controlled size domain of the phase separated system, consisting in distributing P(VDF-TrFE) NPs in a P3HT solution. By spin coating this system, the obtained morphology consists of a continuous film of P3HT with protuberances arising from the P(VDF-TrFE) NPs. The two components can be distinguished by C-AFM and PFM. To understand the influence of NPs under confinement and the embedded substrates, we measured the ferroelectricity of the nanocomposites. In the NPs the crystal size and crystallinity are limited by confinement, and therefore the ferroelectric domains are restrained, thus exhibiting a narrow hysteresis loop. Annealing around its Curie temperature can enhance the ferroelectric properties due to the induced increase of crystallinity and crystalline size. And lastly, P3HT/P(VDF-TrFE) bilayers have been prepared. We have observed that the thickness of the P3HT layers affects the dewetting of the upper P(VDF-TrFE) layer. By performing CA measurements with different liquids, we have been able to obtain the total surface energy and its components of P3HT and P(VDF-TrFE) layer, and infer the reason for this dewettingto to take place.

4.5 References

[1] Khikhlovskyi, V., Wang, R., van Breemen, A. J. J. M., Gelinck, G. H., Janssen, R. A. J. and Kemerink, M. Nanoscale Organic Ferroelectric Resistive Switches. *The Journal of Physical Chemistry C* **118**, 3305-3312 (2014).

[2] Martinez-Tong, D. E., Soccio, M., Garcia-Gutierrez, M. C., Nogales, A., Rueda, D. R., Alayo, N., Perez-Murano, F. and Ezquerra, T. A. Improving Information Density in Ferroelectric Polymer Films by Using Nanoimprinted Gratings. *Applied Physics Letters* **102**, 191601-191605 (2013).

[3] Martínez-Tong, D. E., Soccio, M., Sanz, A., García, C., Ezquerra, T. A. and Nogales, A. Ferroelectricity and Molecular Dynamics of Poly(vinylidenefluoride-trifluoroethylene) Nanoparticles. *Polymer* **56**, 428-434 (2015).

[4] Martínez-Tong, D. E. *Confinamiento en Nanoestructuras Poliméricas: Preparación Propiedades, Aplicaciones e Implicaciones Físicas*, 2015).

[5] Nougaret, L., Kassa, H. G., Cai, R., Patois, T., Nysten, B., van Breemen, A. J. J. M., Gelinck, G. H., de Leeuw, D. M., Marrani, A., Hu, Z. and Jonas, A. M. Nanoscale Design of Multifunctional Organic Layers for Low-power High-density Memory Devices. *ACS Nano* **8**, 3498-3505 (2014).

[6] Kassa, H. G., Cai, R., Marrani, A., Nysten, B., Hu, Z. and Jonas, A. M. Structure and Ferroelectric Properties of Nanoimprinted Poly(vinylidene fluoride-ran-trifluoroethylene). *Macromolecules* **46**, 8569-8579 (2013).

[7] Tanaka, R., Tashiro, K. and Kobayashi, M. Annealing Effect on the Ferroelectric Phase Transition Behavior and Domain Structure of Vinylidene Fluoride (VDF)–trifluoroethylene Copolymers: A Comparison Between Uniaxially Oriented VDF 73 and 65% Copolymers. *Polymer* **40**, 3855-3865 (1999).

[8] Tashiro, K. and Tanaka, R. Structural Correlation Between Crystal Lattice and Lamellar Morphology in the Ferroelectric Phase Transition of Vinylidene Fluoride–trifluoroethylene Copolymers As Revealed By the Simultaneous Measurements of Wide-angle and Small-angle X-ray Scatterings. *Polymer* **47**, 5433-5444 (2006).

[9] Prabu, A. A., Kim, K. J. and Park, C. Effect of Thickness on the Crystallinity and Curie Transition Behavior in P(VDF/TrFE) (72/28) Copolymer Thin Films using FTIR-transmission Spectroscopy. *Vibrational Spectroscopy* **49**, 101-109 (2009).

[10] Kim, K. J., Kim, G. B., Vanlencia, C. L. and Rabolt, J. F. Curie Transition, Ferroelectric Crystal Structure, and Ferroelectricity of a VDF/TrFE(75/25) Copolymer 1. The Effect of the Consecutive

Annealing in the Ferroelectric State on Curie Transition and Ferroelectric Crystal Structure. *Journal of Polymer Science Part B: Polymer Physics* **32**, 2435-2444 (1994).

[11] Napolitano, S. *Non-equilibrium Phenomena in Confined Soft Matter: Irreversible Adsorption, Physical Aging and Glass Transition at the Nanoscale*. (Springer International Publishing, 2015).

[12] Guan, F., Wang, J., Yang, L., Tseng, J.-K., Han, K., Wang, Q. and Zhu, L. Confinement-Induced High-Field Antiferroelectric-like Behavior in a Poly(vinylidene fluoride-co-trifluoroethylene-co-chlorotrifluoroethylene)-graft-polystyrene Graft Copolymer. *Macromolecules* **44**, 2190-2199 (2011).

[13] Yang, L., Li, X., Allahyarov, E., Taylor, P. L., Zhang, Q. M. and Zhu, L. Novel Polymer Ferroelectric Behavior via Crystal Isomorphism and the Nanoconfinement Effect. *Polymer* **54**, 1709-1728 (2013).

[14] Lutkenhaus, J. L., McEnnis, K., Serghei, A. and Russell, T. P. Confinement Effects on Crystallization and Curie Transitions of Poly(vinylidene fluoride-co-trifluoroethylene). *Macromolecules* **43**, 3844-3850 (2010).

[15] Zhu, L. and Wang, Q. Novel Ferroelectric Polymers for High Energy Density and Low Loss Dielectrics. *Macromolecules* **45**, 2937-2954 (2012).

[16] George, A. S. The Relaxational Properties of Compositionally Disordered ABO 3 Perovskites. *Journal of Physics: Condensed Matter* **15**, R367-410 (2003).

[17] Naber, R. C. G., Tanase, C., Blom, P. W. M., Gelinck, G. H., Marsman, A. W., Touwslager, F. J., Setayesh, S. and de Leeuw, D. M. High-performance Solution-processed Polymer Ferroelectric Field-effect Transistors. *Nature Materials* **4**, 243-248 (2005).

[18] Hu, Z., Tian, M., Nysten, B. and Jonas, A. M. Regular Arrays of Highly Ordered Ferroelectric Polymer Nanostructures for Non-volatile Low-voltage Memories. *Nature Materials* **8**, 62-67 (2009).

[19] Green, M. A. Self-consistent Optical Parameters of Intrinsic Silicon at 300 K Including Temperature Coefficients. *Solar Energy Materials and Solar Cells* **92**, 1305-1310 (2008).

5

Influence of substrate and film thickness on polymer LIPSS formation

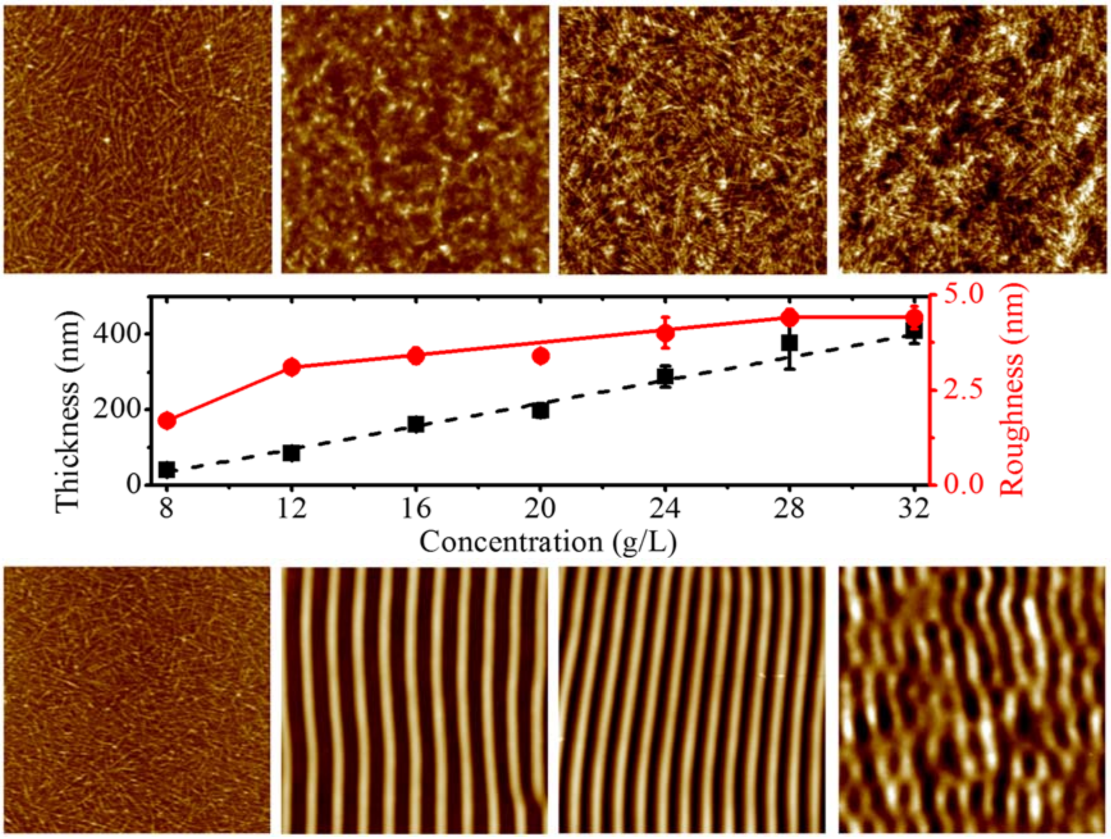

This chapter is structured in two different parts. In the first one, a precise description of LIPSS formation in films with different thicknesses of a model polymer, polystyrene, is given. The relation between the quality of the ripples induced by multipulse laser irradiation of polymer films, substrate properties, and the number of pulses was established. In the second part of the chapter, LIPSS formation in a functional polymer, poly(3 hexyl thiophene) (P3HT) spin-coated film with different thicknesses was studied, and the LIPSS created on these P3HT films provide a new possibility to prepare solar cells based on this type of nanostructures.

5.1 Samples

Spin coated films of PS and P3HT have been prepared following the protocols explained in Chapter 2 (Section 2.2.3.1). The details of the PS samples and the corresponding labels are listed in Table 5.1. The thicknesses of the prepared PS thin films as a function of solution concentration were presented in Figure 2.4.

Table 5.1 Labels of PS films for the different solution concentrations.

Substrate	**Silicon**						**Glass**		**Quartz**		**PS casting**
Concentration (g/L)	8	10	15	20	25	30	10	20	10	20	60
Label	Si08	Si10	Si15	Si20	Si25	Si30	G10	G20	Q10	Q20	PS60

5.2 Absorption properties

UV-Vis absorption spectra of PS and P3HT films were recorded in order to choose the irradiation wavelength at which the materials efficiently absorb, and they are shown in Figure 5.1. According to the spectra it is clear that PS absorbs significantly in the UV region while P3HT absorbs more efficiently in the Vis region. As stated in the introduction (Section 1.4.2.1), the requirement for LIPSS formation is that the polymer efficiently absorbs laser light. For this reason PS was irradiated at 266 nm, since at this wavelength its absorption coefficient is 1.6×10^{5} m^{-1} while P3HT was irradiated at 532 nm and the absorption coefficient at this wavelength is 8.62×10^{5} m^{-1}.

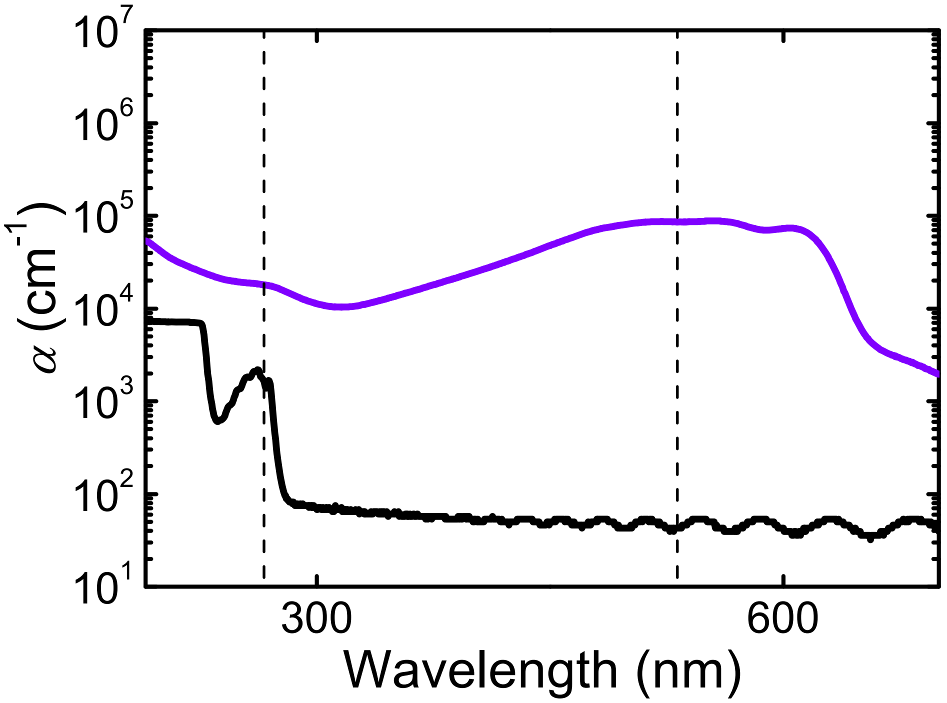

Figure 5.1 UV-Vis-NIR absorption spectra for PS (black line) and P3HT (purple line). Spectra have been normalized to the sample thickness. The vertical dashed line in the figure correspond to the wavelengths of 266 nm and 532 nm.

5.3 Study of LIPSS formation on a model polymer: polystyrene Assessment of the effect of film thickness and substrates on the quality of the generated structures

5.3.1 Effect of the number of pulses on LIPSS formation

In order to understand the effect of varying the number of pulses (*N*) on the quality of the formed LIPSS patterns, PS films were irradiated at a fixed fluence of F=10 mJ/cm^2 and a repetition rate of 10 Hz varying *N* up to 6000. AFM height images of the silicon supported thin films as a function of *N* are shown in Figure 5.2 for the sample Si30 with a thickness of 434 ± 10 nm.

As observed in Figure 5.2, to obtain relevant features in the surface of the polymer film, it is necessary to irradiate with a relative large number of pulses. The periodic surface structures are not formed until the number of pulses is around 3600. However, before the LIPSS are formed, irradiation with a low number of pulses affects the roughness of the PS surface. The right panel of Figure 5.2 shows that the surface roughness increases in the time period previous to LIPSS formation, referred to hereafter as incubation regime. Also in that plot, the values of both period (*L*) and height (*H*) of the LIPSS are shown.

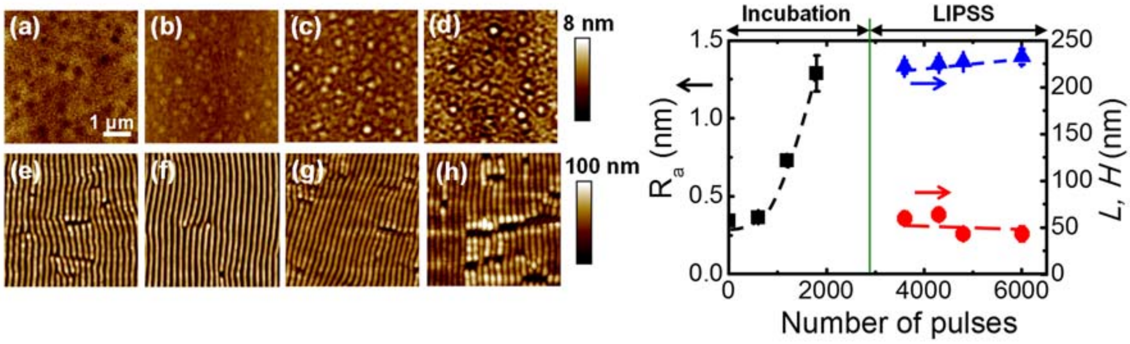

Figure 5.2 (Left panel) AFM height images (5 µm × 5 µm) of Si30 (434 nm) (a) non-irradiated and irradiated at 266 nm with a fluence of 10 mJ/cm^2 with (b) 600, (c) 1200, (d) 1800, (e) 3600, (f) 4300, (g) 4800, and (h) 6000 pulses. (Right panel) Roughness, (R_a, black squares), Period (*L*, ▲) and height (*H*, ●) as a function of number of laser pulses for Si30 irradiated at constant fluence of 10 mJ/cm^2. The dashed lines are plotted to guide the eye.

As previously reported [1], when a polymer film is exposed to the laser light, the uneven film surface scatters it due to its roughness and the scattered waves interfere with the incident laser beam, resulting in a modulated distribution of the energy on the surface [1]. This energy induces a modulated change in temperature in such a way that when this temperature is higher than the glass transition temperature of the irradiated polymer, a softening of the outermost layer occurs, allowing diffusion of the polymeric chains [2].

As shown in Figure 5.2, repetitive irradiation produces changes in the topography of the polymer surface and ripples morphology develops after a sufficient number of laser pulses. Considering laser irradiation as the only heating source of the polymer film, the corresponding temperature increase can be estimated by solving the one–dimensional heat equation as previously done in similar works [1]. Thus, the temperature at a given time (*t*) and different depth (*x*) from the surface should follow the equation [1,3]

$$\frac{\partial^2 T(x,t)}{\partial x^2} - a^2 \frac{\partial T(x,t)}{\partial t} = -\frac{\alpha}{\kappa} P(t) e^{-\alpha x} F_0 \tag{5- 1}$$

Where $a^2 = \frac{\rho c}{\kappa}$ being ρ the density, c the specific heat at constant pressure, κ the thermal conductivity, and α the absorption coefficient. F_0 is the incident fluence, 10 mJ/cm^2 in this work and P(*t*) is a function that describes the temporal shape of the laser pulse; for the fourth harmonic of the Q-switched Nd:YAG laser, this function is approximated by a modified Gaussian beam:

$$P(t) = \frac{2t}{\tau^2} \exp\left[-\left(\frac{t}{\tau}\right)^2\right] \qquad t > 0 \tag{5- 2}$$

Where the *t* factor ensures that intensity vanishes at *t* =0 and τ is the pulse duration, in this case 8 ns. The function is normalized to unity in the whole temporal range:

$$\int_0^{\infty} P(t)dt = \int_0^{\infty} \frac{2t}{\tau^2} \exp\left[-\left(\frac{t}{\tau}\right)^2\right] dt = 1 \tag{5- 3}$$

Formally, the heat conduction equation (5- 1) is solved as

$$T\,(x,t) = \int dt' \int dx'\, G(x,t;x',t')\ J(x',t') + K \tag{5- 4}$$

Where K is the initial temperature , $J(x',t')$ is defined as

$$J(x',t') = t\ \exp(-t^2)\ \exp\left[-\frac{x\alpha\sqrt{\tau}}{a}\right] \tag{5- 5}$$

and $G(x,t;x',t')$ is the kernel of the operator, with a relation with heat-equation operator O:

$$\mathrm{O} = \frac{\partial}{\partial t} - \frac{\partial^2}{\partial x^2} \tag{5- 6}$$

Satisfying

$$\mathrm{O}\ G(x,t;x',t') = \partial(x'-x)\partial\ (t-t') \tag{5- 7}$$

and known from quantum mechanics as

$$G(x,t;x',t') = \frac{1}{\sqrt{4\pi(t-t')}}\ exp\left[-\frac{(x-x')^2}{4(t-t')}\right] \tag{5- 8}$$

Finally the temperature is given by

$$T = \int_0^t dt'\ \int_{-\infty}^{\infty} dx'\ \frac{1}{\sqrt{4\pi(t-t')}}\ exp\left[-\frac{(x-x')^2}{4(t-t')}\right] \exp(-t')^2 \exp\left(\frac{-\alpha\sqrt{\tau}}{a}\right)\ |x'| + K \tag{5- 9}$$

This function is a solution of equation (5- 1), which can be verified by applying partial derivatives with the appropriate boundary conditions. The temperature is obtained by calculating numerically the integral of equation (5- 9) considering an initial temperature of 23 ºC. The integration is also performed for negative *x* values, but since the absolute value of the integrand is taken, it is guaranteed that the derivative at *x* = 0 vanishes. Physical properties used for the calculations are listed in Table 5.2.

For a single pulse, the variation of the calculated temperature at the surface as a function of the time elapsed from the beginning of the pulse is presented in Figure 5.3a. The result shows that, once the first pulse reaches the film, the temperature of the surface increases since the laser energy absorbed by PS is transformed into heat. As the pulse finishes, the surface of the sample starts to cool down due to the dissipation of heat into the cooler surrounding bulk material. The highest temperature achieved at the polymer surface by the initial single pulse is estimated to be around 32 ºC, far below the T_g of PS, which is 105 ºC. Although at first glance it seems that the temperature for long times is similar to the initial temperature, a small positive offset is still present at the time the next pulse arrives (0.1 s later than the onset of the previous one for the repetition rate of 10 Hz). Accumulation of laser pulses on the irradiated spot induces subsequent cycles of heating and cooling. Assuming that none of the physical magnitudes of the polymer change with temperature, one can estimate that each pulse will heat the sample and that the surface will be at a slightly higher temperature than the previous one after the arrival of the next laser pulse, as shown in Figure 5.3b. A minimum number of pulses is therefore necessary to ensure that the surface temperature overcomes the T_g. Thus, with this approximate estimation of the temperature increase, this number of pulses is estimated to be, in this case, larger than 200. This result suggests that the increase on roughness observed in Figure 5.2 (right panel) during the incubation regime before LIPSS formation occurs when the temperature has increased above the T_g of PS. In fact, for the sample Si30 slight changes in roughness are observed by AFM inspection already after irradiation with 450 pulses. After laser induced local heating, the material cools down and surface inhomogeneities are expected to be enhanced as the next pulse would find a rougher surface, thus facilitating the feedback mechanism needed for LIPSS formation [4]. It should be contemplated that here we performed a simplified temperature calculation where the temperature dependence of the polymer physical parameters was not considered. Additionally, the possible changes in the thermal properties of the surface during the transformations caused by the previous laser pulses (i.e., incubation effects) were also neglected. Nevertheless, considering only the thermal effects induced by every laser pulse and the repetitive heating/cooling cycles the calculation can explain LIPSS formation and supports the presence of the feedback mechanism.

Table 5.2 Linear absorption coefficient (α) at 266 nm, specific heat (c), density (ρ), thermal conductivity (κ) and refractive index at 266 nm (n), of PS material and of the supporting substrates.

	PS	Silicon	Quartz	Glass
α (m^{-1})	1.6×10^5	1.97×10^8 [5,6]	3 [7]	~ 10^8
c (J/(Kg·K))	1223 [8]	703 [9]	710 [9]	858 [9]
ρ (Kg·m^{-3})	1043 [41]	2330 [9]	2649 [9]	2510 [9]
κ (W/(m·K))	0.11 [8]	163.3 [9]	10.7 [9]	1.11 [9]
n	1.49 [10]	1.9 [5,11]	~1.5 [12]	1.51 [13]

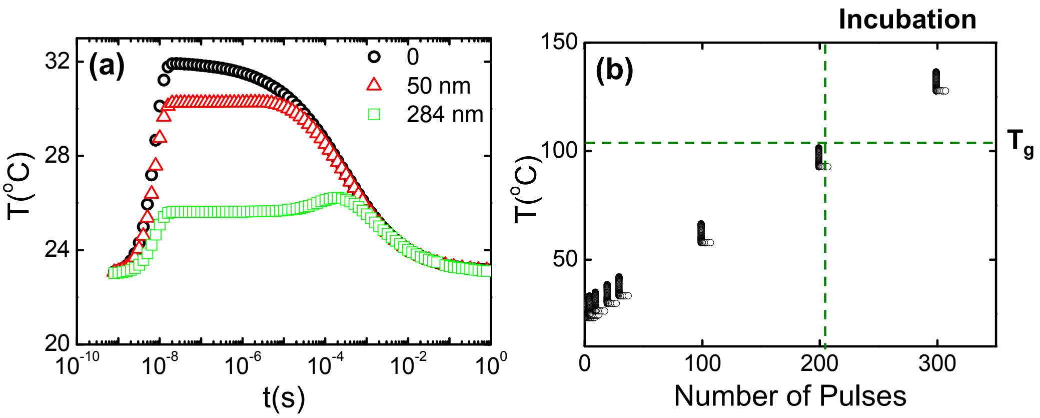

Figure 5.3 (a) Time dependence of the surface temperature irradiated after the first pulse at 266 nm at a fluence of 10 mJ/cm^2 at the indicated depths. (b) Temperature estimation at the polymer surface (0 nm) upon irradiation with successive laser pulses.

5.3.2 Influence of the film thickness on LIPSS formation

To assess the influence of film thickness in the LIPSS formation, PS thin films with thickness values ranging from 70 nm to 150 × 10^3 nm were irradiated at fixed values of fluence, 10 mJ/cm^2, and number of pulses, $N = 4800$. Figure 5.4 shows the corresponding AFM topography images. For the thinnest film, Si08 (Figure 5.4a), disordered LIPSS are formed. This is in agreement with previous results by Csete et al. [30] reporting about the existence of a critical thickness below which line-shaped structure cannot be formed. In contrast for thicker films, Si10 (Figure 5.4b), Si30 (Figure 5.4e) and PS60 (Figure 5.4f), parallel ripples are observed. Curiously enough, in the case of films with intermediate thicknesses, Si15 Figure 5.4c), Si20 (Figure 5.4d) and Si25 (not shown), distorted LIPSS decorated with droplet-like entities can be observed. The thickness dependence of the period and height of LIPSS is also displayed in Figure 5.4g and Figure 5.4h. The period and height values of the obtained LIPSS in Si10, Si30 and PS60 are similar (around 220 nm and 50 nm respectively). In contrast, films with intermediate thickness exhibit larger average period, around 270 nm, and deeper structures. From the above results it is possible to conclude that, for silicon supported thin films, a critical range of film thicknesses exist at which the formation of well-ordered LIPSS is hindered.

The variation of the R_a with the number of pulses in the incubation regime for samples with different thicknesses is shown in Figure 5.5a. The roughness starts increasing slowly for a low number of pulses, and at a given value of N, around 600 in this case, the surface starts to corrugate. Changes are more significant for the film Si30 (434 ± 10 nm thick), in comparison to thinner films.

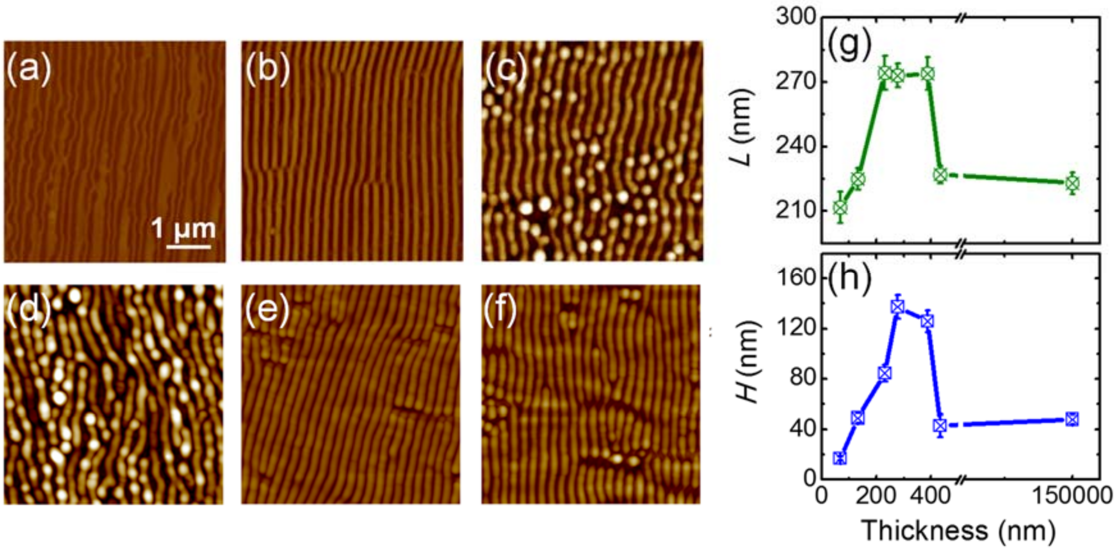

Figure 5.4 (Left) AFM height images (5 μm × 5 μm) of PS films with different thicknesses irradiated at a fluence of 10 mJ/cm^2 and number of pulses of 4800: (a) Si08, (b) Si10, (c) Si15, (d) Si20, (e) Si30 and (f) PS60. (Right) (g) Period length (*L*) and (h) the LIPSS height (*H*) as a function of the film thickness for PS film at a fluence of 10 mJ/cm^2 and number of pulses of 4800. Lines are plotted to guide the eyes.

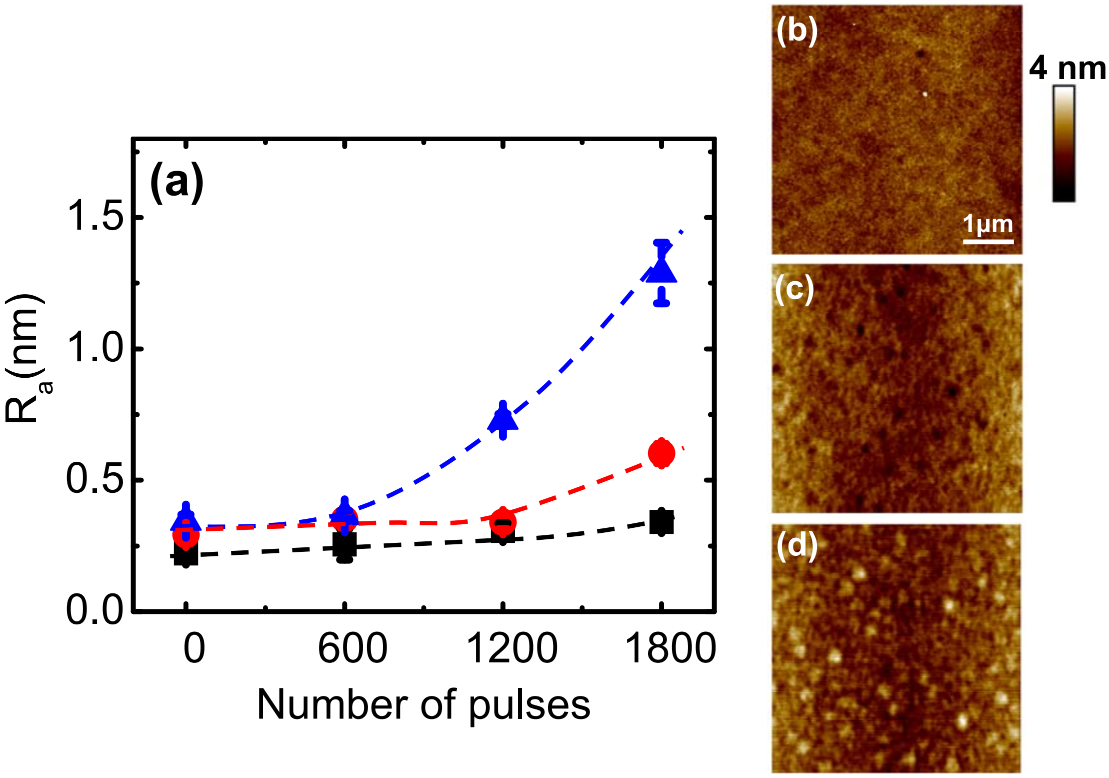

Figure 5.5 (a) R_a as a function of number of laser pulses for Si10 (■) Si20 (●), Si30 (▲). (Right) AFM height images of (b) Si10, (c) Si20 and (d) Si30 irradiated at constant *N* = 600. Dashed lines are plotted as a guide for the eyes.

For a given sample, once well-defined LIPSS are formed, the period and heights have values around 220 nm and 50 nm respectively except for the case of Si20 for which both values are larger, in particular around 270 nm and 120 nm respectively. The differences observed for the polymer films with different thicknesses in terms of modification onset and LIPSS properties cannot simply be explained by considering exclusively the heating/cooling effects induced by repetitive irradiation discussed in the previous paragraph. Hence, the influence of the silicon substrate will be discussed in the following section. As it will be shown, specifically for silicon substrates, the laser irradiation of the PS films of different thicknesses provokes the substrate temperature to increase very fast (Table 5.3). However, the heat is effectively dissipated on the basis of the high thermal diffusivity of silicon (Table 5.3). Thus, the high thermal conductivity and thermal diffusivity of silicon makes the cooling of the polymer material heated by the laser pulse to be more efficient for thinner films. Accordingly, the silicon substrate acts as a thermal heat sink making that thinner films need more irradiation energy, in terms of either pulses or fluence, in order to reach similar temperature values than those reached by thicker films [14]. In this case, a thin film like Si10 (132 nm) needs a higher number of pulses than a thicker one in order to exhibit morphological changes as shown in Figure 5.5a. To further corroborate this effect additional irradiations varying laser fluence were performed. In this case, two films with different thicknesses, Si10 (132 nm) and Si20 (278 nm) were irradiated at different fluences, 7 and 12 mJ/cm^2. Figure 5.6 shows the corresponding AFM topographic images. In the case of the thinner film, Si10, irradiation with 7 mJ/cm^2 does not induce any significant morphological change (Figure 5.6a). However, an evident change in roughness can be detected for Si20 at the same irradiation conditions (Figure 5.6d).

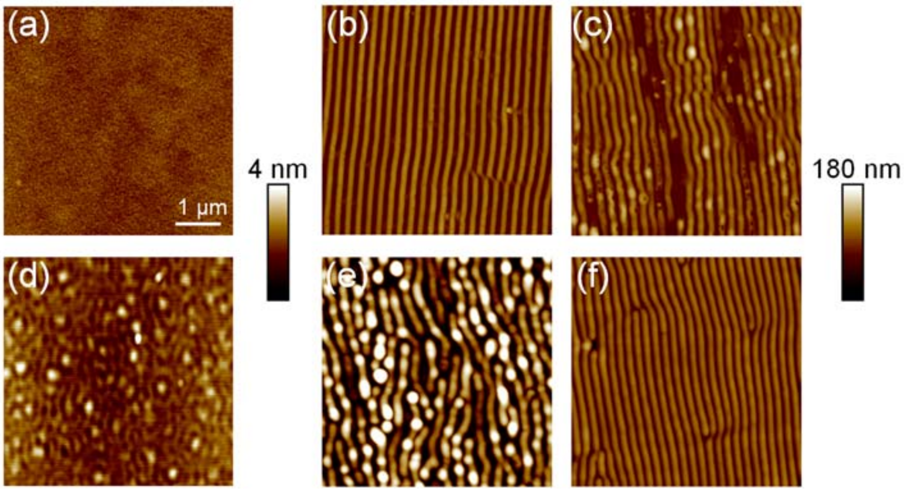

Figure 5.6 Fluence effect on Si10 (upper row) and Si20 (bottom row), irradiated at 266 nm with 4800 pulses and (a, d) 7 mJ/cm^2, (b, e) 10 mJ/cm^2 and (c, f) 12 mJ/cm^2.

For a fluence of 12 mJ/cm^2 LIPSS obtained at the thinner film Si10 are conspicuously disrupted (Figure 5.6c) indicating that this fluence is above the optimal fluence range at which LIPSS are optimally formed (Figure 5.6b). It is known that dealing with LIPSS in polymers when the fluence is above certain limit, the whole polymer film is thermally affected and devitrification of the complete film can take place leading to dewetting and/or material ablation [15]. In the case of Si20, the irradiation at 12 mJ/cm^2 leads to the increase of the superficial temperature and to the heating of deeper material [1] inducing the formation of more ordered ripples (Figure 5.6f) in comparison to the irradiation at 10 mJ/cm^2 (Figure 5.6e).

In order to explain the singular behavior of the PS films with intermediate thicknesses in the range 200-400 nm, for which droplet-like entities are observed upon irradiation with 4800 pulses at 10 mJ/cm^2 (Figure 5.4d) we can consider different facts. On the one hand, the heat dissipation by the substrate of the heat generated by surface irradiation is less efficient than for the thinner Si10 film, but still it plays a role since, as shown in Figure 5.5, a higher amount of pulses is needed in order to modify the polymer surface in comparison to thicker films. On the other hand, we can consider the optical properties of the silicon, in particular the refractive index at 266 nm, which for silicon is higher than for PS. When the laser light reaches the substrate, in the case of silicon, the reflection from the substrate may introduce additional thermal effects and thus, less ordered LIPSS are expected. In fact in the case of Si20 the higher values of period and height (Figure 5.4) suggest that the heat remains longer. Thus, a softer material exists for longer time with lower superficial viscosity allowing the development of ripples with larger periods. Additionally, the height of the nanostructures in this sample is also higher, suggesting that more material is heated upon irradiation and this fact cannot be explained considering only heating by absorption of the laser light discussed in the previous paragraph. As shown in Figure 5.3 while for a depth of 50 nm, which results to be the typical height of the LIPSS obtained for most of the PS samples studied in this work, the temperature is slightly lower but similar than the one at the surface, for a depth of 280 nm the temperature increase is smaller than 3 ºC.

In order to go deeper into the role of the substrate in LIPSS formation, experiments with different substrates will be discussed in the next section.

5.3.3 Effect of substrate on LIPSS formation

To evaluate the role of the substrate on LIPSS formation in PS, thin films of the polymer were prepared onto silicon, glass and quartz. These three substrates were selected on the basis of their different thermal and optical properties. Again, LIPSS were prepared by irradiation with 4800 pulses at a fluence of 10 mJ/cm^2 of spin-coated PS films from solutions with two different concentrations, 10 g/L and 20 g/L. The topography images of the nanostructured samples onto different substrates and two different thicknesses are presented in Figure 5.7.

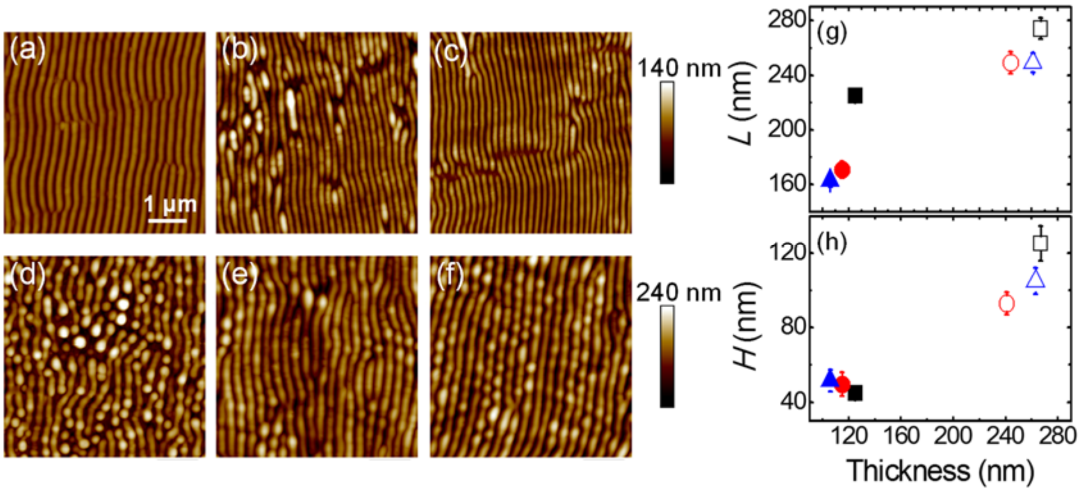

Figure 5.7 (Left) AFM height images (5 μm × 5 μm) of PS with 10 g/L (upper) and PS 20 g/L (bottom) deposited on different substrates: (a, d) Silicon (Si10, Si20), (b, e) Glass (G10, G20) and (c, f) quartz (Q10, Q20). (Right) (g) Period length (*L*) and (h) height (*H*) of formed ripples for PS with 10 g/L (filled symbols) and 20 g/L (open symbols) deposited on different substrates: silicon (■), glass (●) and quartz (▲). Films were irradiated at 266 nm using a fluence of 10 mJ/cm^2 and constant number of pulses of 4800.

Figure 5.7 demonstrates that the formed nanostructures on the polymer surface depend on the underlying substrate. Although linear ripples are formed on the film with thickness around 120 nm for all the substrates, different levels of order can be visualized. While the polymer on silicon, Si10, forms rather continuous and homogeneous ripples (Figure 5.7a), LIPSS induced in the polymer on quartz, Q10 (Figure 5.7c), although well-defined, appear disturbed in several places. In contrast, LIPSS generated on the polymer on glass, G10 (Figure 5.7b), consists of several domains, disrupted or with coalescence between ripples. At a first glance it appears that less-ordered LIPSS form on a thicker PS film of 260 nm in all the three substrates. However, the sample on silicon (Figure 5.7d) presents a significant lower order than the others characterized by distorted lines decorated by drop-like structures. The dependence of the period and ripple height on different substrates is presented in Figure 5.7g and Figure 5.7h. There is a clear influence of the nature of the substrate in the period of the LIPSS especially for thinner PS films. While LIPSS on quartz (Q10) and glass (G10) exhibit similar period values ($L \approx 170$ nm), a larger L is obtained for LIPSS on silicon (Si10) ($L \approx 220$ nm). Although weaker, a similar trend is observed for the thicker films. Substrate seems to have little effect on the ripples height in the case of thin films, but in the case of the thicker ones the height of the LIPSS obtained on glass is smaller than the observed for silicon (Si20) and quartz (Q20).

As mentioned before, when a laser pulse reaches the polymer surface the radiation can be reflected, scattered and/or absorbed. The fraction which is absorbed by the polymer transforms into heat while the rest of the energy, if the film is thin enough, eventually may reach the underlying substrate and be dissipated by it. The amount of energy at a given depth x from the surface can be determined by the Beer-Lambert law (introduced in Chapter 2 Section 2.3.4). For instance, for a 434 nm thick PS sample (PS30), 93 % of the incident energy is transmitted and it will reach the substrate. Thus, the thermal properties of the substrate can be relevant. The differences observed in the morphology of the LIPSS formed on PS films with different thicknesses and deposited onto different substrates may be explained on the basis of the substrate physical properties, in particular to their thermal and optical properties. For a single pulse, the temperature increase at the substrate surface due to the transmitted light through the PS film can be estimated by using the values of the corresponding physical properties listed in Table 5.2 as:

$$\Delta T = \frac{F\alpha}{c\rho} \tag{5- 10}$$

Where F is the fluence, α the absorption coefficient, c the specific heat and ρ the density. The estimated temperature increase has been calculated using the value of the incoming fluence and the values are reported in Table 5.3.

Considering the high amount of energy transmitted through the polymer film and reaching the substrate (as high as 93% even in the thickest supported sample Si30 studied here), the estimated temperature increase has been calculated using the value of incoming fluence and the estimated temperatures obtained are listed in Table 5.3.

Table 5.3 Temperature increase (ΔT), Thermal diffusivity (D), and thermal diffusion time (t_d) of the substrates.

	Silicon	**Quartz**	**Glass**
ΔT (K)	1.2×10^{3}	1.6×10^{-5}	460
D (m^2/s)	9.97×10^{-5}	5.7×10^{-6}	5.15×10^{-7}
t_d (ns)	2.6×10^{-4}	-	0.19

After the fast increase of temperature the heat is dissipated depending on the thermal conductivity of the substrate. The thermal diffusion time, t_d, is given by [1,16]:

$$t_d = \frac{1}{D\alpha^2} \tag{5- 11}$$

Where D is thermal diffusivity of the material expressed by $D = \frac{\kappa}{c\rho}$. The calculated parameters are listed in Table 5.3.

Although for silicon the temperature increase is higher than for glass, the thermal diffusivity is two orders of magnitude larger, and thus, the thermal diffusion time is shorter. In the case of quartz, it can be considered that temperature does not increase upon irradiation since the absorption at 266 nm is negligible. Accordingly, the mismatch in thermal conductivities between the polymer, PS, and the substrate in the case of glass and quartz, is smaller than when the substrate is silicon. This could explain the similar results obtained for irradiation of the different film thicknesses on glass and quartz. Additionally, only thermal effects need to be considered for these two substrates since their refractive index is roughly the same than the one of PS. Therefore, the reflection effects at the polymer-substrate interface are less important than in the case of the silicon substrate.

5.4 Study of LIPSS formed on P3HT films

After assessing the different factors which may have an effect on the formation of LIPSS patterns of good quality in thin films of a model polymer [17], in this section we will apply the obtained knowledge to the case of a functional polymer: P3HT. For that, P3HT films of different thicknesses were prepared. Figure 5.8 shows the thickness and roughness dependence of the spin-coated (SC) P3HT films with the solution concentration. A nearly linear relationship between the P3HT film thickness and its solution concentration can be observed. The upper row in Figure 5.8 exhibits AFM topography images of SC P3HT films of selected solution concentrations covering the full range of film thicknesses investigated.

The as-prepared SC films present a characteristic morphology of semicrystalline P3HT consisting of needle crystals [18]. The roughness of the SC films increases with thickness, levelling off for thicker samples. LIPSS formation in these films depends on thickness as exemplified by the bottom row in Figure 5.8. While, under the same irradiation conditions (26 mJ/cm^2, 3600 pulses), thin films of ≈ 41 ± 15 nm (Figure 5.8e) do not exhibit LIPSS, those with intermediate thicknesses, in the range of ca. 80-280 nm (Figure 5.8f and g) present a regular periodic relief with a period of ca. 430 nm. As described in the previous section, in general, thinner films need more irradiation energy, in terms of either pulses or fluence, in order to reach similar temperature values than those reached by thicker films. Specifically for silicon substrates, the laser irradiation of the polymer film provokes the substrate temperature to increase very fast. However, the heat is effectively dissipated on the basis of the high thermal diffusivity of silicon. Thus, the high thermal conductivity and thermal diffusivity of silicon makes the cooling of the polymer material heated by the laser pulse to be more efficient for thinner films. In the case of thicker films, although they show the presence of LIPSS (Figure 5.8h), these are significantly distorted in comparison with those formed in intermediate thickness films. For these samples, in a first approach, roughness may play a significant role on the quality of LIPSS producing complex light scattering processes on the sample surface leading to non-parallel interferences It is important to mention that in the case of P3HT it is needed to heat the polymer above its T_m, which is around 240 ºC, in order to provide enough polymer dynamics and allow the redistribution of the material.

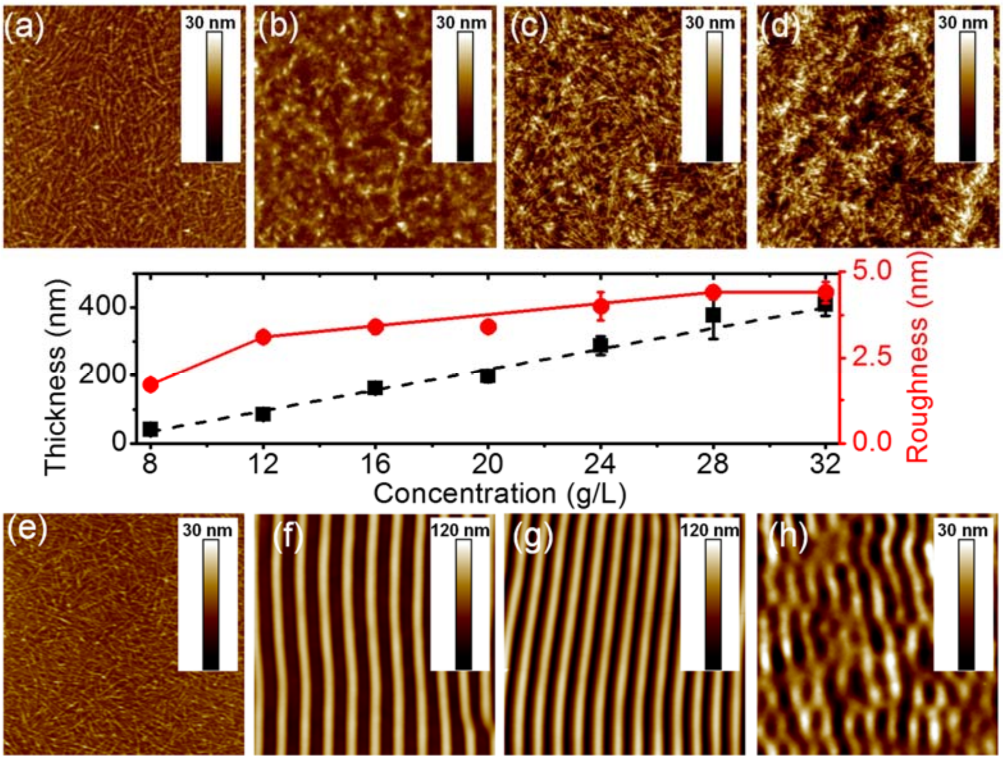

Figure 5.8 Thickness (■) and roughness (●) dependence of the SC P3HT films on the solution concentration (middle row). Selected AFM topography images (5 µm ×5 µm) of SC P3HT (upper row) films before irradiation prepared from (a) 8 (b) 12 (c) 20 and (d) 28 g/L, and after irradiation at a fluence of 26 mJ/cm^2 with 3600 pulses from (e) 8 (f) 12 (g) 20 and (h) 28 g/L.

GISAXS technique can be useful to characterize structural order in LIPSS formed on polymer films as it provides statistical information integrated over a large sample area of the material surface [1,18,19]. Figure 5.9 shows a series of GISAXS patterns of irradiated films as a function of the concentration taken with an incidence angle of α_i =0.2°.

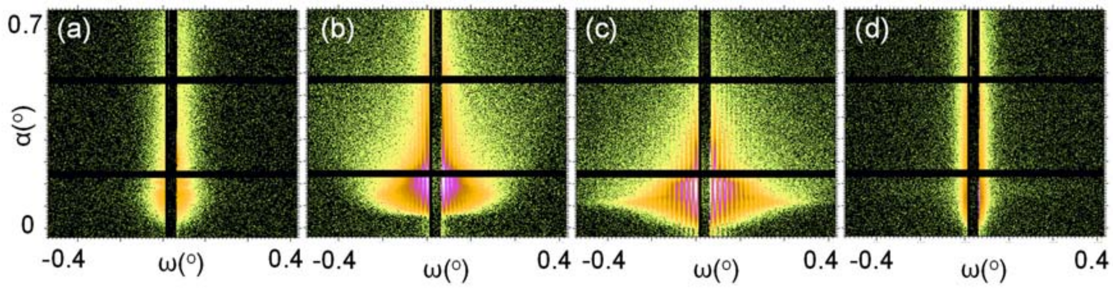

Figure 5.9 GISAXS patterns taken with an incidence angle of $\alpha_i = 0.2^o$ for P3HT LIPSS films prepared from (a) 8, (b) 12, (c) 20 and (d) 28 g/L solutions with LIPSS generated at a fluence of 26 mJ/cm^2 with 3600 pulses. The horizontal black lines are the detector inter-module gaps.

For the thinner (8 g/L, 41 ± 15 nm, Figure 5.9a) and the thicker (≥ 28 g/L, ≥ 370 nm, Figure 5.9d) irradiated P3HT samples the scattering patterns show the characteristic scattering features as those of unstructured spin-coated films [18]. On the contrary, GISAXS patterns of the intermediate films (12-20 g/L, 80-280 nm, Figure 5.9b,c) exhibit vertical diffraction maxima which are characteristic features of a LIPSS and can be described as produced by a quasi-one-dimensional grating [20]. Figure 5.10 shows scattering intensity profiles at $\alpha_i = 0.2^o$ taken at an exit angle $\alpha = 0.15^o$ from the GISAXS patterns. While the intensity profiles for the thinner and thicker irradiated films exhibit no features, those of the intermediate films show vertical diffraction maxima. It is observed that the number of scattering maxima increases with the concentration, i.e. film thickness. The number of scattering maxima, which is associated to the structure factor of the lattice [20], is related to the level of order of the structure [18]. The inset of Figure 5.10 shows the thickness dependence of the number of scattering maxima observed in the GISAXS pattern. It is clear that LIPSS films prepared from solutions with polymer concentration between 16 g/L and 20 g/L are those exhibiting a richer GISAXS pattern in terms of the number of scattering maxima. These results are in agreement with AFM images (Figure 5.8) which reveal that optimal LIPSS, understood as those with a higher order, appear within this polymer solution concentration range.

The semicrystalline nature of P3HT as well as of most poly(alkylthiophene) polymers [21,22], is a key feature of their film morphology and plays a capital role in the performance of a posterior organic solar cell. Therefore, characterization of the effect of LIPSS treatment on the crystallinity of P3HT:PCBM films provides greater insight on polymer film solar cell-relevant features.

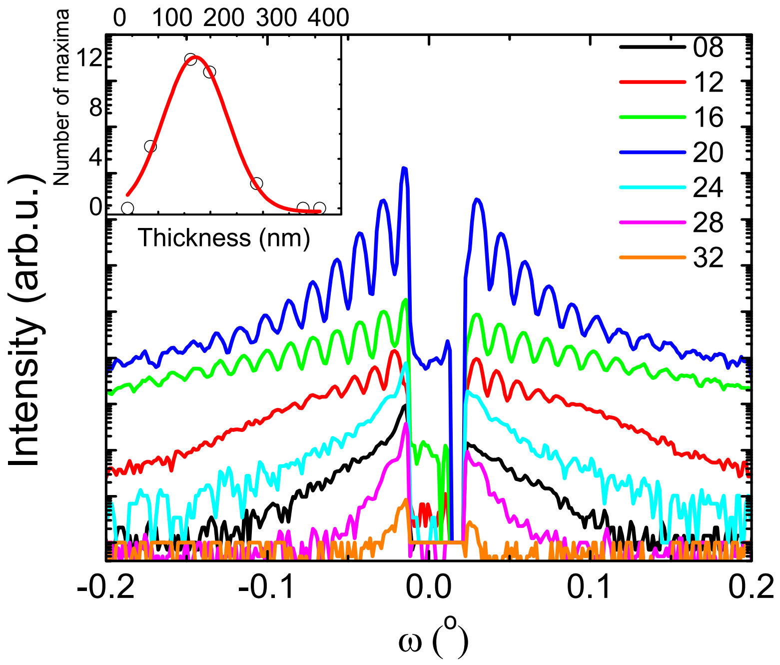

Figure 5.10 Selected horizontal line cuts in logarithmic scale from the 2D GISAXS data taken at an exit angle α = 0.15°, for LIPSS generated at 26 mJ/cm^2 with 3600 pulses on P3HT films prepared from different solution concentrations (g/L) as labeled. Patterns were shifted vertically for the sake of comparison. The inset displays the number of scattering maxima obtained from GISAXS patterns as a function of thickness. The continuous line is a guide for the eye.

Figure 5.11 shows GIWAXS patterns illustrating the evolution of the structure of P3HT SC films before and after generation of LIPSS with solution concentration. It is known that quantitative analysis of GIWAXS patterns requires a thorough knowledge of the scattering pattern in the reciprocal space [23,24]. The real to reciprocal space transformation has been accomplished according to the procedure described in ref [25]. In this case, the intensity of the GIWAXS scattering patterns are represented as a function of the reciprocal scattering vectors q_z and of $q_R = \sqrt{q_x^2 + q_y^2}$ where q_x, q_y and q_z are the scattering vectors.

The SC films exhibit the characteristic three meridional reflections (h00) of the crystalline phase of P3HT which are higher orders of the (100) reflection (Figure 5.11a-d). The equatorial reflection is attributed to the superposition of the (020) and (002) reflections [26,27]. These GIWAXS patterns are in agreement with previous studies reporting a crystal distribution of P3HT sheets formed by the π–π stacking of the thiophene rings on a mainly edge-on configuration, with polymer backbone chains parallel to the substrate [27]. P3HT films with LIPSS exhibit similar reflections as observed in Figure 5.11e-h. In addition, by visualizing the reciprocal space patterns for the different samples a significant crystal orientation is suggested. The interlayer distance between 2D sheets of conjugated polythiophene backbones separated by planes of alkyl side chains has been calculated in 1.58 ± 0.02 nm and 1.60 ± 0.03 nm for unstructured and LIPSS films respectively, and the the π–π stacking distance between polythiophene backbones is 0.38 ± 0.02 nm in both cases. These results are in agreement with previous reports [26,27].

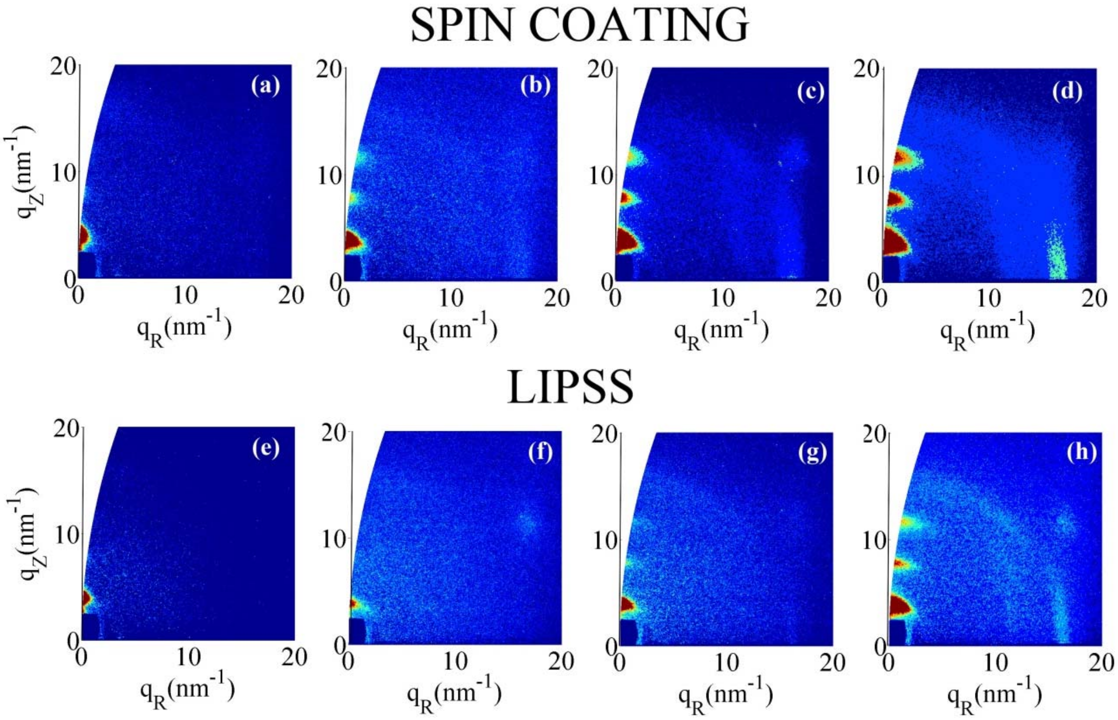

Figure 5.11 Upper row: GIWAXS patterns in reciprocal space taken with an incidence angle α_i =0.2° for the SC P3HT films prepared from different solution concentrations: (a) 8 (b) 12 (c) 20 and (d) 28 g/L and bottom row: corresponding irradiated P3HT films (26 mJ/cm^2, 3600 pulses) prepared from different solution concentrations: (e) 8 (f) 12 (g) 20 and (h) 28 g/L Intensity scale is logarithmic.

Qualitative information about the crystallinity can be obtained by the radial integration of the GIWAXS pattern in the meridian direction shown in Figure 5.12. For the sake of comparison, the data have been normalized to the intensity of the main maximum.

From Figure 5.12, we can find that the crystalline structure is similar for non-nanostructured P3HT and for P3HT with LIPSS films. If one considers the intensity ratio among the consecutive maxima, then it is possible to infer that the crystallinity of the spin-coated films tends to be reduced as the thickness of the film decreases. Crystallization under the confined environment imposed by a thin film has been reported to have a negative impact on the crystallinity of the polymer film [28-30]. Although films with LIPSS exhibit crystallinity it is clear that the irradiation reduces the crystalline phase as deduced from the decrease of the ratio between the intensity of the main maximum in relation to the consecutive orders. This effect is consistent with previous resonance Raman spectroscopy observations indicating that the amount of non-ordered phase in P3HT films with LIPSS increases upon irradiation [30]. Heating due to the laser irradiation occurs in the nanosecond range as explained before while the subsequent cooling down after the pulse action takes place in a microsecond/millisecond range. This fast quenching precludes the recovery of the initial crystallinity of the spin-coated film.

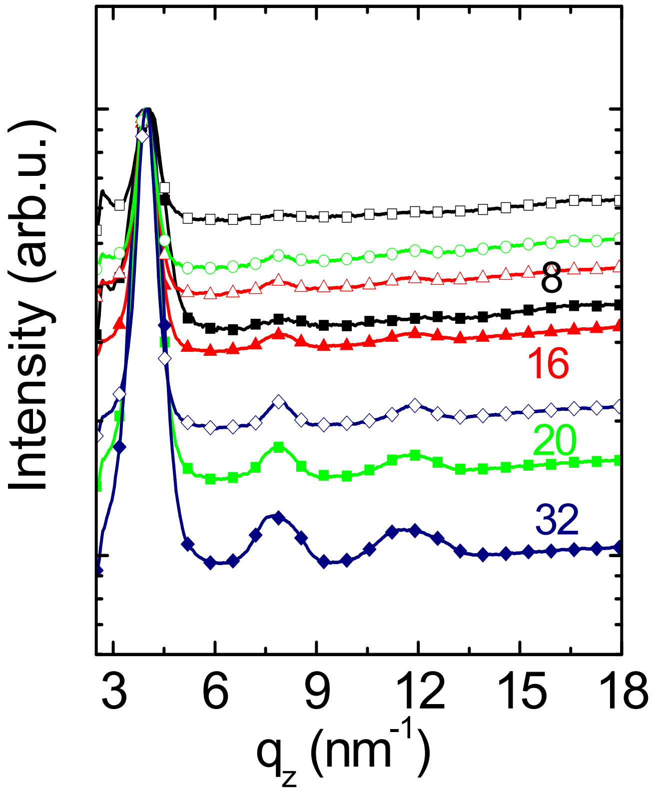

Figure 5.12 GIWAXS (α_i =0.2°) intensity profiles, normalized to the main maximum, across the meridian direction for the SC P3HT films (solid symbols) and for the laser irradiated films (open symbols) prepared from different solution concentrations: (■) 8, (▲) 12, (●) 20 and (♦) 28 g/L.

All the results presented so far refer to films with LIPSS prepared at a single fluence of 26 mJ/cm^2 and 3600 pulses. LIPSS films have been prepared in a broader range of fluences irradiating with 3600 pulses. Figure 5.13a and Figure 5.13b show in a 3D plot the surfaces defining the heights and the period of the LIPSS obtained from AFM measurements as a function of the fluence for the different thicknesses investigated. For the thinnest film (41 ± 15 nm) no LIPSS are formed (see Figure 5.8e). As one can see, once the LIPSS are formed on P3HT film their period is almost constant around a value of 432 ± 29 nm, while the height of the LIPSS exhibits dependence with both fluence and initial thickness of the spin-coated precursor film. Deeper LIPSS are obtained for films thicknesses between 100 and 250 nm, with values up to 100 nm. This thickness range corresponds to the region of optimal LIPSS formation according to AFM (Figure 5.8) and GISAXS (Figure 5.9). For thicker films the height of the obtained LIPSS decreases down to few nanometers.

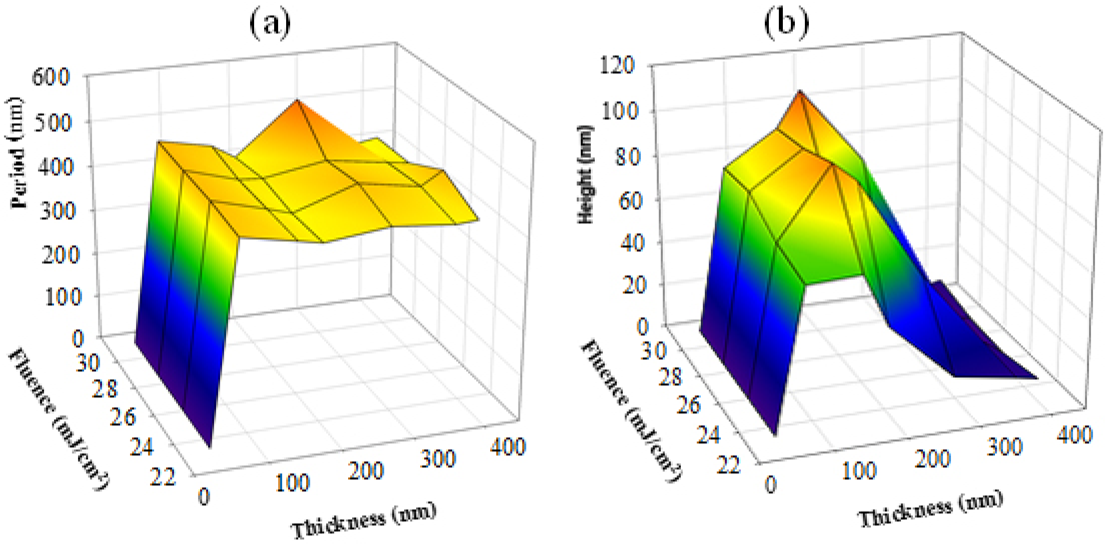

Figure 5.13 3D plots showing the surfaces defining the (a) period and (b) heights of the LIPSS (3600 pulses) as a function of the fluence for the different thicknesses investigated.

5.5 Conclusion

In this chapter LIPSS formation in polystyrene, considered as a model polymer, has been reported upon irradiation at 266 nm since at this wavelength PS absorbs efficiently. In particular the effect of the number of pulses, the film thickness and the supporting substrates properties on the quality of LIPSS have been studied. It has been shown that LIPSS can be obtained with different degrees of order by adjusting the film thickness and the substrate used for supporting the PS films. The thinner (< 200 nm) and thicker (> 400 nm) films can form parallel LIPSS, whereas less-ordered LIPSS with drop-like structure form in the films with intermediate values of thickness (200-400 nm). When the polymer film is irradiated the energy absorbed provokes a temperature increase and in order to induce morphological modification the temperature should be high enough to grant significant polymer chain mobility. In this case, PS must be heated above its glass transition temperature, which is 105 ºC. The estimation of temperature upon irradiation with successive pulses shows that at least 200 pulses are needed. In a first step changes in roughness occur, in what we call incubation regime, and after a larger number of pulse, around 3600, LIPSS are formed.

The supporting substrates can influence the LIPSS formation process. Thus, differences observed in the fluence and number of pulses needed for the onset of morphological modifications is explained considering the differences in thermal conductivity between the polymer and the substrate. The quality of the LIPSS can be also affected by the optical properties of the substrate which determine the energy reflected by it. Similar to the study on PS, LIPSS formation in P3HT spin-coated films has been studied. In this case thin films have been deposited on silicon and have been irradiated at 532 nm as P3HT is a strong absorbing material at this wavelength. LIPSS formation takes place optimally in certain range of thicknesses between 80 and 280 nm and for a fluence range between 22 and 31 mJ/cm^2. The initially smooth surface increases its roughness as a consequence of the heating of polymer film, in this case above the T_m, around 240 ºC. It is important to mention that thick films present larger roughness values which may affect the quality of LIPSS since complex light scattering processes may occur leading to non-parallel interferences.

P3HT LIPSS films prepared in this way has been thought to be used in OPVS devices, although the preparation and characterization of such devices using present technology are still under way [31].

5.6 References

[1] Rebollar, E., Pérez, S., Hernández, J. J., Martín-Fabiani, I., Rueda, D. R., Ezquerra, T. A. and Castillejo, M. Assessment and Formation Mechanism of Laser-Induced Periodic Surface Structures on Polymer Spin-Coated Films in Real and Reciprocal Space. *Langmuir* **27**, 5596-5606 (2011).

[2] Li, M., Lu, Q. H., Yin, J., Qian, Y. and Wang, Z. G. Effects of Post-thermal Treatment on Preparation of Surface Microstructures Induced by Polarized Laser on Polyimide Film. *Materials Chemistry and Physics* **77**, 895-898 (2003).

[3] Csete, M. and Bor, Z. Laser-induced Periodic Surface Structure Formation on Polyethylene-terephthalate. *Applied Surface Science* **133**, 5-16 (1998).

[4] Mate, C. M., Toney, M. F. and Leach, K. A. Roughness of Thin Perfluoropolyether Lubricant Films: Influence on Disk Drive Technology. *IEEE Transactions on Magnetics* **37**, 1821-1823 (2001).

[5] Green, M. A. Self-consistent Optical Parameters of Intrinsic Silicon at 300 K Including Temperature Coefficients. *Solar Energy Materials and Solar Cells* **92**, 1305-1310 (2008).

[6] Lasagni, F. A. and Lasagni, A. F. *Fabrication and Characterization in the Micro-nano Range: New Trends for Two and Three Dimensional Structures*. Vol. 10 (Springer Berlin Heidelberg, 2011).

[7] Beder, E. C., Bass, C. D. and Shackleford, W. L. Transmissivity and Absorption of Fused Quartz Between 0.22 μ and 3.5 μ from Room Temperature to 1500°C. *Applied Optics* **10**, 2263-2268 (1971).

[8] Mark, J. E. *Physical Properties of Polymers Handbook*. (Springer, New York, 2007).

[9] Crystran Ltd, P., UK,. *Quartz Crystal (SiO2)*, <http://www.crystran.co.uk/optical-materials/quartz-crystal-sio2> (2016).

[10] De Nicola, S., Carbonara, G., Finizio, A. and Pierattini, G. Measurement of the Temperature Dependence of Quartz Refractive Indices. *Applied Physics B* **58**, 133-135 (1994).

[11] Li, H. H. Refractive Index of Silicon and Germanium and its Wavelength and Temperature Derivatives. *Journal of Physical and Chemical Reference Data* **9**, 561-658 (1980).

[12] Malitson, I. H. Interspecimen Comparison of the Refractive Index of Fused Silica. *Journal of the Optical Society of America* **55**, 1205-1209 (1965).

[13] Palik, E. D. *Handbook of Optical Constants of Solids*. Vol. 3 (Academic press, US, 1998).

[14] Fardel, R., Nagel, M., Lippert, T., Nüesch, F., Wokaun, A. and Luk'yanchuk, B. S. Influence of Thermal Diffusion on the Laser Ablation of Thin Polymer Films. *Applied Physics A* **90**, 661-667 (2008).

[15] Rebollar, E., Castillejo, M. and Ezquerra, T. A. Laser Induced Periodic Surface Structures on Polymer Films: From Fundamentals to Applications. *European Polymer Journal* **73**, 162-174 (2015).

[16] Vogel, A. and Venugopalan, V. Mechanisms of Pulsed Laser Ablation of Biological Tissues. *Chemical Reviews* **103**, 577-644 (2003).

[17] Cui, J., Nogales, A., Ezquerra, T. A. and Rebollar, E. Influence of substrate and film thickness on polymer LIPSS formation. *Applied Surface Science*, In press (2016).

[18] Rebollar, E., Rueda, D. R., Martín-Fabiani, I., Rodríguez-Rodríguez, Á., García-Gutiérrez, M.-C., Portale, G., Castillejo, M. and Ezquerra, T. A. In Situ Monitoring of Laser-induced Periodic Surface Structures Formation on Polymer Films by Grazing Incidence Small-Angle X-ray Scattering. *Langmuir* **31**, 3973-3981 (2015).

[19] Martín-Fabiani, I., Rebollar, E., Pérez, S., Rueda, D. R., García-Gutiérrez, M. C., Szymczyk, A., Roslaniec, Z., Castillejo, M. and Ezquerra, T. A. Laser-induced Periodic Surface Structures Nanofabricated on Poly(trimethylene terephthalate) Spin-coated Films. *Langmuir* **28**, 7938-7945 (2012).

[20] Rueda, D. R., Martin-Fabiani, I., Soccio, M., Alayo, N., Perez-Murano, F., Rebollar, E., Garcia-Gutierrez, M. C., Castillejo, M. and Ezquerra, T. A. Grazing-incidence Small-angle X-ray Scattering of Soft and Hard Nanofabricated Gratings. *Journal of Applied Crystallography* **45**, 1038-1045 (2012).

[21] Bolognesi, A., Porzio, W., Provasoli, F. and Ezquerra, T. The Thermal Behaviour of Low-molecular-weight Poly(3-decylthiophene). *Die Makromolekulare Chemie* **194**, 817-827 (1993).

[22] Bolognesi, A., Porzio, W., Zhuo, G. and Ezquerra, T. The Thermal Behaviour of Poly(3-octylthienylene) Synthesized by an Ni-Based Catalyst: DSC, Optical Microscopy and XRD Analyses. *European Polymer Journal* **32**, 1097-1103 (1996).

[23] Baker, J. L., Jimison, L. H., Mannsfeld, S., Volkman, S., Yin, S., Subramanian, V., Salleo, A., Alivisatos, A. P. and Toney, M. F. Quantification of Thin Film Crystallographic Orientation Using X-ray Diffraction with an Area Detector. *Langmuir* **26**, 9146-9151 (2010).

[24] DeLongchamp, D. M., Kline, R. J. and Herzing, A. Nanoscale Structure Measurements for Polymer-fullerene Photovoltaics. *Energy & Environmental Science* **5**, 5980-5993 (2012).

[25] Jiang, Z. GIXSGUI: a MATLAB Toolbox for Grazing-incidence X-ray Scattering Data Visualization and Reduction, and Indexing of Buried Three-dimensional Periodic Nanostructured Films. *Journal of Applied Crystallography* **48**, 917-926 (2015).

[26] Wu, Z., Petzold, A., Henze, T., Thurn-Albrecht, T., Lohwasser, R. H., Sommer, M. and Thelakkat, M. Temperature and Molecular Weight Dependent Hierarchical Equilibrium Structures in Semiconducting Poly(3-hexylthiophene). *Macromolecules* **43**, 4646-4653 (2010).

[27] Kohn, P., Rong, Z., Scherer, K. H., Sepe, A., Sommer, M., Mueller-Buschbaum, P., Friend, R. H., Steiner, U. and Huettner, S. Crystallization-Induced 10-nm Structure Formation in P3HT/PCBM Blends. *Macromolecules* **46**, 4002-4013 (2013).

[28] Capitán, M. J., Rueda, D. R. and Ezquerra, T. A. Inhibition of the Crystallization in Nanofilms of Poly(3-hydroxybutyrate). *Macromolecules* **37**, 5653-5659 (2004).

[29] Ma, Y., Hu, W. and Reiter, G. Lamellar Crystal Orientations Biased by Crystallization Kinetics in Polymer Thin Films. *Macromolecules* **39**, 5159-5164 (2006).

[30] Rodríguez-Rodríguez, Á., Rebollar, E., Soccio, M., Ezquerra, T. A., Rueda, D. R., Garcia-Ramos, J. V., Castillejo, M. and Garcia-Gutierrez, M.-C. Laser-Induced Periodic Surface Structures on Conjugated Polymers: Poly(3-hexylthiophene). *Macromolecules* **48**, 4024-4031 (2015).

[31] Cui, J., Rodríguez-Rodríguez, Á., Hernández, M., García-Gutiérrez, M.-C., Nogales, A., Castillejo, M., González, D. M., Müller-Buschbaum, P., Ezquerra, T. A. and Rebollar, E. On the Laser Induced Periodic Surface Structures of P3HT and of its Blend with PC71BM. *Submitted to ACS Applied Materials & Interfaces* (2016).

6

On the laser induced surface structures of ferroelectric polymers

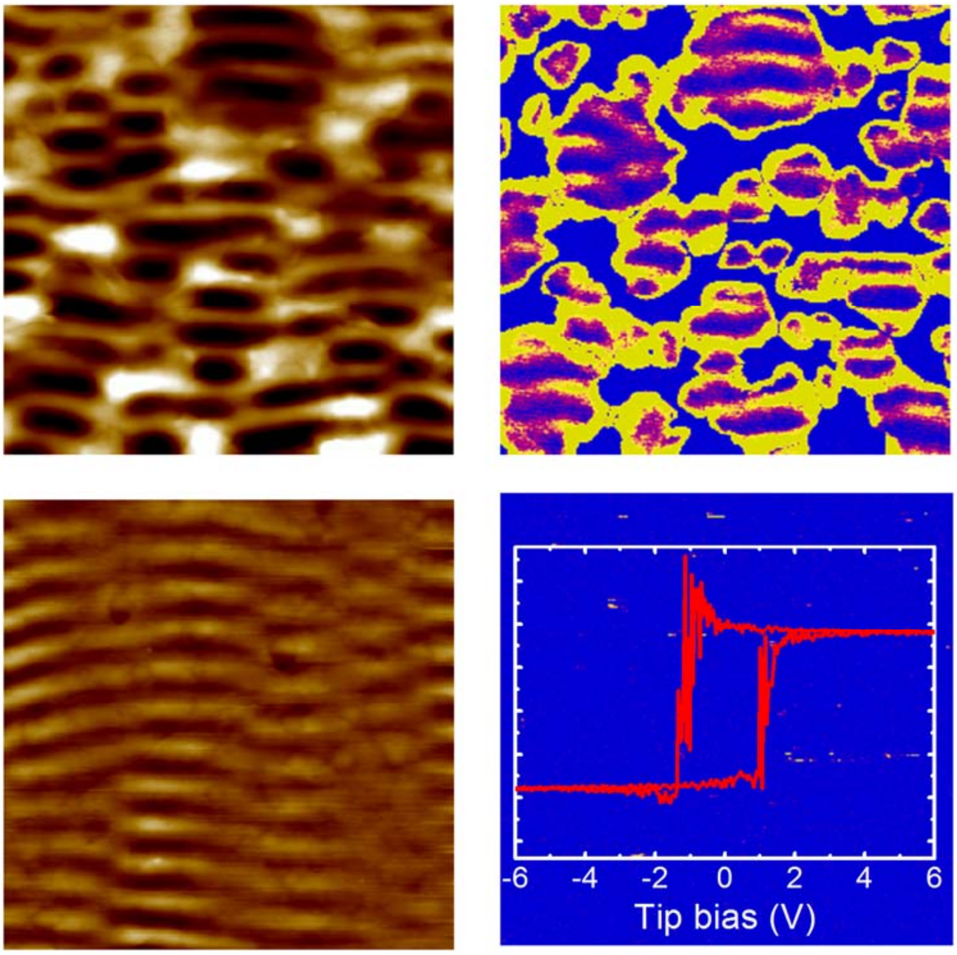

In this chapter, bilayer films were prepared selecting P3HT as bottom and P(VDF-TrFE) as upper layer, respectively, and varying the thicknesses of both layers. LIPSS on a non-absorbing polymer, in this case P(VDF-TrFE), can be fabricated by using nanosecond laser pulses. Samples were irradiated at a wavelength of 532 nm and a laser fluence of 26 mJ/cm^2 with a constant number of pulses of 3600, since the previous chapter has proved that these conditions are the optimal ones for LIPSS formation on P3HT thin films. Different structures, from grating-like to rod-like structures can be obtained by varying the thickness of the upper layer and the bottom layer. Those results indicate that both the bottom layer and the upper layer thickness can influence the nanostructure formation on P(VDF-TrFE). The crystallinity and orientation of both components are studied by GIWAXS and GISAXS, while the ferroelectricity of formed P(VDF-TrFE) nanostructure is characterized by PFM.

6.1 Samples

Preparation of bilayer films has been illustrated in Chapter 2 in Section 2.2.3.2. Bilayers were prepared in a broad range of thickness of the two components, P3HT and P(VDF-TrFE). The labels of the prepared bilayers, together with the concentration of both components are listed in Table 6.1. Regarding P(VDF-TrFE) single layer, due to its weak absorption coefficient, no LIPSS are formed independently of the film thickness and the irradiation conditions. In fact, high fluences and larger number of pulses leads to material ablation without formation of any ordered or periodical structures [1]. Thus, these films have not been irradiated and are shadowed in green in Table 6.1. For a P(VDF-TrFE) concentration of 2 g/L dewetting is clearly observed as shown in Chapter 4, and thus these films have not been irradiated either.

Table 6.1 Labels as a function of the concentration of the two components for the prepared bilayer films. Samples shadowed in green are those non-irradiated.

P3HT (g/L)	**P(VDF-TrFE) (g/L)**						
	0	**2**	**3**	**5**	**7**	**12**	**15**
0	-	0002	0003	0005	0007	0012	0015
8	0800	0802	0803	0805	0807	0812	0815
12	1200	1202	1203	1205	1207	1212	1215
16	1600	1602	1603	1605	1607	1612	1615
20	2000	2002	2003	2005	2007	2012	2015

6.2 Characterization of polymer bilayers

6.2.1 As-prepared polymer bilayers

The topography of the spin-coated bilayer films formed by P3HT and P(VDF-TrFE) was examined by AFM, and the thickness and surface average roughness as a function of the concentration of both P3HT and P(VDF-TrFE) are shown in Figure 6.1. Figure 6.1a shows that for P3HT and P(VDF-TrFE) single layers, a nearly linear relationship between the film thickness and its solution concentration can be observed. For the prepared bilayers, the thickness also increases gradually with the concentration of both components. The thicknesses of the single layers on silicon as a function of solution concentration were presented in Figured 2.5 and 2.6. The roughness of the prepared bilayers (Figure 6.1b) is relatively high when the upper layer is prepared by spin coating of a solution with low P(VDF-TrFE) concentration (2 and 3 g/L) since dewetting takes place as it has been discussed in Chapter 4. Increasing the concentration of the upper layer leads to smoother films, with average roughness ranging from 0.8 to 1.2 nm. These roughness values are comparable to the roughness of a pure P(VDF-TrFE) film.

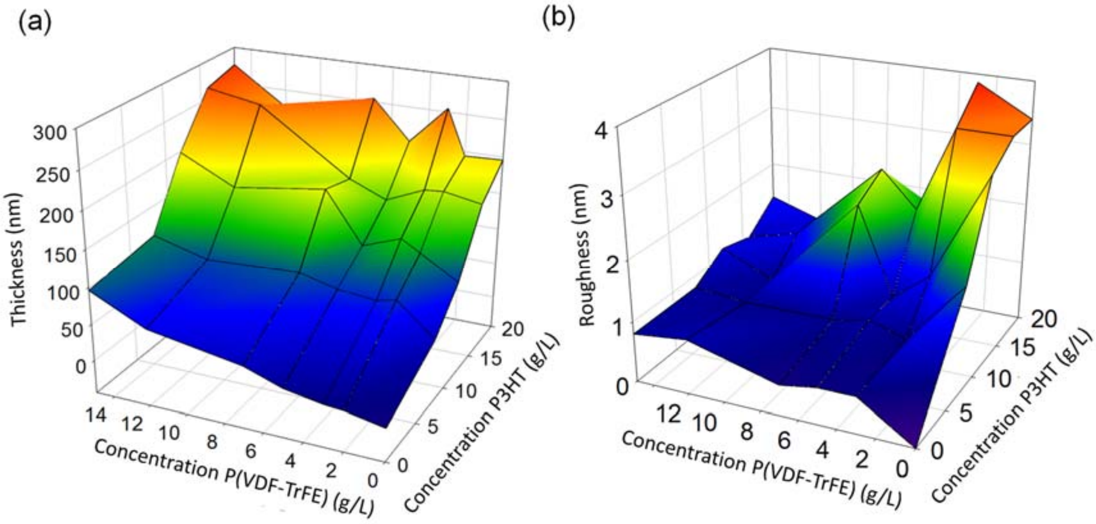

Figure 6.1 3D plot of (a) thickness and (b) R_a of bilayers as a function of the P3HT and P(VDF-TrFE) concentrations.

Figure 6.2 shows as an example 5 µm × 5 µm AFM topography images of the spin-coated bilayer films based on P3HT layers with a constant thickness of 150 nm (16 g/L) and different concentrations of P(VDF-TrFE). For the sake of comparison, P3HT (16 g/L) and P(VDF-TrFE) (3 g/L) are also presented in Figure 6.2a and b. For both single layers, AFM images show a continuous surface without dewetting and agglomerates. The P3HT single film exhibits a roughness of 3.4 ± 0.2 nm, while the P(VDF-TrFE) single film shows a roughness of 0.5 nm. The roughness values of the two single films are related to the presence of crystallites on the surface, since both polymers are semicrystalline.

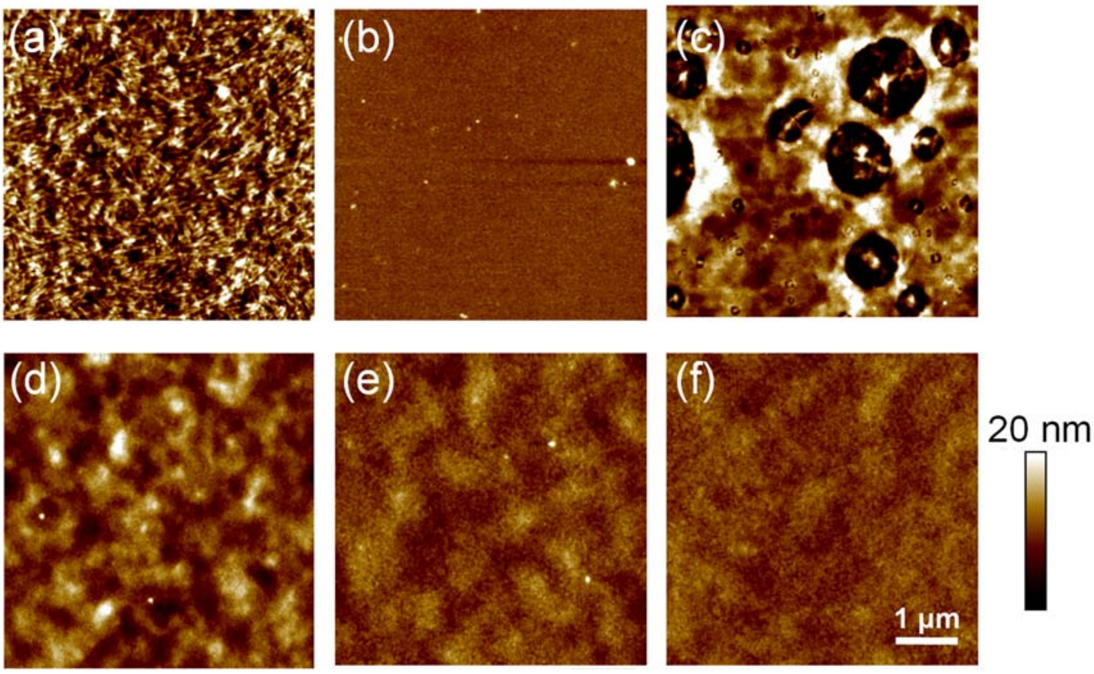

Figure 6.2 AFM topography images (5 µm × 5 µm) of single layers of (a) P3HT 16 g/L, (b) P(VDF-TrFE) 3 g/L, and P3HT /P(VDF-TrFE) spin-coated bilayer films: (c) 1603,(d) 1605, (e) 1612 and (f)1615.

Figure 6.2c–f show AFM topography images of the bilayer films with different thickness of the upper layer from 12 nm (1603) to 95 nm (1615). Dewetting takes place for the sample 1603, (Figure 6.2c) while the increase of P(VDF-TrFE) concentration leads to the formation of continuous upper film. Roughness of the spin-coated film decrease from 3 to 1 nm, comparable with that of P(VDF-TrFE) single film.

6.2.2 Nanostructure formation on bilayer films

LIPSS can only be formed on polymer surfaces by nanosecond laser irradiation when the laser wavelength is within the region in which the polymer has a strong absorption. For this reason, the UV-Vis absorption spectra for P3HT and P(VDF-TrFE) were measured in order to determine the absorption coefficient of both materials. The spectra of P3HT has been previously shown in chapter 5 and in Figure 6.3 is displayed in comparison to the spectra corresponding to P(VDF-TrFE). All data are normalized to the film thicknesses. The results reveal that the P3HT has an absorption coefficient α at 532 nm of 86200 cm^{-1}, while the α for P(VDF-TrFE) at that wavelength is much smaller, in particular 461 cm^{-1}.

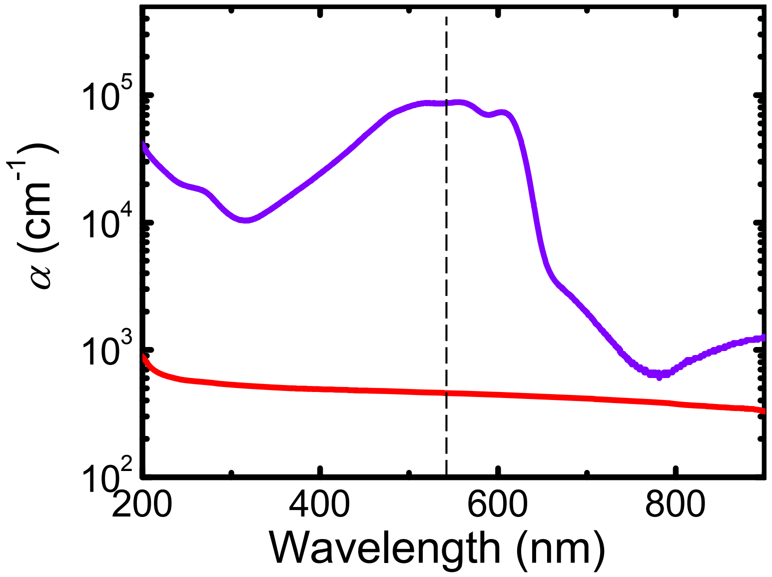

Figure 6.3 UV-Vis-NIR absorption spectra for P3HT (purple) and P(VDF-TrFE) (red). Spectra have been normalized to the sample thickness. The vertical dashed line in the figure corresponds to the wavelengths 532 nm.

In Chapter 5 it was shown that in P3HT single layer films irradiated with a laser at the wavelength of 532 nm with 3600 pulses, and a fluence of 26 mJ/cm^2, parallel well-ordered LIPSS can be obtained within a thickness range from 80 to 280 nm (concentration 12 to 20 g/L) [2]. In particular, a film thickness larger than 50 nm is needed to induce the formation of periodic structures while LIPSS start to distort when the thickness is larger than 280 nm. Bilayers with P3HT concentrations in the range 8-20 g/L and P(VDF-TrFE) concentration in the range 3-15 g/L were irradiated at the same conditions that have been shown to be optimal for LIPSS formation in P3HT single layers, i.e. 26 mJ/cm^2 and 3600 pulses. Figure 6.4 shows AFM topography images of the bilayers based on P3HT 16 g/L and different thickness of the upper layer from 12 to 96 nm. P3HT single layer film irradiated under the same condition is also presented in Figure 6.4a for comparison.

From the Figure 6.4 it is clear that the thickness of the upper layer influences the structures formed upon irradiation and the effect becomes especially important for thicker upper layers. When the P(VDF-TrFE) layer is thin and with slight dewetting, as is the case of the sample 1603 (Figure 6.4b), laser irradiation induces LIPSS formation on P3HT layer and favours additional dewetting of the upper ferroelectric layer. For the samples 1605 and 1607 (Figure 6.4c and d) LIPSS are clearly formed with a period around 425 nm, similar to the one observed for the P3HT single layers. For a further increase of the upper layer thickness (samples 1612 and 1615, Figure 6.4e and f), in the range from 60 to 90 nm, the LIPSS start to distort and the patterns change from parallel ripples to an isotropic distribution of short rod-like structures with no preferential orientation.

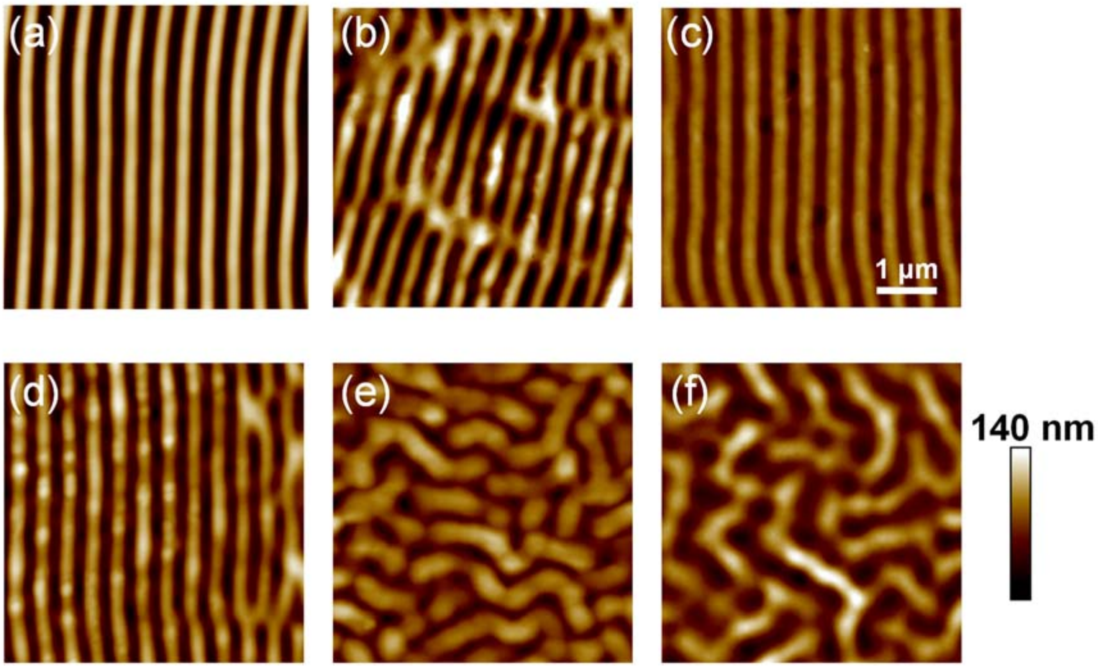

Figure 6.4 AFM topography images (5 μm×5 μm) of films irradiated at 532 nm with a fluence of 26 mJ/cm^2 and 3600 pulses: (a) P3HT single layer film (16 g/L) and P3HT/P(VDF-TrFE) bilayer films: (b) 1603,(c) 1605, (d) 1607, (e) 1612 and (f) 1615.

Ripple periods and heights for bilayer films with various thicknesses are plotted in Figure 6.5. LIPSS for P3HT single layer film with different thickness irradiated under the same condition are also plotted for comparison. For those bilayer films in which LIPSS are formed, the period and height values are similar to those observed for the P3HT single layers. However, for P(VDF-TrFE) concentration above 7 g/L, corresponding to a thickness of 40 nm, no LIPSS are obtained and the height of formed rod-like nanostructure decreases in comparison to the height of LIPSS.

To rule out the possibility of discontinuity of the ferroelectric upper layer C-AFM measurements were performed. Figure 6.6 shows the height and corresponding C-AFM current image for the nanostructured bilayer 1603, by applying a constant voltage of -5 V.

In the case of the bilayer film 1603, in which the upper P(VDF-TrFE) layer is not continuous (see Figure 6.2), also a conductivity contrast can be observed. It seems that there is a non-continuous upper layer which is non-conducting and can be assigned to P(VDF-TrFE) while in the bottom layer there are regions with different conductivity. Those regions that exhibit higher conductivity correspond to the valleys of the LIPSS and those showing lower conductivity correspond to the ridges, similar to previously reported results [3]. The difference in conductivity in LIPSS can be explained considering the crystallinity decrease in P3HT when is melted upon laser irradiation. This provokes that ridges have a lower molecular order than that of the valleys [3].

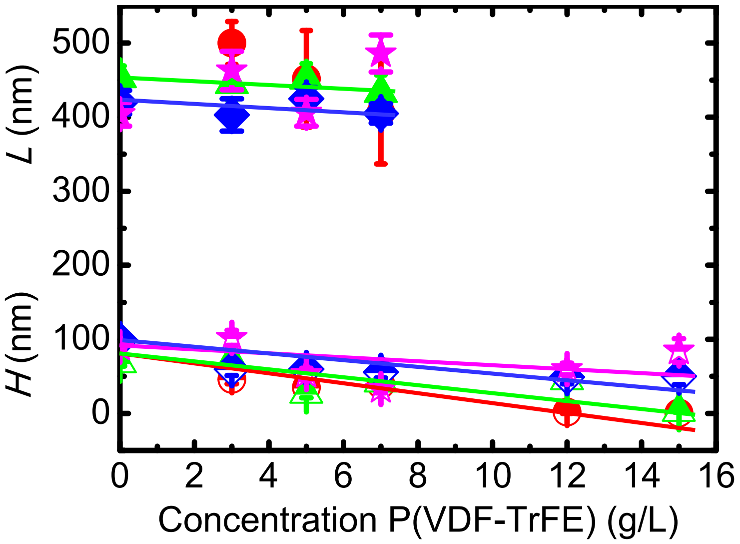

Figure 6.5 Variation of period L (filled symbols) and height H (half filled symbos) of LIPSS as a function of thickness of P3HT layer: (●) 8 g/L, (▲) 12 g/L, (◆) 16 g/L and (★) 20 g/L. Lines are shown as visual guides. Values corresponding to LIPSS formed on P3HT single layers with different thicknesses irradiated under the same condition are also plotted (P(VDF-TrFE) concentration 0 g/L) for comparison.

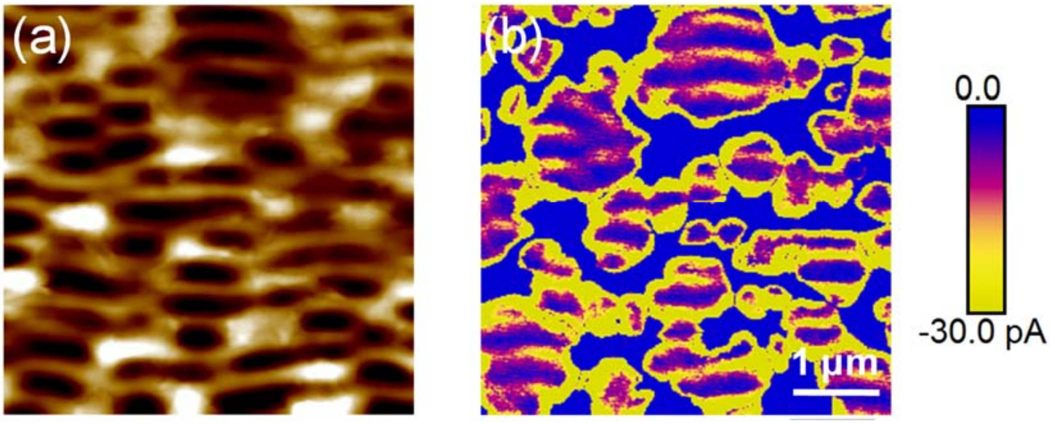

Figure 6.6 C-AFM measurement of the P3HT/P(VDF-TrFE) bilayer 1603, irradiated at 532nm, 26 mJ m^{-2} and 3600 pulses, measured at a constant bias of -5 V. (a) height and (b) current maps.

In Figure 6.7, corresponding to the bilayer 1605, it can be observed that the sample is not conducting, confirming that the upper layer must be the P(VDF-TrFE) film, homogeneously covering the P3HT layer.

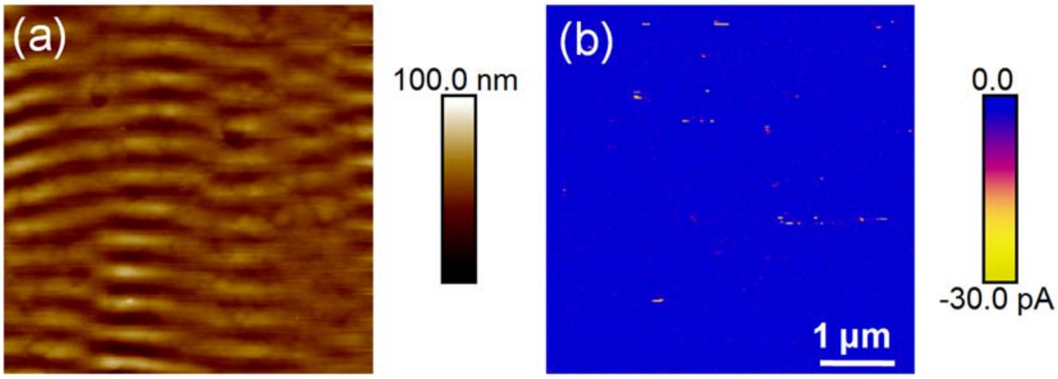

Figure 6.7 C-AFM measurement of the P3HT/P(VDF-TrFE) bilayer 1605, irradiated at 532 nm, 26 mJ m^{-2} and 3600 pulses, measured at a constant bias of -5 V. (a) height and (b) current maps.

6.2.3 Structural characterization of LIPSS by GISAXS

GISAXS experiments have been performed on nanostructured bilayer films, since they can provide statistical information over a large sample area on the structural order of LIPSS formed in polymers [4-6]. The GISAXS measurements were performed with incidence angle α_i range from 0.14 to 0.4° for all samples. Figure 6.8 displays characteristic GISAXS patterns of selected bilayer films, with P3HT 16 g/L as bottom layer and different thickness of P(VDF-TrFE) as upper layer. The number of scattering maxima out of the meridian (i.e., for $q_y \neq 0$) is associated to the structure factor of the lattice [7] and reflects the level of order of the structure [6]. For the thinnest upper layer irradiated (sample 1603) and the thicker ones (samples 1612 and 1615), the scattering patterns show similar scattering features as those unstructured spin-coated films (see Chapter 5). In contrast, GISAXS patterns corresponding to the bilayers with intermediate thickness of the upper layer (1605 and 1607) exhibit vertical diffraction maxima, which are characteristic of LIPSS formation [2]. These features can be described as produced by a quasi-one-dimensional grating [7].

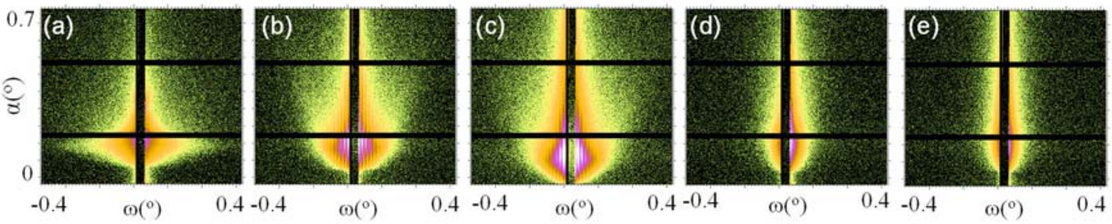

Figure 6.8 GISAXS patterns taken with an incidence angle of α_i=0.2° for P3HT/P(VDF-TrFE) bilayer films irradiated at 26 mJ/cm^2 and 3600 pulses: (a) 1603, (b) 1605, (c) 1607, (d) 1612 and (e) 1615.

Figure 6.9 shows horizontal line cuts from the 2D GISAXS data at $\alpha_i = 0.2^\circ$ taken at an exit angle $\alpha = 0.15^\circ$. The GISAXS intensity profiles show no features for 1603, 1612 and 1615, while those bilayers with intermediate thickness of the upper layer (1605 and 1607) exhibit vertical diffraction maxima. All these results are in agreement with the AFM study (Figure 6.4).

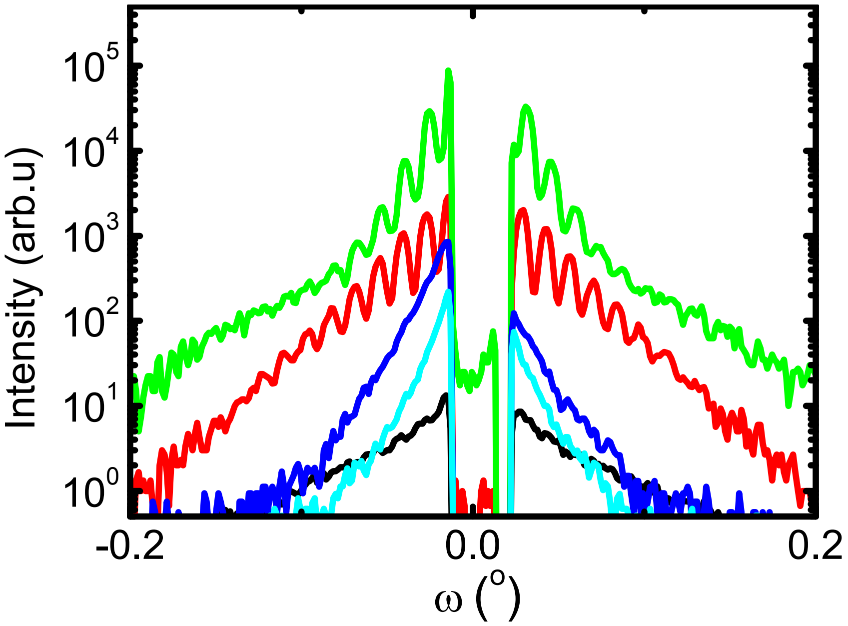

Figure 6.9 Selected horizontal line cuts from the 2D GISAXS data taken at an exit angle $\alpha=0.15^\circ$, in logarithmic scale, for LIPSS generated at 26 mJ/cm^2 and 3600 pulses on P3HT/P(VDF-TrFE) bilayer films prepared from P3HT of 16 g/L as bottom film covered with different solution concentrations of P(VDF-TrFE) layer: 3 g/L (black), 5 g/L (red line), 7 g/L (green), 12 g/L (blue) and 15 g/L (cyan). Patterns were shifted vertically for the sake of comparison.

GISAXS measurements were also performed at different incident angles to probe the structure of the bilayer at different depths. The results for the bilayer 1605 are shown as an example in Figure 6.10. Figure 6.11 shows the scattering intensity profiles at an exit angle $\alpha=0.15^\circ$. Although the intensity decreases as the incident angle increases, the number of maxima remains constant for $\alpha_i = 0.14$, 0.2 and 0.3°, while the low intensity for $\alpha_i = 0.4^\circ$ does not allow to distiguish clearly the scattering maxima. This is due to the fact that when the incident angle is close to the critical angle (for the lowest angles used), the refracted beam is nearly parallel to the film interface, and coupled into waveguide modes, increasing the effective path-length of the beam through the sample, which thereby increases the intensity of the scattering. For higher incident angles well above the critical angle, the beam probes deeper material and the reflected beam becomes weaker, thus the detected intensity decreases. Since the order of patterns is related to the number of GISAXS scattering maxima [6], we can deduce that the order of formed LIPSS are the same from the surface to the bottom layer.

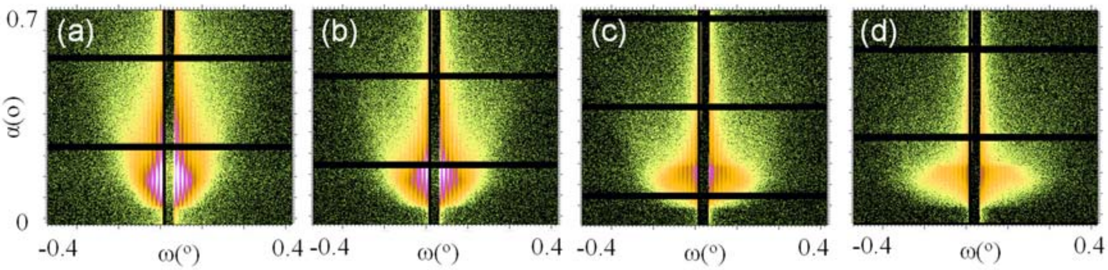

Figure 6.10 GISAXS patterns of P3HT/P(VDF-TrFE) bilayers 1605 nanostructured with LIPSS, measured with different incident angles: (a) $\alpha_i = 0.14^o$, (b) $\alpha_i = 0.2^o$, (c) $\alpha_i = 0.3^o$ and (d) $\alpha_i = 0.4^o$.

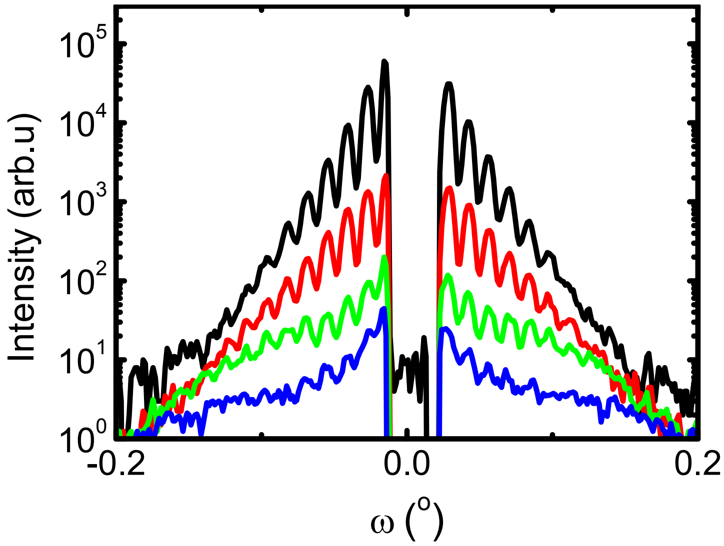

Figure 6.11 Selected horizontal line cuts from the 2D GISAXS data taken at an exit angle α=0.15°, of different incident angles: 0.14° (black),0.2° (red), 0.3° (green) and 0.4° (blue), in logarithmic scale, for LIPSS generated at 26 mJ/cm^2 and 3600 pulses on P3HT/P(VDF-TrFE) bilayer films. Patterns were shifted vertically for the sake of comparison.

6.2.4 Crystalline structure of bilayer films by GIWAXS

GIWAXS study of P3HT single layer films has proved that changes in the crystalline structure take place upon irradiation as shown in Chapter 5. In this chapter we attempt to investigate the changes induced in P(VDF-TrFE) and whether the presence of this upper layer influences the changes occurring at the bottom P3HT one. Thus, crystalline structure of the bilayer films is investigated as a function of the P(VDF-TrFE) film thickness. The 2D X-ray scattering patterns of the as spin-coated bilayers (top) and of the irradiated films (bottom) for various thicknesses of the P(VDF-TrFE) upper layer are presented in Figure 6.12. For the sake of comparison, the 2D patterns of P(VDF-TrFE) and P3HT single layer films are also presented in Figure 6.12.

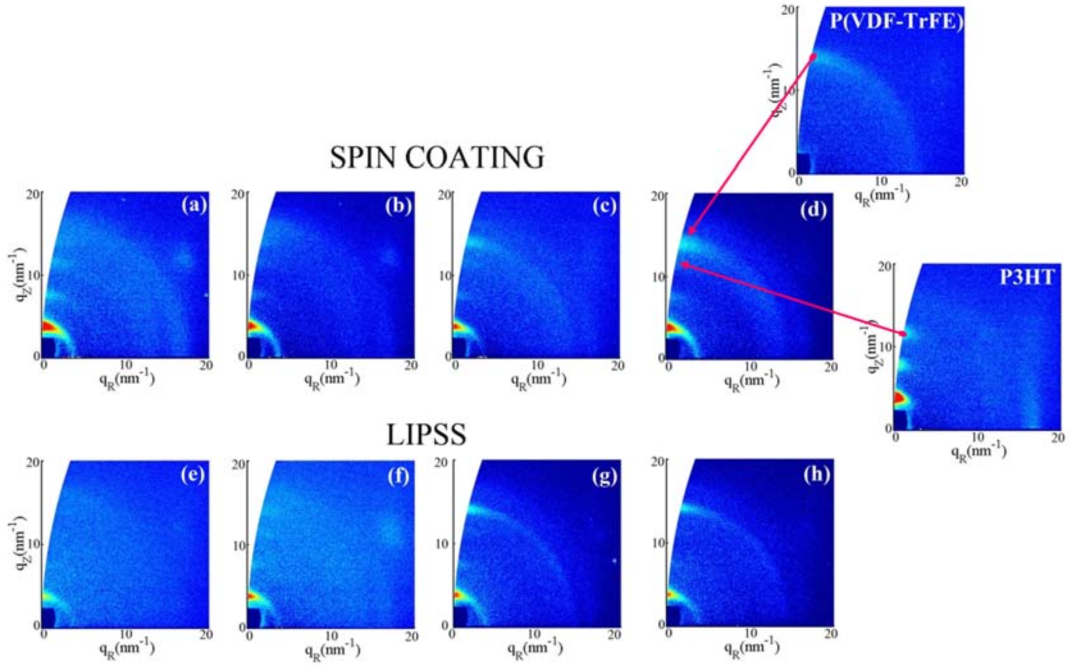

Figure 6.12 GIWAXS patterns taken with an incidence angle α_i =0.2° of the spin-coated (upper row) bilayer films with different thickness of P(VDF-TrFE) layer deposited on the P3HT film: (a) 1603, (b) 1605, (c) 1612 and (d) 1615. Bottom row presents corresponding GIWAXS patterns of the irradiated bilayer (26 mJ/cm^2, 3600 pulses): (e) 1603, (f) 1605, (g) 1612 and (h) 1615 g/L. GIWAXS patterns of single layers of P(VDF-TrFE) 15 g/L and P3HT 16 g/L are displayed in the top right corner for comparison.

As described in Chapter 5, in P3HT single layers the three meridional reflections (h00) are consecutive orders of the (100) reflection with a q-value of 3.8 nm^{-1} [8]. The equatorial weak reflection with a reciprocal scattering vector q-value of 16.39 nm^{-1} is attributed to the superposition of the (020) and (002) reflections [9,10]. In addition, the meridional reflections reveal that the P3HT thin film is uniaxially oriented with mainly an edge-on configuration, which corresponds to the usual conformation adopted by P3HT films consisting of polymer chains parallel to the substrate [46]. A similar orientation is observed for the film nanostructured with LIPSS as previously discussed in Chapter 5.

From the 2D GIWAXS pattern of P(VDF-TrFE) single layer film shown in Figure 6.12, both polymer chain and lamellae orientation of the polymer can be characterized [11]. There is an intense reflection on the meridian with a reciprocal scattering vector of approximately $q = 14.3\ \text{nm}^{-1}$. This reflection arises from either the (110) or (200) plane of an orthorhombic crystal lattice in which the similar lattice spacing of (110) and (200) gives rise to a pseudo-hexagonal diffraction pattern [12,13]. The reflection of P(VDF-TrFE) appearing at the meridian direction suggests that the P(VDF-TrFE) crystals have preferential orientation aligned along the film surface normal with the polymer chains lying on the surface [12].

The characterization of the single layers allows the analysis of the GIWAXS patterns of the P3HT/P(VDF-TrFE) bilayers. For all the spin-coated bilayer films (Figure 6.12 a-d), four semi-ring reflections are observed at the meridian direction. The crystalline reflections of the two components distribute independently, indicating that both polymers do not mix together. Thus, the inner three meridional reflections h00 with q value located at 3.86, 7.42 and 11.26 nm^{-1}, are those consecutive orders of the (100), (200), and (300) reflections of P3HT crystals aligned parallel to the surface normal. That at $q_z = 14.1\ \text{nm}^{-1}$ is attributed to P(VDF-TrFE) and its intensity increases when increasing P(VDF-TrFE) thickness.

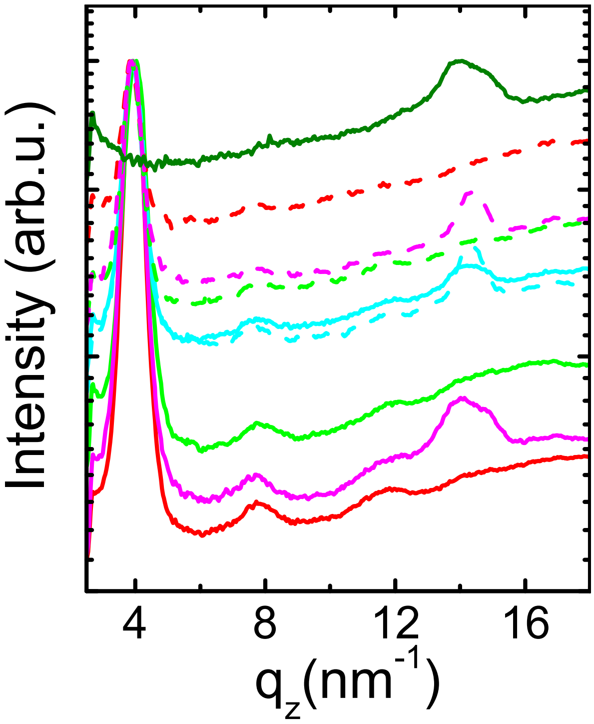

Figure 6.13 GIWAXS ($\alpha_i = 0.2^\circ$) intensity profiles, normalized to the main maximum, across the meridian direction for the spin-coated (continuous lines) and for the irradiated films (26 mJ/cm^2, 3600 pulses, dashed lines) bilayers prepared from different relative thickness: 1603 (red), 1605 (green), 1612 (cyan) and 1615 (magenta). Pattern profile of P(VDF-TrFE) single layers is also displayed (olive) for comparison.

Figure 6.13 presents the GIWAXS intensity profiles across the meridian direction by the radial integration of the 2D GIWAXS patterns as a function of the thickness of the upper layer. For the sake of comparison, the data have been normalized to the intensity of the main maximum. Comparing the GIWAXS patterns and the intensity profiles of the irradiated bilayers with those of the spin-coated bilayers, several interesting changes can be observed. After irradiation, the scattering intensity for P3HT decreases in comparison to that of P(VDF-TrFE), which could be due to the reduced crystallinity of P3HT when LIPSS are formed [3] as previously shown and discussed in Chapter 5. In contrast P(VDF-TrFE) (200/110) reflections become sharper in all irradiated samples, which could be related to an increase of the domain size [14] as a consequence of the heating and cooling cycles taking place upon laser irradiation.

6.3 Mechanism of LIPSS formation in non-absorbing polymer films

Since LIPSS are not formed in the P(VDF-TrFE) single layers upon laser irradiation, the development of periodic nanostructures on the bilayer must be associated with the P3HT bottom layer. As the P(VDF-TrFE) absorbs very weakly at the irradiating laser wavelength of 532 nm, the laser beam passes through the upper polymer layer without significantly altering its energy before reaching the P3HT bottom layer. Then, structuring takes place just as in the P3HT single layers film shown in Chapter 5, heating the polymer above its melting temperature, in case of P3HT around 240 ºC [15,16], in such a way that the polymer segments acquire enough mobility as to rearrange following the modulation imposed by the laser. Afterwards, heat dissipation from the P3HT allows cooling and fixing the nanostructure of the bottom layer while heating the P(VDF-TrFE) on top. This heat transfer is expected to melt the ferroelectric polymer, since temperature is above its T_m, which is 150 ºC [17,18], gaining mobility and accommodating on the pattern of the bottom layer. This is observed for upper layers thinner than 40 nm. However, for thicker upper layers, rod-like structures are formed rather than LIPSS. In principle this could be influenced either by the bottom layer structure or by the agglomeration of P(VDF-TrFE) during the melting and recrystallization process. When P(VDF-TrFE) recrystallizes from melt, the growing crystals and the heterogeneous material distribution on P3HT structure give rise to large domain and more perfect crystals. This has been evidenced in GIWAXS patterns, which show sharper crystal reflections for the irradiated P(VDF-TrFE) samples.

To answer whether the structures observed upon irradiation of thicker upper layers are due to the bottom layer or to the upper one, the laser-irradiated 1605 bilayer was washed with MEK for 30 minutes at 72 ºC, which completely dissolves the upper P(VDF-TrFE) layer. The topography of the washed sample is displayed in Figure 6.14b, and for comparison the irradiated bilayer before being washed is also shown.

Comparing the AFM images of the irradiated bilayer film before and after the selective removal of P(VDF-TrFE), it can be observed that the morphology does not change. This result reveals that the disordered rod-like structures are formed in P3HT layer and again the upper P(VDF-TrFE) accommodates on the pattern of the bottom layer. Further proof of this are the GISAXS patterns obtained at different incidence angles, i.e. different depths analyzed (Figure 6.14c-f), which show no vertical diffraction maxima, indicating that no periodic structures are formed. So, even if also for thick P(VDF-TrFE) upper layers the laser light reaches the P3HT and is efficiently absorbed inducing the heating and melting of the material, a mechanical constraint exists caused by the upper layer, which prevents LIPSS formation. P3HT cannot rearrange freely during the time it is melted and the formation of grating-like structure is not possible.

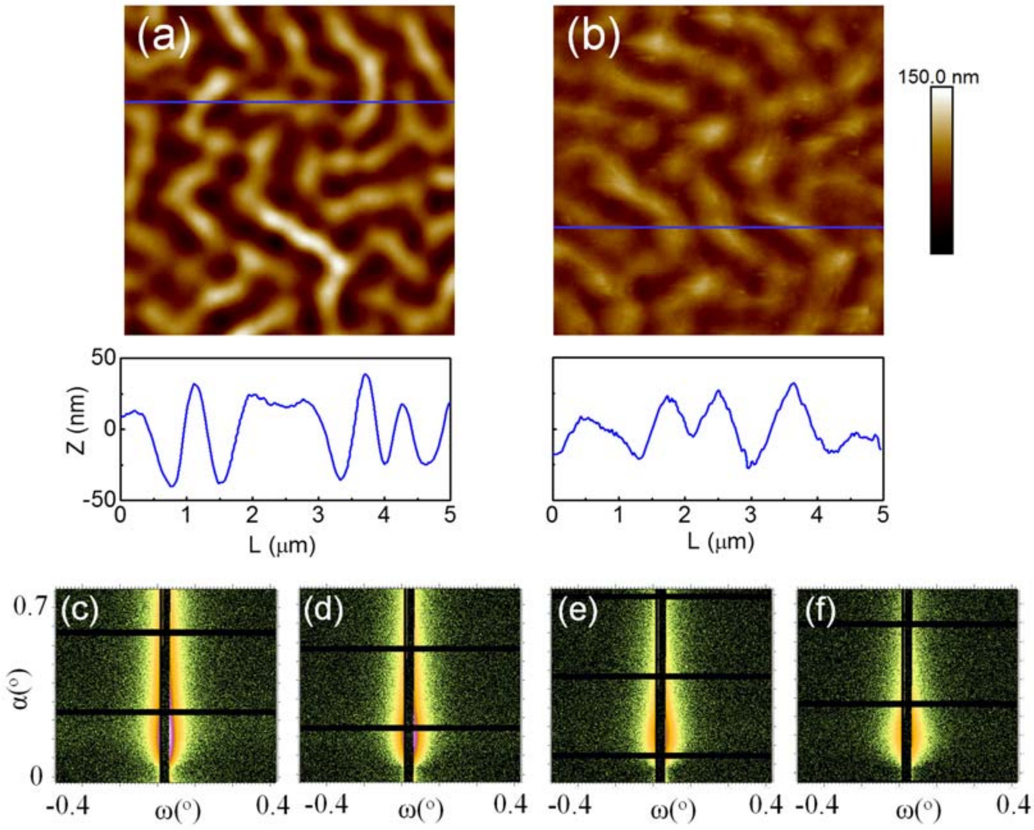

Figure 6.14 AFM images of the P3HT/P(VDF-TrFE) bilayer film 1615 irradiated at 26 mJ/cm^2 with 3600 pulses (a) before and (b) after immersing in MEK for 30 min at 72 ºC. The corresponding height profiles are below the height images. GISAXS pattern of bilayers 1605 LIPSS with different incident angles: (c) α_i=0.14º, (d) α_i=0.2º, (e) α_i=0.3º and (f) α_i=0.4º.

6.4 Ferroelectric response of nanostructured bilayers

Figure 6.15 shows the PFM phase shifts as a function of the applied tip bias for the 1605 bilayer. Both the non-irradiated bilayer film and the nanostructured one exhibit polarization reversibility, i.e., the polarization directions can be switched at both polarities of tip voltage. The coercive field in the case of non-irradiated bilayer films can be estimated to be $E_c = (25 \pm 10)$ MV/m, considering that the thickness of P(VDF-TrFE) layer is 25 ± 5 nm. This value is similar to those found in previous works for continuous films of this ferroelectric polymer [11,19]. Then, nanostructured bilayers also exhibit a ferroelectric response, with a coercive field $E_c = (30 \pm 10)$ MV/m considering the same P(VDF-TrFE) thickness than the initial one. Evidence of ferroelectricity in the nanostructured layer further supports that the top layer follows the topography of the P3HT one.

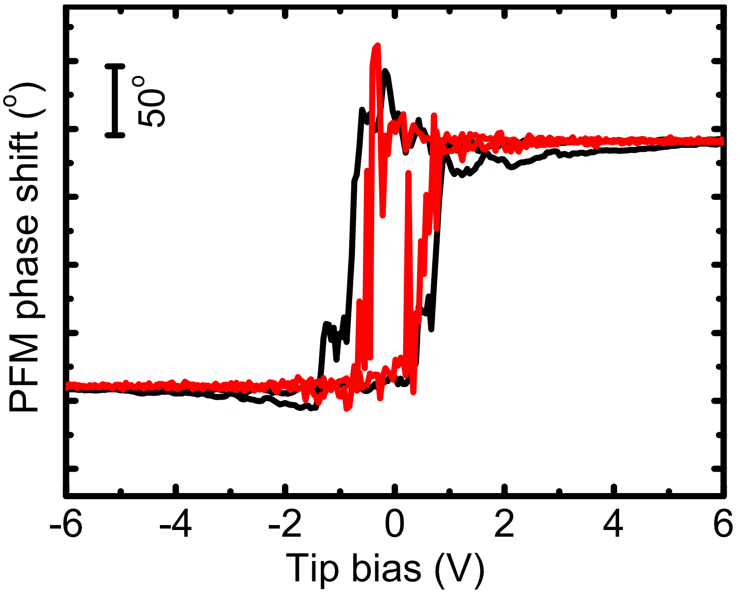

Figure 6.15 PFM phase shift as a function of applied electric voltage for P3HT/P(VDF-TrFE) 1605 bilayer: spin-coated bilayer film (red) and bilayer with LIPSS (black).

Figure 6.16 shows the topography, PFM amplitude and PFM phase images obtained simultaneously for an area of 5 μm ×1 μm of the spin-coated and irradiated bilayers 1605 and 1615. The topographic images of the spin-coated bilayers show smooth surfaces and neither the PFM amplitude nor the phase shift show any contrast along the entire area, which indicates a non-preferential orientation of the polymer dipoles in the as casted films. In the case of the nanostructured bilayers PFM was carried out by scanning the tip in a direction parallel to the LIPSS to minimize the possible damage caused by tip-surface interaction. For the bilayer 1605 there is no preferential ferroelectric response indicating that the laser induced ripples do not align the P(VDF-TrFE) dipole moment in any preferential direction. However, there are some P(VDF-TrFE) droplets on top of the LIPSS in which the ferroelectric amplitude signal seems to have a different value which could be related to different crystallinity inside the droplets. In the case of 1615 there are clear differences both in the PFM amplitude and phase indicating a different crystalline structure which must be related to the different processes occurring upon laser irradiation in this case. As mentioned, for upper layers thicker than 40 nm, the P3HT cannot rearrange freely after being heated by the laser due to a constraint induced by the upper layer, and this can cause an inhomogeneous heating of the P(VDF-TrFE) over it and thus a different crystalline structure.

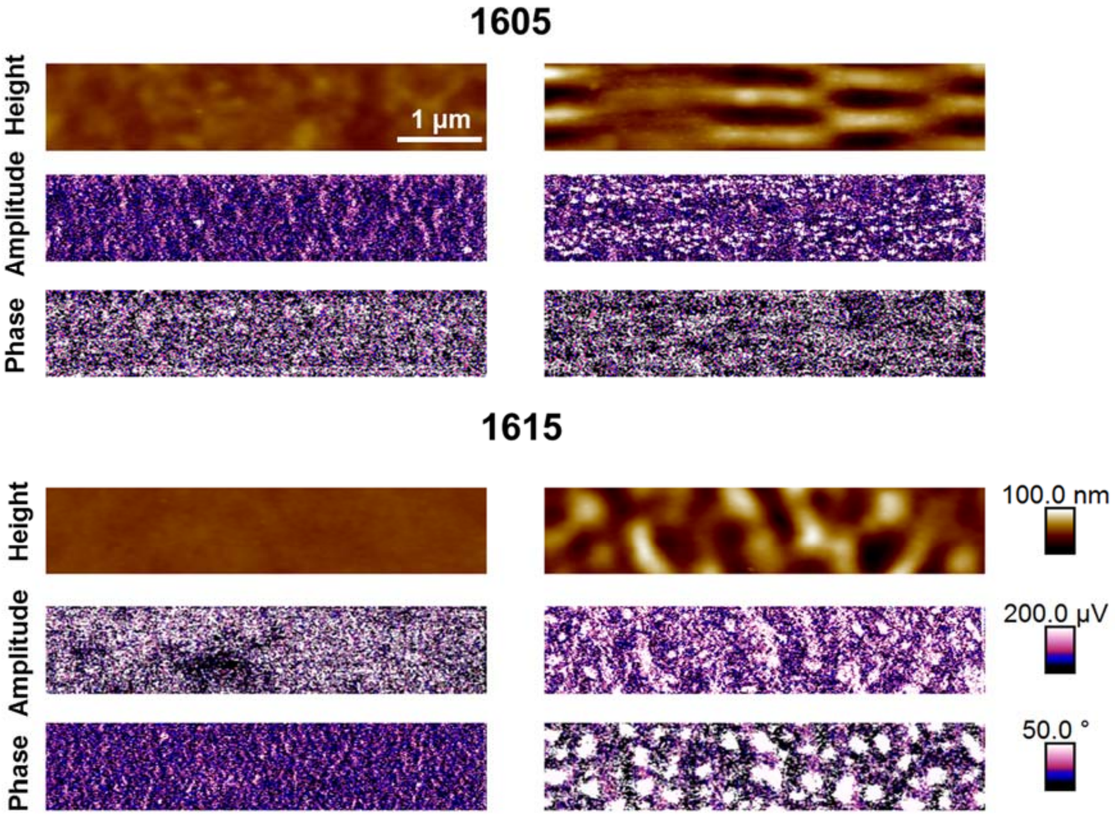

Figure 6.16 Left column: topography, PFM amplitude, and PFM phase shift of the bilayer spin-coated films for (top) 1605 and (bottom) 1615. Right Column: topography PFM amplitude and PFM phase shift of the bilayer LIPSS irradiated at 26 mJ/cm^2 with 3600 pulses for (top) 1605 and (bottom) 1615.

6.5 Ferroelectric information storage on polymer bilayers

PFM has the potential to achieve ultrahigh density and high rate data storage in ferroelectric materials using the tip as a stylus to write the information by applying a bias above the coercive field of the material. Reading is carried out by monitoring the piezoelectric response of the sample, which gives different contrast between written and unwritten zones. The right panel of Figure 6.17 shows the topographic and ferroelectric state of the nanostructured bilayer 1605 after poling at three different points with 12 V during 100 s. The corresponding images before poling are also shown for comparison. Assuming that the electrical poling generates circular domains of about 130 ± 20 nm in diameter, the data storage density is estimated to be 37 Gbit/inch^2. The average size of the spot obtained in these nanostructured systems is smaller than the ones obtained for as prepared bilayers which have a size of 400-800 nm [1]. Also there is a decrease of the spot size in comparison to single layers and to systems nanostructured by other techniques as NIL [11].

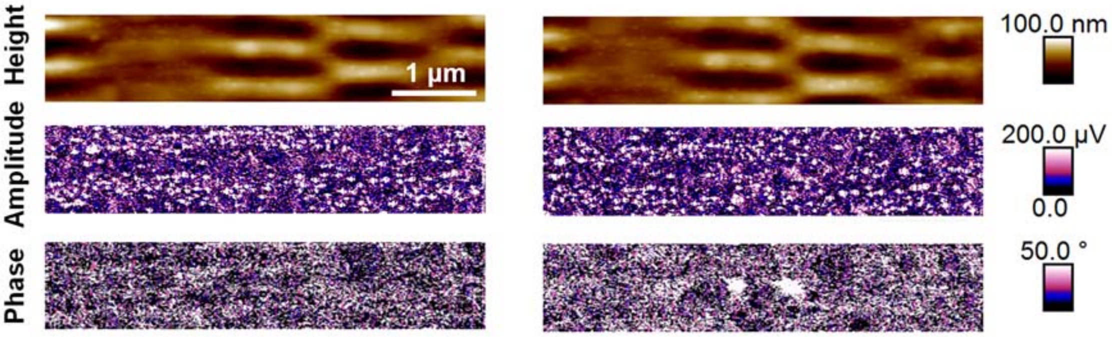

Figure 6.17 Left column: topography, PFM amplitude, and PFM phase shift of the nanostructured bilayer 1605 before poling. Right Column: topography, PFM amplitude and PFM phase shift of the nanostructured LIPSS (1605) after poling at three points at 12 V for 100 s.

It is important to mention that at least at laboratory times the bilayers nanostructured by laser retain the dipole information. Additionally, the fact that the bilayer architectures can be operated by a few volts and with high writing speed, comply with the requirements for developing applications in non-volatile organic memories.

6.6 Conclusion

Laser-induced periodic surface structures can be prepared on polymer thin films, despite the absence of light absorption at the wavelength of the irradiating laser, by using a bilayer approach. We have shown that the nanostructuring of a P3HT layer, by laser irradiation at 532 nm, covered by a thin layer of a non-absorbing polymer, in this case, the ferroelectric polymer P(VDF-TrFE), allows the development of a grating-like structure on the surface. This approach will be useful not only for the case of P(VDF-TrFE) but for any other non-absorbing polymer, making this technique more versatile and thus paving the way for a wider range of applications. The range of thicknesses of the upper layer which leads to the formation of LIPSS has been determined. In this case, for a thickness larger than 40 nm, no periodic structures are formed, neither in the upper layer nor in the bottom P3HT one. This can be explained considering a mechanical restriction which prevents P3HT rearrangement. The presence of LIPSS preserves the ferroelectric properties of the P(VDF-TrFE), as evidenced by PFM and the laser fabricated nanogratings are proposed as appropriate systems for non-volatile organic memories.

6.7 References

[1] Martínez-Tong, D. E. *Confinamiento en Nanoestructuras Poliméricas: Preparación Propiedades, Aplicaciones e Implicaciones Físicas*, 2015).

[2] Cui, J., Rodríguez-Rodríguez, Á., Hernández, M., García-Gutiérrez, M.-C., Nogales, A., Castillejo, M., González, D. M., Müller-Buschbaum, P., Ezquerra, T. A. and Rebollar, E. On the Laser Induced Periodic Surface Structures of P3HT and of its Blend with PC71BM. *Submitted to ACS Applied Materials & Interfaces* (2016).

[3] Rodríguez-Rodríguez, Á., Rebollar, E., Soccio, M., Ezquerra, T. A., Rueda, D. R., Garcia-Ramos, J. V., Castillejo, M. and Garcia-Gutierrez, M.-C. Laser-Induced Periodic Surface Structures on Conjugated Polymers: Poly(3-hexylthiophene). *Macromolecules* **48**, 4024-4031 (2015).

[4] Rebollar, E., Pérez, S., Hernández, J. J., Martín-Fabiani, I., Rueda, D. R., Ezquerra, T. A. and Castillejo, M. Assessment and Formation Mechanism of Laser-Induced Periodic Surface Structures on Polymer Spin-Coated Films in Real and Reciprocal Space. *Langmuir* **27**, 5596-5606 (2011).

[5] Martín-Fabiani, I., Rebollar, E., Pérez, S., Rueda, D. R., García-Gutiérrez, M. C., Szymczyk, A., Roslaniec, Z., Castillejo, M. and Ezquerra, T. A. Laser-induced Periodic Surface Structures Nanofabricated on Poly(trimethylene terephthalate) Spin-coated Films. *Langmuir* **28**, 7938-7945 (2012).

[6] Rebollar, E., Rueda, D. R., Martín-Fabiani, I., Rodríguez-Rodríguez, Á., García-Gutiérrez, M.-C., Portale, G., Castillejo, M. and Ezquerra, T. A. In Situ Monitoring of Laser-induced Periodic Surface Structures Formation on Polymer Films by Grazing Incidence Small-Angle X-ray Scattering. *Langmuir* **31**, 3973-3981 (2015).

[7] Rueda, D. R., Martin-Fabiani, I., Soccio, M., Alayo, N., Perez-Murano, F., Rebollar, E., Garcia-Gutierrez, M. C., Castillejo, M. and Ezquerra, T. A. Grazing-incidence Small-angle X-ray Scattering of Soft and Hard Nanofabricated Gratings. *Journal of Applied Crystallography* **45**, 1038-1045 (2012).

[8] Hwang, S. K., Bae, I., Cho, S. M., Kim, R. H., Jung, H. J. and Park, C. High Performance Multi-Level Non-Volatile Polymer Memory with Solution-blended Ferroelectric Polymer/high-k Insulators for Low Voltage Operation. *Advanced Functional Materials* **23**, 5484-5493 (2013).

[9] Wu, Z., Petzold, A., Henze, T., Thurn-Albrecht, T., Lohwasser, R. H., Sommer, M. and Thelakkat, M. Temperature and Molecular Weight Dependent Hierarchical Equilibrium Structures in Semiconducting Poly(3-hexylthiophene). *Macromolecules* **43**, 4646-4653 (2010).

[10] Kohn, P., Rong, Z., Scherer, K. H., Sepe, A., Sommer, M., Müller-Buschbaum, P., Friend, R. H., Steiner, U. and Hüttner, S. Crystallization-Induced 10-nm Structure Formation in P3HT/PCBM Blends. *Macromolecules* **46**, 4002-4013 (2013).

[11] Martinez-Tong, D. E., Soccio, M., Garcia-Gutierrez, M. C., Nogales, A., Rueda, D. R., Alayo, N., Perez-Murano, F. and Ezquerra, T. A. Improving Information Density in Ferroelectric Polymer Films by Using Nanoimprinted Gratings. *Applied Physics Letters* **102**, 191601-191605 (2013).

[12] Kang, S. J., Bae, I., Shin, Y. J., Park, Y. J., Huh, J., Park, S.-M., Kim, H.-C. and Park, C. Nonvolatile Polymer Memory with Nanoconfinement of Ferroelectric Crystals. *Nano Letters* **11**, 138-144 (2011).

[13] Garcia-Gutierrez, M.-C., Linares, A., Martin-Fabiani, I., Hernandez, J. J., Soccio, M., Rueda, D. R., Ezquerra, T. A. and Reynolds, M. Understanding Crystallization Features of P(VDF-TrFE) Copolymers under Confinement to Optimize Ferroelectricity in Nanostructures. *Nanoscale* **5**, 6006-6012 (2013).

[14] Tashiro, K. and Tanaka, R. Structural Correlation Between Crystal Lattice and Lamellar Morphology in the Ferroelectric Phase Transition of Vinylidene Fluoride–trifluoroethylene Copolymers As Revealed By the Simultaneous Measurements of Wide-angle and Small-angle X-ray Scatterings. *Polymer* **47**, 5433-5444 (2006).

[15] Liu, F., Chen, D., Wang, C., Luo, K., Gu, W., Briseno, A. L., Hsu, J. W. P. and Russell, T. P. Molecular Weight Dependence of the Morphology in P3HT:PCBM Solar Cells. *ACS Applied Materials & Interfaces* **6**, 19876-19887 (2014).

[16] Joshi, S., Pingel, P., Grigorian, S., Panzner, T., Pietsch, U., Neher, D., Forster, M. and Scherf, U. Bimodal Temperature Behavior of Structure and Mobility in High Molecular Weight P3HT Thin Films. *Macromolecules* **42**, 4651-4660 (2009).

[17] Martínez-Tong, D. E., Soccio, M., Sanz, A., García, C., Ezquerra, T. A. and Nogales, A. Ferroelectricity and Molecular Dynamics of Poly(vinylidenefluoride-trifluoroethylene) Nanoparticles. *Polymer* **56**, 428-434 (2015).

[18] Li, W., Zhu, Y., Hua, D., Wang, P., Chen, X. and Shen, J. Crystalline Morphologies of P(VDF-TrFE) (70/30) Copolymer Films above Melting Point. *Applied Surface Science* **254**, 7321-7325 (2008).

[19] Hu, Z., Tian, M., Nysten, B. and Jonas, A. M. Regular Arrays of Highly Ordered Ferroelectric Polymer Nanostructures for Non-volatile Low-voltage Memories. *Nature Materials* **8**, 62-67 (2009).

7

Conclusions

In this Thesis we have developed different procedures to prepare nanostructured functional polymers and we have attempted to understand some of the underlying modifications of fundamental physical processes that this nanostructuring imposes.

The main conclusions of this Thesis are listed below.

- The dynamics and charge transport of a functional blend with applications in organic photovoltaics as bulk heterojunctions have been investigated by dielectric spectroscopy. At low temperature of P3HT in blends of it with $PC_{71}BM$ is mainly due to the local motion of the lateral hexyl chains in P3HT, and is nearly unaffected by the presence of the other component of the blend: $PC_{71}BM$. In terms of charge transport, the conductivity of these blends exhibits two different behaviors in different temperature ranges. At lower temperatures the conductivity can be described by an Arrhenius behavior whereas it follows the Gaussian Disorder model in the higher temperature region. By this analysis we were able to estimate the energetic offsets of the bulk heterojunction system due to the presence of the $PC_{71}BM$.
- The combination of a semiconducting polymer as P3HT and a ferroelectric polymer, as P(VDF-TrFE) in blends provides a two-fold functionality, but the need of control on the domains obtained by direct mixing is a drawback. We have been able to design strategies to prepare blends with controlled morphology. Precisely, ferroelectric polymer nanoparticles embedded in a continuous P3HT matrix, or bilayers of both polymers. In both cases we have proved that the functionality of each of the components is preserved.
- In the case of the bilayers we have observed that the thickness of the P3HT bottom layer plays a crucial role in the morphology of the upper P(VDF-TrFE) layer. We have concluded that the polar component of the surface energy is the responsible for this behavior.
- Nanostructuring functional polymer surfaces is often the way to implement these materials in devices. We have demonstrated that the functional nanostructured surfaces of P3HT can be fabricated by the repetition of pulsed laser irradiation, creating Laser Induced Periodic Surface Structures (LIPSS). We have carried out a deep study on the

creation of LIPSS on a model polymer, polystyrene for which the most important thermal characteristics are known and tabulated in the literature. By the careful assessment of all the relevant parameters of the studied system, like thickness, substrate and light absorption coefficient, we have been able to model the distribution of temperatures in the film during irradiation. The results allow us to determine the optimal conditions for LIPSS formation, that were later applied to functional polymer (P3HT).

- With the above knowledge, we have been able to create LIPSS on the ferroelectric polymer P(VDF-TrFE). P(VDF-TrFE) has a weak absorption at the laser wavelength, and therefore it cannot form LIPSS on its own. By preparing a bilayer structure with a light-absorbing polymer as bottom layer, in this case P3HT, laser irradiation induces LIPSS formation on the P(VDF-TrFE) layer. However, the perfection of these LIPSS depends on the thickness of both layers.
- The crystal structure and orientation of P(VDF-TrFE) do not significantly change upon irradiation, as we have concluded from grazing incident X ray diffraction. Thus, its ferroelectric character would not be affected. PFM techniques evidenced that P(VDF-TrFE) LIPSS preserve the ferroelectric properties on the bilayer polymer system.

Articles from this thesis

- D.E. Martínez-Tong, J. Cui, M. Soccio, M.C. García, T.A. Ezquerra and A. Nogales C. Does the glass transition of polymers changes upon 3D confinement? **Macromolecular Chemistry and Physics**, 2014, 215, 1620-1624.

- J. Cui, D.E. Martínez-Tong, A. Sanz, T.A. Ezquerra, E. Rebollar, and A. Nogales. Relaxation and Conductivity in P3HT/PC71BM Blends as Revealed by Dielectric Spectroscopy. **Macromolecules**, 2016, 49, 2709-2717.

- J. Cui, A. Nogales, T.A. Ezquerra, E. Rebollar. Effect of Film Thickness and Substrate Properties on Polymer LIPSS Formation. **Applied Surface Science** (In press).

- J. Cui, A. Rodríguez, M. Hernández, M.C. García-Gutiérrez, A. Nogales, M. Castillejo, D. Moseguí-González, P. Müller-Buschbaum, T.A. Ezquerra and E. Rebollar. On the Laser Induced Periodic Surface Structures of P3HT and of its Photovoltaic Blend with PC71BM. **ACS Applied Materials & Interfaces**. Submitted, in revision.

- J. Cui, M. Hernández, E. Rebollar, T.A. Ezquera, A. Nogales. Tuning Dewetting of Polymer Bilayers by Controlling the Thickness of the Polymer Substrate. In preparation.

- J. Cui, D. Fernández Martín, E. Rebollar, A. del Campo, J. Rodriguez- Hernández, A. Nogales. Long Range Breath Figures Self-assembly of Blends of P3HT/PC_{71}BM: Optical and Morphological Characterization. In preparation.

- J. Cui, D. Martínez-Tong, E. Rebollar, T.A. Ezquerra, A. Nogales. PiezoResponse Force Microscopy in P(VDF-TrFE) Nanoparticles Embedded in Continuous P3HT Thin Films. In preparation.

- J. Cui, M. Hernández, A. Rodriguez-Rodriguez, A. Nogales, M.C. García-Gutierrez, T.A. Ezquerra, E. Rebollar. On the Laser Induced Surface Structures of Ferroelectric Polymers. In preparation.

Other articles published

- B. Zhang, J. Chen, J. Cui, H. Zhang, F. Ji, G. Zheng, B. Heck, G. Reiter, and C. Shen. Effect of Shear Stress on Crystallization of Isotactic Polypropylene from a Structured Melt. **Macromolecules**, 2012, 45, 8933-8937.